

**MULTIPLE-TERMINAL GRID
INTERCONNECTED OFFSHORE WIND
FARMS: DEVELOPMENT OF TRANSIENT
BEHAVIOURAL SIMULATION MODELS
AND PROTECTION SCHEMES**

Thesis

Submitted in partial fulfillment of the requirements for the degree of

DOCTOR OF PHILOSOPHY

by

M. MOHAN



DEPARTMENT OF ELECTRICAL AND ELECTRONICS ENGINEERING

NATIONAL INSTITUTE OF TECHNOLOGY KARNATAKA

SURATHKAL, MANGALORE - 575025

FEBRUARY 2021

DECLARATION

by the Ph.D. Research Scholar

I hereby *declare* that the Research Thesis entitled **Multiple-Terminal Grid Interconnected offshore wind Farms: Development of Transient Behavioural Simulation Models and Protection Schemes** which is being submitted to the **National Institute of Technology Karnataka, Surathkal** in partial fulfillment of the requirement for the award of the Degree of **Doctor of Philosophy in Department of Electrical and Electronics Engineering** is a *bonafide report of the research work carried out by me*. The material contained in this Research Thesis has not been submitted to any University or Institution for the award of any degree.

.....

M. Mohan, 145075EE14F04

Department of Electrical and Electronics Engineering

Place: NITK Surathkal

Date:

CERTIFICATE

This is to *certify* that the Research Thesis entitled **Multiple-Terminal Grid Interconnected offshore wind Farms: Development of Transient Behavioural Simulation Models and Protection Schemes** submitted by **M. Mohan** (Register Number: 145075EE14F04) as the record of the research work carried out by him, is *accepted as the Research Thesis submission* in partial fulfillment of the requirements for the award of degree of **Doctor of Philosophy**.

Dr. K. Panduranga Vittal
(Research Guide)
Professor and Dean (AA&IR)
Department of Electrical and Electronics Engineering
NITK Surathkal – 575025

Dr. Shubhanga K N
(Chairman - DRPC)
Professor and Head of the Department
Department of Electrical and Electronics Engineering
NITK Surathkal – 575025

ACKNOWLEDGEMENTS

It gives me immense pleasure and a great sense of satisfaction to express my heartfelt gratitude to those who made this dissertation possible.

I would like to express my sincere gratitude to *Dr. K. Panduranga Vittal*, Professor and Dean (AA&IR), Department of Electrical and Electronics Engineering, NITK Surathkal, for his guidance, encouragement, and for having been my Ph.D. supervisor. He has been a constant source of inspiration throughout this journey. I feel proud to have worked under his guidance.

I wish to thank my research progress assessment committee (RPAC) members *Dr. Vinatha U*, Associate Professor, Department of Electrical and Electronics Engineering, NITK Surathkal, and *Dr. P. Santhi Thilagam*, Professor, Department of Computer Science and Engineering, NITK Surathkal, for their constructive feedback and guidance.

I thank National Institute of Technology Karnataka (NITK), Surathkal for giving me an opportunity for doing research and Ministry of Human Resource Development (MHRD), Government of India for awarding research scholarship.

I would like to express my deepest gratitude towards my family for their love and patience which kept me going in this journey. Their faith and unconditional love towards me are the reason for whatever I have achieved in my life.

Finally, I thank Madurai Veeran, for giving me strength at all times.

ABSTRACT

Offshore wind farms (OWF) are the highly penetrative energy sources in the electric power systems due to the continuous increase in energy demand. The generated offshore wind power cannot be supplied directly to the customers due to the variable generations and installed locations; instead, it can be integrated with the AC grid using high voltage alternating current (HVAC) or high voltage direct current (HVDC) link. The HVDC link is mostly preferred for the long-distance bulk power transmission due to its various advantages such as low losses, possible to control the power flow and perform an asynchronous operation, no charging current and stability issues. Voltage source converters (VSC)-based HVDC transmission system is a favorable option to interconnect the remote renewable sources with the AC grids since it has fault current blocking capability, operation with weak AC grids and maintains constant DC voltage even if power direction changes. Multi-terminal (MT) HVDC network becomes more attractive over two-terminal configurations due to the reduced number of terminals and sustains the power flow even under fault in a DC line. The research work in this thesis built transient behavioural model of the multi-terminal VSC-based HVDC link connected offshore wind farms, and also different case studies are carried out to evaluate the performance of the MT VSC-based HVDC system under power system disturbances.

One of the main limitations of VSC is its vulnerability to DC faults. The protection of the DC line is more challenging due to low impedance, no natural zero crossing, low rise time and high steady-state fault currents. DC faults in a multi-terminal VSC-based HVDC transmission system gives very high peak fault current within a few milliseconds. The protection unit installed in the AC grid can address only steady-state faults in the DC grid. Protection unit has to be developed before semiconductor-based device damages due to very less overload capability. Two-end measurement gives certain time delay for long transmission lines which will slow down the protection decision speed. This thesis presents the development of a single-ended protection scheme for DC faults in multi-terminal VSC-based HVDC transmission system both without and with current limiting reactors. In this protection scheme, the protection

starting unit uses the under-voltage criterion to detect the faults. The fault discrimination is done by using three conditions such as rate of change of DC voltage and current, and increment of transient energy. Current limiting reactors are designed and connected in series with the DC circuit breaker (CB) to maintain the DC fault current within the breaker capacity until protection unit isolates the faulty line.

With the penetration of VSC-based HVDC system into the AC grid, the challenges in the distance relaying of AC transmission line has increased. When the fault occurs in a line close to the point of common coupling (PCC) in an AC grid with VSC-based HVDC transmission system, Zone-2 distance relay overestimates the fault distance due to the fast control of VSC. This makes distance relay to treat Zone-2 fault as Zone-3 fault, whereas Zone-3 fault is pushed out of the protection zones, leads to protection miscoordination. Therefore, the research work in this thesis intends to investigate the impact of VSC-based HVDC system on distance protection of AC transmission lines.

Keywords:

Wind Energy, High Voltage Direct Current (HVDC), Voltage Source Converters (VSC), Multi-terminal Grids, Power System Disturbances, DC Fault Protection, Distance Relay.

TABLE OF CONTENTS

| | |
|--|--------------|
| ACKNOWLEDGEMENTS..... | i |
| ABSTRACT..... | ii |
| TABLE OF CONTENTS..... | iv |
| LIST OF FIGURES..... | ix |
| LIST OF TABLES..... | xvi |
| LIST OF ABBREVIATIONS..... | xviii |
| | |
| CHAPTER 1 | |
| INTRODUCTION..... | 1 |
| 1.1 Offshore Wind Mills as Remote Renewable Energy Sources..... | 1 |
| 1.1.1 Grid Connection of Offshore Wind Farms..... | 1 |
| 1.1.2 Multi-terminal Grids..... | 3 |
| 1.1.3 HVDC Links..... | 5 |
| 1.2 Faults in Transmission Links..... | 7 |
| 1.2.1 AC Faults..... | 7 |
| 1.2.2 DC Faults..... | 8 |
| 1.3 Survey of Literature on Faults in Multi-terminal DC Links and Protection Methodology..... | 11 |
| 1.3.1 DC Fault Protection Methods in HVDC Links..... | 12 |
| 1.3.2 Challenges in Distance Relaying of AC Grid in the presence of HVDC Links..... | 19 |
| 1.4 Objectives of The Thesis..... | 21 |
| 1.5 Organization of The Thesis..... | 22 |
| | |
| CHAPTER 2 | |
| MULTI-TERMINAL VSC-HVDC LINK CONNECTED OFFSHORE WIND FARMS..... | 24 |
| 2.1 PMSG Coupled Offshore Wind Power Generation..... | 24 |
| 2.1.1 Wind Farm Model..... | 25 |

| | | |
|---------|--|----|
| 2.1.1.1 | Wind Turbine..... | 25 |
| 2.1.1.2 | Permanent Magnet Synchronous Generator..... | 27 |
| 2.1.2 | Modeling of Grid Connected Wind Energy System..... | 28 |
| 2.1.2.1 | Behaviour under Start-up Conditions..... | 30 |
| 2.1.2.2 | Behaviour under Gust Wind Conditions | 32 |
| 2.1.2.3 | Behaviour under Ramp Wind conditions..... | 33 |
| 2.1.2.4 | Behaviour under Noisy Wind Conditions..... | 34 |
| 2.2 | AC Grid Connected Voltage Source Converter on No Load Condition | 35 |
| 2.2.1 | Modeling of AC Grid Connected VSC..... | 35 |
| 2.2.1.1 | Converter transformer..... | 36 |
| 2.2.1.2 | Phase Reactor..... | 36 |
| 2.2.1.3 | AC Filters..... | 37 |
| 2.2.1.4 | Voltage Source Converters..... | 38 |
| 2.2.1.5 | Control Model of VSC..... | 38 |
| 2.2.1.6 | Sinusoidal Pulse Width Modulation..... | 42 |
| 2.2.1.7 | DC Capacitor..... | 43 |
| 2.2.1.8 | DC Transmission Line..... | 44 |
| 2.2.2 | Simulation of AC Grid Connected VSC System on PSCAD.... | 45 |
| 2.2.2.1 | Steady State Behaviour..... | 45 |
| 2.2.2.2 | Harmonic Distortions..... | 46 |
| 2.2.2.3 | AC Fault Conditions..... | 48 |
| 2.3 | Windmill Connected Voltage Source Converter on No Load Condition..... | 50 |
| 2.3.1 | Modeling of Windmill Connected VSC..... | 50 |
| 2.3.2 | Analysis of Simulation Results..... | 52 |
| 2.3.2.1 | Steady State Behaviour..... | 52 |
| 2.3.2.2 | Changes in the Wind Speed..... | 53 |
| 2.4 | Windmill and AC Source Connected VSC on No Load Condition..... | 55 |
| 2.4.1 | Analysis of Simulation Results on Harmonic Distortions..... | 56 |
| 2.5 | Conclusions..... | 58 |

| | |
|--|-----------|
| CHAPTER 3 | |
| SIMULATION STUDIES ON POWER SYSTEM DISTURBANCES IN MULTI-TERMINAL VSC-BASED HVDC SYSTEMS..... | 60 |
| 3.1 Test Case 1..... | 60 |
| 3.1.1 AC Fault Conditions..... | 61 |
| 3.1.2 DC Fault Conditions..... | 63 |
| 3.1.3 Influence of Variability of Wind Energy Generation on System Fault Conditions..... | 64 |
| 3.1.3.1 Gust Wind Conditions..... | 64 |
| 3.1.3.2 Ramp Wind Conditions..... | 67 |
| 3.2 Test Case 2..... | 69 |
| 3.2.1 AC Fault Conditions..... | 70 |
| 3.2.2 DC Fault Conditions..... | 71 |
| 3.3 Test Case 3..... | 74 |
| 3.3.1 Influence of Dynamic Conditions of VSC on System Performance..... | 76 |
| 3.4 Conclusions..... | 79 |

| | |
|---|-----------|
| CHAPTER 4 | |
| A SINGLE-ENDED PROTECTION SCHEME FOR DC FAULTS IN MULTI-TERMINAL VSC-BASED HVDC SYSTEMS..... | 80 |
| 4.1 Modeling of Single-ended Protection Scheme..... | 80 |
| 4.1.1 Fault Detection..... | 81 |
| 4.1.2 Fault Discrimination..... | 83 |
| 4.2 Simulation Studies..... | 84 |
| 4.2.1 Three-terminal VSC-HVDC System without Current Limiting Reactors..... | 84 |
| 4.2.1.1 Pole-to-Pole Fault Condition..... | 84 |
| 4.2.1.2 Pole-to-Ground Fault Condition..... | 88 |
| 4.2.2 Three-terminal VSC-HVDC System with Current Limiting Reactors..... | 92 |

| | |
|--|-----|
| 4.2.2.1 Design of Current Limiting Reactors..... | 93 |
| 4.2.2.2 Pole-to-Pole Fault Condition..... | 95 |
| 4.2.2.3 Pole-to-Ground Fault Condition..... | 100 |
| 4.3 Conclusions..... | 103 |

CHAPTER 5

THE IMPACT OF VSC-BASED HVDC SYSTEMS ON DISTANCE

| | |
|---|------------|
| PROTECTION OF AC TRANSMISSION LINES..... | 105 |
| 5.1 AC Grid Protection..... | 105 |
| 5.2 Modeling of the Distance Relay..... | 107 |
| 5.3 Study of VSC-HVDC Impacts on Distance Protection of AC Transmission Lines..... | 112 |
| 5.4 Simulation Studies to Evaluate the VSC-HVDC Impacts on Distance Relay Performance..... | 114 |
| 5.4.1 Fault on Zone-1 Area of Relay..... | 114 |
| 5.4.1.1 Phase-to-Ground Fault Condition..... | 115 |
| 5.4.1.2 Phase-to-Phase Fault Condition..... | 119 |
| 5.4.1.3 Effect of Fault Resistance on Relay Performance under Phase-to-Ground Fault Condition..... | 121 |
| 5.4.2 Fault on Zone-2 Area of Relay..... | 124 |
| 5.4.2.1 Phase-to-Ground Fault Condition..... | 125 |
| 5.4.2.2 Phase-to-Phase Fault Condition..... | 129 |
| 5.4.2.3 Relay Performance under Change in VSC AC Voltage Reference Input..... | 133 |
| 5.4.2.4 Effect of Fault Resistance on Relay Performance under Phase-to-Ground Fault Condition..... | 135 |
| 5.4.3 Fault on Zone-3 Area of Relay..... | 138 |
| 5.4.3.1 Phase-to-Ground Fault Condition..... | 138 |
| 5.4.3.2 Phase-to-Phase Fault Condition..... | 142 |
| 5.4.3.3 Relay Performance under Change in VSC AC Voltage Reference Input..... | 145 |

| | |
|---|-----|
| 5.4.3.4 Effect of Fault Resistance on Relay Performance under Phase-to-Ground Fault Condition..... | 147 |
| 5.5 Conclusions..... | 150 |
| CHAPTER 6 | |
| DESIGN AND SIMULATION OF EARTH FAULT QUADRILATERAL RELAYS FOR AC TRANSMISSION LINES WITH VSC-BASED HVDC SYSTEMS..... | |
| 6.1 Introduction..... | 152 |
| 6.2 Study System..... | 153 |
| 6.3 Design of Quadrilateral Relays..... | 154 |
| 6.3.1 Zone-1 setting..... | 155 |
| 6.3.2 Zone-2 setting..... | 156 |
| 6.3.3 Zone-3 setting..... | 157 |
| 6.3.4 PSCAD Simulation Model..... | 157 |
| 6.4 Simulation Studies..... | 160 |
| 6.4.1 Phase-to-Ground Fault Condition..... | 161 |
| 6.4.2 Step Change in VSC AC Voltage Reference Input during Phase-to-Ground Fault Condition..... | 163 |
| 6.4.3 Comparison of Mho and Quadrilateral Relay..... | 164 |
| 6.4.3.1 Zone-1 Faults..... | 164 |
| 6.4.3.2 Zone-2 Faults..... | 166 |
| 6.5.3.3 Zone-3 Faults..... | 169 |
| 6.5 Conclusions..... | 172 |
| CHAPTER 7 | |
| CONCLUSIONS..... | 174 |
| REFERENCES..... | 178 |
| PUBLICATIONS BASED ON THESIS..... | 191 |
| CURRICULUM VITAE..... | 193 |

LIST OF FIGURES

| | | |
|------|--|----|
| 1.1 | Wind farm connected to AC grid. (a) via HVAC link, (b) via HVDC link..... | 2 |
| 1.2 | Multi-terminal DC (MTDC) grid configurations..... | 4 |
| 1.3 | Basic configurations of HVDC links..... | 5 |
| 1.4 | AC faults. (a) L-L fault, (b) L-G fault, (c) 2-L-G fault, (d) 3-phase fault..... | 8 |
| 1.5 | DC pole-to-pole fault in VSC-based HVDC system..... | 9 |
| 1.6 | DC pole-to-ground fault in VSC-based HVDC system..... | 11 |
| 2.1 | The offshore wind farms are connected to the AC grid using Multi-terminal VSC-based HVDC Link..... | 24 |
| 2.2 | Wind power generation model..... | 25 |
| 2.3 | Power coefficient (C_p) vs tip speed ratio (λ) curve..... | 26 |
| 2.4 | The power curve of the wind turbine..... | 26 |
| 2.5 | The equivalent circuit of the PMSG, (a) q-axis, (b) d-axis..... | 28 |
| 2.6 | The block diagram of the grid connected wind energy system..... | 29 |
| 2.7 | The response of the wind energy system during start-up conditions..... | 31 |
| 2.8 | The response of the wind energy system during gust wind conditions.... | 32 |
| 2.9 | The response of the wind energy system during ramp wind conditions.. | 34 |
| 2.10 | The response of the wind energy system during noisy wind conditions.. | 35 |
| 2.11 | AC grid connected to the HVDC converter..... | 36 |
| 2.12 | Two-level voltage source converter..... | 38 |
| 2.13 | The decoupled d-q control strategy for VSC-HVDC system..... | 41 |
| 2.14 | Block diagram of SPWM..... | 42 |
| 2.15 | PSCAD simulation for the generation of gate pulses using SPWM..... | 43 |
| 2.16 | AC source connected VSC model..... | 45 |
| 2.17 | Steady-state response of the AC source connected VSC..... | 46 |
| 2.18 | Harmonic analysis of AC source connected VSC without filter..... | 47 |

| | | |
|------|--|----|
| 2.19 | Harmonic analysis of AC source connected VSC with high pass filter... | 48 |
| 2.20 | Schematic diagram of AC grid connected VSC under A-B fault..... | 49 |
| 2.21 | The response of the AC source connected VSC under line-to-line fault condition..... | 50 |
| 2.22 | Windmill connected VSC model..... | 51 |
| 2.23 | Steady state response of the windmill connected VSC..... | 53 |
| 2.24 | The response of the windmill connected VSC under gust wind conditions..... | 54 |
| 2.25 | Windmill and AC source connected VSC model..... | 55 |
| 2.26 | Harmonic analysis of the wind mill and AC source connected VSC without filter..... | 57 |
| 2.27 | Harmonic analysis of the windmill and AC source connected VSC with LC filter..... | 58 |
| 3.1 | Test case 1- Three terminal VSC-based HVDC transmission system linked offshore wind farms..... | 61 |
| 3.2 | The performance of the test case 1 - three-terminal VSC-HVDC system under phase A to ground fault at the LV side of T ₃ | 63 |
| 3.3 | The performance of the test case 1 - three-terminal VSC-HVDC system under DC pole-to-pole fault at terminal-2..... | 64 |
| 3.4 | The performance of the test case 1 - three-terminal VSC-HVDC system under gust wind during A-G fault at PMSG terminal of OWF-2..... | 66 |
| 3.5 | The performance of the test case 1 - three-terminal VSC-HVDC system under ramp wind during A-G fault at PMSG terminal of OWF-2..... | 68 |
| 3.6 | Test case 2 – Three-terminal VSC-based HVDC transmission system..... | 69 |
| 3.7 | The performance of the test case 2 - three-terminal VSC-HVDC system under three-phase-to-ground fault at HV side of T ₄ | 71 |
| 3.8 | The performance of the test case 2 - three-terminal VSC-HVDC system under DC pole-to-pole fault at 50 km distance from terminal-1..... | 72 |

| | | |
|------|--|----|
| 3.9 | The performance of the test case 2 - three-terminal VSC-HVDC system under DC pole-to-ground fault at 50 km distance from terminal-1..... | 73 |
| 3.10 | Test case 3 – two-terminal VSC-based HVDC transmission system..... | 74 |
| 3.11 | The decoupled d-q control strategy for test case 3 – two-terminal VSC-based HVDC transmission system..... | 75 |
| 3.12 | The performance of the test case 3 - two-terminal VSC-HVDC system under step variation of AC voltage reference ($V_{s-rms-ref}$) input at VSC ₂ | 77 |
| 3.13 | The performance of the test case 3 - two-terminal VSC-HVDC system under step variation of active power reference (P_{ref}) input at VSC ₂ | 78 |
| 4.1 | Protection of multi-terminal VSC-HVDC system..... | 81 |
| 4.2 | Single-ended protection logic flow diagram..... | 82 |
| 4.3 | Three-terminal VSC-HVDC system without current limiting reactors..... | 84 |
| 4.4 | The DC voltage and current measured at the relay R ₁₃ location under pole-to-pole fault at various locations in a line 1-3..... | 85 |
| 4.5 | The DC voltage and current measured at the relay R ₁₃ location under pole-to-pole fault at various locations in a line 3-2..... | 86 |
| 4.6 | The DC voltage and current measured at the relay R ₁₃ location under positive pole-to-ground fault at various locations in a line 1-3..... | 89 |
| 4.7 | The DC voltage and current measured at the relay R ₁₃ location under negative pole-to-ground fault at various locations in a line 1-3..... | 90 |
| 4.8 | Three-terminal VSC-HVDC system with current limiting reactors..... | 93 |
| 4.9 | The DC current (I_{dc}) at the relay R ₁₃ location for the different value of current limiting reactors under pole-to-pole fault at 10 km distance from terminal-1..... | 95 |
| 4.10 | The DC voltage and current measured at the relay R ₁₃ location under pole-to-pole fault at various locations in a line 1-3..... | 96 |

| | | |
|------|---|-----|
| 4.11 | The DC voltage and current measured at the relay R_{13} location under pole-to-pole fault at various locations in a line 3-2..... | 97 |
| 4.12 | The DC voltage and current measured at the relay R_{13} location under positive pole-to-ground fault at various locations in a line 1-3..... | 100 |
| 4.13 | The DC voltage and current measured at the relay R_{13} location under negative pole-to-ground fault at various locations in a line 1-3..... | 101 |
| 5.1 | The principles of operation of distance relay..... | 106 |
| 5.2 | The three-bus system with distance relay model..... | 106 |
| 5.3 | Flowchart Illustrates the Function of Distance Relaying..... | 108 |
| 5.4 | The frequency response of the full cycle window Fourier considering the number of samples per cycle (N) is 20..... | 109 |
| 5.5 | Mho relay with protection zones..... | 112 |
| 5.6 | The three-bus system with VSC-HVDC..... | 113 |
| 5.7 | The simulation model of the three-bus system connected to a VSC-HVDC..... | 114 |
| 5.8 | The performance of the relay R_{12} under the phase-to-ground (A-G) fault at 150 km distance from the bus-1 terminal in an AC system without VSC-HVDC..... | 116 |
| 5.9 | The performance of the relay R_{12} under the phase-to-ground (A-G) fault at 150 km distance from the bus-1 terminal in an AC system with VSC-HVDC..... | 118 |
| 5.10 | The performance of the relay R_{12} under the phase-to-phase (A-B) fault at 150 km distance from the bus-1 terminal in an AC system without VSC-HVDC..... | 120 |
| 5.11 | The performance of the relay R_{12} under the phase-to-phase (A-B) fault at 150 km distance from the bus-1 terminal in an AC system with VSC-HVDC..... | 121 |
| 5.12 | Effect of fault resistance (R_f) on relay R_{12} performance under A-G fault at 150 km distance from the bus-1 terminal in an AC system without VSC-HVDC..... | 122 |

| | | |
|------|---|-----|
| 5.13 | Effect of fault resistance (R_f) on relay R_{12} performance under A-G fault at 150 km distance from the bus-1 terminal in an AC system with VSC-HVDC..... | 123 |
| 5.14 | The performance of the relay R_{12} under the phase-to-ground (A-G) fault at 30 km distance from the bus-2 terminal in an AC system without VSC-HVDC..... | 126 |
| 5.15 | The performance of the relay R_{12} under the phase-to-ground (A-G) fault at 30 km distance from the bus-2 terminal in an AC system with VSC-HVDC..... | 129 |
| 5.16 | The performance of the relay R_{12} under A-B fault at 30 km distance from the bus-2 terminal in an AC system without VSC-HVDC..... | 130 |
| 5.17 | The performance of the relay R_{12} under A-B fault at 30 km distance from the bus-2 terminal in an AC system with VSC-HVDC..... | 132 |
| 5.18 | The performance of the relay R_{12} under A-G and A-B fault at 30 km distance from the bus-2 terminal in an AC system with VSC-HVDC for the different value of $V_{s-rms-ref}$ input during fault period..... | 134 |
| 5.19 | Effect of fault resistance (R_f) on relay R_{12} performance under A-G fault at 30 km distance from the bus-2 terminal in an AC system without VSC-HVDC..... | 136 |
| 5.20 | Effect of fault resistance (R_f) on relay R_{12} performance under A-G fault at 30 km distance from the bus-2 terminal in an AC system with VSC-HVDC..... | 137 |
| 5.21 | The performance of the relay R_{12} under A-G fault at 180 km distance from the bus-2 terminal in an AC system without VSC-HVDC..... | 140 |
| 5.22 | The performance of the relay R_{12} under A-G fault at 180 km distance from the bus-2 terminal in an AC system with VSC-HVDC..... | 142 |
| 5.23 | The performance of the relay R_{12} under A-B fault at 180 km distance from the bus-2 terminal in an AC system without VSC-HVDC..... | 143 |
| 5.24 | The performance of the relay R_{12} due to A-B fault at 180 km distance from the bus-2 terminal in an AC system with VSC-HVDC..... | 145 |

| | | |
|------|---|-----|
| 5.25 | The performance of the relay R_{12} under A-G and A-B fault at 180 km distance from the bus-2 terminal in an AC system with VSC-HVDC for the different value of $V_{s-rms-ref}$ during fault period..... | 147 |
| 5.26 | Effect of fault resistance (R_f) on relay R_{12} performance under A-G fault at 180 km distance from the bus-2 terminal in an AC system without VSC-HVDC..... | 148 |
| 5.27 | Effect of fault resistance (R_f) on relay R_{12} performance under A-G fault at 180 km distance from the bus-2 terminal in an AC system with VSC-HVDC..... | 149 |
| 6.1 | The three-bus system with VSC-HVDC..... | 154 |
| 6.2 | Three-zone quadrilateral characteristic-based distance relay..... | 155 |
| 6.3 | The PSCAD simulation model of Zone-1 quadrilateral relay..... | 158 |
| 6.4 | Zone-1 quadrilateral relay in PSCAD..... | 158 |
| 6.5 | Three-zone quadrilateral relay in PSCAD..... | 159 |
| 6.6 | Simulation cases for testing all the quadrant in the quadrilateral relay... | 160 |
| 6.7 | The performance of the quadrilateral relay R_{12} under A-G fault in an AC system for both without and with VSC-HVDC..... | 162 |
| 6.8 | The performance of quadrilateral relay R_{12} under A-G fault in an AC system with VSC-HVDC and step variation of $V_{s-rms-ref}$ of VSC_2 from 1.0 to 0.8 per unit during fault period..... | 163 |
| 6.9 | The comparison of Zone-1 mho and quadrilateral relay R_{12} under A-G fault with various fault resistance (R_f) at 150 km distance from the relay location in an AC system with VSC-HVDC..... | 165 |
| 6.10 | The comparison of Zone-2 mho and quadrilateral relay R_{12} under A-G fault with various fault resistance (R_f) at 230 km distance from the relay location in an AC system with VSC-HVDC. ($V_{s-rms-ref} = 1.0$ p.u.)..... | 167 |
| 6.11 | The comparison of Zone-2 mho and quadrilateral relay R_{12} under A-G fault with various fault resistance (R_f) at 230 km distance from the relay location in an AC system with VSC-HVDC and step variation of $V_{s-rms-ref}$ of VSC_2 from 1.0 to 0.8 per unit during fault period..... | 168 |

| | | |
|------|---|-----|
| 6.12 | The comparison of Zone-3 mho and quadrilateral relay R_{12} under A-G fault with various fault resistance (R_f) at 380 km distance from the relay location in an AC system with VSC-HVDC. ($V_{s-rms-ref} = 1.0$ p.u.)..... | 170 |
| 6.13 | The comparison of Zone-3 mho and quadrilateral relay R_{12} under A-G fault with various fault resistance (R_f) at 380 km distance from the relay location in an AC system with step variation of $V_{s-rms-ref}$ of VSC ₂ from 1.0 to 0.8 per unit during fault period..... | 171 |

LIST OF TABLES

| | | |
|-----|---|-----|
| 1.1 | Comparison of asymmetric and symmetric monopolar configurations. | 6 |
| 4.1 | The threshold determination of voltage and current derivatives, and increment of transient energy for the pole-to-pole fault condition in a three-terminal VSC-HVDC system without current limiting reactors..... | 87 |
| 4.2 | The fault detection time of relay R_{13} under pole-to-pole fault condition in the three-terminal VSC-HVDC system without current limiting reactors..... | 88 |
| 4.3 | The threshold determination of voltage and current derivatives, and increment of transient energy for the pole-to-ground fault condition in the three-terminal VSC-HVDC system without current limiting reactors..... | 91 |
| 4.4 | The fault detection time of relay R_{13} under pole-to-ground fault condition in the three-terminal VSC-HVDC system without current limiting reactors..... | 92 |
| 4.5 | The threshold determination of voltage and current derivatives, and increment of transient energy for the pole-to-pole fault condition in the three-terminal VSC-HVDC system with current limiting reactors..... | 98 |
| 4.6 | The fault detection time of relay R_{13} under pole-to-pole fault condition in the three-terminal VSC-HVDC system with current limiting reactors..... | 99 |
| 4.7 | The threshold determination of voltage and current derivatives, and increment of transient energy for the pole-to-ground fault condition in the three-terminal VSC-HVDC system with current limiting reactors..... | 102 |

| | | |
|-----|--|-----|
| 4.8 | The fault detection time of relay R_{13} under pole-to-ground fault condition in the three-terminal VSC-HVDC system with current limiting reactors..... | 103 |
| 5.1 | Fault impedance calculation for the phase and ground faults..... | 110 |
| 5.2 | The apparent impedance (Z_a) seen by the Zone-1 relay for the A-G fault with various fault resistance (R_f) at 150 km distance from the bus-1 terminal in an AC system both without and with VSC-HVDC..... | 124 |
| 5.3 | The apparent impedance (Z_a) seen by the Zone-2 relay for the A-G fault with various fault resistance (R_f) at 30 km distance from the bus-2 terminal in an AC system both without and with VSC-HVDC..... | 137 |
| 5.4 | The apparent impedance (Z_a) seen by the Zone-3 relay R_{12} for A-G fault with various fault resistance (R_f) at 180 km distance from the bus-2 terminal in an AC system for both without and with VSC-HVDC..... | 150 |
| 6.1 | The apparent impedance (Z_a) seen by the relay R_{12} under A-G fault condition..... | 162 |
| 6.2 | The apparent impedance (Z_a) seen by the relay R_{12} under A-G fault condition in an AC system with VSC-HVDC for different value of reference AC voltage ($V_{s-rms-ref}$)..... | 164 |
| 6.3 | The comparison of apparent impedance (Z_a) seen by the Zone-2 relay R_{12} for different value of $V_{s-rms-ref}$ of VSC_2 under A-G fault with different fault resistance (R_f) at 230 km distance from the relay location..... | 168 |
| 6.4 | The comparison of apparent impedance (Z_a) seen by the Zone-3 relay R_{12} for different value of $V_{s-rms-ref}$ of VSC_2 under A-G fault with different fault resistance (R_f) at 380 km distance from the relay location..... | 172 |

LIST OF ABBREVIATIONS

| | |
|------------------|--|
| CB | Circuit Breaker |
| CLR | Current Limiting Reactors |
| EMTDC | Electro Magnetic Transients including DC |
| FFT | Fast Fourier Transform |
| HPF | High Pass Filter |
| HVAC | High Voltage Alternating Current |
| HVDC | High Voltage Direct Current |
| IGBT | Insulated Gate Bipolar Transistor |
| LCC | Line Commutated Converter |
| MMC | Modular Multilevel Converter |
| MTDC | Multi-Terminal Direct Current |
| MVA | Mega Volt Ampere |
| MVA _r | Mega Volt Ampere reactive |
| OWF | Offshore Wind Farm |
| PCC | Point of Common Coupling |
| PMSG | Permanent Magnet Synchronous Generators |
| PSCAD | Power System Computer Aided Design |
| ROCOV | Rate Of Change Of Voltage |
| SPWM | Sinusoidal Pulse Width Modulation |
| THD | Total Harmonic Distortion |
| VSC | Voltage Source Converter |
| WT | Wind Turbine |

CHAPTER 1

INTRODUCTION

1.1 Offshore Wind Mills as Remote Renewable Energy Sources

Wind energy is one of the best technologies and widely used source of renewable energy for supplying the electric power to the world due to the availability of the wind and the absence of harmful emissions. Installation of offshore wind farms (OWFs) are growing since the last decade due to the continuous increase in power demand, wind at sea is more and an absence of land requirements. The large scale of the offshore wind farms can be formed by connecting the multiple numbers of the wind power generation unit.

The wind power generation system is mainly consisting of the wind turbine and AC generators. The wind turbine (WT) produces the mechanical energy from the kinetic energy, and it can be classified into two categories such as horizontal axis wind turbine (HAWT) and vertical axis wind turbine (VAWT). In the HAWT, the rotor shaft and the generator are arranged horizontally and located at the top of the tower. In the VAWT, the rotor shaft and the generator are arranged vertically, and it can be placed near the ground. The wind turbine can be used to operate on either fixed or variable speed. The variable speed operation is mostly preferred to extract the maximum available wind power and high-power quality [R. Perveen et al. 2014].

The various AC machines are available to generate the wind power such as doubly fed induction generators (DFIG), wound rotor synchronous generators, permanent magnet synchronous generators (PMSG) and squirrel cage induction generators (SCIG) [M. R. Islam et al. 2014]. The permanent magnet synchronous generator (PMSG) is more suitable for the wind power generation system due to the absence of separate field excitations, high efficiency, less maintenance, and also the power can be generated at any wind speed conditions.

1.1.1 Grid connection of Offshore Wind Farms

The generated offshore wind power cannot be supplied directly to the customers; instead, it can be integrated with the grid due to non-controllable variability,

unpredictable generation, and installed locations [L. Xu et al. 2007]. The large scale OWFs are integrated with the AC grid via high voltage alternating current (HVAC) or high voltage direct current (HVDC) link as shown in Figure 1.1. The HVAC transmission is applicable to the short distance such as below 50 km, but not suitable for long-distance power transmission due to large charging current since the cable capacitance being significantly high. Further, it is difficult to control the power flow, requires reactive power control and also has the limitation of high losses. Moreover, it does not have an asynchronous operation and also having an issue of the skin and Ferranti effect. Due to these drawbacks in the HVAC transmission, an application of high voltage direct current (HVDC) has increased. The HVDC link is the economical option for transmitting bulk power to long distance.

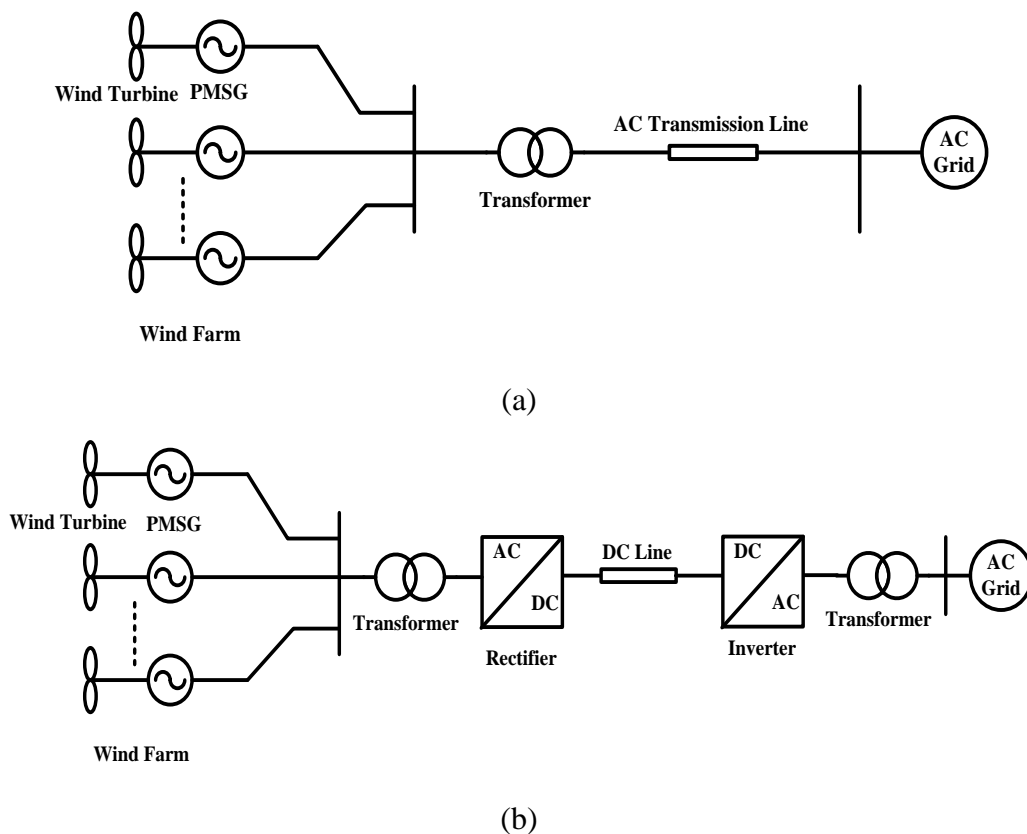


Figure 1.1 Wind farm connected to AC grid. (a) via HVAC link, (b) via HVDC link.

At the initial stage, the current source converters (CSC)-based HVDC system is used for the electrical power transfer for long-distance. The CSC-based HVDC system is developed based on thyristors, and it applies to high power ratings which give fewer

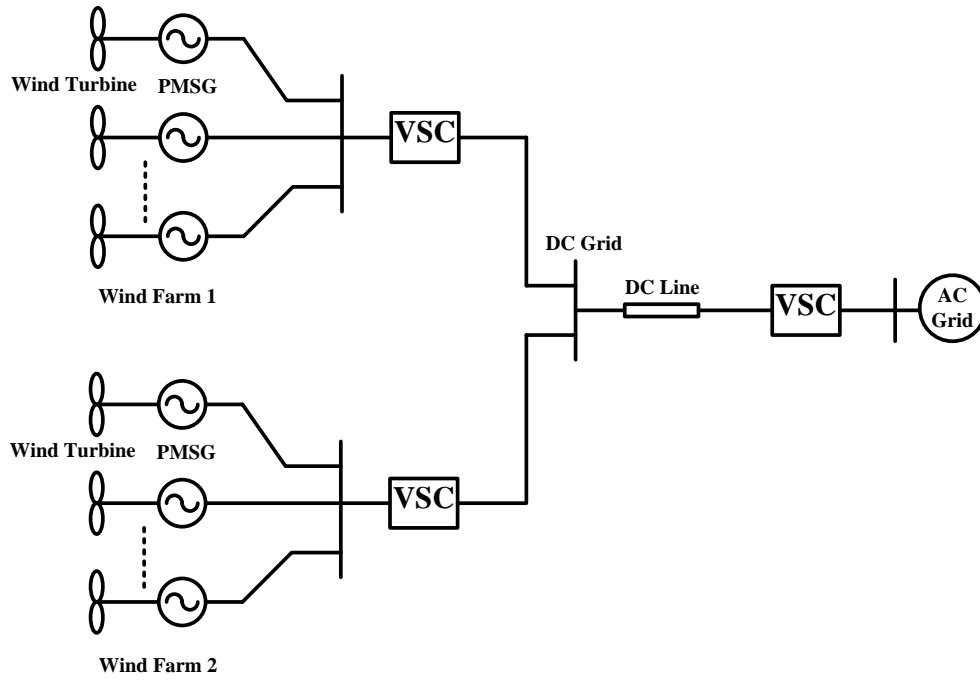
losses (i.e., about 0.7 %) [C. M. Franck 2011]. It is strong on the DC side due to large inductance connected on the DC side. However, the thyristor has only turn-on capability, and it does not have turn-off capability which will not interrupt the fault current. Also, it is vulnerable to AC side faults and requires large filters which will increase the capital cost. Due to these issues, the HVDC system is developed using voltage source converters.

The voltage source converters (VSC) are built by insulated gate bipolar transistor (IGBT). The VSC can block the fault current, operates with the weak AC systems like offshore wind farms due to the fast and robust controller, maintains constant DC voltage even if power direction changes. Therefore, an introduction of VSC into the HVDC system has increased in the past few years. However, the VSC has some drawbacks such as sensitive to DC faults, gives high losses (i.e., about 1.6 %) and lower power ratings [C. M. Franck 2011].

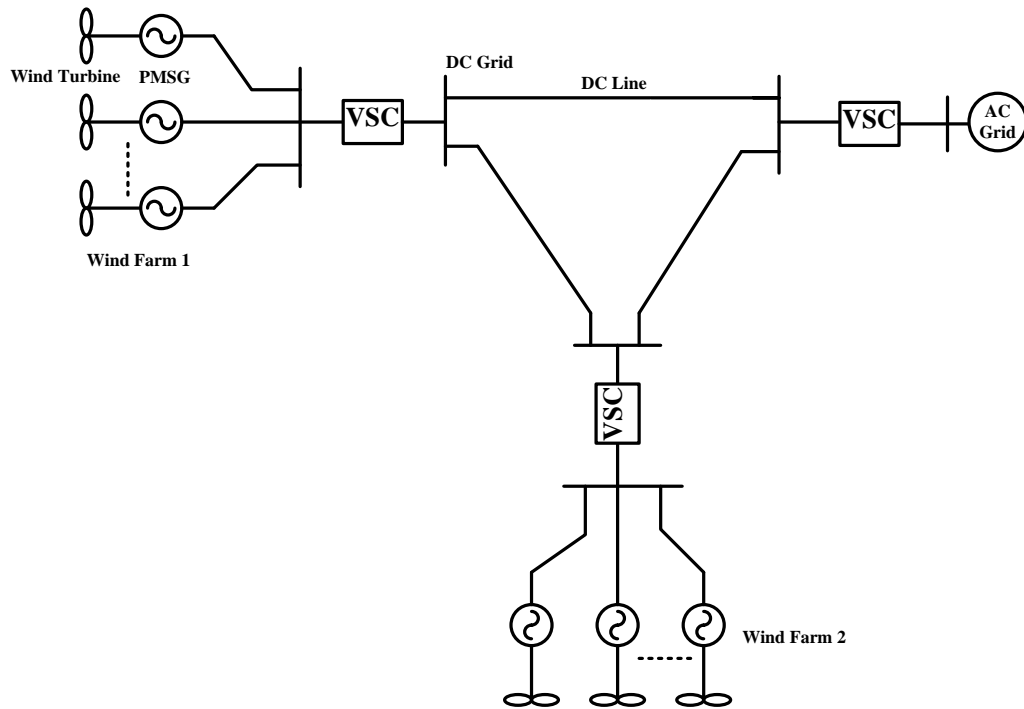
1.1.2 Multi-terminal Grids

At the initial stage, the point-to-point HVDC transmission system (i.e., two terminal HVDC transmission system) is used for the long-distance power transmission. However, the power flow can be interrupted if any fault occurs in a DC line in the point-to-point HVDC transmission system. Therefore, the multi-terminal (MT) configuration is applied for the power transfer in the VSC-based HVDC system. Building the MT network is very easy since the VSC maintains the constant DC voltage even if the power direction changes. The MT configuration gives less cost and more reliability than the two-terminal configurations since it requires a lesser number of terminals and also possible to transfer the power even under the faulty situation.

The multi-terminal direct current (MTDC) grid uses different topologies such as radial and meshed connection as shown in Figure 1.2. The Meshed connection of the MT network gives more reliability and flexibility than the radial network [M. K. Bucker et al. 2014]. Therefore, the meshed connection of the multi-terminal VSC-based HVDC system is the best option for the transmission of electric power from the offshore wind farms to the onshore AC grid.



(a) Radial connection.

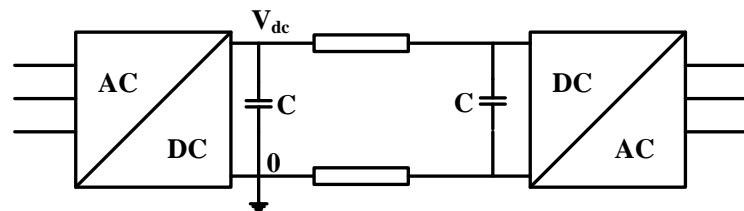


(b) Meshed connection.

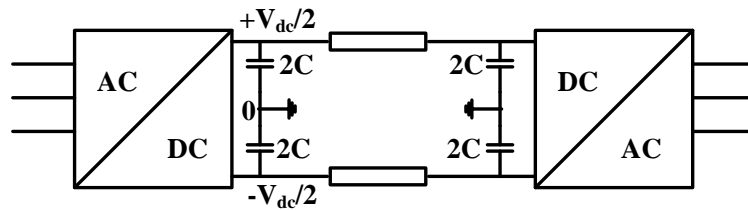
Figure 1.2 Multi-terminal DC (MTDC) grid configurations.

1.1.3 HVDC Links

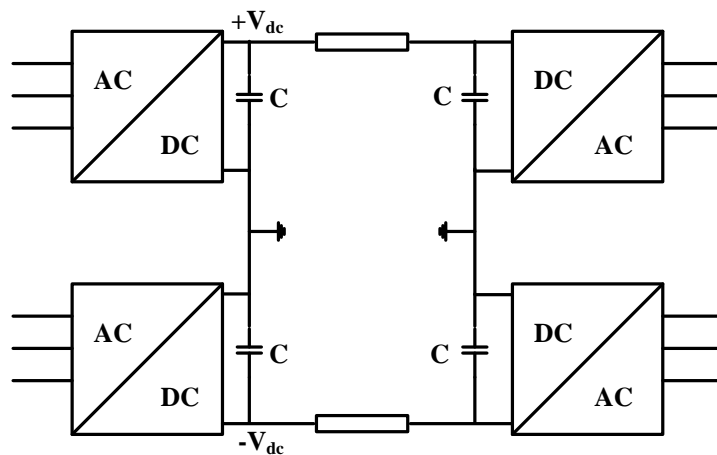
Many types of HVDC links are available to interconnect OWF with the AC grid. The major classification of HVDC links is monopolar and bipolar links. The schematic diagram of the monopolar and bipolar HVDC links are shown in Figure 1.3. It can be connected in the way of symmetric or asymmetric configurations. The asymmetric monopolar with metallic return configuration is shown in Figure 1.3 (a) which is grounded at the converter station, and metallic return path operates at near zero voltage under normal condition. In this case, the positive pole-to-ground voltage is equal to the rating of the converter voltage [W. Leterme et al. 2014].



(a) Asymmetric monopolar configuration.



(b) Symmetric monopolar configuration.



(c) Bipolar configuration.

Figure 1.3 Basic configurations of HVDC links.

The symmetric monopolar configuration is shown in Figure 1.3 (b), and it provides various voltage levels such as $\left(\frac{+V_{dc}}{2}, \frac{-V_{dc}}{2}\right)$, where V_{dc} is the pole-to-pole DC voltage. The positive pole-to-ground DC voltage is $\frac{+V_{dc}}{2}$. The schematic diagram of the bipolar HVDC link is shown in Figure 1.3 (c). The bipolar configuration can be connected by way of symmetric or asymmetric topology. It takes two converters at each end of the HVDC station when compared to the monopolar configuration. It can be applied for the higher power rating and voltage levels. However, it increases control complexity and total cost of the converters [E. Kontos et al. 2015]. Table 1.1 presents the comparison of asymmetric and symmetric monopolar configurations.

Table 1.1 Comparison of asymmetric and symmetric monopolar configurations.

| | Asymmetric Monopolar | Symmetric Monopolar |
|--|---|--|
| Configuration | Either Metallic return or ground return. | DC link capacitors are grounded at their middle point. |
| Grounding type | Low impedance (to limit the voltage rise on the metallic return conductor). | High impedance (grounded through DC capacitors or resistors). |
| Steady-state voltage in normal operation | Positive pole voltage is equal to the nominal voltage of the converter. (metallic return conductor is operated at almost zero voltage). | The voltage on each pole is half the nominal voltage of the converter. |
| Operating voltages | 0, V_{dc} | $\frac{+V_{dc}}{2}, \frac{-V_{dc}}{2}$ |
| Steady-state fault current | Large | Zero |
| Protection requirements | Fast protection | Less stringent time constraints |

The advantages of the symmetric monopolar configuration over asymmetric monopolar configuration are given below:

- The DC capacitor is grounded at the middle point of the DC link to avoid imbalance between the positive and negative DC voltages and currents.
- The steady-state voltage in the normal operation on each pole is half the converter voltage rating.
- In the symmetric monopolar configuration, the converter transformer is not affected by the DC voltage stress due to its symmetry.
- In the case of a pole-to-ground fault in the symmetric monopolar configuration, the DC side is not fed by AC side currents.
- The constraints of the fault clearance time have less stringent in case of symmetric monopolar configuration when compared to asymmetric monopolar configuration.

Due to these various advantages, the symmetric monopolar configuration is used for the multi-terminal VSC-based HVDC link which is interconnecting the OWFs with the AC grid.

1.2 Faults in Transmission Links

Various faults can exist in an HVDC system such as AC faults at the rectifier and inverter side, converter faults and DC faults. Usually, the faults can occur due to an insulation failure which is caused by a short circuit, switching event and lightning. The AC side faults can be divided into symmetric and asymmetric faults. The converter faults are the misfire, fire-through, DC link capacitor failure and flashover [A. F. Abdou et al. 2015]. The DC side faults are mainly categorized as the pole-to-pole fault and pole-to-ground fault.

1.2.1 AC Faults

The AC faults are symmetric, i.e., three-phase short circuit and asymmetric faults such as line-to-line (L-L) fault, line-to-ground (L-G) fault and double line-to-ground (2-L-G) fault which are shown in Figure 1.4. When the fault occurs in an AC transmission line connected with CSC-based HVDC station, commutation failure can

happen which leads to the voltage collapse. The distance relay can be used to protect the transmission line from the AC faults.

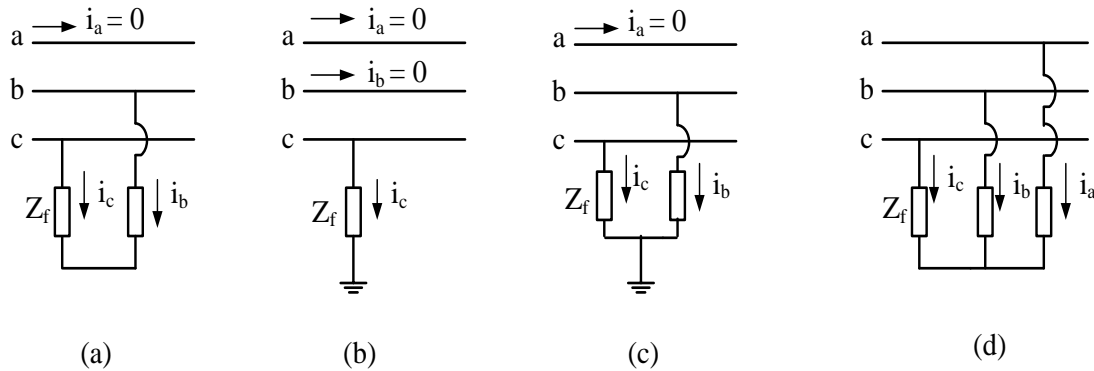


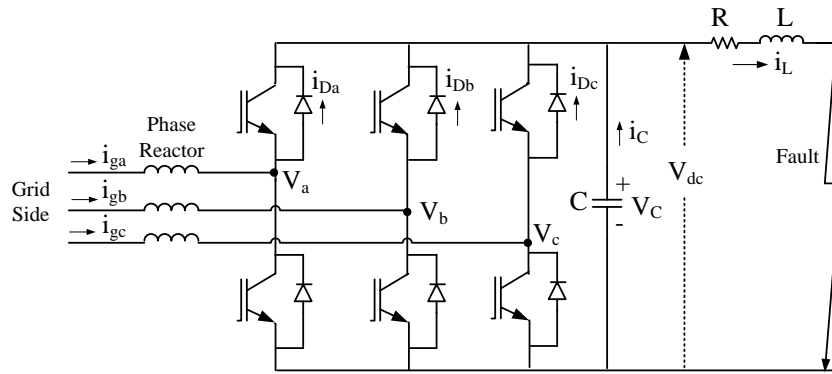
Figure 1.4 AC faults. (a) L-L fault, (b) L-G fault, (c) 2-L-G fault, (d) 3-phase fault.

1.2.2 DC Faults

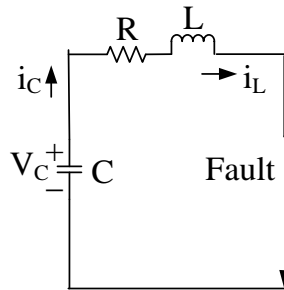
Various faults can occur on the DC side which are the pole-to-pole fault, positive and negative pole-to-ground fault, and double pole-to-ground fault. The DC fault is not much severe in the case of CSC-based HVDC line since the fault current has controlled by the higher value of the reactor which is used at the terminal point. However, the VSC-based HVDC system is very weak in the case of DC faults due to low rise time and higher peak and steady value of the fault current. Therefore, DC fault studies and its protection scheme gets more attention due to the increase in the application of multi-terminal VSC-based HVDC systems.

(i) DC Pole-to-Pole Fault

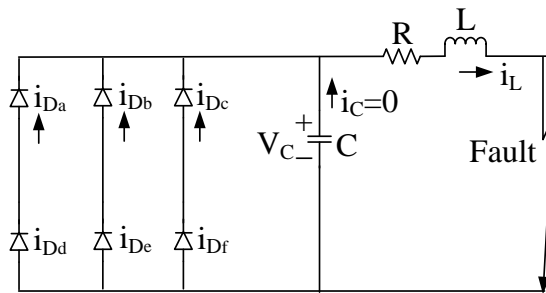
DC pole-to-pole fault is the worst case of DC faults in the operation of the VSC-based HVDC system. The two-level VSC with pole-to-pole fault condition is shown in Figure 1.5 (a). The pole-to-pole fault has three stages such as capacitor discharging, diode freewheeling and grid current feeding phases as shown in Figure 1.5 (b) to (d) [J. Yang 2011], [N. R. Chaudhuri et al. 2014].



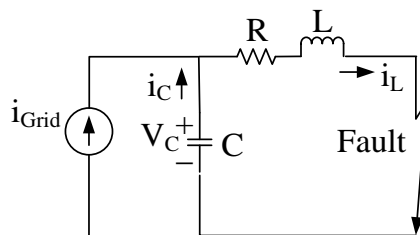
(a) VSC with pole-to-pole fault condition.



(b) Stage 1 - Capacitor discharging phase.



(c) Stage 2 - Diode freewheeling phase.



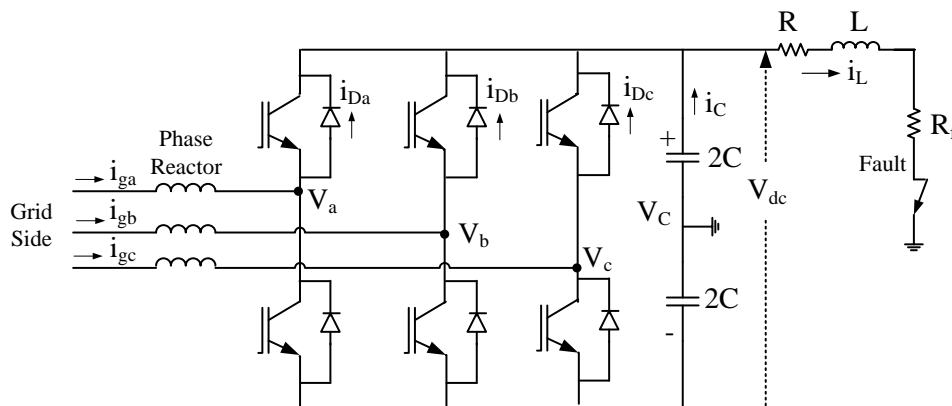
(d) Stage 3 - Grid current fed phase.

Figure 1.5 DC pole-to-pole fault in VSC-based HVDC system.

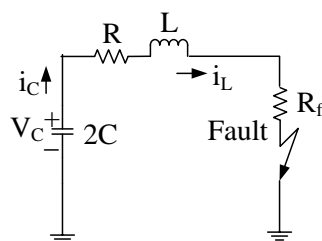
After the fault event, the fault current is blocked by the insulated gate bipolar transistors (IGBT) of the VSC, and its antiparallel diode will allow the path to flow. First, DC capacitor discharging action takes place which causes DC voltage decreased to zero. In the second stage, line inductor drives the current through the antiparallel diode path. In the third stage, converter behaves like an uncontrolled rectifier. The grid current will flow to the fault point through an uncontrolled rectifier.

(ii) DC Pole-to-Ground Fault

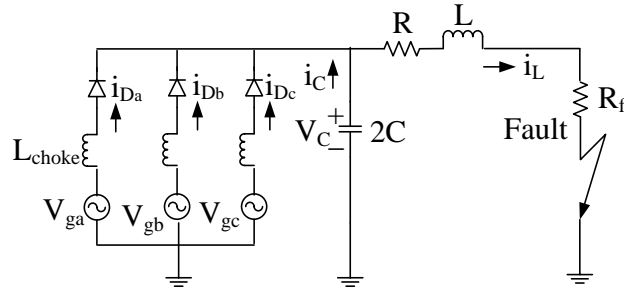
DC pole-to-ground faults frequently occur and mainly rely on the grounding system of the HVDC system. In this case, the fault resistance should not be neglected since it has higher value and plays a significant role in the system response. The two-level VSC with pole-to-ground fault condition is shown in Figure 1.6 (a). The pole-to-ground faults can be analyzed using two stages such as capacitor discharging and grid current feeding phases as shown in Figure 1.6 (b) and (c) [J. Yang 2011], [N. R. Chaudhuri et al. 2014].



(a) VSC with pole-to-ground fault condition.



(b) Stage 1 - Capacitor discharging phase.



(c) Stage 2 - Grid current fed phase.

Figure 1.6 DC pole-to-ground fault in VSC-based HVDC system.

In the first stage, DC capacitor discharging action happens but the DC voltage will not go to zero, i.e., faulty line voltage collapse to zero, on the other hand, non-faulted line voltage increases when the symmetric monopole configuration is used in the HVDC system. Therefore, no freewheeling diode conduction occurs in this case. In the second stage, the grid current feeding phase occurs via an antiparallel diode path in the VSC.

1.3 Survey of Literature on Faults in Multi-terminal DC links and Protection Methodology

Protection of the HVDC transmission line is very challenging due to low impedance, no zero crossing of DC current, power electronic devices are very less overload capability, and also conventional relay is not suitable for the HVDC line. The protection of the CSC-based HVDC transmission line is less severe when compared to the VSC-based HVDC transmission line. In the case of protection of VSC-based HVDC line, high-speed protection is essential due to low rise time and high steady-state fault currents. Also, identifying the faulted line is very difficult in the case of multi-terminal HVDC networks. Hence, the first part of this section presents the survey of literature on DC fault protection methods in both CSC and VSC-based HVDC transmission line in two-terminal and multi-terminal networks.

With the penetration of MT VSC-based HVDC system into the AC grid, the challenges in the distance relaying of AC transmission line gets increased. Hence, the second part of this section presents the survey of literature on distance protection of AC transmission line with VSC-based HVDC systems.

1.3.1 DC Fault Protection Methods in HVDC Links

(i) Conventional Protection Methods: D. Jovcic et al. [2011] have explained the difficulties of the conventional protection scheme such as distance, overcurrent, and differential protection when it is applied to HVDC grid protection. Distance relay is not suitable for the HVDC grid protection since the complex impedance at the fundamental frequency is different. In the overcurrent protection, the relay might give the trip decision for the fault on the adjacent line. The differential relay takes a longer time to detect the fault in the HVDC lines due to communication delay. Therefore, the conventional relay is not applicable to the HVDC grid protection. It was mentioned that developing a protection scheme for the HVDC grid level is still a challenge. Also, it was suggested that the derivative, second derivative, and wavelet transform based protection scheme has to be investigated due to the short time response.

The protection unit installed in the AC grid can address only steady-state based protection [H. Ha, and S. Subramanian 2015]. Here, the Fourier transform (FT) is applied to extract the magnitude and frequency information for the relay calculation which uses the steady-state signals. The high-frequency transient period is no longer than 10 ms. Therefore, the operating time of the AC grid protection is generally more than 20 ms. But, in the case of the HVDC line, the transient period is more extended when compared AC system, and also the peak fault current goes to the abnormal value which is not tolerable by the converters. Therefore, the protection algorithm has to be developed based on the transient components instead of the fundamental frequency component.

(ii) Handshaking Method: A handshaking method is proposed to identify the DC faults in the multi-terminal VSC-based HVDC systems [L. Tang 2003], [L. Tang and B. T. Ooi 2007]. In this method, the AC circuit breaker (CB) with the DC switch is used which is cheaper than the DC circuit breaker. If the fault occurs in a DC line, the AC circuit breaker opens the line from the AC side, and DC switch will isolate the faulty line. It can apply to point-to-point HVDC transmission system. But, when it is applied to the multi-terminal HVDC network, an entire converter goes to shut down due to the action of AC CB which will create the power flow interruption in the unfaulty line too. The transient phases such as capacitor discharge and diode freewheeling stages occur

very fast within a few milliseconds which will damage the semiconductor-based devices and other components before the AC circuit breaker operates.

(iii) Impedance Based Methods: J. Suonan et al. [2006], [2010] and X. Yang et al. [2008] have presented the time-domain fault location method based on the distributed parameter approach for the DC transmission line. It uses the voltage distribution calculation of the line to locate the fault using the synchronously measured voltage and current at both ends of the line. It can take any section of the data from the fault transient to the steady-state. Here, the low sampling frequency itself adequate to get accurate results. However, it is sensitive to the uncertainty of the parameters such as velocity, line resistance, and characteristic impedance which will affect the accuracy of the voltage distribution calculation. Also, the unsynchronized two end measurements are affecting the protection scheme. L. Yuansheng et al. [2015] have considered the uncertain line parameters and unsynchronized measurement time difference to locate the fault in an HVDC transmission line.

J. Yang et al. [2010] and [2012] have used the two voltage divider arrangement to calculate the fault distance. Here, the DC current measurement is not accounted for the distance calculation due to the immediate change of huge fault current which might lead to the measurement error. However, this protection scheme considers only the fault location, and it does not consider the fault detection process. For high resistance fault cases, the fault distance estimation might not be accurate. Also, this protection scheme takes a longer time for the distance calculation.

J. Suonan et al. [2013] have proposed a solution to the remote end faults in the two-terminal bipolar HVDC transmission line. In this method, the distance protection with the consideration of frequency-dependent parameters is taken to evaluate the fault distance in an HVDC line since the line parameters such as resistance and inductance mainly depend on the frequency also. However, the accuracy of the protection scheme might get affected due to the reduction of the allowable error to very less value when the fault occurs near or at the setting distance.

(iv) Traveling Wave Based Methods: H. Packard [1997] and M. A. Baseer [2013] have explained the theory of the traveling waves and its fault location principle for the transmission line. The traveling wave method is more suitable for the HVDC

transmission line since the transient traveling wave is present when the fault occurs at any point in a DC transmission line. The traveling wave based protection scheme for the point-to-point HVDC system has been presented by X. Liu et al. [2009], [2011]. However, it is not capable of giving protection for the close-up faults, difficult to detect the wave-heads and influenced by noise. Therefore, the boundary protection also used along with traveling wave method to identify the fault in the HVDC line [X. Liu et al. 2009]. It uses a one end high-frequency transient signal to discriminate the internal fault from the external fault and also it can able to detect the close-up faults. However, it requires high sampling frequency. In the case of VSC-based HVDC system, the boundary protection might not be capable of differentiating the internal and external faults. Y. Zhang et al. [2012] have used the characteristics of initial values of the traveling waves to detect the fault. Also, the gradient of the traveling wave is used to discriminate the internal fault from the external fault since it is limited by the reactor which is connected at the terminal end of the HVDC line. O. K. Nanayakkara et al. [2012] have used the two-terminal traveling wave-based fault location method to protect the MT VSC-HVDC line against DC faults. It uses the surge arrival time difference to locate the fault with the use of the velocity of propagation.

However, In the traveling wave based method, the detection of the wave head is the key challenge for identifying the faults in an HVDC line. Also, it is tough to detect the surge arrival time since the traveling wave is very weak in case of high fault resistance and continues variation in the transition resistance.

(v) Natural Frequency Based Methods: The frequency components of the generated traveling wave due to the fault or any transient event can be called the natural frequency which is the combination of harmonic frequencies. In the natural frequency-based method, no need to track the wave head; instead, one end transient signal is sufficient to detect the fault. The natural frequency concept can be seen in G. W. Swift [1979] which uses the distributed parameter model. Also, it has explained the relationship between the natural frequency and fault distance when the impedance of the system is zero or infinite. In the case of the DC transmission line, the transient energy is very high even the fault occurs at any time. Therefore, it is very suitable to locate the fault in a DC line due to the more availability of the natural frequency content in the DC fault transient signals.

Z. Y. He [2014] have used the method which uses the natural frequency to locate the fault in a bipolar CSC-based HVDC system. It uses the dominant natural frequency for finding the fault distance by calculating the traveling wave velocity and reflection coefficient. S. Guobing et al. [2011] and [2014] have presented the fault location method in a two-terminal VSC-based HVDC system by extracting the natural frequency of the fault current. When the fault occurs, the DC line has huge transient energy which will create a more natural frequency component. Also, the natural frequency can be generated by the distributed parameter characteristics and reflection of a traveling wave.

The accuracy of the protection scheme depends on the extraction of natural frequency and the calculation of the velocity of the traveling wave. Any section of the data during the fault period can be applied to identify the fault in an HVDC line unlike wave-head detection in the traveling wave method. However, the natural frequency-based method might not be suitable for the time-varying transients. Also, the accuracy of the measurement decreases if the fault distance increases.

(vi) Wavelet Transform Based Methods: At first, the Fourier transform (FT) is used to extract the spectral component of the signal. But, it gives only what frequency components exist in the signal and will not provide the time information. It is not suitable for non-stationary signals which are very important for the protection of the HVDC transmission line. In the next stage, short time Fourier transform (STFT) is used to extract the spectral content of the signal which gives what frequency bands exist at what time intervals, i.e., the resolution is fixed. However, it does not provide what frequency exist at what time instant. Therefore, the wavelet transform is used to extract the transient signals due to faults and other disturbances. A wavelet transform is a powerful tool in the signal processing methods for tracking the fault transients in the non-stationary signals [R. Polikar 1996], [D. C. Robertson et al. 1996]. The protection scheme based on the wavelet transform can be seen in F. B. Costa et al. [2010], H. Zhengyou et al. [2011], S. A. Gafoor and P. V. R. Rao [2011], N. Perera and A. D. Rajapakse [2012], F. E. Perez et al. [2012].

X. Liu et al. [2009], [2011] have used the wavelet transform to detect the traveling waves and voltage transients for the detection of the DC fault in an HVDC line. K. D. Kerf et al. [2011] have applied the wavelet transform to identify the DC fault in the MT

VSC-HVDC system using the local measurements. Here, the DC voltage, current, and its derivatives are used as the wavelet coefficients. The triple modular redundancy is used to achieve the selectivity. Y. M. Yeap and A. Ukil [2014] have applied the wavelet transform to capture the fault current rising time in an HVDC system. J. Cheng et al. [2014] have used the complex wavelet transform to extract the characteristic and non-characteristic frequency current for the fault detection in the MTDC line. The wavelet transform is used to extract the high-frequency transient of the cable sheath voltage to detect the fault in the VSC-HVDC line [S. H. A. Niaki et al. 2015].

However, in the wavelet transform based protection methods, the wavelet coefficient is predefined for fault detection. The fault inception angle and fault resistance might influence the effectiveness of the wavelet co-efficient-based protection scheme. Also, it might not be suitable for the stand-alone protection method.

(vii) Transient Based Protection Methods: X. Zheng et al. [2012] have used the difference of the transient energy between the rectifier and inverter end to detect and discriminate the internal and external fault in a two-terminal HVDC line. It uses the DC voltage and current measured at both sides to calculate the difference of the transient energy. Also, it is calculated based on the transmission line equations with the consideration of distributed parameter model. However, the transmission line length and fault resistance might be affecting the accuracy of the protection scheme. The non-unit protection scheme which is the combination of starting, boundary, directional and faulty line identification unit has proposed and tested in the hardware [M. You et al. 2009], [S. Zhang et al. 2010], F. Kong et al. [2014]. The starting unit uses the voltage gradient to differentiate the abnormal state from the normal condition. The boundary unit which is based on the energy calculated from the high-frequency transient signal has applied to distinguish the internal and external fault. The directional unit uses the forward and backward traveling wave to detect the direction of fault. The transient energy of the faulted line has a higher value than the normal line. Therefore, the faulty line identification unit uses the comparison of the transient energy which is generated in the HVDC line.

Z. X. Dong et al. [2012] have used the transient harmonic current to detect and discriminate the internal and external fault in a two-terminal HVDC line. The transient harmonic current is very less in case of external fault condition since it can be limited

by the DC filter and smoothing reactor which are installed at both terminal ends of the HVDC system. But, it has huge value for the internal fault when compared to the external fault. Hence, the calculated difference of the transient harmonic current at both ends has applied to differentiate the internal fault from the external fault. However, the sensitivity of the protection scheme is affected by the fault resistance and location. Also, this protection scheme requires double side information to take the decision. The fault location is achieved by using the characteristics of the DC filters in the MTDC line [J. Cheng et al. 2014]. Here, the internal and external faults are distinguished by using the current at the characteristic and non-characteristic frequency which is extracted with the help of complex WT. The internal fault occurs when the characteristic frequency current is more than the non-characteristic frequency current; otherwise, it is considered as an external fault.

S. H. A. Niaki et al. [2015] has presented a novel fault location method based on sheath voltage for two-terminal VSC-HVDC system. Here, the sheath of the cable is grounded at each end of the HVDC system in a substation, and the sheath voltage is measured at this point. Under normal condition, the transient voltage in the cable sheath is zero, and no current flows through it. Under the fault situation, the transient voltage of the cable sheath will have some value and also fault current flows through it. Therefore, the transient voltage of the cable sheath is used to identify the fault, and its sign on both sides such as rectifier and inverter end is applied to discriminate the DC fault and capacitor unbalance.

However, in real-time, accurate fault detection might not be possible by capturing only the fault induced transient signals since the switching and other transient events also can generate the same transients.

(viii) Voltage and Current Derivatives Based Methods: J. Wang et al. [2015] have presented the voltage derivative $\left(\frac{dv}{dt}\right)$ and the current derivative $\left(\frac{di}{dt}\right)$ based protection scheme for the MTDC system using the single-end measurements. The fault can be identified if the rate of change of DC voltage and current exceeds the preset threshold. The fault detection in an earthed HVDC grid has presented based on the rate of change of voltage (ROCOV) [J. Seneath and A. D. Rajapakse 2016]. Here, the DC inductor is used in series with the DC breaker to control the peak fault current which is below to

the breaker rating. The variation range of the ROCOV can be used to distinguish the different zone and bus faults by setting the preset threshold value. Also, it was given that the rate of rise of the fault current can be limited by increasing the inductor value which is connected in series with the breaker. However, it has taken that the DC voltage of the converter output is constant after the fault. The variation range of the DC reactor voltage is used to detect the fault in the meshed MT HVDC systems [R Li et al. 2017]. The changes in the DC reactor voltage is observed continuously and compared with the preset threshold value to identify the fault. Here, the threshold setting of the proposed protection scheme is predefined. However, the setting of the threshold value for the protection scheme is challenging for discriminating the different zone or line fault and high resistance faults.

W. Leterme et al. [2016] have presented the non-unit protection scheme for DC faults in the MT VSC-HVDC grid. It uses an inductive termination to decide the protection zone. It applies the under-voltage detection to identify the fault. The threshold value for the under-voltage criterion is set as 85% of the rated DC voltage. After the fault identification, the voltage and current derivatives are used to discriminate the first and second zone fault. But, the voltage derivative is vulnerable to the close-up faults, measurement error, and noise. Therefore, the direction of the current derivative is used to differentiate the forward and backward faults. However, discrimination of the Zone-1 high resistance fault from the Zone-2 solid fault becomes very difficult, and the second zone boundaries are not considered in this paper. Also, the threshold setting for the fault discrimination criterion might not work when the fault resistance variation is a significant value.

(ix) Summary of the Survey: The important observations from the literature survey on DC fault protection methods are given in the following points:

- The conventional protection scheme such as distance, overcurrent, differential protection schemes which are used in the AC grid protection cannot be suitable for the HVDC grid protection since the characteristics of the DC fault is different from the AC fault and other transient events.
- The traveling wave based method can provide fast fault detection. But, the detection of the wave-head is the key challenge for identifying the DC fault in

an HVDC line. Also, the traveling wave is very weak for the high resistance fault cases.

- The wave-head detection is not required in the case of the natural frequency-based method since it can use any section of the fault data to detect the fault. But, the extraction of the natural frequency is challenging under time-varying fault and transient conditions.
- The wavelet transform-based method can be used to extract the time-varying transients and also it provides fast fault detection. Here, the wavelet coefficient has predefined for fault detection. Also, the fault inception angle and fault resistance might influence the effectiveness of the wavelet co-efficient-based protection scheme.
- The single-ended transient based method gives high-speed fault detection for the DC fault in an HVDC grid. But in real-time, the accurate fault detection might not be possible by capturing only the fault induced transient signals since the switching and other transient events also can generate the same transients. The single-ended voltage and current derivative-based method also give fast fault detection in an HVDC grid. Here, the setting of the threshold value to discriminate the internal fault from the external fault is a challenge. In such condition, the DC reactor can be used at the terminal end of the HVDC grid to limit the DC voltage and current change rate. Therefore, the combination of the single-ended transient based method and voltage and current derivatives based method with the operation of the DC reactor might be the best option to detect and discriminate the DC fault in an HVDC grid.

1.3.2 Challenges in Distance Relaying of AC Grid in the presence of HVDC Links

On the occurrence of a fault on the transmission line close to a PCC, the fault current increases and the PCC voltage collapses. If a VSC-based device has coupled to the AC grid through the same PCC, it might have a significant impact on the performance of the protective devices, such as distance protection supported on the AC grid.

The steady-state and transient components of the voltage and current measured at the relay location might get affected by the fault loop with the flexible AC transmission system (FACTS) devices [P. K. Dash et al. 2000], [M. Khederzadeh 2002]. Thyristor

controlled series capacitor (TCSC) has very complex impedance characteristics and fast dynamic process. In case of ground faults in a TCSC compensated transmission line, the complex variation of sequence current influence on the distance relay mho characteristics. As a result, the protected system can go to an unstable condition [W. G. Wang et al. 1998].

K. El-Arroudi et al. [2002] have investigated the impact of midpoint shunt compensation using a static synchronous compensator (STATCOM) on the performance of impedance-based protective relay under normal and fault conditions at different load angles. The impedance measurement, phase selection, and an operating time of a distance relay might get influenced by the STATCOM compensated transmission line. In the case of a single-pole tripping operation, either standalone or channel-aided distance scheme might not work well [T. S. Sidhu et al. 2005]. M. V. Sham and K. P. Vittal [2011] have studied the effect of zero sequence compensation factor on the distance relay performance in a STATCOM based midpoint shunt compensated transmission line under single line-to-ground fault conditions. The impact of unified power flow controller (UPFC) on the distance relay performance is significantly higher when compared to the STATCOM due to the alteration of active power [X. Zhou et al. 2006]. The impact of unified interphase power controller (UIPC) on the apparent impedance measured by a distance relay is significant, leads to a relay under-reach problem for the primary protection [M. Alizadeh et al. 2015].

H. Wang [2014] have investigated the impact of line-commutated converters (LCC)-based HVDC system on the performance of the distance relay under fault and power swing conditions. It showed that the result of the apparent impedance value is different than the actual case when the fault occurred in Zone-2 area of a protective relay. L. He et al. [2014] have analyzed the performance of the distance relays in an AC grid with VSC-HVDC link connected OWFs. It has identified that the miscoordination of the Zone-2 protection can occur due to VSC-HVDC control action. Also, the apparent impedance calculation method is proposed to identify the miscoordination of the distance relays. However, the dynamic operating conditions of the VSC-HVDC system and its influence on the performance of the distance relay is not reported. M. M. Alam et al. [2017] have analyzed the dynamic impact of the VSC-HVDC system on the quadrilateral characteristic-based distance relay in an AC transmission line. However,

the reach setting of the quadrilateral characteristics might be different for the phase and ground fault relays since the variation of the fault resistance is more significant for the phase-to-ground fault cases when compared to the phase-to-phase fault cases.

VSC-based HVDC transmission system stands as a challenge for the distance relays to perform the normal operation as they can control both the active and reactive power flow independently. The distance relay might mal-operate when the AC grid operated with the VSC-based HVDC system. Therefore, VSC-based HVDC system serves as an excellent testbed for testing the behavior of these distance relays under power system disturbances.

1.4 Objectives of The Thesis

The overall objectives of the research work are as follows:

1. Design, modeling, and simulation of the multi-terminal VSC-based HVDC systems interconnecting offshore wind farms. Also, different case studies are carried out to understand the transient behaviour of the multi-terminal VSC-based HVDC systems linked offshore wind farms.
2. Developing a single-ended protection scheme for DC faults in multi-terminal VSC-based HVDC transmission systems.
3. Investigations on protection challenges in an AC grid with the effect of VSC-based HVDC transmission systems.

Objective-1: The multi-terminal (MT) VSC-based HVDC link is the recent interest for grid integration of large-scale OWFs. The research work in this thesis built the transient behavioural model of the MT VSC-based HVDC link connected OWFs, and also different case studies are carried out to evaluate the performance of the MT VSC-based HVDC system under power system disturbances. The main purpose of this simulation study is to understand the transient behaviour of the MT VSC-based HVDC systems before developing the protection scheme.

Objective-2: A single-ended protection scheme is proposed for DC faults in MT VSC-based HVDC transmission systems for both without and with current limiting reactor cases. In this protection scheme, the protection starting unit uses the under-voltage criterion to detect the fault. The fault discrimination is done by using three conditions

such as rate of change of DC voltage and current, and variation of transient energy. Also, the current limiting reactors are designed to connect in series with the DC circuit breaker to maintain the DC fault current within the breaker capacity until the protection unit isolates the faulty line.

Objective-3: With the penetration of VSC-based HVDC system into the AC grid, the challenges in the distance relaying of AC transmission line has been investigated. The dynamic operating conditions of the VSC-HVDC system on the performance of the distance relays have been analyzed. Moreover, the earth fault quadrilateral relay is designed, and its simulation studies are carried out in the AC grid with VSC-HVDC system.

1.5 Organization of The Thesis

The thesis is organized into seven chapters. This section provides information about the major contribution of each chapter.

Chapter 1: This chapter presents a brief introduction about the MT VSC-based HVDC systems which is used to interconnect the OWFs with the AC grid. It gives the survey of literature on DC fault protection methods in the MT HVDC links and also the impact of HVDC systems on distance protection of AC transmission lines. Also, the objectives and organization of the thesis are presented.

Chapter 2: This chapter presents the modeling of the components used for the MT VSC-based HVDC systems, i.e., PMSG coupled offshore wind power generation system, grid-connected voltage source converter, and windfarm connected VSC and also the combination of grid and windfarm connected VSC. The simulation study of the modeled component is carried out under steady-state and transient conditions. Moreover, the simulation studies on total harmonic distortion (THD) analysis of the grid and windfarm connected VSC are carried out for both without and with filter case.

Chapter 3: In this chapter, different case studies are carried out to test the performance of the MT VSC-based HVDC system linked OWFs under various power system disturbances. The simulation study of the

MT VSC-HVDC systems is conducted under different fault and wind variable conditions. The main purpose of this simulation study is to understand the transient behaviour of the MT VSC-based HVDC systems, and the fault studies help to develop the protection scheme.

Chapter 4: This chapter presents the modeling of the single-ended protection scheme for DC faults in MT VSC-based HVDC systems. Also, the design of current limiting reactors which will limit the fault current within the breaker capacity are presented. Simulation studies are carried out to test the performance of the proposed protection scheme for the various DC fault cases in the MT VSC-based HVDC systems for both without and with current limiting reactor cases.

Chapter 5: In this chapter, the modeling of the mho characteristic-based distance relay has been developed to analyze the influence of VSC-based HVDC system. The analytical and simulation studies are conducted to evaluate the performance of the distance relay in an AC grid with MT VSC-based HVDC systems under various fault conditions. The effect of the dynamic operating conditions of the VSC-HVDC system on distance relay has presented. Also, the effect of fault resistance on ground relay performance is analyzed.

Chapter 6: In this chapter, the effect of the VSC-based HVDC system on the performance of quadrilateral characteristic-based distance relays are presented under the condition of phase-to-ground fault with different fault resistance. The comparison of the quadrilateral relay with the mho relay is presented. Also, the effect of the dynamic operating conditions of VSC-HVDC system on the performance of mho and quadrilateral relays under phase-to-ground fault with high resistance cases are presented.

Chapter 7: This chapter presents the conclusions obtained from the simulation results which are presented in the different chapters and also suggests some of the areas for future work.

CHAPTER 2

MULTI-TERMINAL VSC-HVDC LINK CONNECTED OFFSHORE WIND FARMS

The large-scale of the offshore wind farms are connected to the AC grid using the multi-terminal VSC-based HVDC link as shown in Figure 2.1. The wind power generation system is modeled as an offshore wind farm model. The generated wind power is stepped-up to high voltage (HV) levels that are suitable for the HVDC converter rating by using the converter transformer. The High voltage AC is converted to high voltage DC by using voltage source converters. The DC transmission line is used to interconnect the sending end and receiving end for long-distance. The output of the voltage source inverter, i.e., converted AC power is stepped-up to the suitable grid level and connected to the AC grid.

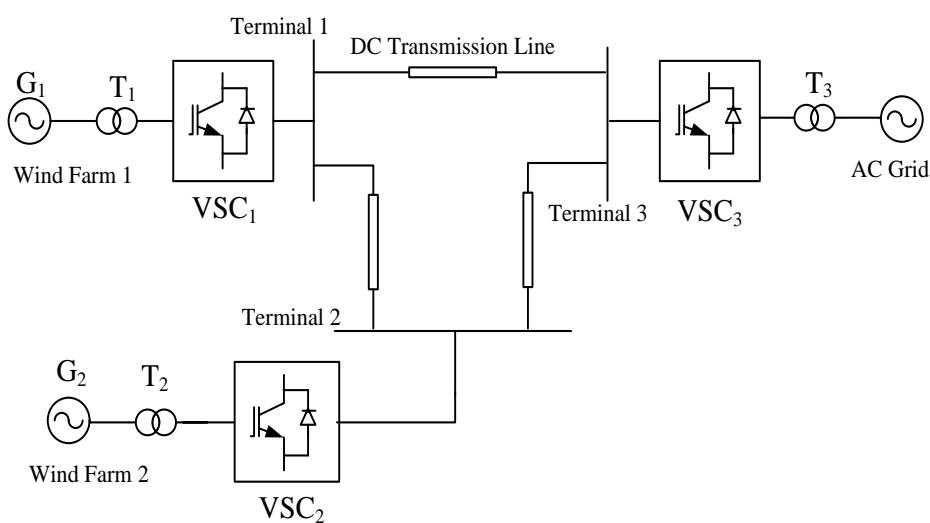


Figure 2.1 The offshore wind farms are connected to the AC grid using Multi-terminal VSC-based HVDC Link.

2.1 PMSG Coupled Offshore Wind Power Generation

In this section, the modeling of the wind power generation system and its simulation study under steady-state and dynamic conditions are presented.

2.1.1 Wind Farm Model

The wind power generation system which is mainly consisting of the wind turbine, gearbox, permanent magnet synchronous generator, and control system is shown in Figure 2.2. The turbine blade starts to rotate by wind passes over the blade. The wind turbine produces mechanical power by taking the input as kinetic energy. The shaft of the PMSG is coupled with the wind turbine through the gearbox. The mechanical power is given as input to the PMSG, and it produces the electrical power with the help of permanent magnets.

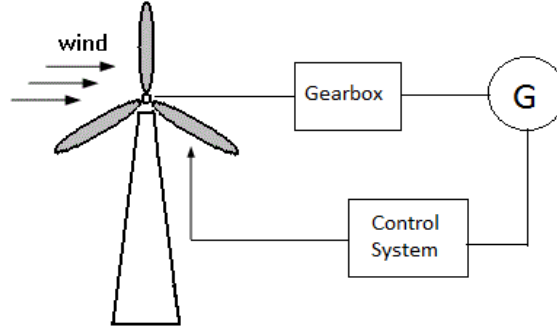


Figure 2.2 Wind power generation model.

2.1.1.1 Wind Turbine

The mechanical power output of the wind turbine (WT) is given by,

$$P_m = \frac{1}{2} \rho A v^3 C_p(\theta, \lambda) \quad (2.1)$$

where, ρ is the air density, A is the swept area of the rotor in m^2 , v is wind speed in m/s , C_p is the power coefficient and it depends on the pitch angle of the rotor blades (θ) and tip speed ratio (λ). It can be calculated by,

$$C_p = 0.73 \left(\frac{151}{\lambda_i} - 0.58\theta - 0.002\theta^{2.14} - 13.2 \right) e^{\frac{-18.4}{\lambda_i}} \quad (2.2)$$

where,

$$\frac{1}{\lambda_i} = \frac{1}{\lambda - 0.02\theta} - \frac{0.003}{\theta^3 + 1} \quad (2.3)$$

$$\text{Tip speed ratio, } \lambda = \frac{\omega_r R}{v} \quad (2.4)$$

where, ω_r is the rotor rotational speed in rad/sec, R is the radius of the rotor blade in m. Tip speed ratio changes occur if any changes in the rotor speed which will lead to the power coefficient variation [F. Deng, and Z. Chen 2011], [J. G. Slootweg et al. 2003]. Figure 2.3 shows the tip speed ratio (λ) vs power coefficient (C_p) curve. The power coefficient can be calculated with the help of the tip speed ratio.

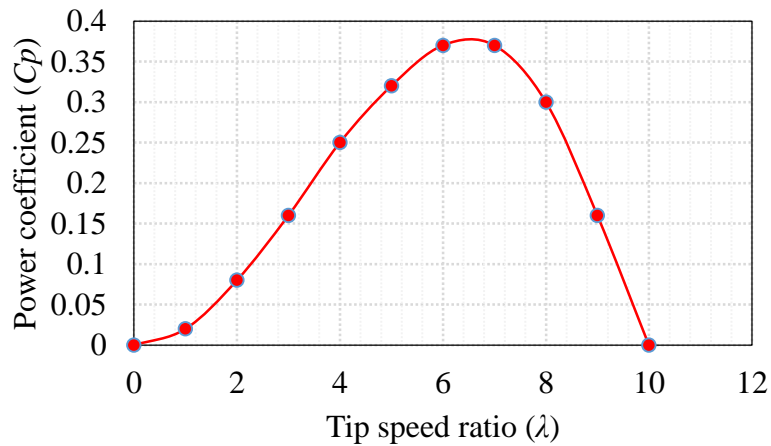


Figure 2.3 Power coefficient (C_p) vs tip speed ratio (λ) curve.

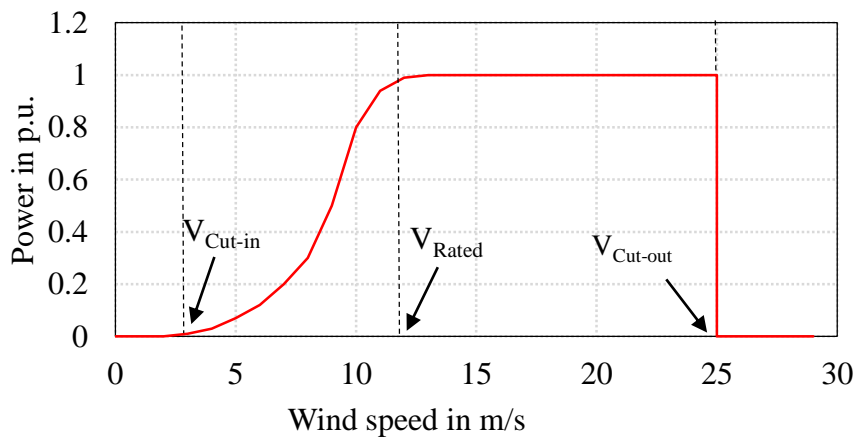


Figure 2.4 The power curve of the wind turbine.

The output power of the WT can be varied with the help of wind speed as shown in Figure 2.4. The WT output power is zero when the wind speed is lower than the cut-in speed (V_{Cut-in}). The turbine starts to operate once the wind speed reaches higher than V_{Cut-in} . The power output of the WT is a cubic relationship with the wind speed (it can

be varied using the C_p) until the rated wind speed (V_{Rated}) is reached. Then, the power output remains constant up to the cut-out wind speed ($V_{\text{Cut-out}}$). The WT will go to shut down once the wind speed exceeds the cut-out wind speed. The WT designer sets the cut-in, rated and cut-out wind speed limits [O. Anaya-Lara et al. 2014].

The dynamic model of the wind turbine is given by,

$$J \frac{d\omega_r}{dt} + B\omega_r = T_m - T_e \quad (2.5)$$

where, J and B are the inertia and friction coefficient, T_m is the turbine mechanical torque, and T_e is the electromagnetic torque [O. Carranza et al. 2013].

2.1.1.2 Permanent Magnet Synchronous Generator

The Permanent magnet synchronous generator (PMSG) is more suitable for wind turbine technology. It does not require separate field excitations. It is developed by using voltage and flux equations, does not depend on the equations related to the rotor windings due to its permanent magnets. The voltage (V_s^{abc}) and magnetic flux (λ_s^{abc}) in the stator windings are given by,

$$V_s^{abc} = r_s i_s^{abc} + \frac{d\lambda_s^{abc}}{dt} \quad (2.6)$$

$$\lambda_s^{abc} = L_s i_s^{abc} + \lambda_m \quad (2.7)$$

where, i_s^{abc} are the three-phase currents flowing through the stator windings, r_s and L_s are the resistance and inductance of the stator windings. λ_m is the amplitude of the flux linkages established by the permanent magnets. The dynamic model of the PMSG can be represented by using the rotor reference frame.

The stator voltage in d-q frame is given by,

$$V_{qs} = r_s i_{qs} + \omega_r \lambda_{ds} + \frac{d\lambda_{qs}}{dt} \quad (2.8)$$

$$V_{ds} = r_s i_{ds} - \omega_r \lambda_{qs} + \frac{d\lambda_{ds}}{dt} \quad (2.9)$$

where,

$$\lambda_{ds} = L_d i_{ds} + \lambda_m \quad (2.10)$$

$$\lambda_{qs} = L_q i_{qs} \quad (2.11)$$

where, L_d and L_q are the inductance in the d and q axis. i_{ds} and i_{qs} are the stator current in the d and q axis. Substitute the equations (2.10) and (2.11) into (2.8) and (2.9). We get,

$$V_{qs} = r_s i_{qs} + \omega_r L_d i_{ds} + \omega_r \lambda_m + L_q \frac{di_{qs}}{dt} \quad (2.12)$$

$$V_{ds} = r_s i_{ds} + L_d \frac{di_{ds}}{dt} - \omega_r L_q i_{qs} \quad (2.13)$$

where, $\frac{d\lambda_m}{dt} = 0$. The equivalent circuit of the PMSG which consists of the q and d axis circuit is shown in Figure 2.5. It can be implemented based on the equations (2.12) and (2.13) [Ohm, D. Y. 2000], [Krause, P. et al. 2013], [M. Cheah-mane et al. 2014].

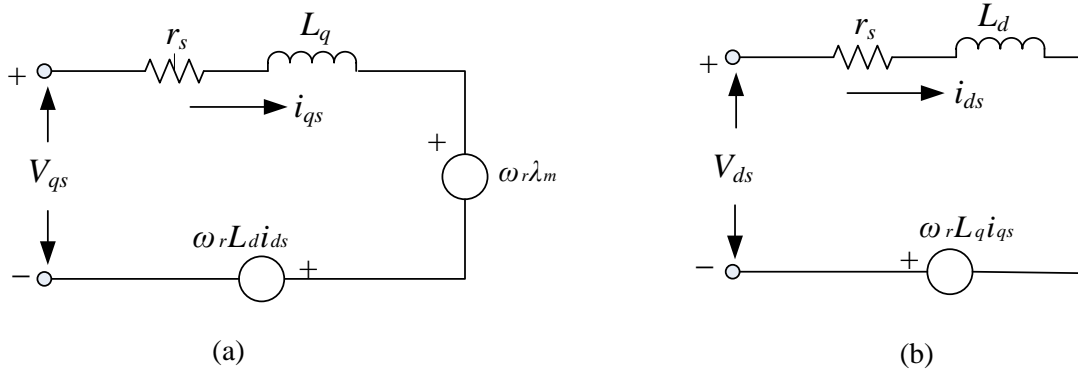


Figure 2.5 The equivalent circuit of the PMSG, (a) q-axis, (b) d-axis.

The electromagnetic torque (T_e) is given by,

$$T_e = \frac{3}{2} \left(\frac{p}{2} \right) (\lambda_m i_{qs} + (L_d - L_q) i_{qs} i_{ds}) \quad (2.14)$$

where, p is the number of poles.

2.1.2 Modeling of Grid Connected Wind Energy System

The general block diagram of the grid-connected PMSG-coupled wind energy system is shown in Figure 2.6. The WT produces mechanical power by taking the input as wind speed. The shaft of the PMSG is connected with the WT through the gearbox. The generated mechanical power is given as input to the PMSG, and it produces the electrical power with the help of permanent magnets. The generator

terminal voltage is stepped-up to the suitable voltage level using the step-up transformer, and lastly, it can be connected to the three-phase power system.

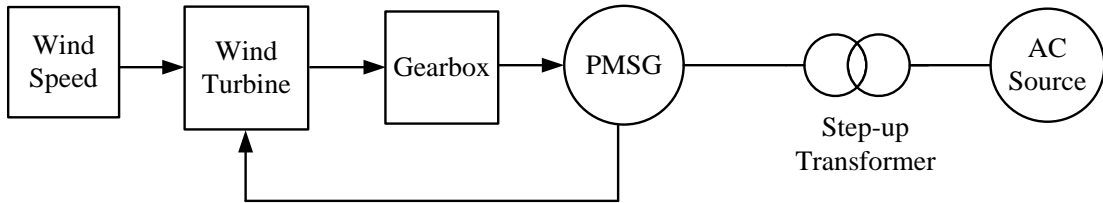


Figure 2.6 The block diagram of the grid connected wind energy system.

The model calculation for the 5 MW wind power generation system is presented with the help of the data available in the Gamesa G128-5.0MW offshore - 5 MW - wind turbine.

Rotor blade diameter, (D) = 128 m

Radius of the rotor blade, (R) = 64 m

Swept area, (A) = $\pi R^2 = 12868 \text{ m}^2$

Blade length = 62.5 m

Average wind speed, (v) = 11-12 m/s

Cut-in wind speed, ($V_{\text{Cut-in}}$) = 3-5 m/s

Cut-out wind speed, ($V_{\text{Cut-out}}$) = 25 m/s

Air density, (ρ) = 1.225 kg/m³

Rotor rotational speed in rpm, (N_r) = 5 - 11.7 rpm

Generator rotational speed in rpm, (N_s) = 490 rpm

Gearbox ratio = $\frac{490}{11.7} = 41.88$

Tip speed ratio, $\lambda = \frac{\omega_r R}{v} = \frac{\frac{2\pi N_r R}{60}}{v} = \frac{\frac{2\pi \times 11.7}{60} \times 64}{12} = 6.5$

Pitch angle of the rotor blade, (θ) = 2.4°

Using equation (2.3), λ_i can be calculated by,

$$\frac{1}{\lambda_i} = \frac{1}{6.5 - 0.02 \times 2.4} - \frac{0.003}{2.4^3 + 1}$$

$$\lambda_i = 6.4642$$

Using equation (2.2), the power coefficient (C_p) is calculated by,

$$C_p = 0.73 \left(\frac{151}{6.4642} - 0.58 \times 2.4 - 0.002 \times 2.4^{2.14} - 13.2 \right) e^{\frac{-18.4}{6.4642}}$$

$$C_p = 0.37$$

The mechanical power output of the WT (P_m) is calculated by,

$$P_m = \frac{1}{2} \rho A v^3 C_p = 5 \text{ MW}$$

The model calculation used for the PMSG machine is given by,

AC line voltage, $V_s = 0.69 \text{ kV}$

Frequency, $f = 50 \text{ Hz}$

Active power, $P = \sqrt{3} V_s I_s \cos \phi = 5 \text{ MW}$

Power factor (p.f.), $\cos \phi = 0.9$ (assume the machine is operating at 0.9 p.f. lagging)

$\cos \phi = 0.9$; $\phi = 25.84$

AC line current, $I_s = \frac{5 \text{ MW}}{\sqrt{3} \times 0.69 \text{ kV} \times 0.9} = 4.648 \angle -25.84^\circ \text{ kA}$

Number of poles, $(p) = \frac{120f}{N_s} = \frac{120 \times 50}{490} = 12$

Number of Pole pair, $= \frac{p}{2} = 6$

Step-up transformer = 5 MVA, 0.69/ 33 kV, 50 Hz

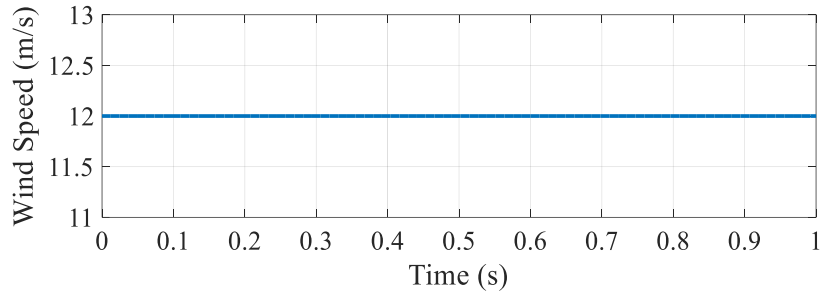
AC source = 5 MVA, 33 kV, 50 Hz.

The PMSG-coupled wind power generation system is modeled in the PSCAD/EMTDC simulation with the help of the model calculation, and its performance is analyzed under start-up and dynamic conditions such as the gust, ramp and noisy variation of the wind speed.

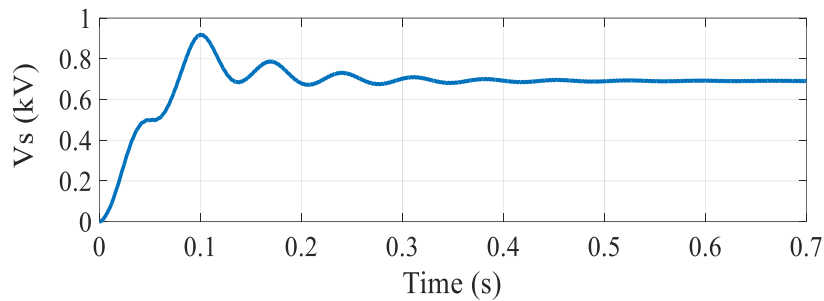
2.1.2.1 Behaviour under Start-up Conditions

The start-up process and steady-state response of the PMSG-coupled wind energy system are presented in Figure 2.7. The wind speed remains constant as the nominal wind speed (i.e., 12 m/s). The response of the wind power generation gives an oscillation during start-up. The AC line voltage (V_s) goes up to 0.92 kV and reaches a steady value of 0.69 kV. The AC line current (I_s) goes up to 4.72 kA and settle the stable value as 4.64 kA. The active power (P) is increased up to 6.92 MW peak and comes to the steady value as 5 MW. Therefore, the response of the wind turbine-

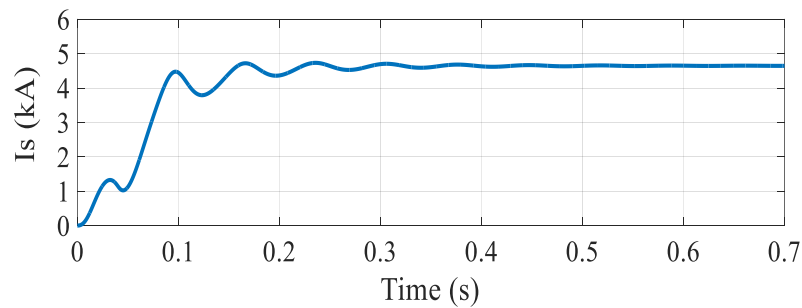
generator system gives an oscillation during the start-up process and provide steady nominal value.



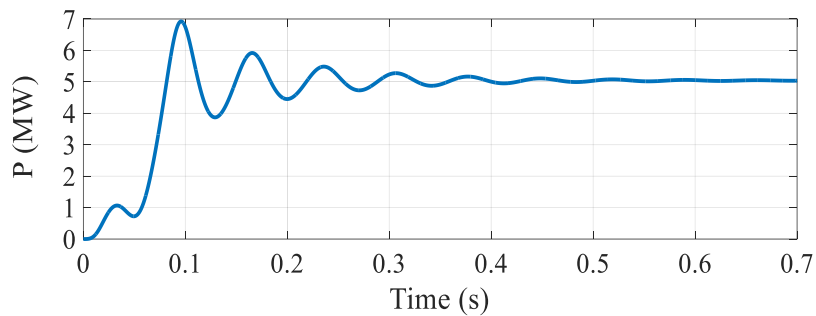
(a) Wind speed.



(b) AC line voltage (V_s).



(c) AC line current (I_s).

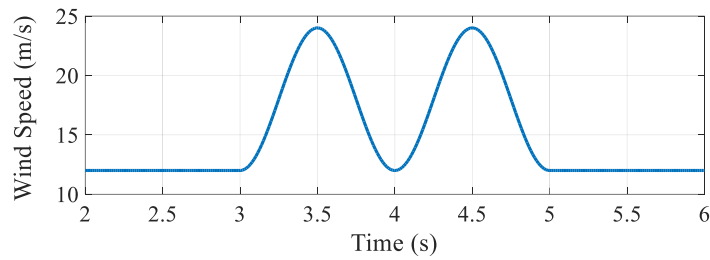


(d) Active Power (P).

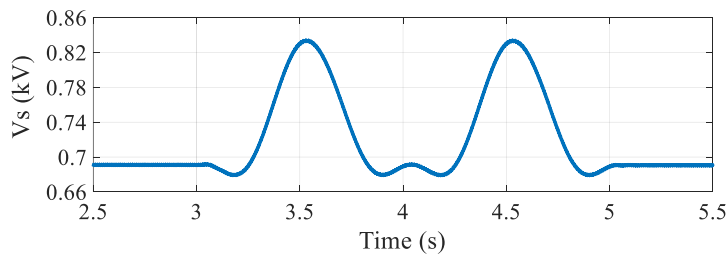
Figure 2.7 The response of the wind energy system during start-up conditions.

2.1.2.2 Behaviour under Gust Wind Conditions

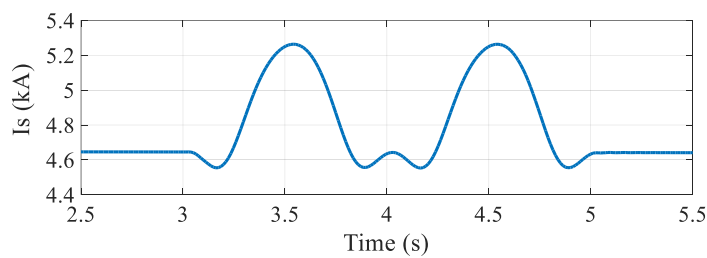
In this case, the performance of the PMSG-coupled wind energy system is analyzed under the gust variation of wind condition. The nominal wind speed is given as 12 m/s. The gust wind data are the following: gust peak velocity is 12 m/s, gust period is 2 s, gust starting time is 3 s, and the number of gusts is 1. The response of the PMSG output such as AC line voltage (V_s), AC line current (I_s), and active power (P) during gust wind condition is shown in Figure 2.8.



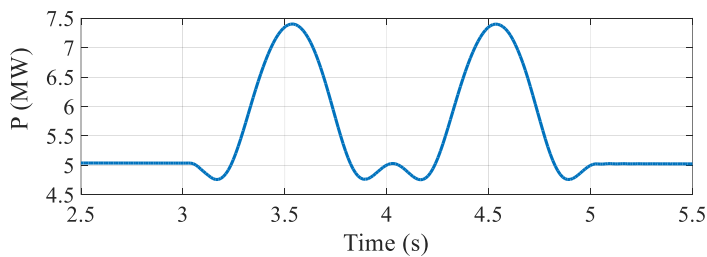
(a) Wind speed.



(b) AC line voltage (V_s).



(c) AC line current (I_s).



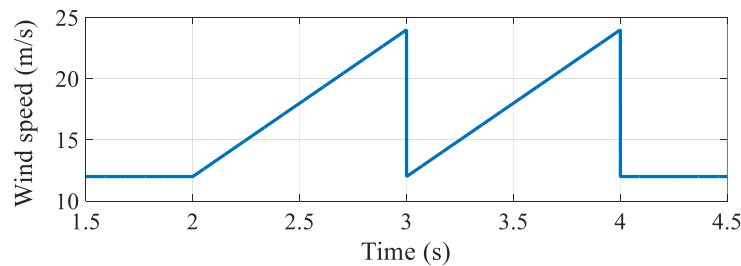
(d) Active Power (P).

Figure 2.8 The response of the wind energy system during gust wind conditions.

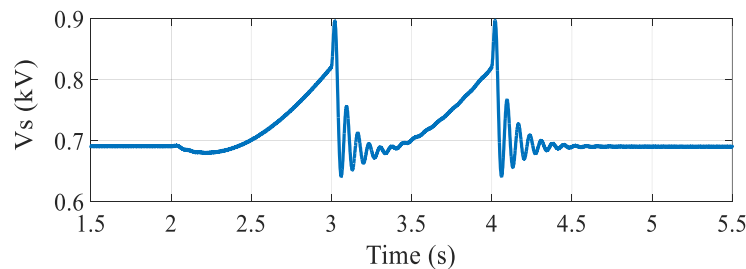
At $t = 3.0$ s, the wind speed starts to vary as in the form of a gusty pattern. The gust wind speed has increased up to 24 m/s. From the obtained results, it can be seen that the response of the PMSG output is linearly increasing with the wind speed. Therefore, the response of the PMSG output gives the gusty variation during gust wind period and come back to the steady-state value once the gust wind period gets over. If the gust wind peak velocity goes more than 12 m/s, the operation of the system might get affected because the wind speed will reach higher than the cut-out wind speed (i.e., $V_{\text{Cut-out}} = 25$ m/s).

2.1.2.3 Behaviour under Ramp Wind Conditions

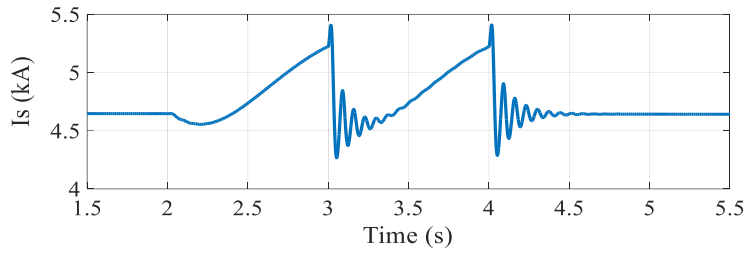
In this case, the performance of the PMSG-coupled wind energy system is analyzed under the ramp variation of wind condition. The nominal wind speed is 12 m/s, and the ramp wind is applied at $t = 2.0$ s. The ramp wind data are the following: ramp maximum velocity is 12 m/s, ramp start time is 2 s, ramp period is 1 s, and the number of ramps is 2. Figure 2.9 shows the response measured at the PMSG output terminal during ramp wind condition. The response of the PMSG output such as AC line voltage (V_s), AC line current (I_s), and active power (P) is increased as in the form of ramp pattern during the ramp variation of wind speed condition. The response of the PMSG output reaches the steady-state value after the small oscillation once the ramp period gets over.



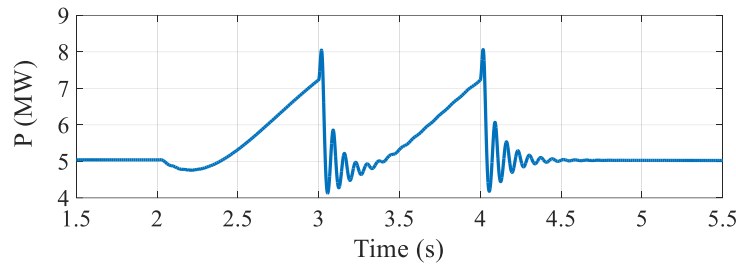
(a) Wind speed.



(b) AC line voltage (V_s).



(c) AC line current (I_s).

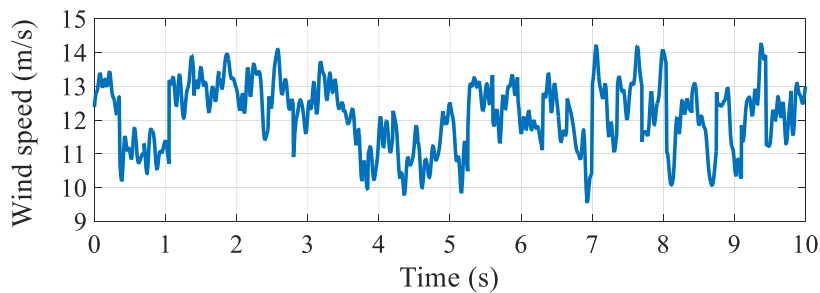


(d) Active power (P).

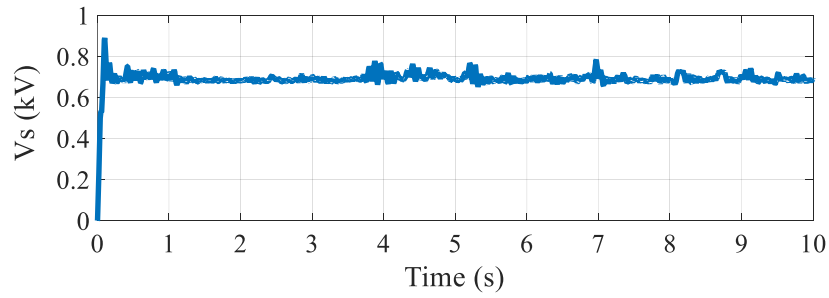
Figure 2.9 The response of the wind energy system during ramp wind conditions.

2.1.2.4 Behaviour under Noisy Wind Conditions

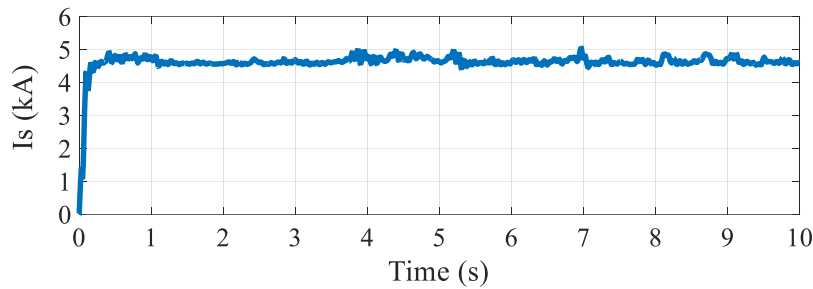
In this case, the performance of the PMSG-coupled wind energy system is analyzed under the variation of noisy wind condition. The noisy wind data are the following: number of noise component is 10, noise amplitude controlling parameter is 10 rad/sec, turbulence scale is 500 m, random seed number is 10 and the time interval for random generation is 0.35. Figure 2.10 presents the response of the PMSG output under noisy wind condition. The nominal wind speed is 12 m /s, and the noisy wind varies from 10 m /s to 14 m /s. The response measured at the PMSG output terminal such as AC line voltage (V_s), AC line current (I_s), and active power (P) gives the noisy response without losing the stability.



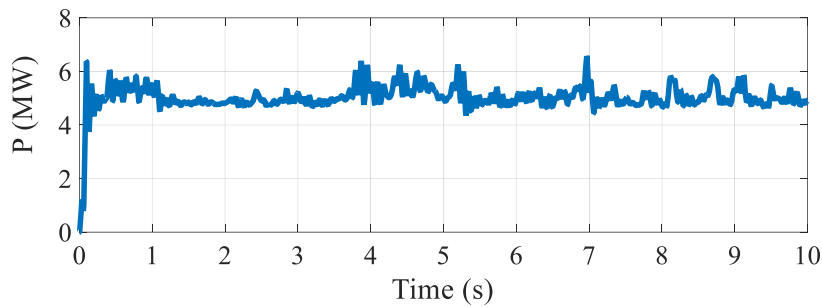
(a) Wind speed.



(b) AC line voltage V_s .



(c) AC line current I_s .



(d) Active power P .

Figure 2.10 The response of the wind energy system during noisy wind conditions.

2.2 AC Grid Connected Voltage Source Converter on No Load Condition

In this section, modeling of each component used for AC grid-connected VSC, and its simulation study under steady-state and dynamic conditions and harmonic distortions are presented.

2.2.1 Modeling of AC Grid Connected VSC

Figure 2.11 shows the AC grid connected to the HVDC converter, which consists of AC source, converter transformer, AC filter, phase reactor, VSC and its control model, DC capacitor and DC transmission line. The AC Source is 100 MVA, 220 kV,

50 Hz and the detailed modeling of the components used for this system is presented below:

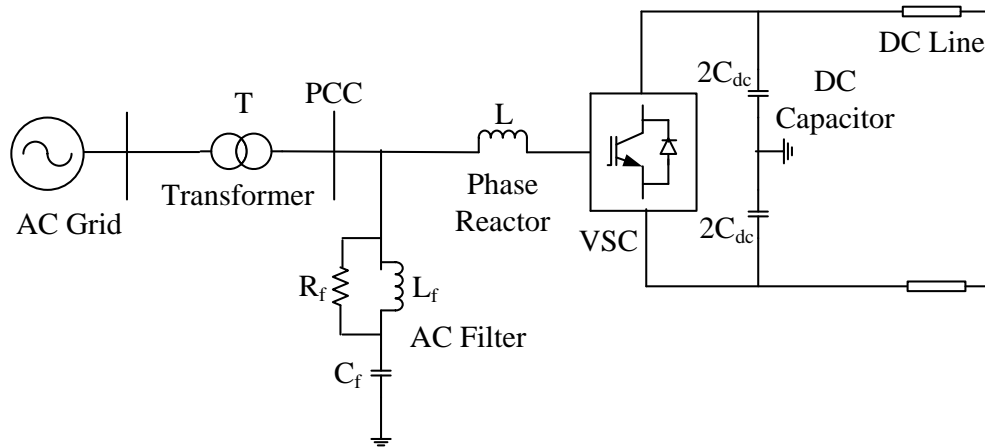


Figure 2.11 AC grid connected to the HVDC converter. (where, PCC refers to point of common coupling).

2.2.1.1 Converter Transformer

Converter transformer is used to transform the AC voltage of the grid or wind farm level to a suitable converter level. It provides a coupling reactance between the VSC and AC system. Leakage reactance value of the converter transformer is in the range of 0.1 to 0.2 per unit [C. Du 2003]. Converter transformer can also reduce the fault currents and size of the filter. In this test case, the AC grid voltage as 220 kV is stepped-down to 66 kV using 100 MVA, 220/ 66 kV transformer with a leakage reactance of 0.1 per unit.

2.2.1.2 Phase Reactor

The phase reactor can be used to control the power flow of VSC by altering the current flow through it. Also, it can be used as the filter to mitigate the high-frequency harmonic contents of AC currents. Practically the reactor value is 0.15 per unit [D. P. Dorantes et al. 2013]. The phase reactor calculation for 100 MVA, 66 kV rating is given below.

$$\text{Base current, } I_B = \frac{S_B}{\sqrt{3} \times V_B} = \frac{100 \text{ MVA}}{\sqrt{3} \times 66 \text{ kV}} = 0.8747 \text{ kA} \quad (2.15)$$

$$\text{Base impedance, } Z_B = \frac{V_B / \sqrt{3}}{I_B} = \frac{66 / \sqrt{3}}{0.8747} = 43.56 \Omega \quad (2.16)$$

$$\text{Phase A reactance, } X_{LA} = 0.15 \text{ p.u.} \times Z_B = 0.15 \times 43.56 = 6.5345 \Omega \quad (2.17)$$

$$\text{Phase A inductance, } L_A = \frac{X_{LA}}{\omega} = 0.0208 \text{ H} \quad (2.18)$$

$$\text{Nominal reactive power of phase A reactance, } Q_{XLA} = I_A^2 \times X_{LA} = 5 \text{ MVar} \quad (2.19)$$

where, I_A is the phase A current.

$$\text{Peak-to-peak ripple current} = \frac{V_{dc}}{4 \times L_A \times f_{sw}} \quad (2.20)$$

where, V_{dc} is the pole-to-pole DC voltage and f_{sw} is the switching frequency.

2.2.1.3 AC Filters

In the HVDC system, the harmonic voltages and currents can be generated due to the non-uniform distribution of flux on the armature winding of the AC generator, saturation of the converter transformer and switching of the PWM converter. The Harmonic voltages which are generated on the AC side can distort the supply nature and reduce the power quality. The switching instant of VSC and the resonance between L and C are the main reason for the generation of high-frequency harmonics. In particular, switching frequency is the primary source of harmonics.

Usually, passive filters are used to eliminate high-frequency harmonics. Single tuned, double tuned and high pass filters are commonly used in the HVDC applications. The single tuned and double tuned filters are designed to eliminate the single frequency and two discrete frequencies only. The high pass filter (HPF) can be applied to mitigate the high-frequency harmonics, and its design for 5 MVar and 2050 Hz cut-off frequency is given below [G. Shi et al. 2012].

$$C_f = \frac{Q_f}{2 \times \pi \times f \times V_L^2} = 3.655 \mu F \quad (2.21)$$

$$R_f = \frac{1}{2 \times \pi \times f_{cut-off} \times C_f} = 21.25 \Omega \quad (2.22)$$

$$L_f = m \times R_f^2 \times C_f = 3.31 \text{ mH} \quad (2.23)$$

where, Q_f is the reactive power rating of HPF, $f_{cut-off}$ is the cut-off frequency, V_L is the line-to-line voltage, f is the fundamental frequency, m is the parameter which relates the shape of filter impedance and the frequency curve. It can be varied from 0.5 to 2.

2.2.1.4 Voltage Source Converter

The voltage source converters (VSC) are developed based on insulated gate bipolar transistor (IGBT) switches with turn-on and turn-off capabilities. It uses the six switch valves which contains many switches in series depending on the voltage and current ratings. The two-level topology is commonly used for the HVDC converters. The AC source connected HVDC converter, i.e., two-level VSC which is shown in Figure 2.12.

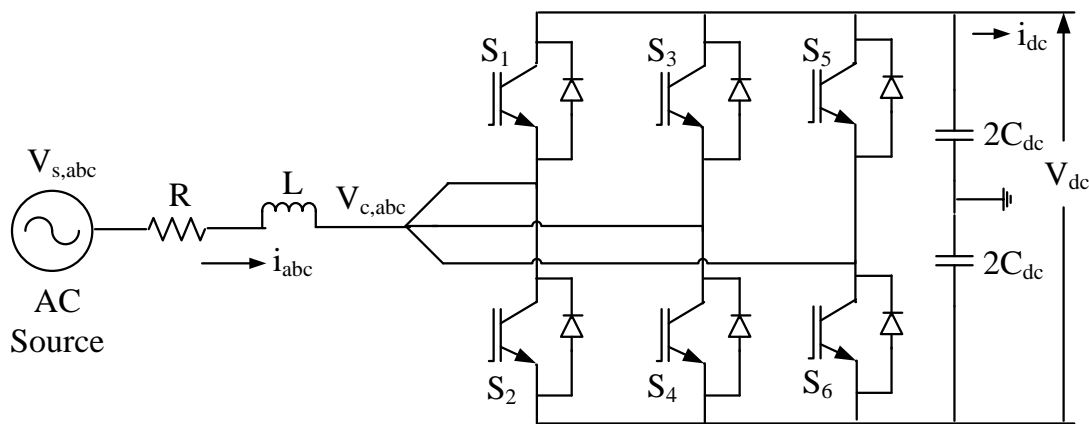


Figure 2.12 Two-level voltage source converter.

2.2.1.5 Control Model of VSC

The AC source is connected to the VSC as shown in Figure 2.12. Apply Kirchhoff's voltage law (KVL) to the circuit, the three-phase AC voltage at source terminal ($V_{s,abc}$) is given by,

$$V_{s,abc} = Ri_{abc} + L \frac{di_{abc}}{dt} + V_{c,abc} \quad (2.24)$$

where, $V_{c,abc}$ is the three-phase AC voltage at the converter terminal, i_{abc} is the AC current, R and L are resistance and inductance between the converter and AC source. After rearranging the equation (2.24), we get,

$$\Delta V_{abc} = Ri_{abc} + L \frac{di_{abc}}{dt} \quad (2.25)$$

where, $\Delta V_{abc} = V_{s,abc} - V_{c,abc}$

Consider the q-axis of the rotor reference frame is aligned to the AC voltage vector, and the q-axis is leading the d axis by 90° . The AC current in d-q frame can be derived from the park transformation as given by,

$$\begin{bmatrix} i_q \\ i_d \\ i_0 \end{bmatrix} = \frac{2}{3} \begin{bmatrix} \cos\omega t & \cos(\omega t - 120) & \cos(\omega t + 120) \\ \sin\omega t & \sin(\omega t - 120) & \sin(\omega t + 120) \\ 1/2 & 1/2 & 1/2 \end{bmatrix} \begin{bmatrix} i_a \\ i_b \\ i_c \end{bmatrix} \quad (2.26)$$

where, $\omega = 2 \times \pi \times f$

After rearranging equation (2.26), we get,

$$i_q = \frac{2}{3} [i_a \cos\omega t + i_b \cos(\omega t - 120) + i_c \cos(\omega t + 120)] \quad (2.27)$$

$$i_d = \frac{2}{3} [i_a \sin\omega t + i_b \sin(\omega t - 120) + i_c \sin(\omega t + 120)] \quad (2.28)$$

Similarly,

$$\Delta V_q = \frac{2}{3} [\Delta V_a \cos\omega t + \Delta V_b \cos(\omega t - 120) + \Delta V_c \cos(\omega t + 120)] \quad (2.29)$$

$$\Delta V_d = \frac{2}{3} [\Delta V_a \sin\omega t + \Delta V_b \sin(\omega t - 120) + \Delta V_c \sin(\omega t + 120)] \quad (2.30)$$

Differentiate the equations (2.27) and (2.28), we get,

$$\begin{aligned} \frac{di_q}{dt} &= \frac{2}{3} \left[\frac{di_a}{dt} \cos\omega t + \frac{di_b}{dt} \cos(\omega t - 120) + \frac{di_c}{dt} \cos(\omega t + 120) \right] \\ &\quad - \frac{2}{3} \omega [i_a \sin\omega t + i_b \sin(\omega t - 120) + i_c \sin(\omega t + 120)] \end{aligned} \quad (2.31)$$

$$\begin{aligned} \frac{di_d}{dt} &= \frac{2}{3} \left[\frac{di_a}{dt} \sin\omega t + \frac{di_b}{dt} \sin(\omega t - 120) + \frac{di_c}{dt} \sin(\omega t + 120) \right] \\ &\quad + \frac{2}{3} \omega [i_a \cos\omega t + i_b \cos(\omega t - 120) + i_c \cos(\omega t + 120)] \end{aligned} \quad (2.32)$$

From equation (2.25),

$$\frac{di_a}{dt} = \frac{\Delta V_a}{L} - \frac{Ri_a}{L} \quad (2.33)$$

$$\frac{di_b}{dt} = \frac{\Delta V_b}{L} - \frac{Ri_b}{L} \quad (2.34)$$

$$\frac{di_c}{dt} = \frac{\Delta V_c}{L} - \frac{Ri_c}{L} \quad (2.35)$$

Substitute the equations (2.33), (2.34) and (2.35) into (2.31), we get,

$$\begin{aligned}
\frac{di_q}{dt} &= \frac{2}{3} \left[\left(\frac{\Delta V_a}{L} - \frac{Ri_a}{L} \right) \cos \omega t + \left(\frac{\Delta V_b}{L} - \frac{Ri_b}{L} \right) \cos(\omega t - 120) + \left(\frac{\Delta V_c}{L} - \frac{Ri_c}{L} \right) \cos(\omega t + 120) \right] \\
&\quad - \frac{2}{3} \omega [i_a \sin \omega t + i_b \sin(\omega t - 120) + i_c \sin(\omega t + 120)] \\
\frac{di_q}{dt} &= \left[\frac{2}{3 \times L} (\Delta V_a \cos \omega t + \Delta V_b \cos(\omega t - 120) + \Delta V_c \cos(\omega t + 120)) \right] \\
&\quad - \frac{2R}{3L} [i_a \cos \omega t + i_b \cos(\omega t - 120) + i_c \cos(\omega t + 120)] - \omega i_d \\
\frac{di_q}{dt} &= \frac{1}{L} \Delta V_q - \frac{R}{L} i_q - \omega i_d \\
L \frac{di_q}{dt} &= \Delta V_q - R i_q - \omega L i_d \\
L \frac{di_q}{dt} &= V_{s,q} - V_{c,q} - R i_q - \omega L i_d \\
V_{s,q} &= R i_q + L \frac{di_q}{dt} + \omega L i_d + V_{c,q} \tag{2.36}
\end{aligned}$$

Similarly, substitute the equations (2.33), (2.34) and (2.35) into (2.32). we get,

$$\begin{aligned}
\frac{di_d}{dt} &= \frac{2}{3} \left[\left(\frac{\Delta V_a}{L} - \frac{Ri_a}{L} \right) \sin \omega t + \left(\frac{\Delta V_b}{L} - \frac{Ri_b}{L} \right) \sin(\omega t - 120) \right. \\
&\quad \left. + \left(\frac{\Delta V_c}{L} - \frac{Ri_c}{L} \right) \sin(\omega t + 120) \right] + \omega i_q \\
\frac{di_d}{dt} &= \frac{2}{3 \times L} (\Delta V_a \sin \omega t + \Delta V_b \sin(\omega t - 120) + \Delta V_c \sin(\omega t + 120)) \\
&\quad - \frac{2R}{3L} (i_a \sin \omega t + i_b \sin(\omega t - 120) + i_c \sin(\omega t + 120)) + \omega i_q \\
L \frac{di_d}{dt} &= \Delta V_d - R i_d + \omega L i_q \\
L \frac{di_d}{dt} &= V_{s,d} - V_{c,d} - R i_d + \omega L i_q \\
V_{s,d} &= R i_d + L \frac{di_d}{dt} - \omega L i_q + V_{c,d} \tag{2.37}
\end{aligned}$$

The following relations can be used to control the active power (P) and DC voltage (V_{dc}) as given by,

$$P = \frac{3}{2} (V_d i_d + V_q i_q) \tag{2.38}$$

$$P_{dc} = V_{dc}i_{dc} \quad (2.39)$$

$$V_q^{base} = \sqrt{\frac{2}{3}} \times V_{ac}^{base} ; \text{ and } i_q^{base} = \sqrt{2} \times i_{ac}^{base} \quad (2.40)$$

where i_{dc} is the DC current.

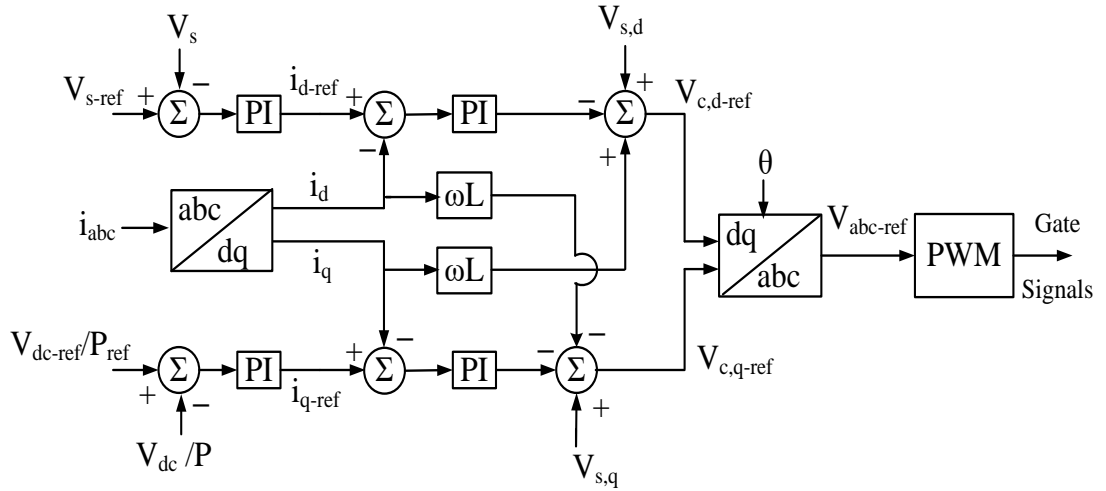


Figure 2.13 The decoupled d-q control strategy for VSC-HVDC system.

The decoupled d-q control strategy is used as the control system for the voltage source converter as shown in Figure 2.13. It can be implemented with the help of the equations (2.36)-(2.40). It consists of the outer controller and an inner current controller. The DC voltage (V_{dc}) and AC voltage (V_s) controller are used as an outer controller for the wind farm side VSC, and it regulates the AC and DC voltages under variable conditions. The constant DC voltage can automatically balance the active power. The active power (P) and AC voltage (V_s) controller are used as an outer controller for the grid side VSC, and it has retained the active power and also provide reactive power support for the AC grid to maintain the PCC voltage at a pre-determined level. The inner current controller is used to control the direct and quadrature axis components of the current independently. The generated d-q axis components of the reference voltage are transformed back to the three-phase abc frame and given as a reference signal for the sinusoidal pulse width modulation (SPWM). The converter output voltage can be controlled by using the SPWM. Due to

the high-frequency switching technology, the response of the VSC is very fast which is higher than the excitation system of synchronous generators [C. Bajracharya et al. 2008], [L. Xu and S. Li 2010], [E. Kontos et al. 2013].

2.2.1.6 Sinusoidal Pulse Width Modulation

Sinusoidal pulse width modulation (SPWM) is used to generate the firing pulses for the VSC. In SPWM, the switching signal is generated by comparing the carrier signal with the reference sinusoidal signal, which is generated by the decoupled d-q control. The PWM based three-phase inverter output voltage is given by,

$$V_{LL-rms} = \frac{\sqrt{3}}{2\sqrt{2}} \times M \times V_{dc} = 0.612 \times M \times V_{dc} \quad (2.41)$$

where, V_{LL-rms} is the line-to-line voltages, M is the modulation index, and it can be used to control the inverter output voltage. Usually, the modulation index value will be 0 to 1. The three-phase inverter operates under over-modulation when $M > 1$. The width of the pulses depends on the amplitude of the reference sinusoidal signal. The ratio of the peak magnitude of the reference sinusoidal signal (V_r) to the carrier signal (V_c) is called as the amplitude modulation index ($M = \frac{V_r}{V_c}$) [T. W. Shire 2009]. The switching frequency is 2050 Hz.

Using equation (2.41), the pole-to-pole DC voltage (V_{dc}) is calculated by,

$$V_{dc} = \frac{66 \text{ kV}}{0.612 \times 0.898} = 120 \text{ kV}; \text{ where, } M = 0.898 \quad (2.42)$$

In the case of the symmetric monopolar configuration, the pole-to-ground DC voltage (V_{dc-p-g}) is ± 60 kV.

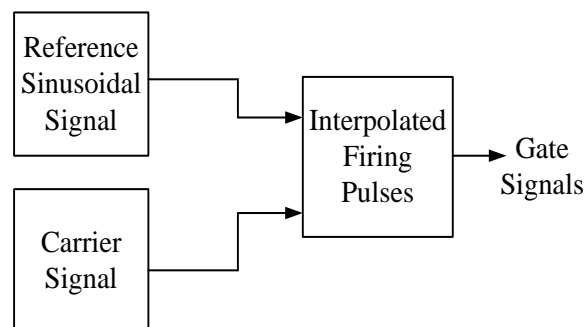
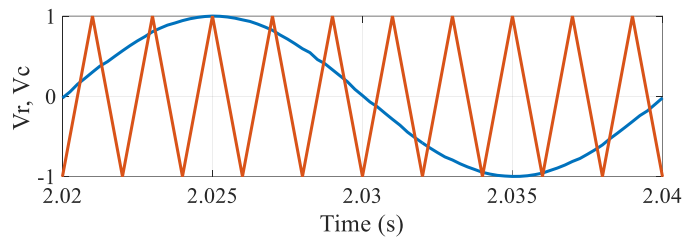
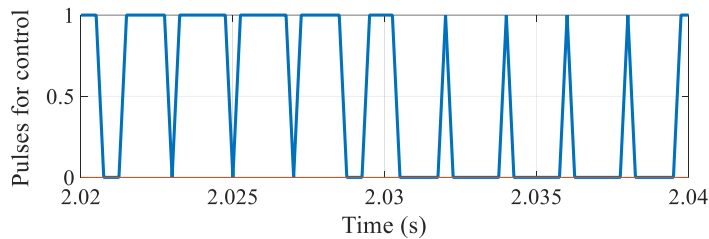


Figure 2.14 Block diagram of SPWM.

Figure 2.14 shows the block diagram of the sinusoidal pulse width modulation (SPWM). In the PSCAD/EMTDC simulation, the interpolated firing pulses are used to generate the switching pulses for the VSC. In normal fixed time step programs, the switching time resolution is limited, i.e., switching can occur only at the time points that are multiples of the time step. The advantage of interpolation is to remove this limitation by allowing any instant of time defined by the switching criteria. It will enable the simulation to run with a larger time step without affecting the accuracy. Figure 2.15 shows the simple PSCAD model for the generation of pulses for VSC by SPWM technique.



(a) Reference sine wave (V_r) and carrier wave (V_c).



(b) Gate pulses for control.

Figure 2.15 PSCAD simulation for the generation of gate pulses using SPWM.

2.2.1.7 DC Capacitor

DC capacitor (C_{dc}) is the energy storage element in the VSC. It provides the VSC with the stiff DC voltage between switching instants. The design requirements for the DC capacitor is to limit the DC voltage ripple under transient conditions, harmonic contents passing to the DC side and peak discharge current for DC faults. It can be calculated by,

$$C_{dc} = \frac{2S_{VSC} E_s}{V_{dc}^2} \quad (2.43)$$

$$E_s = \frac{E_c}{S_{VSC}} ; \text{ and } E_c = \frac{1}{2} C_{dc} V_{dc}^2 \quad (2.44)$$

where, S_{VSC} is converter power in VA, E_c is the capacitor energy in J and E_s is the energy to power ratio in J/VA. Practically, E_s value ranges from 10 kJ/MVA to 50 kJ/MVA [D. Jovcic and K. Ahmed 2015]. For this configuration, the DC capacitor value (C_{dc}) is calculated as 0.05 mF.

2.2.1.8 DC Transmission Line

The transmission line model can be divided into two categories such as π section and distributed parameter line model. The distributed line (traveling wave) model can be classified into Bergeron model, frequency dependent mode model, and frequency dependent phase model.

(i) Bergeron Model: In Bergeron model, the L and C are in distributed nature. This method is accurate for the system with a specific frequency. It can be applied for the AC relay studies where the specified frequency is very important. However, it is not suitable for electromagnetic transients and harmonic studies due to the absence of information about some frequency response [PSCAD/EMTDC online help].

(ii) Frequency dependent mode model: The frequency dependent mode model represents the frequency dependence of all parameters. It is based on the constant transformation matrix. It applies the model techniques to solve the transmission line constants. However, it is accurate for only the system of ideally transposed conductors or single conductors [PSCAD/EMTDC online help]. Also, the modal decomposition might go to unstable when this method is applied to overhead transmission lines [B. Gustavsen et al. 1999].

(iii) Frequency dependent phase model: The frequency dependent phase model is mostly preferred for the HVDC transmission line due to the accurate representation of the frequency dependency and distributed nature of all parameters. It can be called a distributed RLC traveling wave model and also widely used for the electromagnetic transient studies. It can eliminate the problems associated with the modal transformation matrices due to the direct formulation of the phase domain. It is accurate for all the transmission line configurations which include both the balanced and unbalanced line geometry. Therefore, the frequency dependent phase model is considered for the MT VSC-HVDC transmission lines. [PSCAD/EMTDC online help], [J. R. Marti 1982], [J. R. Marti et al. 1993], [T. K. Vrana et al. 2013].

2.2.2 Simulation of AC Grid connected VSC system on PSCAD

The simulation model of the AC source connected VSC is shown in Figure 2.16. In this section, the performance of the AC grid connected VSC is analyzed under steady-state and fault conditions. Also, the harmonic analysis of the AC grid connected VSC for both without and with filter cases is presented.

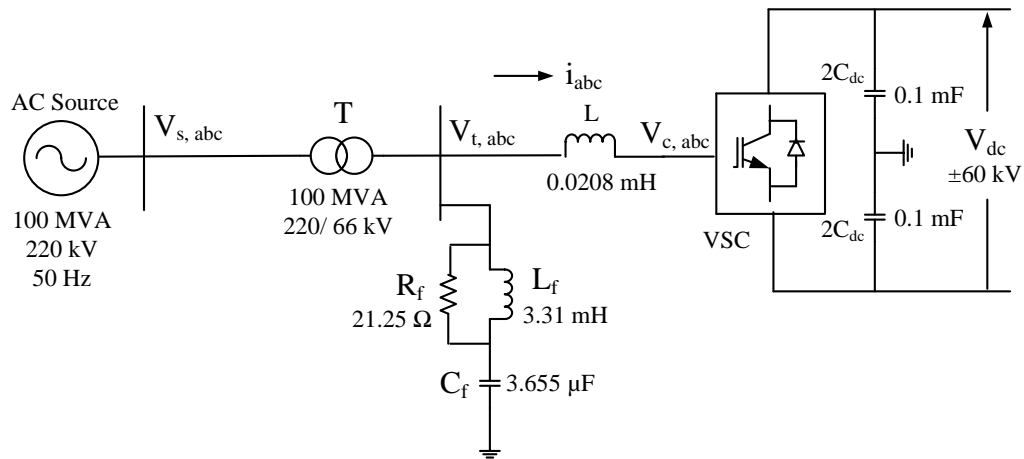
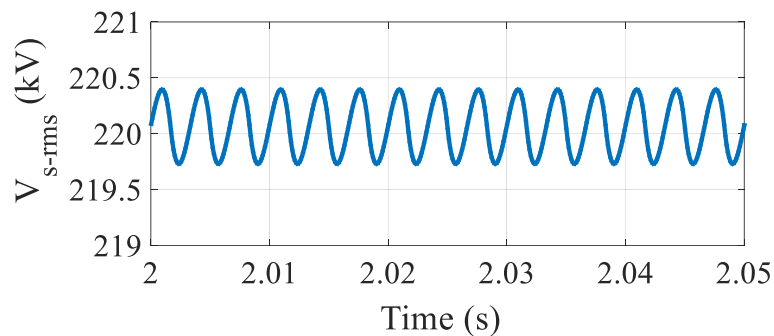


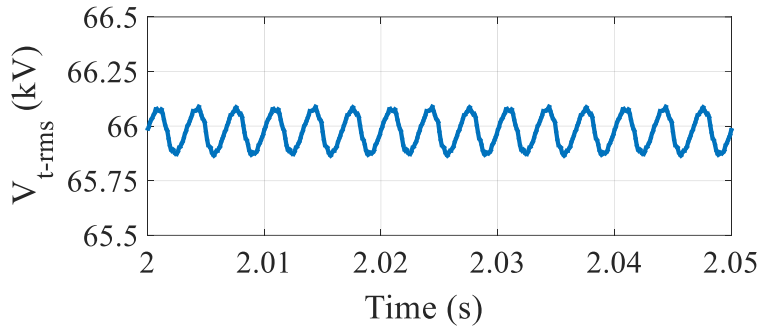
Figure 2.16 AC source connected VSC model.

2.2.2.1 Steady State Behaviour

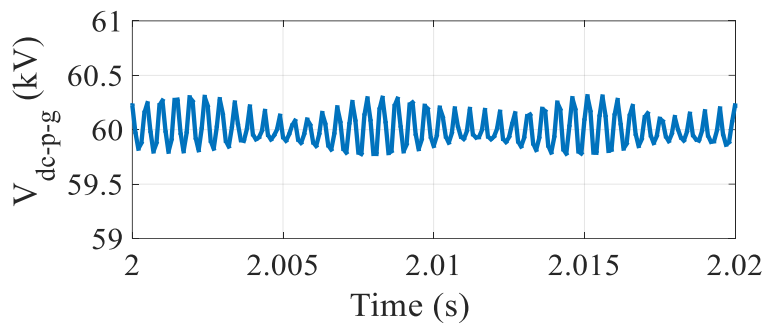
The steady-state response of the AC source connected VSC system on a no-load condition is shown in Figure 2.17. In steady-state, the RMS value of the AC line voltage at the source terminal is 220 kV, RMS value of the AC line voltage at low voltage (LV) side of the transformer is 66 kV, and positive pole-to-ground DC voltage is 60 kV.



(a) RMS value of AC line voltage at source terminal (V_{s-rms}).



(b) RMS value of AC line voltage at LV side of transformer (V_{t-rms}).

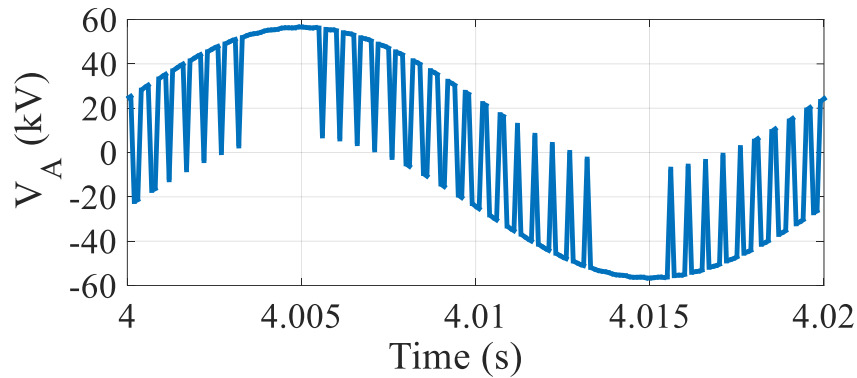


(c) Positive pole-to-ground DC voltage (V_{dc-p-g}).

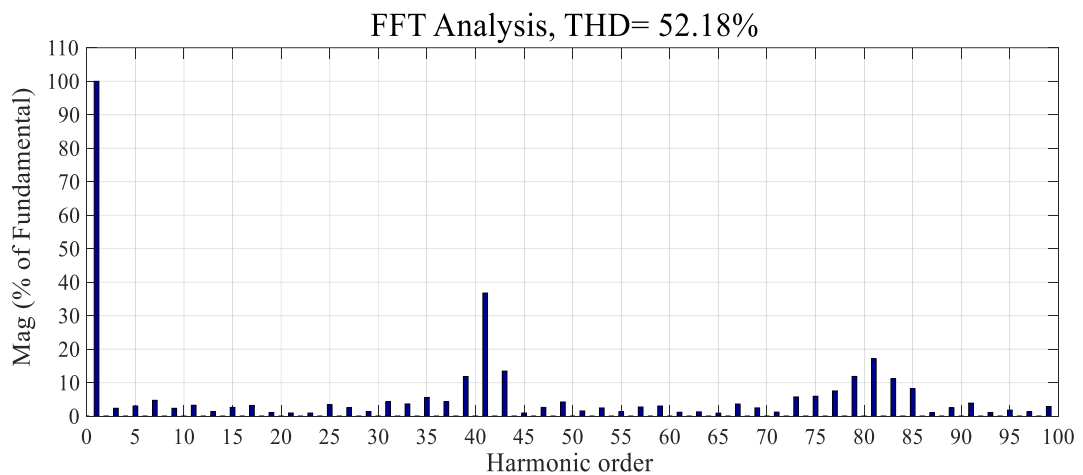
Figure 2.17 Steady-state response of the AC source connected VSC.

2.2.2.2 Harmonic Distortions

In this section, the simulation study of the harmonic distortion of the AC source connected VSC on a no-load condition is presented. Usually, the harmonics are generated in the HVDC system due to the switching function of the VSC and resonance between L and C. Switching frequency is the main source of harmonics on both sides of the VSC. The harmonic analysis of the AC source connected VSC without a filter is shown in Figure 2.18. The phase A voltage at the converter terminal contains high-frequency harmonics and that is shown in Figure 2.18 (a). The switching frequency is 2050 Hz, and the fundamental frequency is 50 Hz. The magnitude of harmonic voltage is very high when the harmonics are at the switching frequency [Chien, C. H., and Bucknall, R. W. 2007]. Therefore, 41st Harmonic has a higher magnitude which is demonstrated in Figure 2.18 (b). The total harmonic distortion (THD) of the phase A voltage at the converter terminal without the filter is 52.18 %.



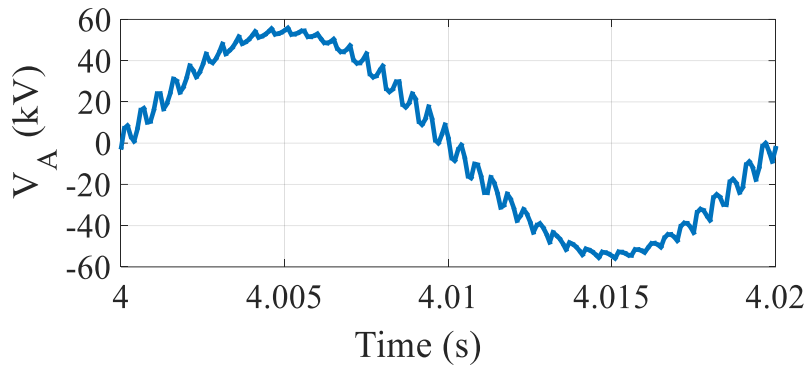
(a) Phase A voltage at converter terminal (V_A).



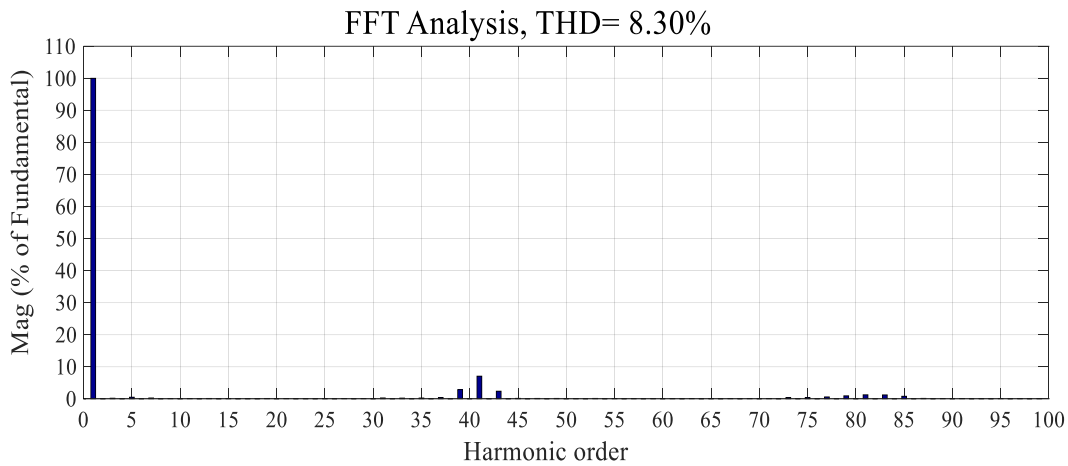
(b) Harmonic content of Phase A voltage (V_A).

Figure 2.18 Harmonic analysis of AC source connected VSC without filter.

From the above analysis, it is observed that 41st harmonics has the highest peak magnitude. Therefore, the cutoff frequency for the filter design is selected as 2050 Hz. The high pass filter design for the selected cutoff frequency is reported in section 2.2.1.3. The harmonic analysis of AC source connected VSC with a high pass filter is shown in Figure 2.19. The harmonic content of the phase A voltage at the converter terminal is reduced by connecting the high pass filter which can be seen in Figure 2.19 (a). Figure 2.19 (b) shows that the 41st harmonic and other harmonic contents are greatly reduced. Also, the total harmonic distortion (THD) of converter terminal phase A voltage with the high pass filter is 8.30 %.



(a) Phase A voltage at converter terminal (V_A).



(b) Harmonic content of Phase A voltage (V_A).

Figure 2.19 Harmonic analysis of AC source connected VSC with high pass filter.

2.2.2.3 AC Fault Conditions

A line-to-line fault (L-L) is applied for 50 ms on the low voltage (LV) side of the converter transformer to investigate the behaviour of AC source connected VSC on a no-load under unbalanced fault conditions. The schematic diagram of the AC grid connected VSC under line-to-line fault is shown in Figure 2.20. The line-to-line fault has occurred on phase A-B at $t = 3.0$ s, and fault resistance is considered as 0.01Ω . Figure 2.21 presents the response of the AC source connected VSC system under phase A-B fault on the LV side of the transformer.

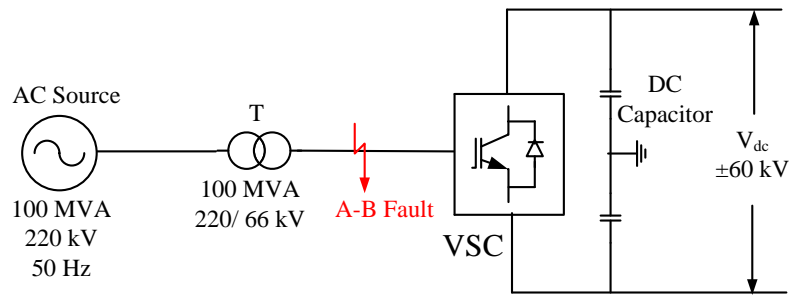
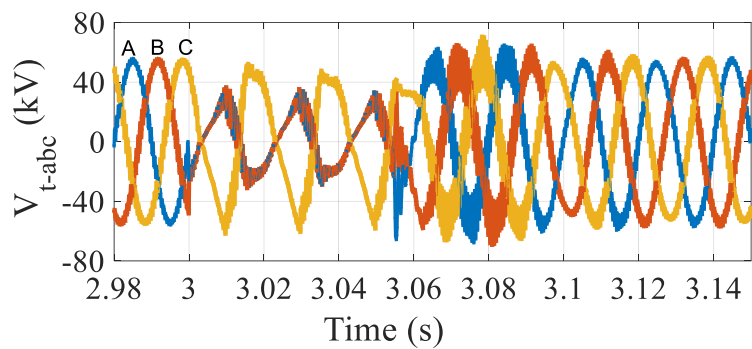
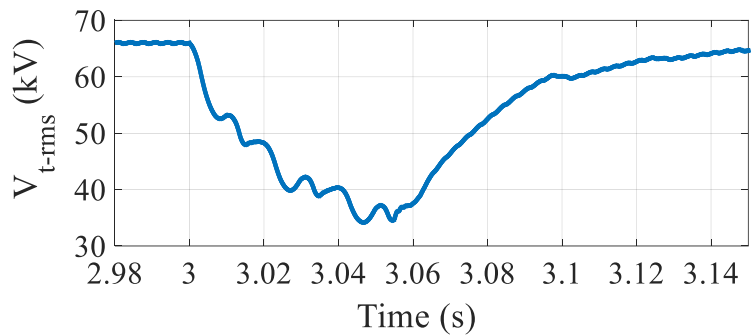


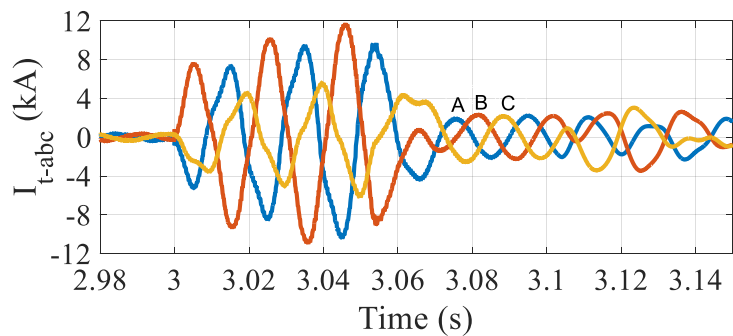
Figure 2.20 Schematic diagram of AC grid connected VSC under A-B fault.



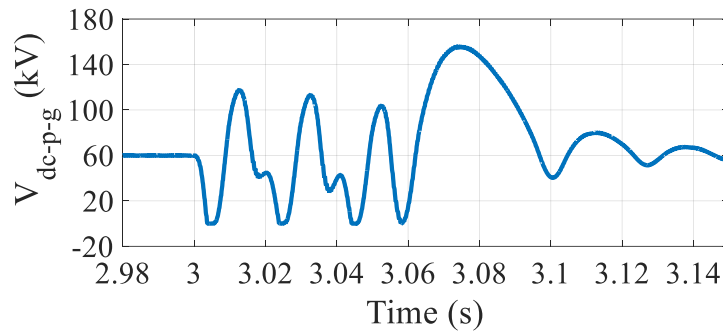
(a) Three phase AC voltage at LV side of transformer (V_{t-abc}).



(b) RMS value of AC line voltage at LV side of transformer (V_{t-rms}).



(c) Three phase AC current at LV side of transformer (I_{t-abc}).



(d) Positive pole-to-ground DC voltage (V_{dc-p-g}).

Figure 2.21 The response of the AC source connected VSC under line-to-line fault condition.

The AC line voltage at the fault point is reduced from 66 kV to 35 kV during fault period and recovered to the steady-state value once the fault is cleared. After the fault, the peak value of the three-phase AC current at the LV side of the transformer is increased up to 11.6 kA. Transients are present in the positive pole-to-ground DC voltage and retain to the steady value after the time, $t = 3.14$ s. Therefore, the response of the DC side gets disturbed due to faults on the AC side under the no-load condition.

2.3 Windmill Connected Voltage Source Converter on No Load Condition

In this section, the modeling of windmill connected VSC and its simulation study under steady-state and dynamic conditions are presented.

2.3.1 Modeling of Windmill Connected VSC

The simulation model of the windmill connected VSC is shown in Figure 2.22. The calculation used for this simulation study is presented below.

Rating of the wind power generation system = 5 MW, 0.69 kV, 50 Hz

Converter transformer = 25 MVA, 0.69/ 66 kV, leakage reactance = 10%

Phase reactor = 0.15 per unit

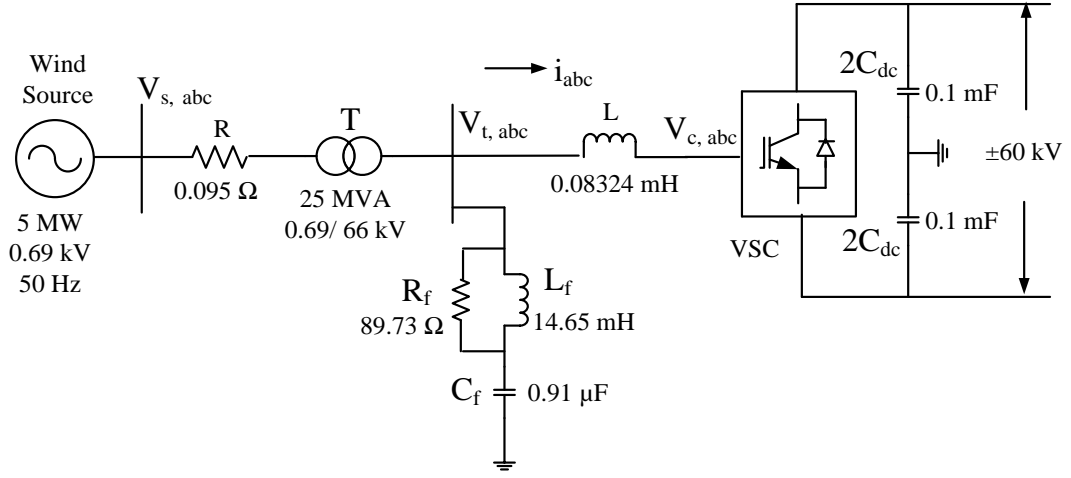


Figure 2.22 Windmill connected VSC model.

Phase reactor calculation for 25 MVA, 66 kV rating is given below.

$$\text{Base current, } I_B = \frac{S_B}{\sqrt{3}V_B} = \frac{25 \text{ MVA}}{\sqrt{3} \times 66 \text{ kV}} = 0.2186 \text{ kA}$$

$$\text{Base impedance, } Z_B = \frac{66/\sqrt{3}}{0.2186} = 174.31 \Omega$$

$$\text{Phase A reactance, } X_{LA} = 0.15 \text{ p.u.} \times 174.31 = 26.146 \Omega$$

$$\text{Phase A inductance, } L_A = \frac{X_{LA}}{\omega} = 0.08324 \text{ H}$$

$$\text{Nominal reactive power of phase A reactance, } Q_{XLA} = I_A^2 \times X_{LA} = 1.2494 \text{ MVar}$$

High pass filter design for 1.2494 MVar and 1950 Hz cut-off frequency is given by,

$$C_f = \frac{Q_f}{2 \times \pi \times f \times V_L^2} = 0.91 \mu F$$

$$R_f = \frac{1}{2 \times \pi \times f_{\text{cut-off}} \times C_f} = 89.73 \Omega$$

$$L_f = m \times R_f \times C_f = 14.65 \text{ mH}$$

In decoupled d-q Control, the stator voltage is aligned to q-axis.

$$V_q^{\text{base}} = \sqrt{\frac{2}{3}} \times V_{ac}^{\text{base}} = 0.8164 \times 66 \text{ kV} = 53.88$$

$$i_{ac}^{base} = \frac{S_B}{\sqrt{3} \times V_{ac}^{base}} = \frac{25 \text{ MVA}}{\sqrt{3} \times 66 \text{ kV}} = 0.2186 \text{ kA}$$

$$i_q^{base} = \sqrt{2} \times i_{ac}^{base} = \sqrt{2} \times 0.2186 = 0.3091$$

Modulation index, $M = \frac{V_r}{V_c} = 0.898$; Switching frequency = 1950 Hz

Three-phase inverter output voltage, $V_{LL-rms} = \frac{\sqrt{3}}{2\sqrt{2}} \times M \times V_{dc} = 0.612 \times M \times V_{dc}$

Pole-to-pole DC voltage, $V_{dc} = \frac{66 \text{ kV}}{0.612 \times 0.898} = 120 \text{ kV}$

The pole-to-ground DC voltage, $(V_{dc-p-g}) = \pm 60 \text{ kV}$ (symmetric monopolar configuration)

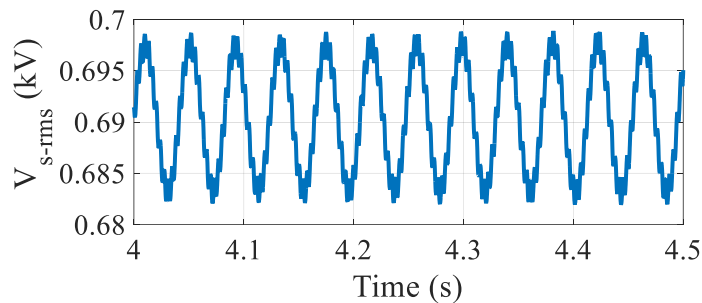
DC capacitor, $C_{dc} = \frac{2S_{VSC} E_s}{V_{dc}^2} = 0.05 \text{ mF}$

2.3.2 Analysis of Simulation Results

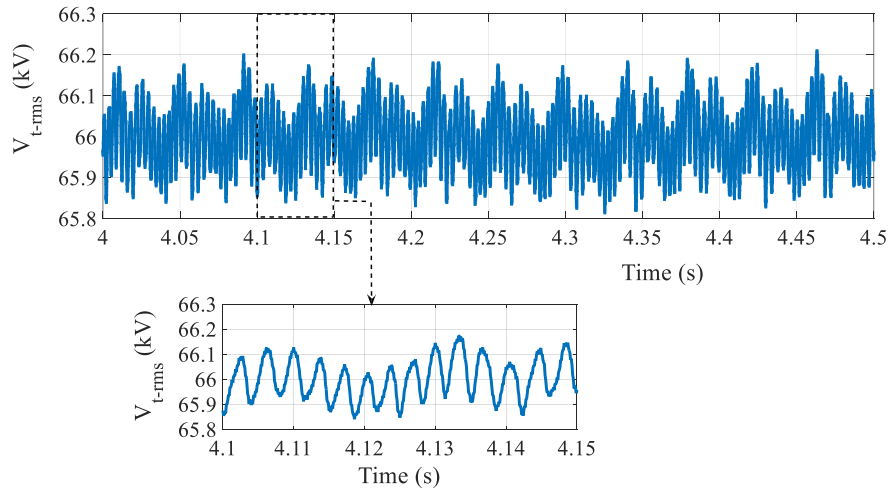
In this section, the simulation study of the windmill connected VSC under steady-state and gust variation of the wind speed conditions are presented.

2.3.2.1 Steady State Behaviour

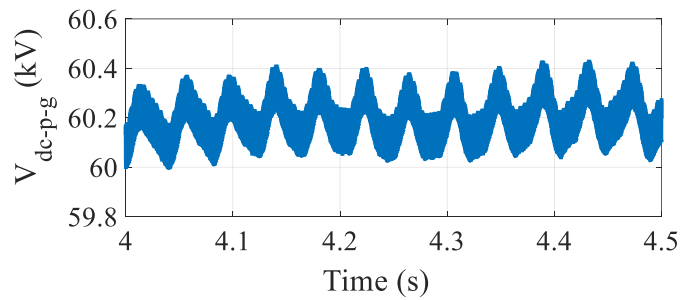
The steady-state response of the windmill connected VSC on a no-load condition is presented in Figure 2.23. In steady-state, the RMS value of the AC line voltage at the PMSG output terminal is 0.69 kV, RMS value of AC line voltage at the high voltage (HV) side of the converter transformer is 66 kV with high-frequency harmonics, and positive pole-to-ground DC voltage is 60 kV.



(a) RMS value of AC line voltage at PMSG output terminal (V_{s-rms}).



(b) RMS value of AC line voltage at HV side of transformer (V_{t-rms}).

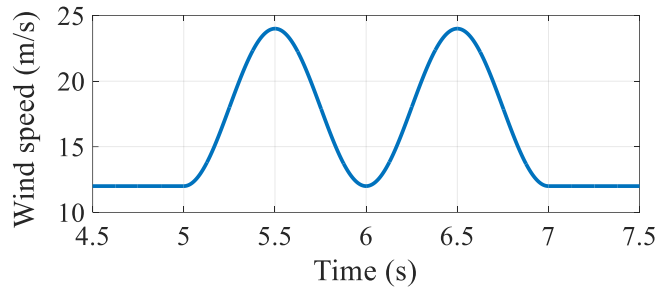


(c) Positive pole-to-ground DC voltage (V_{dc-p-g}).

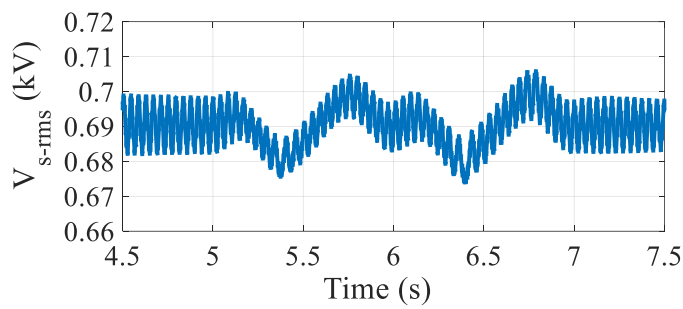
Figure 2.23 Steady state response of the windmill connected VSC.

2.3.2.2 Changes in the Wind Speed

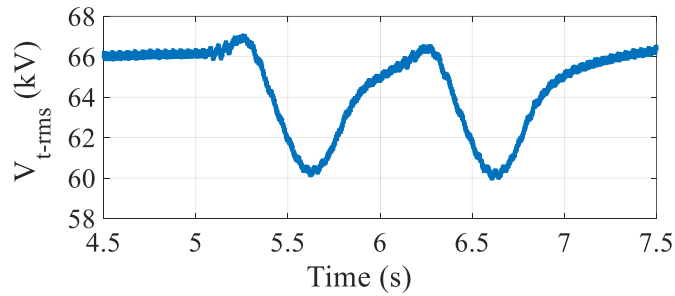
In this case, the performance of the windmill connected VSC is tested with the gust variation of wind speed condition. Gust wind data are the following: gust peak velocity is 12 m/s, gust-starting time is 5 s, gust period is 2 s and number of gusts is 1. The response of the windmill connected VSC under gust wind condition is shown in Figure 2.24. The normal wind speed is 12 m/s. Therefore, the peak wind speed can go up to 24 m/s during gust period. If wind speed increases more than 25 m/s, the operation of wind turbine-generator gets affected. The response of the windmill connected VSC such as AC line voltage at the PMSG output terminal and HV side of the transformer and positive pole-to-ground DC voltage is decreased as in the form of a sinusoidal pattern.



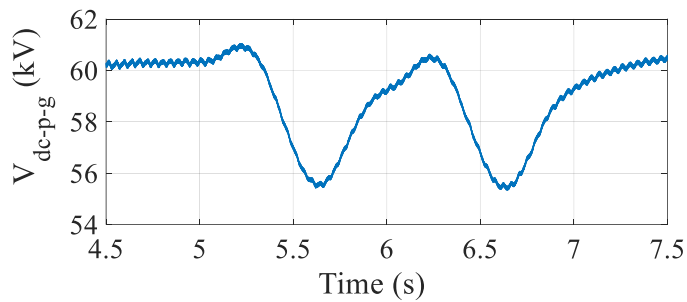
(a) Gust wind speed.



(b) RMS value of AC line voltage at PMSG output terminal (V_{s-rms}).



(c) RMS value of AC line voltage at HV side of transformer (V_{t-rms}).



(d) Positive pole-to-ground DC voltage (V_{dc-p-g}).

Figure 2.24 The response of the windmill connected VSC under gust wind conditions.

2.4 Windmill and AC source Connected VSC on No Load Condition

The simulation model of the windmill and AC source connected VSC is shown in Figure 2.25. The modeling of the system which is used for this simulation study is presented below.

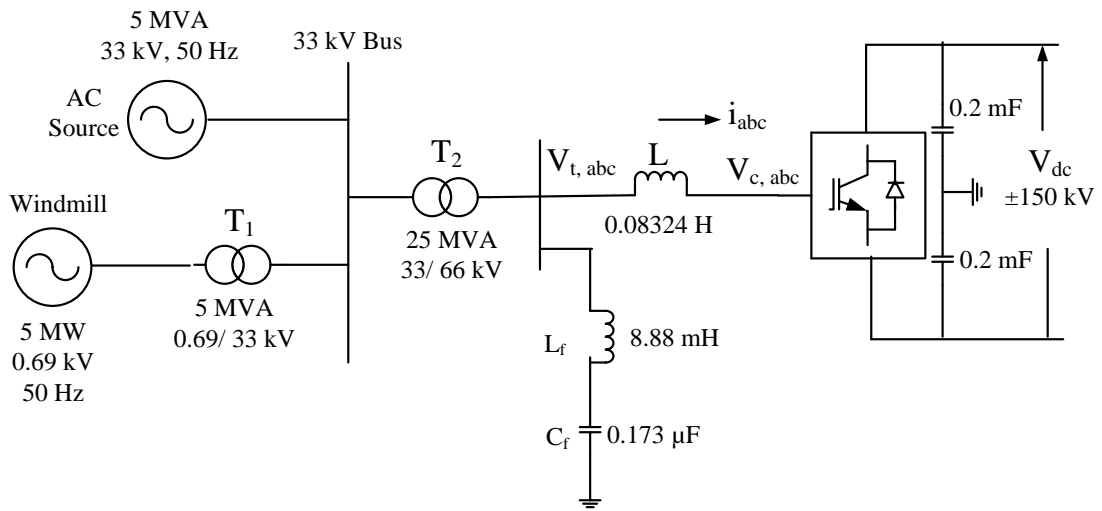


Figure 2.25 Windmill and AC source connected VSC model.

Wind power generation system = 5 MW, 0.69 kV, 50 Hz

AC source = 5 MVA, 33 kV, 50 Hz

Transformer (T_1) = 5 MVA, 0.69/ 33 kV, leakage reactance = 10 %

Transformer (T_2) = 25 MVA, 33/ 66 kV, leakage reactance = 10 %

Phase reactor = 0.15 per unit

$$\text{Base current, } I_B = \frac{S_B}{\sqrt{3}V_B} = \frac{25 \text{ MVA}}{\sqrt{3} \times 66 \text{ kV}} = 0.2186 \text{ kA}$$

$$\text{Base impedance, } Z_B = \frac{66/\sqrt{3}}{0.2186} = 174.31 \Omega$$

$$\text{Phase A reactance, } X_{LA} = 0.15 \text{ p.u.} \times 174.31 = 26.146 \Omega$$

$$\text{Phase A inductance, } L_A = \frac{X_{LA}}{\omega} = 0.08324 \text{ H}$$

Nominal reactive power of phase A reactance, $Q_{XLA} = I_A^2 \times X_{LA} = 1.2494 \text{ MVA}r$

LC filter design for 1.2494 *MVA*r and 2550 Hz cut-off frequency is given by, [D. P. Dorantes et al. 2013]

$$C_f = \frac{Q_f}{\omega_1 \times V_{ph}^2} = 0.173 \mu F$$

$$L_f = \frac{V_{ph}^2 \times \omega_1}{Q_f \times \omega_2^2} = 8.88 \text{ mH}$$

where, ω_1 is the fundamental frequency and ω_2 is the cut-off frequency.

In decoupled d-q control, the stator voltage is aligned to q-axis.

$$V_q^{base} = \sqrt{\frac{2}{3}} \times V_{ac}^{base} = 0.8164 \times 66 \text{ kV} = 53.88$$

$$i_{ac}^{base} = \frac{S_B}{\sqrt{3} \times V_{ac}^{base}} = \frac{25 \text{ MVA}}{\sqrt{3} \times 66 \text{ kV}} = 0.2186 \text{ kA}$$

$$i_q^{base} = \sqrt{2} \times i_{ac}^{base} = \sqrt{2} \times 0.2186 = 0.3092$$

Modulation index, $M = 0.359$; Switching frequency = 3950 Hz

Three-phase inverter output voltage, $V_{LL-rms} = 0.612 \times M \times V_{dc}$

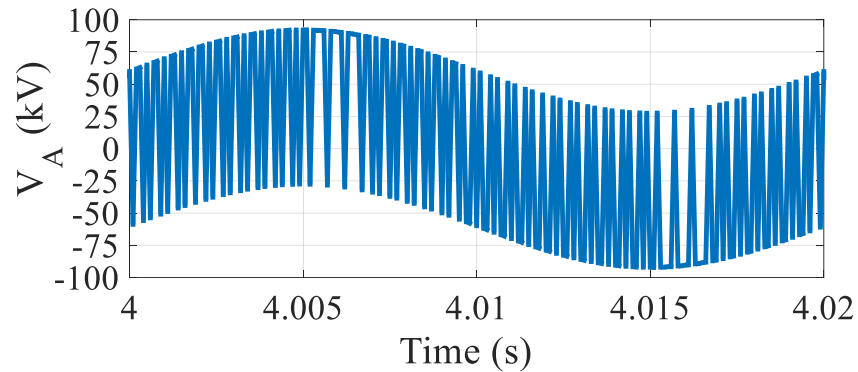
Pole-to-pole DC voltage, $V_{dc} = \frac{66 \text{ kV}}{0.612 \times 0.359} = 300 \text{ kV}$

The pole-to-ground DC voltage, $(V_{dc-p-g}) = \pm 150 \text{ kV}$ (symmetric monopolar configuration)

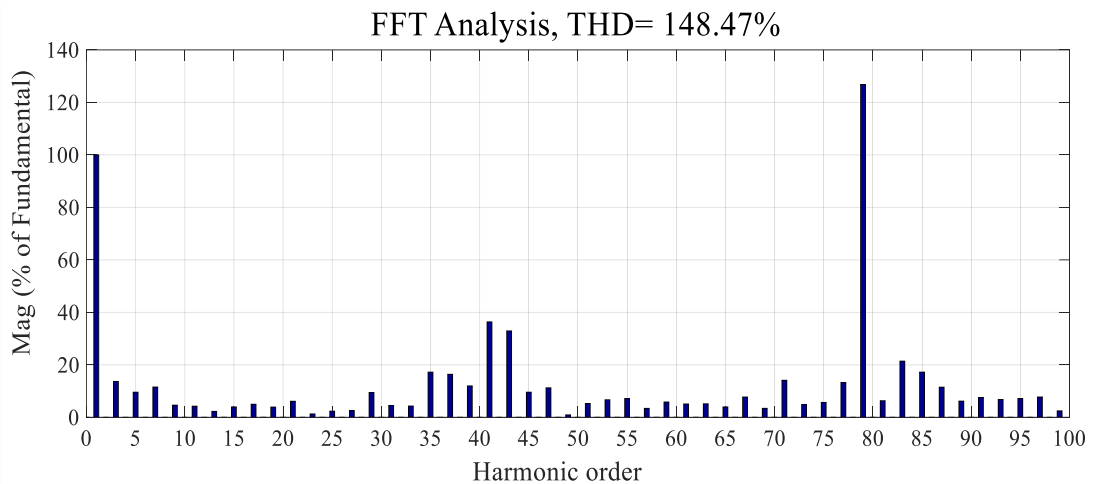
DC capacitor, $C_{dc} = 0.1 \text{ mF}$

2.4.1 Analysis of Simulation Results on Harmonic Distortions

In this section, the harmonic study of the windmill and AC source connected VSC on a no-load condition is presented. The harmonic analysis of the windmill and AC source connected VSC without a filter is shown in Figure 2.26. The phase A voltage at the converter terminal gives non-sinusoidal waveform, and it contains high-frequency harmonics.



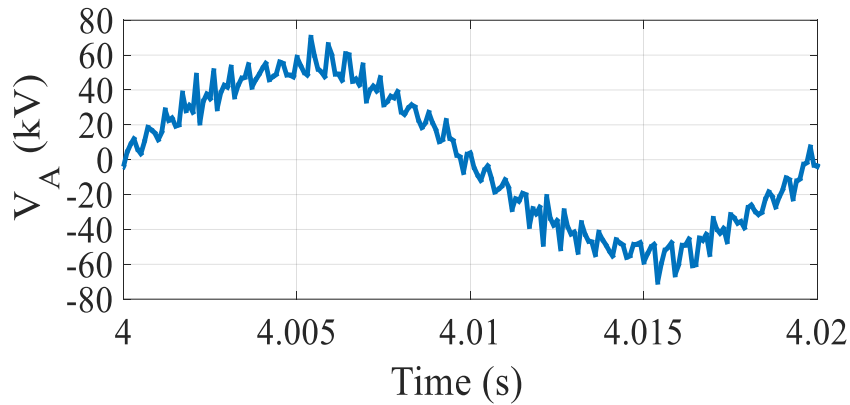
(a) Phase A voltage at converter terminal (V_A).



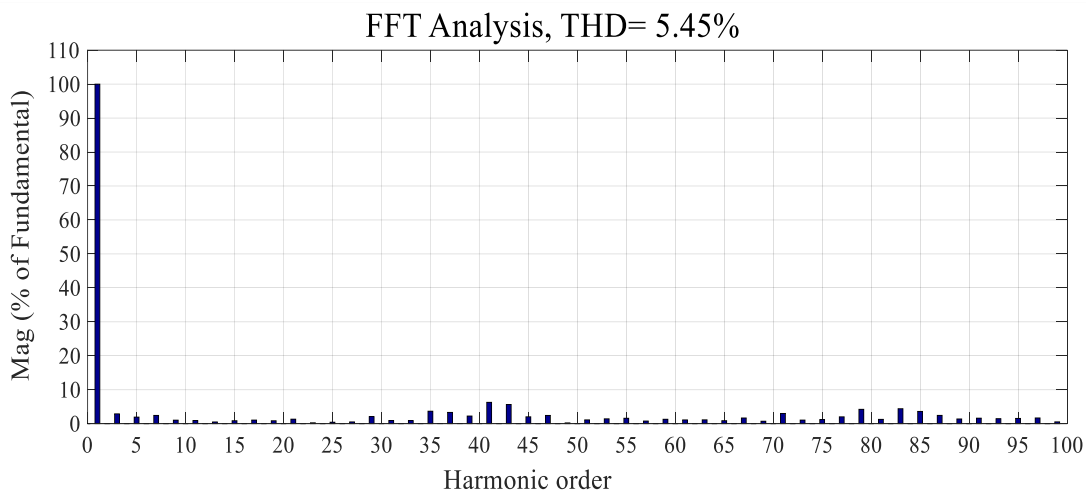
(b) Harmonic content of Phase A voltage (V_A).

Figure 2.26 Harmonic analysis of the windmill and AC source connected VSC without filter.

In this case, the switching frequency is selected as 3950 Hz, and the fundamental frequency is 50 Hz. Therefore, the 79th harmonic magnitude is very high, and that is demonstrated in Figure 2.26 (b). The THD of the phase A voltage at the converter terminal without the filter is 148.47 %. The LC filter is designed to filter out the high-frequency harmonics which are present in the AC voltage at the converter terminal. The cutoff frequency for the LC filter is selected as 2550 Hz. Figure 2.27 shows the harmonic analysis of windmill and AC source connected VSC with LC filter. The THD of the phase A voltage at the converter terminal with the LC filter is 5.45 %.



(a) Phase A voltage at converter terminal (V_A).



(b) Harmonic content of Phase A voltage (V_A).

Figure 2.27 Harmonic analysis of the windmill and AC source connected VSC with LC filter.

2.5 Conclusions

The multi-terminal VSC-based HVDC link is the recent interest for grid integration of large-scale offshore wind farms. In this section, the modeling of the grid-connected offshore wind farms, voltage source converter, and windmill connected VSC on the no-load condition are presented. The simulation study of the modeled component is carried out under steady-state and dynamic conditions. The obtained results indicate that the variation of wind speed influences the response of the offshore wind farm and windmill connected VSC. The transients are presented in the DC side of the grid-

connected VSC on no-load condition due to the fault on the AC side. Also, the simulation studies on total harmonic distortion (THD) of the grid and windmill connected VSC is carried out in both without and with filters. From the simulation results, it is noticed that the harmonic content and THD of the AC voltage at the converter terminal is reduced significantly when the high pass and LC filters are connected with the system.

CHAPTER 3

SIMULATION STUDIES ON POWER SYSTEM DISTURBANCES IN MULTI-TERMINAL VSC-BASED HVDC SYSTEMS

In this chapter, different case studies are presented to analyze the performance of the multi-terminal VSC-based HVDC link connected offshore wind farms under various fault conditions. Also, the performance of the proposed HVDC system is analyzed under varying wind speed conditions during steady-state and fault situations. The main purpose of this simulation study is to understand the transient behaviour of the multi-terminal VSC-based HVDC systems. In order to specify the requirements of circuit breakers, a full understanding of the transient fault currents and voltages is needed. Therefore, the transient fault studies in the multi-terminal VSC-HVDC system becomes very important before developing protection Schemes.

3.1 Test Case 1

A three-terminal VSC-based HVDC transmission system linked offshore wind farms is shown in Figure 3.1. The wind turbine-generator has 5 MW, 0.69 kV capacity which is considered as the offshore wind farm (OWF) due to the availability of a limited version of PSCAD software. The generation of offshore wind power is stepped-up to the transmission level as 66 kV using the converter transformer. The OWF side VSCs, i.e., VSC₁ and VSC₂ are connected by 100 km distance, and it is connected to the grid side VSC, i.e., VSC₃ by 200 km distance. The meshed connection is used for the three-terminal HVDC network due to the advantage of high flexibility and reliability. The symmetric monopolar configuration is applied for the HVDC link operation, and it provides various voltage levels such as $\left(\frac{+V_{dc}}{2}, \frac{-V_{dc}}{2}\right)$, where V_{dc} is the pole-to-pole DC voltage. In steady-state condition, the pole-to-ground DC voltage (V_{dc-p-g}) is ± 60 kV. The output of VSC₃ is stepped-up to grid voltage level as 220 kV, and finally, it has connected to the AC grid.

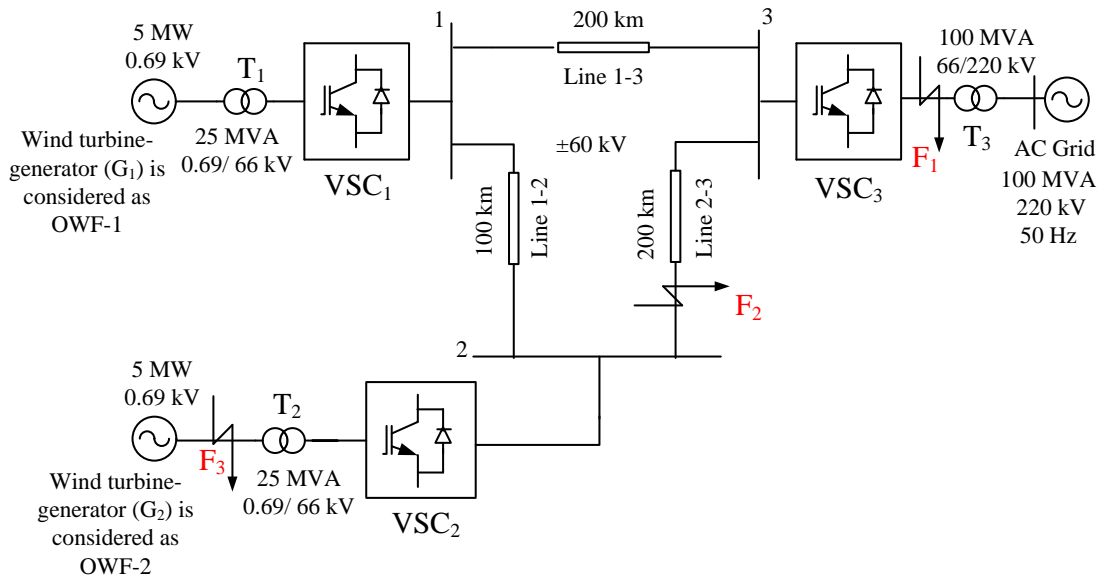
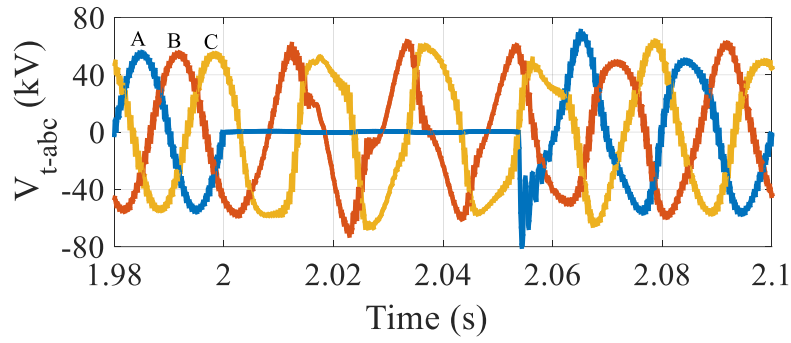


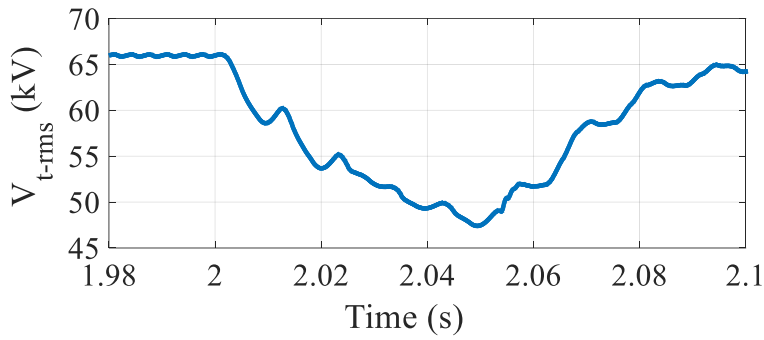
Figure 3.1 Test case 1- Three terminal VSC-based HVDC transmission system linked offshore wind farms.

3.1.1 AC Fault Conditions

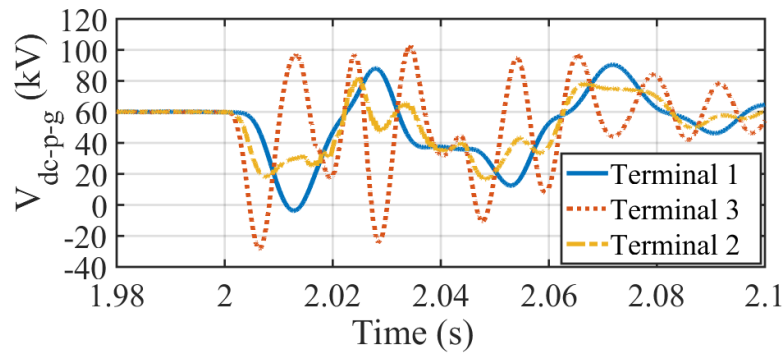
The phase-to-ground (A-G) fault is applied on the LV side of the converter transformer T_3 which is indicated as F_1 in Figure 3.1. The A-G fault is created at time $t = 2.0$ s, the fault duration is considered as 50 ms, and the fault resistance (R_f) is taken as 0.05Ω . The response of the HVDC system under A-G fault is shown in Figure 3.2. After the occurrence of a fault, the AC voltage at LV side of T_3 has decreased from 66 kV to 48 kV and recovers slowly to the nominal value after the clearance of fault which can be seen from the Figure 3.2 (a) and (b). Figure 3.2 (c) indicates that the transients are produced in the DC voltage at the three-terminals of the HVDC system due to the fault on the AC side. At $t = 2.0$ s, the peak value of the DC fault current at terminal-1 and terminal-3 has increased to 30.28 kA and 29.5 kA. The direction of the DC fault current at terminal-3 is reversed due to the A-G fault on the grid side which can be seen from Figure 3.2 (d). The peak value of the DC fault current at terminal-2 is increased to 20.39 kA. Also, the DC voltage and fault current at three terminals of the HVDC system has come back to the steady-state value after an oscillation once the A-G fault on the LV side of T_3 is cleared. The AC line voltage at the HV side of T_1 , i.e., the response of the OWF-1 side also gets affected due to the A-G fault on the grid side as shown in Figure 3.2 (e).



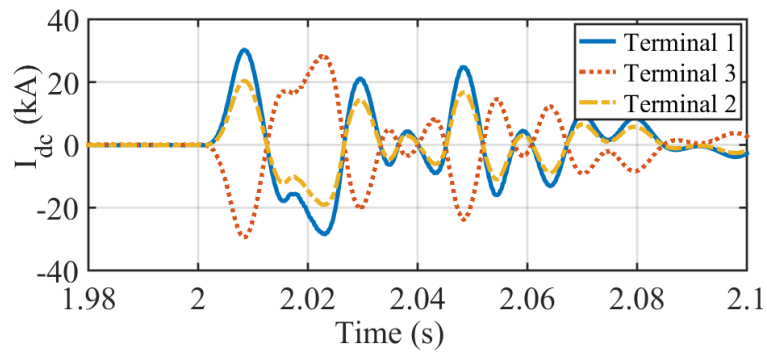
(a) Three-phase AC voltage (V_{t-abc}) at LV side of T₃.



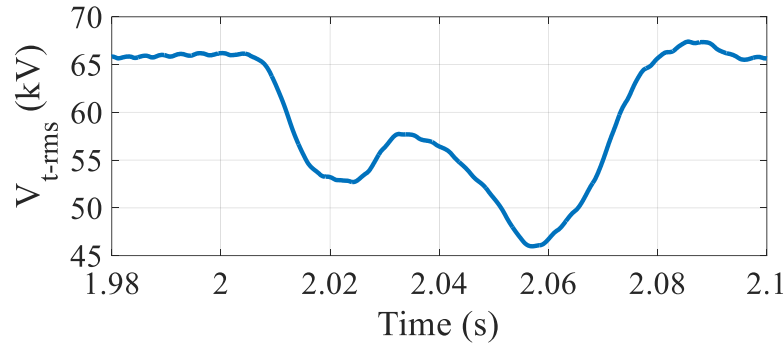
(b) RMS value of AC line voltage (V_{t-rms}) at LV side of T₃.



(c) Positive pole-to-ground DC voltage (V_{dc-p-g}) at three terminals of the HVDC.



(d) DC current (I_{dc}) at three terminals of the HVDC.



(e) RMS value of AC line voltage (V_{t-rms}) at HV side of transformer T_1 (OWF-1 side).

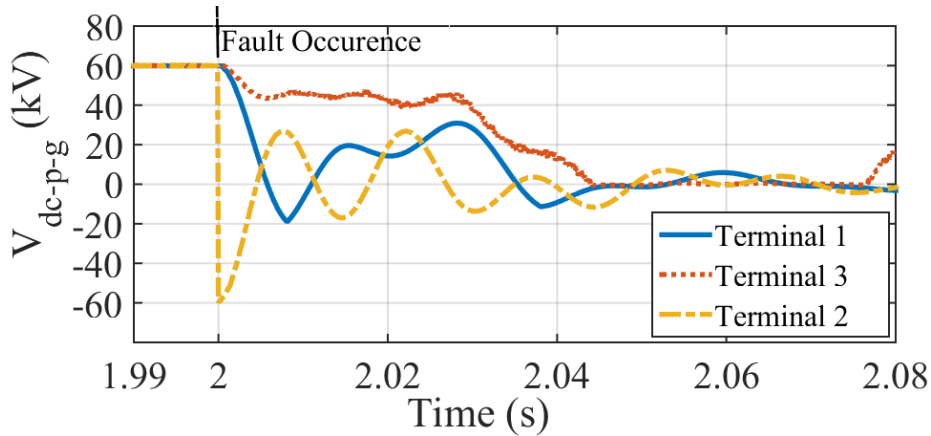
Figure 3.2 The performance of the test case 1 - three-terminal VSC-HVDC System under phase A to ground fault at the LV side of T_3 .

3.1.2 DC Fault Conditions

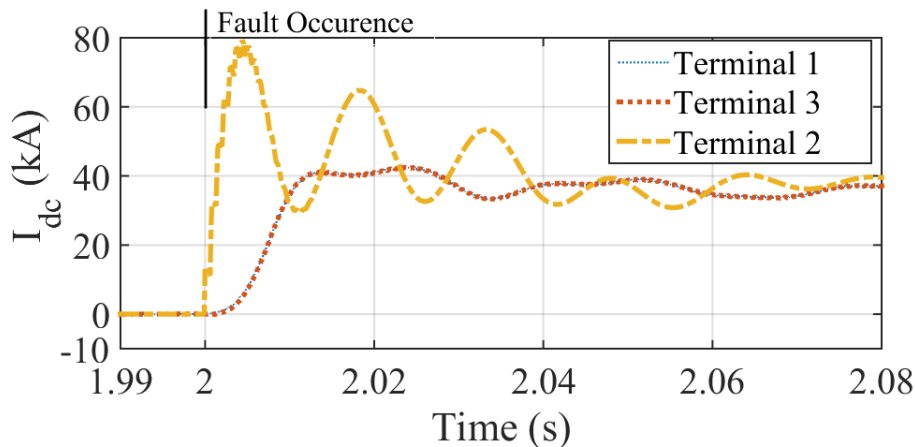
The DC pole-to-pole fault is applied at terminal-2 in the three-terminal HVDC system which is indicated as F_2 in Figure 3.1. The fault is created at time $t = 2.0$ s, the fault duration is considered as 50 ms, and the short circuit fault resistance is taken as 0.01Ω . The response of the proposed HVDC system under DC pole-to-pole fault is shown in Figure 3.3.

After the occurrence of a fault, the DC link capacitor starts to discharge, i.e., the DC voltage at three-terminals of the HVDC system are reduced to zero within a few milliseconds as shown in Figure 3.3 (a). The DC fault current will flow in the diode path of the VSC since the IGBTs are blocked by self-protection. The peak value of DC fault current at terminal-2 has raised up to 79 kA within the few ms, and the peak fault current at terminal-1 and terminal-3 are increased up to 42 kA which can be seen from the Figure 3.3 (b). The major portion of the transients which is generated by the DC fault has come from discharging of energy storage elements such as DC capacitor and line inductor.

From the simulation results of AC and DC faults, it can be seen that the DC fault current has low-rise time and high steady-state values during the transient phases. Therefore, the performance of the multi-terminal VSC-based HVDC system has severely affected due to the fault on the DC side.



(a) Positive pole-to-ground DC voltage (V_{dc-p-g}) at three terminals of the HVDC.



(b) DC current (I_{dc}) at three terminals of the HVDC.

Figure 3.3 The performance of the test case 1 - three-terminal VSC-HVDC system under DC pole-to-pole fault at terminal-2.

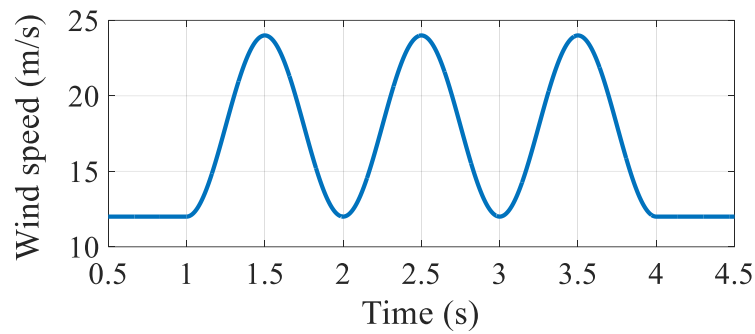
3.1.3 Influence of Variability of Wind Energy Generation on System Fault Conditions

In this section, the performance of the three-terminal VSC-HVDC system is analyzed under variable wind patterns such as gust and ramp wind variations during steady-state and fault conditions.

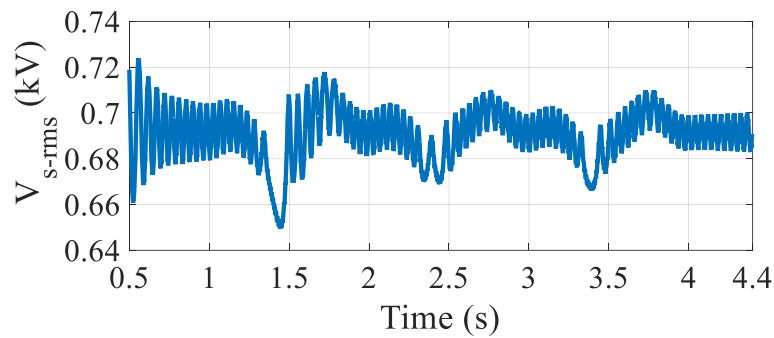
3.1.3.1 Gust Wind Conditions

The performance of the three-terminal VSC-HVDC system is analyzed under gust wind during the phase-to-ground (A-G) fault condition. The gust wind is applied at

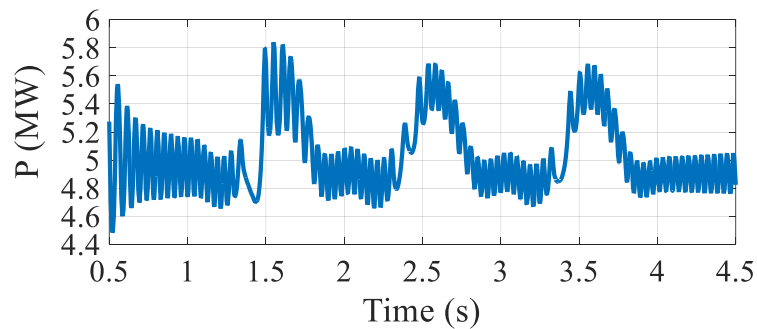
time $t = 1.0$ s. Gust peak velocity is considered as 12 m/s, gust period is taken as 3 s, gust starting time is set as 1 s, the number of the gust is considered as 1. The normal wind speed is 12 m/s. Therefore, the peak value of wind speed can go up to 24 m/s. The A-G fault is applied at the PMSG terminal of OWF-2 (G_2) which is indicated as F_3 in Figure 3.1. The fault is created at time $t = 1.5$ s, the fault duration is considered as 50 ms, and the R_f is taken as 0.04Ω . Figure 3.4 shows the response of the proposed HVDC system under gust wind during A-G fault at PMSG terminal of OWF-2.



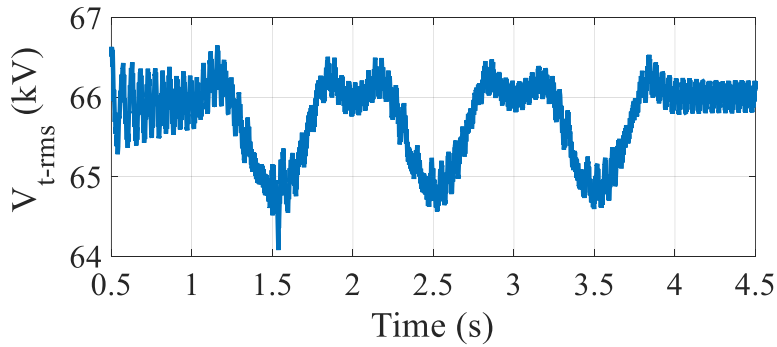
(a) Gust wind speed.



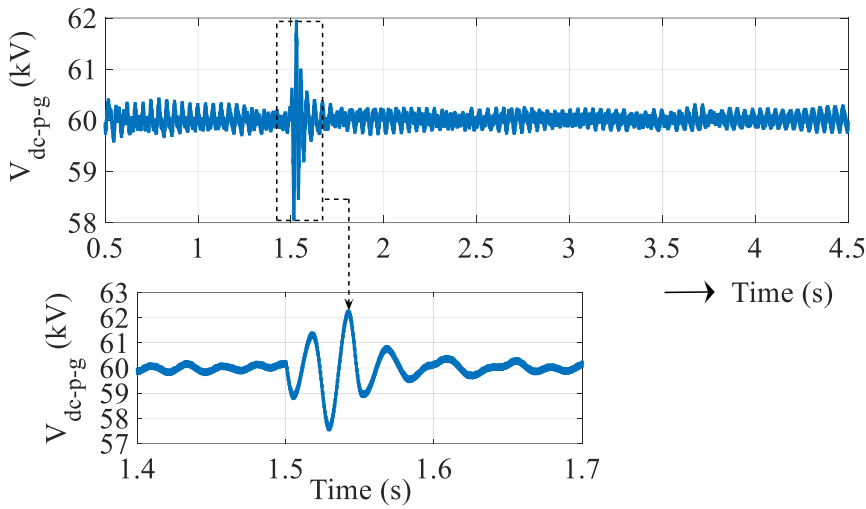
(b) RMS value of AC line voltage (V_{s-rms}) at PMSG terminal of OWF-2.



(c) Active power (P) at PMSG terminal of OWF-2.



(d) RMS value of AC line voltage (V_{t-rms}) at HV side of T₂.



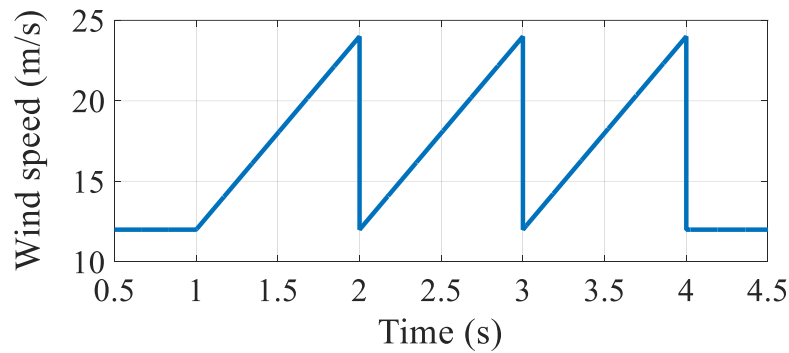
(e) Positive pole-to-ground DC Voltage (V_{dc-p-g}) at terminal-2.

Figure 3.4 The performance of the test case 1 - three-terminal VSC-HVDC system under gust wind during A-G fault at PMSG terminal of OWF-2.

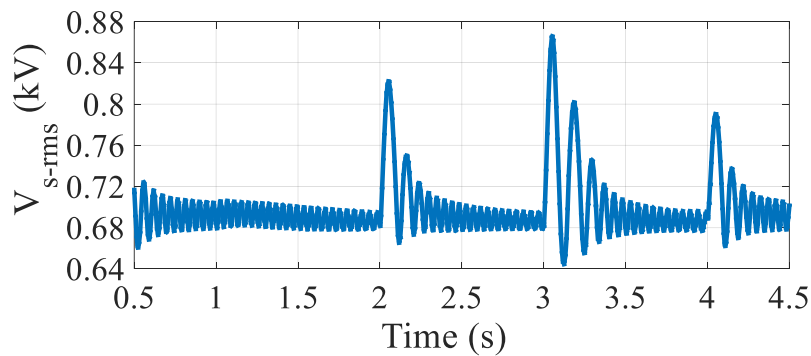
Figure 3.4 (a) indicates the variation of wind speed as in the form of a gust pattern in the OWF-2. The AC line voltage and active power at the PMSG terminal give an oscillation due to the gust wind as shown in Figure 3.4 (b) and (c). During the A-G fault with gust wind, the variation of AC line voltage at PMSG and converter terminal is higher when compared to the case of steady-state with gust wind which can be seen in Figure 3.4 (b) and (d). The transients are present in the DC voltage during the fault period as shown in Figure 3.4 (e). However, the gust wind has no influence on the pole-to-ground DC voltage due to the decoupled d-q controller of VSC and the configuration of the MT HVDC network.

3.1.3.2 Ramp Wind Conditions

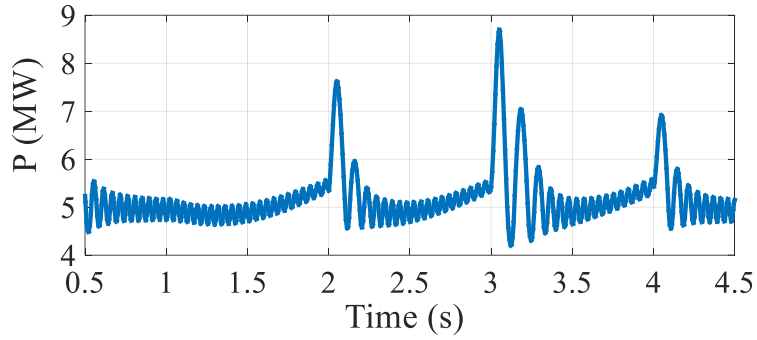
In this case, the performance of the three-terminal VSC-HVDC system is analyzed under ramp wind during A-G fault condition. The normal wind speed is set to 12 m/s. The ramp wind is created at time $t = 1.0$ s. Ramp maximum velocity is considered as 24 m/s, ramp period is taken as 1 s, and ramp starting time is set as 1 s, the number of ramps is considered as 3. The A-G fault is applied at PMSG terminal of OWF-2 (G_2) which is indicated as F_3 in Figure 3.1. The A-G fault is applied at time $t = 3$ s, the fault duration is considered as 50 ms, and the R_f is taken as 0.04Ω . The response of the proposed HVDC system under ramp wind during A-G fault at PMSG terminal of OWF-2 is shown in Figure 3.5.



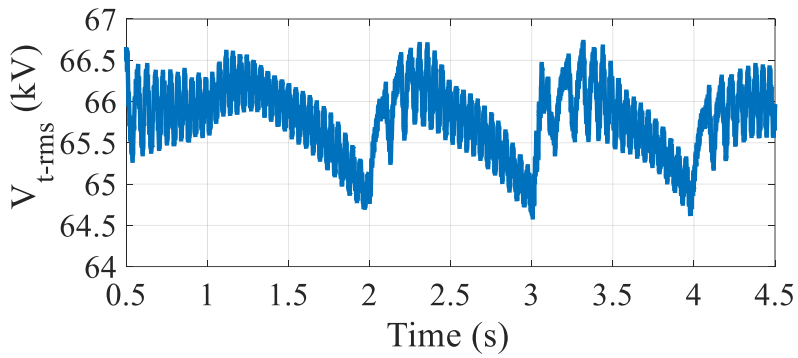
(a) Ramp wind Speed.



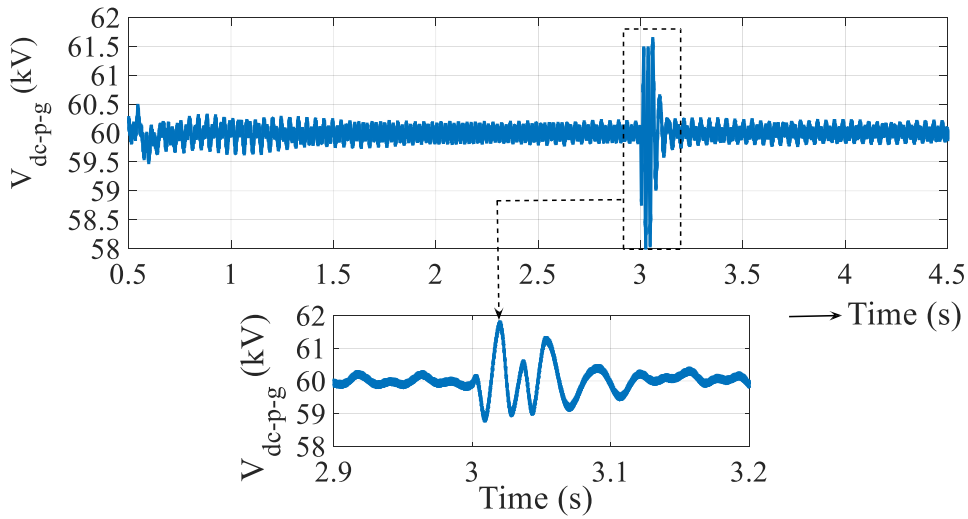
(b) RMS value of AC line voltage (V_{s-rms}) at PMSG terminal of OWF-2.



(c) Active power at PMSG terminal of OWF-2 (P).



(d) RMS value of AC line voltage (V_{t-rms}) at HV side of T₂.



(e) Positive pole-to-ground DC Voltage (V_{dc-p-g}) at terminal-2.

Figure 3.5 The performance of the test case 1 - three-terminal VSC-HVDC system under ramp wind during A-G fault at PMSG terminal of OWF-2.

The variation of the wind speed as in the form of a ramp pattern in the OWF-2 is shown in Figure 3.5 (a). At time $t = 3.0$ s, the variation of AC line voltage and active power at PMSG terminal is more significant when compared to the time $t = 2.0$ s and $t = 4.0$ s which can be seen from the Figure 3.5 (b) and (c). The AC line voltage at the HV side of T_2 has decreased up to 64.5 kV which is given in Figure 3.5 (d). The transients are present in the pole-to-ground DC voltage due to the A-G fault as shown in Figure 3.5 (e). Hence, the performance of the three-terminal VSC-HVDC system gets affected during A-G fault under ramp wind condition.

3.2 Test Case 2

The second case of the three-terminal HVDC transmission system for the connection of offshore wind farms with the AC grid is shown in Figure 3.6.

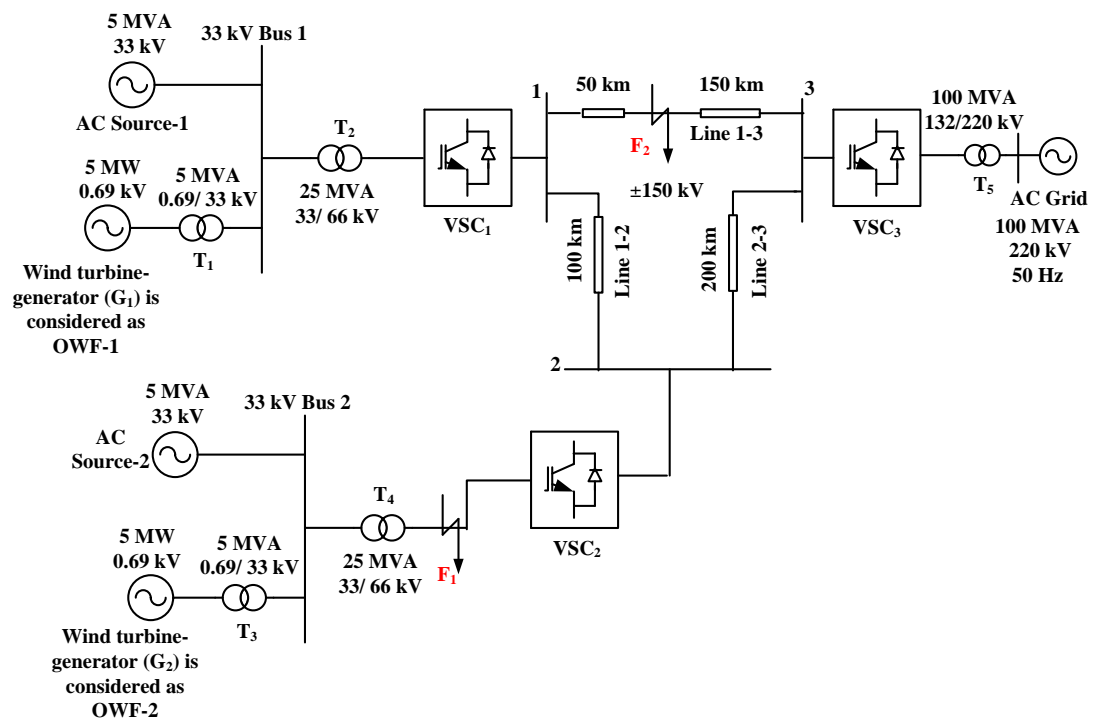


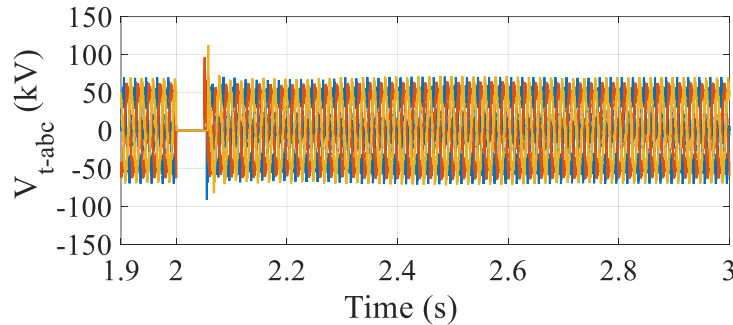
Figure 3.6 Test case 2 – Three-terminal VSC-based HVDC transmission system.

The output of the wind turbine-generator unit has 5 MW, 0.69 kV capacity which is considered as the offshore wind farm. The generated offshore wind power is boosted to the medium voltage level as 33 kV by using 5 MVA, 0.69/33 kV

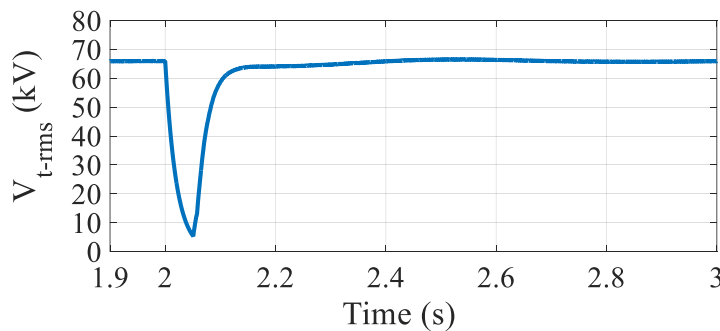
transformer. The rating of the AC source is 5 MVA, 33 kV. The wind farm and AC source are connected to the 33 kV bus. The medium voltage is boosted to the transmission level as 66 kV by using 25 MVA, 33/66 kV transformer. The decoupled d-q controlled two-level VSC is used to connect the three-terminal HVDC with the AC grid. In steady-state condition, the pole-to-ground DC voltage is ± 150 kV. The output of the grid-connected VSC (i.e., VSC₃) is 132 kV, and it is stepped-up to a grid voltage level as 220 kV by using 100 MVA, 132/220 kV transformer and finally it is connected to the AC grid.

3.2.1 AC Fault Conditions

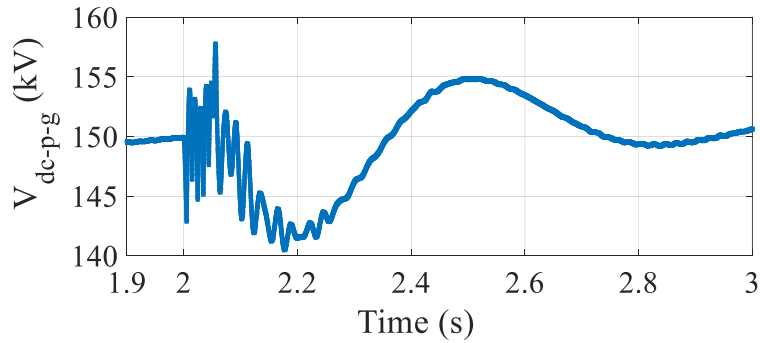
A three phase-to-ground fault is applied at the high voltage (HV) side of the converter transformer T₄ which is indicated as F₁ in Figure 3.6. The fault is created at time $t = 2.0$ s, the fault duration is considered as 50 ms, and the fault resistance (R_f) is taken as 0.02Ω . The response of the proposed HVDC system under three phase-to-ground fault is shown in Figure 3.7.



(a) Three-phase AC voltage (V_{t-abc}) at HV side of T₄.



(b) RMS value of AC line voltage (V_{t-rms}) at HV side of T₄.



(c) Positive pole-to-ground DC voltage (V_{dc-p-g}) at terminal-2.

Figure 3.7 The performance of the test case 2 - three-terminal VSC-HVDC system under three-phase-to-ground fault at HV side of T_4 .

The AC voltage at the HV side of converter transformer T_4 has decreased nearer to zero during fault period, and it starts increasing after the clearance of fault as shown in Figure 3.7 (a) and (b). The response of the DC system such as the positive pole-to-ground DC voltage at terminal-2 gets disturbed due to the three phase-to-ground fault at the HV side of T_4 which can be seen from Figure 3.7 (c).

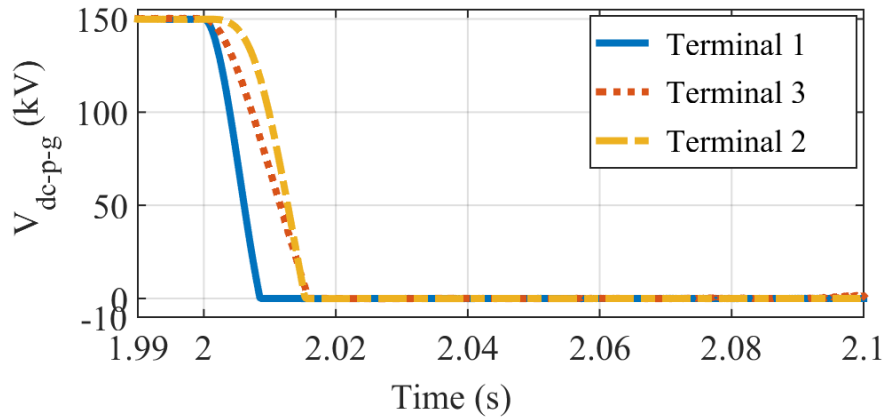
In this case, the instantaneous tripping action will happen since the AC voltage is decreased below the 0.1 per unit. The operating time of the Zone-1 relay is around two cycles [L. He et al. 2014]. The critical clearing time for the 5 MW wind-turbine generator connected AC network is calculated as 89 ms. Therefore, the system remains stable since the fault is cleared before the critical clearing time gets over.

3.2.2 DC Fault Conditions

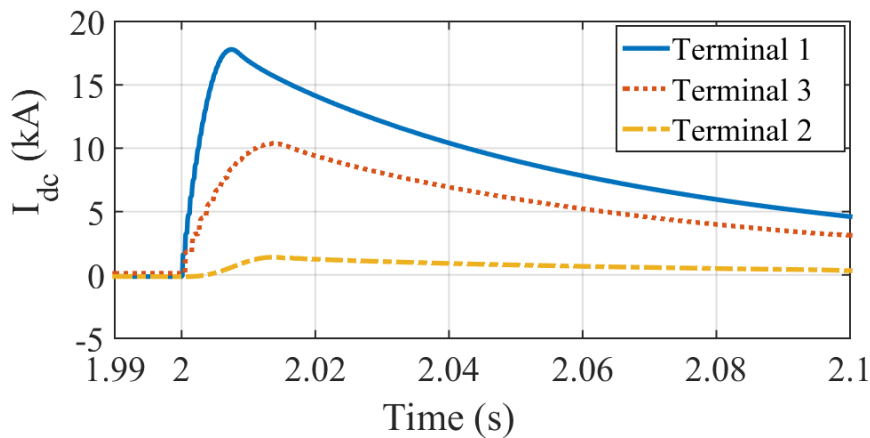
(i) DC Pole-to-Pole Fault: The DC pole-to-pole fault is applied at the 50 km distance from the terminal-1 and 150 km distance from the terminal-3 which is indicated as F_2 in Figure 3.6. The DC pole-to-pole fault is created at $t = 2.0$ s, the fault duration is considered as 50 ms, and the R_f is taken as 0.01Ω . The response of the proposed HVDC system under DC pole-to-pole fault is shown in Figure 3.8.

After the occurrence of the DC pole-to-pole fault, the DC voltage measured at three terminals of the HVDC system is decreased to zero within a few ms which can be seen from Figure 3.8 (a). The DC fault current measured at the terminal-1 has raised to 18 kA within a short period, and the peak fault current at terminal-3 and

terminal-2 are 10.4 kA and 1.4 kA which can be seen from Figure 3.8 (b). Therefore, the response of the HVDC system is significantly affected due to DC pole-to-pole fault condition.



(a) Positive pole-to-ground DC voltage (V_{dc-p-g}) at three terminals of the HVDC.



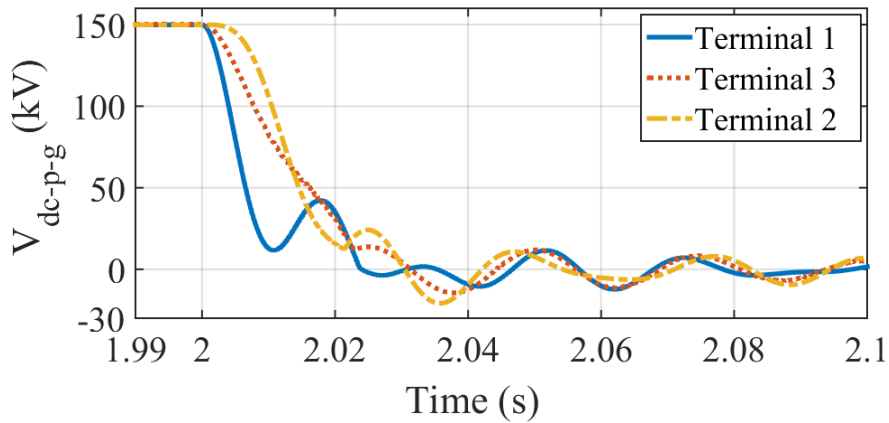
(b) DC current (I_{dc}) at three terminals of the HVDC.

Figure 3.8 The performance of the test case 2 - three-terminal VSC-HVDC system under DC pole-to-pole fault at 50 km distance from terminal-1.

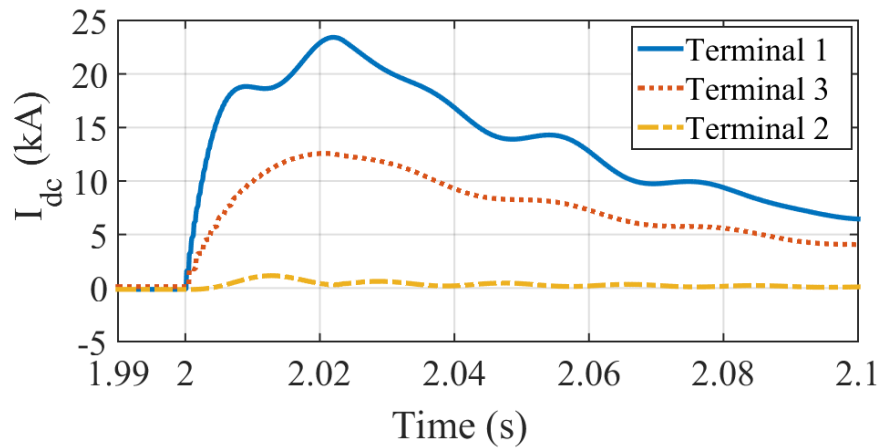
(ii) DC Pole-to-Ground Fault: The DC pole-to-ground fault is applied at 50 km distance from the terminal-1 and 150 km distance from the terminal-3 which is indicated as F_2 in Figure 3.6. The fault is created at $t = 2.0$ s, the fault duration is considered as 50 ms, and the R_f is taken as 0.04Ω . The response of the proposed HVDC system under DC pole-to-ground fault is shown in Figure 3.9.

The pole-to-ground fault is depending on the grounding of the HVDC system. After the occurrence of a fault, the DC voltage measured at the three-terminal of the

HVDC system is reduced abnormally as shown in Figure 3.9 (a). The peak value of the DC fault current at terminal-1 has increased to 24 kA within a few ms. The peak value of DC fault current at the terminal-3 and terminal-2 has increased up to 13 kA and 1.2 kA which can be observed from Figure 3.9 (b). In the pole-to-ground fault case also, the DC fault current has reached the abnormal value which is not an acceptable limit of the rating of components used in the HVDC system.



(a) Positive pole-to-ground DC voltage (V_{dc-p-g}) at three terminals of the HVDC.



(b) DC current (I_{dc}) at three terminals of the HVDC.

Figure 3.9 The performance of the test case 2 - three-terminal VSC-HVDC system under DC pole-to-ground fault at 50 km distance from terminal-1.

From the simulation results, it is observed that the DC faults are having a higher peak and steady fault currents which can damage the power electronic converters, circuit breakers, and other HVDC system components.

3.3 Test Case 3

The test case 3 – two-terminal VSC-based HVDC transmission system which is used to interconnect the two AC sources are shown in Figure 3.6. The AC sources are rated as 100 MVA, 420 kV, 50 Hz and it is stepped-down to the 230 kV by using 1500 MVA, 420/ 230 kV transformer with a leakage reactance of 0.1 per unit. The calculated value of the phase reactor is taken as 0.01684 H, and high pass filter is taken as $R_f = 78.3719 \Omega$, $L_f = 13.86 \text{ mH}$ and $C_f = 4.51 \mu\text{F}$. The two-level VSC is used to convert the AC to DC power at the sending end, and it has converted back to the AC power at the receiving end. The two voltage source converters, i.e., VSC₁ and VSC₂ are interconnected by using 100 km DC line. In steady-state, the pole-to-ground DC voltage (V_{dc-p-g}) is $\pm 200 \text{ kV}$.

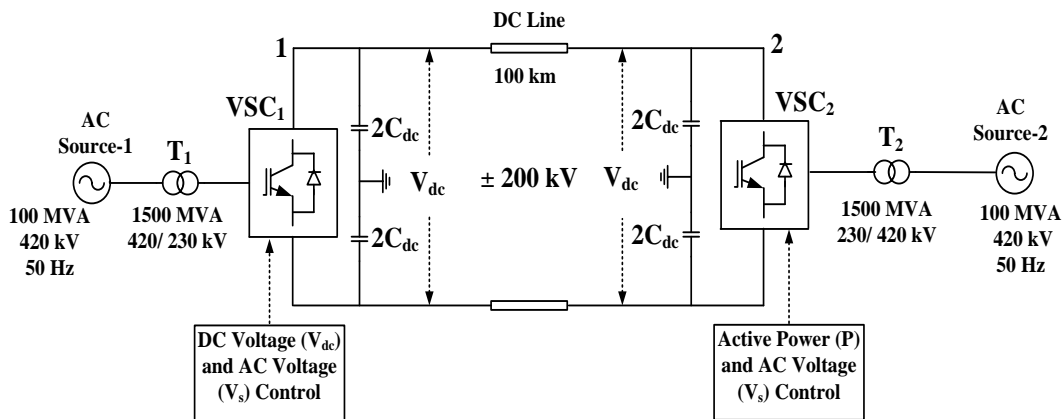


Figure 3.10 Test case 3 – two-terminal VSC-based HVDC transmission system.

The decoupled d-q control strategy for the test case 3- VSC-based HVDC system is shown in Figure. 3.11. The DC voltage (V_{dc}) and AC voltage (V_s) controller has been implemented for the VSC₁ to control the DC and AC voltages. The active power (P) and AC voltage (V_s) controller has been applied for the VSC₂ to maintain the active power and AC voltage at the point of common coupling by providing reactive power support.

In this case, it is modeled that the d-axis of the rotor reference frame is aligned to the stator voltage vector and the q-axis is lagging the d-axis by 90° . After applying the

d-q transformation to the equation (2.24), the AC source voltage in the d-q frame is given by,

$$V_{s,d} = Ri_d + L \frac{di_d}{dt} + \omega Li_q + V_{c,d} \quad (3.1)$$

$$V_{s,q} = Ri_q + L \frac{di_q}{dt} - \omega Li_d + V_{c,q} \quad (3.2)$$

The decoupled d-q control strategy can be implemented based on the equations (2.38)-(2.40) and (3.1)-(3.2). The converter voltage is controlled by using SPWM technique.

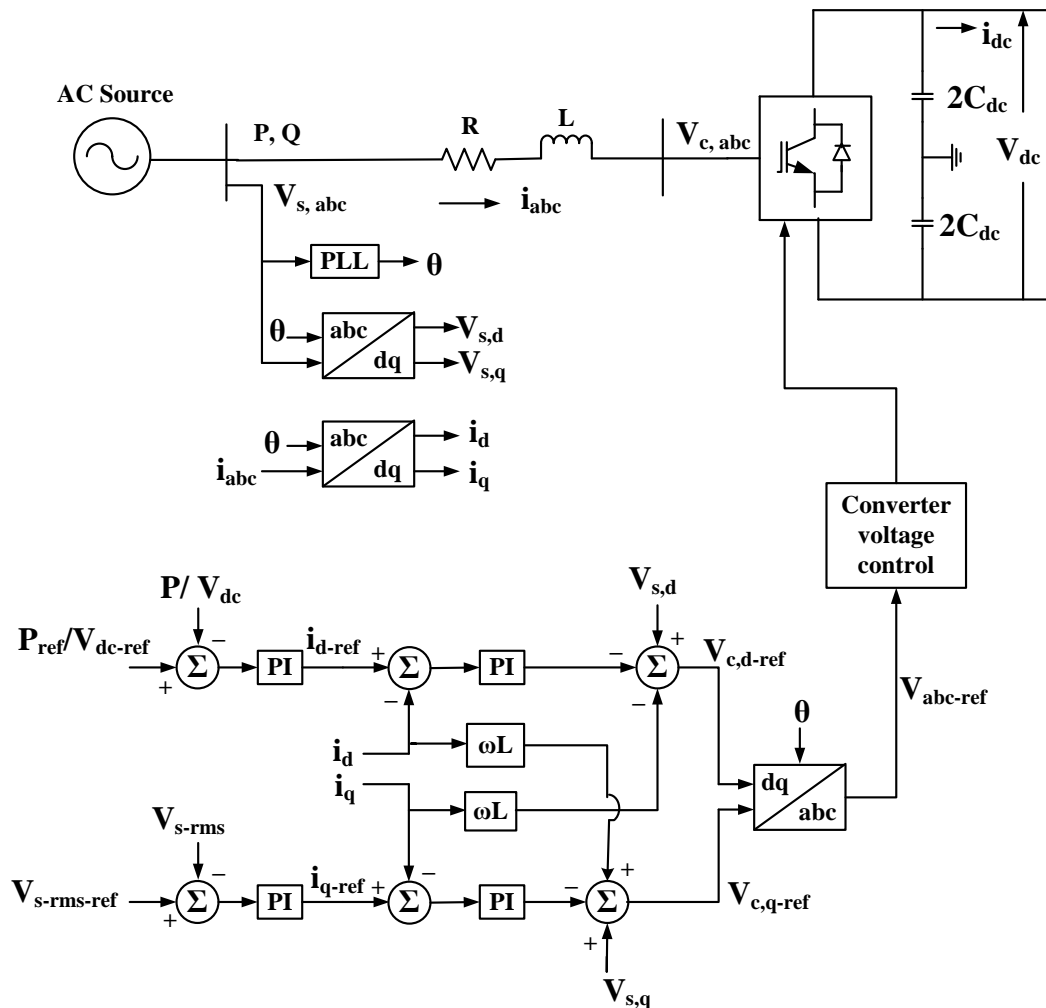
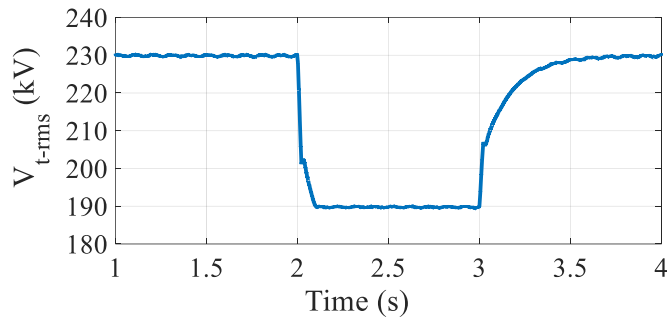


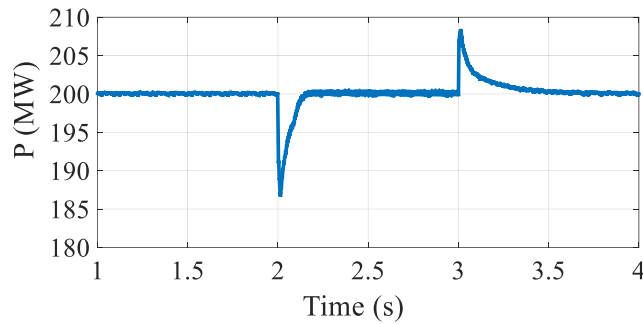
Figure 3.11 The decoupled d-q control strategy for test case 3 – two-terminal VSC-based HVDC transmission system.

3.3.1 Influence of Dynamic Conditions of VSC on System Performance

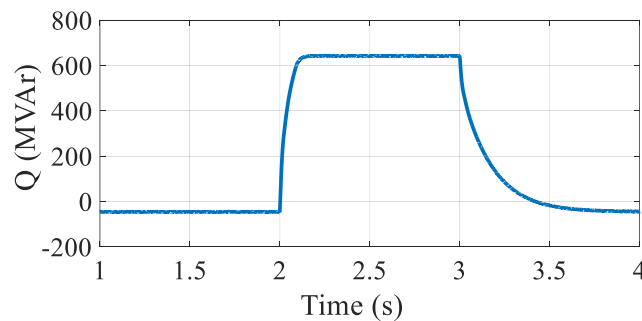
(i) **Step Change in AC voltage Reference Input:** In this case, the performance of the two-terminal VSC-HVDC system is analyzed under the condition of the step variation of the AC voltage reference input of decoupled d-q control of VSC₂. At time $t = 2.0$ s, the AC voltage reference input ($V_{s-rms-ref}$) of the decoupled d-q control is step changed from 1.0 to 0.8 per unit, and it has maintained for the duration of 1 s. At time $t = 3.0$ s, the $V_{s-rms-ref}$ is step changed to 1.0 per unit. The response of the proposed HVDC system is shown in Figure 3.12.



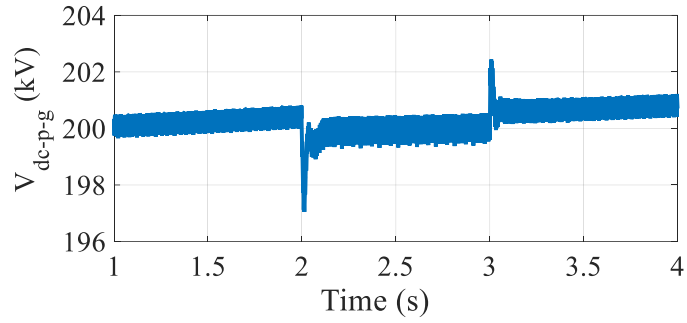
(a) RMS value of AC line voltage (V_{t-rms}) at LV side of T₂.



(b) Active power (P) at VSC₂.



(c) Reactive power (Q) at VSC₂.

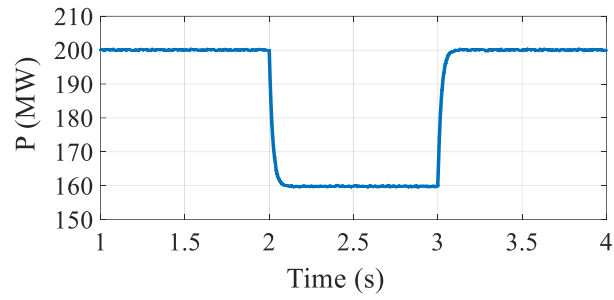


(d) Positive pole-to-ground DC voltage (V_{dc-p-g}) at VSC₂.

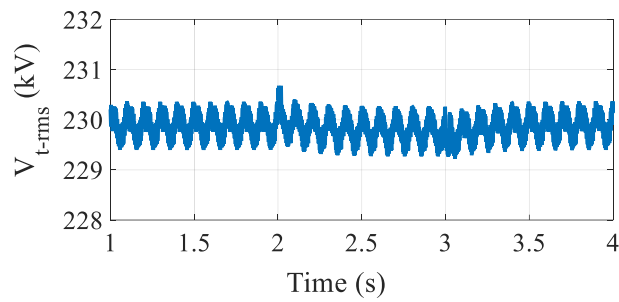
Figure 3.12 The performance of the test case 3 - two-terminal VSC-HVDC system under step variation of AC voltage reference ($V_{s-rms-ref}$) input at VSC₂.

At time $t = 2.0$ s, the RMS value of the AC line voltage at the LV side of the converter transformer T₂ has changed from 230 kV to 189 kV which is shown in Figure 3.12 (a). The active power (P) at VSC₂ gives small changes during the step variation time of the AC voltage reference input which can be seen in Figure 3.12 (b). Also, the active power has maintained as 200 MW during the time 2.15 s to 3.0 s due to control of active power in the VSC₂. Figure 3.12 (c) indicates that the reactive power (Q) at VSC₂ has varied up to 643 MVar since the AC voltage reference input influences the q-axis component. Figure 3.12 (d) show that the step variation of the AC voltage reference input has not much impact on the positive pole-to-ground DC voltage due to the robust controller of the VSC.

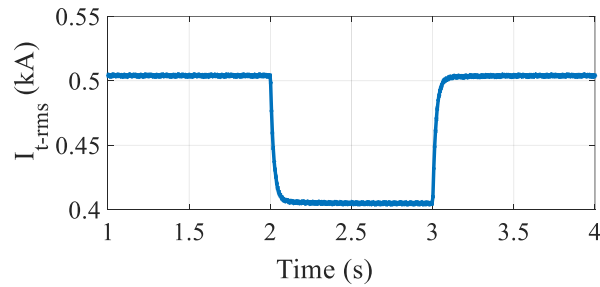
(ii) Step Change in Active Power Reference Input: In this case, the performance of the two-terminal VSC-based HVDC system is analyzed under the condition of the step variation of the active power reference input of decoupled d-q control of VSC₂. Initially, the active power reference (P_{ref}) input of the decoupled d-q control of VSC₂ is given as 200 MW. At time $t = 2.0$ s, the active power reference (P_{ref}) input is step changed from 200 MW to 160 MW, and it has maintained for the duration of 1 s. At time $t = 3.0$ s, the P_{ref} is step changed to 200 MW. The response of the proposed HVDC system under the step variation of active power reference input of VSC₂ is shown in Figure 3.13.



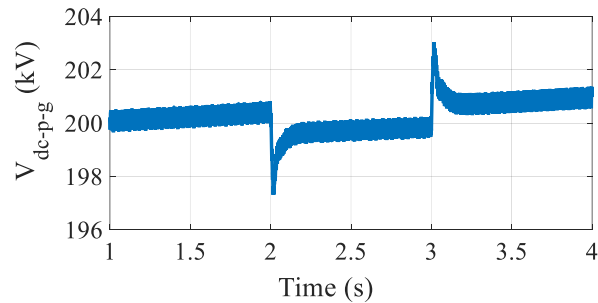
(a) Active power (P) at VSC₂.



(b) RMS value of AC line voltage (V_{t-rms}) at LV side of T₂.



(c) RMS value of AC line current (I_{t-rms}) at LV side of T₂.



(d) Positive pole-to-ground DC voltage (V_{dc-p-g}) at VSC₂.

Figure 3.13 The performance of the test case 3 - two-terminal VSC-HVDC system under step variation of active power reference (P_{ref}) input at VSC₂.

At time $t = 2.0$ s, the active power at VSC₂ has reduced to 20 % (i.e., step changed from 200 MW to 160 MW). The change in active power has no impact on the AC line voltage at the LV side of the transformer T₂. The AC line current at the LV side of the transformer T₂ has reduced from 0.5 kA to 0.4 kA due to the reduction of active power. The change in active power has less influence on the response of positive pole-to-ground DC voltage due to the DC voltage control of VSC₁.

3.4 Conclusions

In this chapter, different case studies are carried out to test the performance of multi-terminal VSC-based HVDC transmission systems under various fault conditions. The obtained results showed that the DC faults have high peak fault current with low-rise time, and this is the most critical stage in the multi-terminal VSC-HVDC link operation.

Simulation studies are carried out to test the response of the proposed HVDC system under gust and ramp wind variations during steady-state and fault conditions. From the simulation results, it is observed that the wind variability has the significant influence on the response of the wind power generation output and converter terminals, no impact on the response of the DC voltage during steady-state and fault conditions.

Simulation studies are carried out to test the response of the proposed HVDC system under dynamic conditions of the VSC such as active power and AC voltage reference changes. Test results showed that reactive power is greatly affected by the step change of the AC voltage reference input. The step change in active power is directly affecting the AC current. However, the dynamic conditions of the VSC have less influence on the response of the DC voltage.

CHAPTER 4

A SINGLE-ENDED PROTECTION SCHEME FOR DC FAULTS IN MULTI-TERMINAL VSC-BASED HVDC SYSTEMS

Most of the protection schemes installed in the AC grid can address only the steady-state based protection. In the DC grid, the steady-state signal is DC, and also the high-frequency transient period is no longer than 10 ms [H. Ha, and S. Subramanian 2015]. The conventional protection schemes are not suitable for the DC grid [D. Jovcic et al. 2011], [N. Bayati et al. 2018]. From the literature, it is observed that the single-ended (i.e., on one side of the line, is referred as single-ended) transient energy, voltage and current derivatives based protection scheme gives better and faster protection when compared to the other DC fault protection schemes. It uses only the local measurements such as DC voltage and current at one terminal. This chapter presents the modeling and simulation studies on the single-ended protection scheme for the DC faults in the MT VSC-HVDC systems. Also, different case studies are considered to evaluate the performance of the proposed protection scheme.

4.1 Modeling of Single-ended Protection Scheme

In this section, the modeling of the single-ended protection scheme for DC faults in the MT VSC-based HVDC transmission systems has been presented. Consider a protection scheme is developed for the relay R₁₃ in the three-terminal VSC-HVDC system which is shown in Figure 4.1. The proposed protection scheme has two stages. The fault detection process initiates the protection unit. Fault discrimination takes place once the fault is detected in an HVDC transmission line. A single-ended protection logic flow diagram is shown in Figure 4.2. The variables used in the flowchart are defined in Section 4.1.2. In this scheme, the protection unit gives the trip decision based on the local measurements such as DC voltage and current at one terminal.

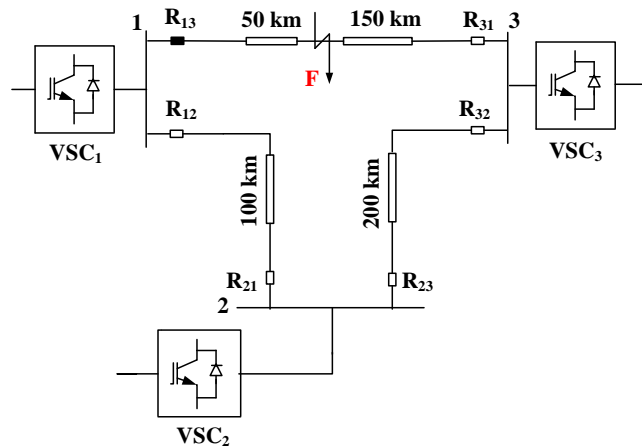


Figure 4.1 Protection of multi-terminal VSC-HVDC system.

4.1.1 Fault Detection

The protection unit takes the input data as DC voltage (V_{dc}), and DC current (I_{dc}) measured at one terminal. The rate of change of DC voltage and current, the variation of transient energy is calculated using the input data. If DC voltage decreases below the threshold value (i.e., 85% of the rated value is considered as the threshold value for an under-voltage criterion based on the analysis of voltage variation ranges for different countries under normal operating conditions which are given in W. Christiansen and D. T. Johnsen [2006], M. R. I. Network [2013]), the protection unit considers that the system is in the abnormal condition.

In the case of the DC fault, the DC voltage is decreased and maintained at almost zero. But in the case of other transients, the DC voltage at three terminals of the HVDC grid gives an oscillation. For example, the DC voltage measured at three terminals of the HVDC grid has decreased below the threshold value and immediately gets increased under AC fault cases. Therefore, for discrimination of the DC faults from the other transient events, it is very important to consider how long time the reduced DC voltage has stayed below the threshold value. Based on the analysis of transient studies, it is considering that 10 ms duration can be used for the detection of DC faults. If DC voltage decreases and stays below the threshold value for 10 ms, the protection unit declares that the DC fault has occurred in the HVDC system. Hence, the DC faults can be discriminated from the AC faults, switching instant and other transient events.

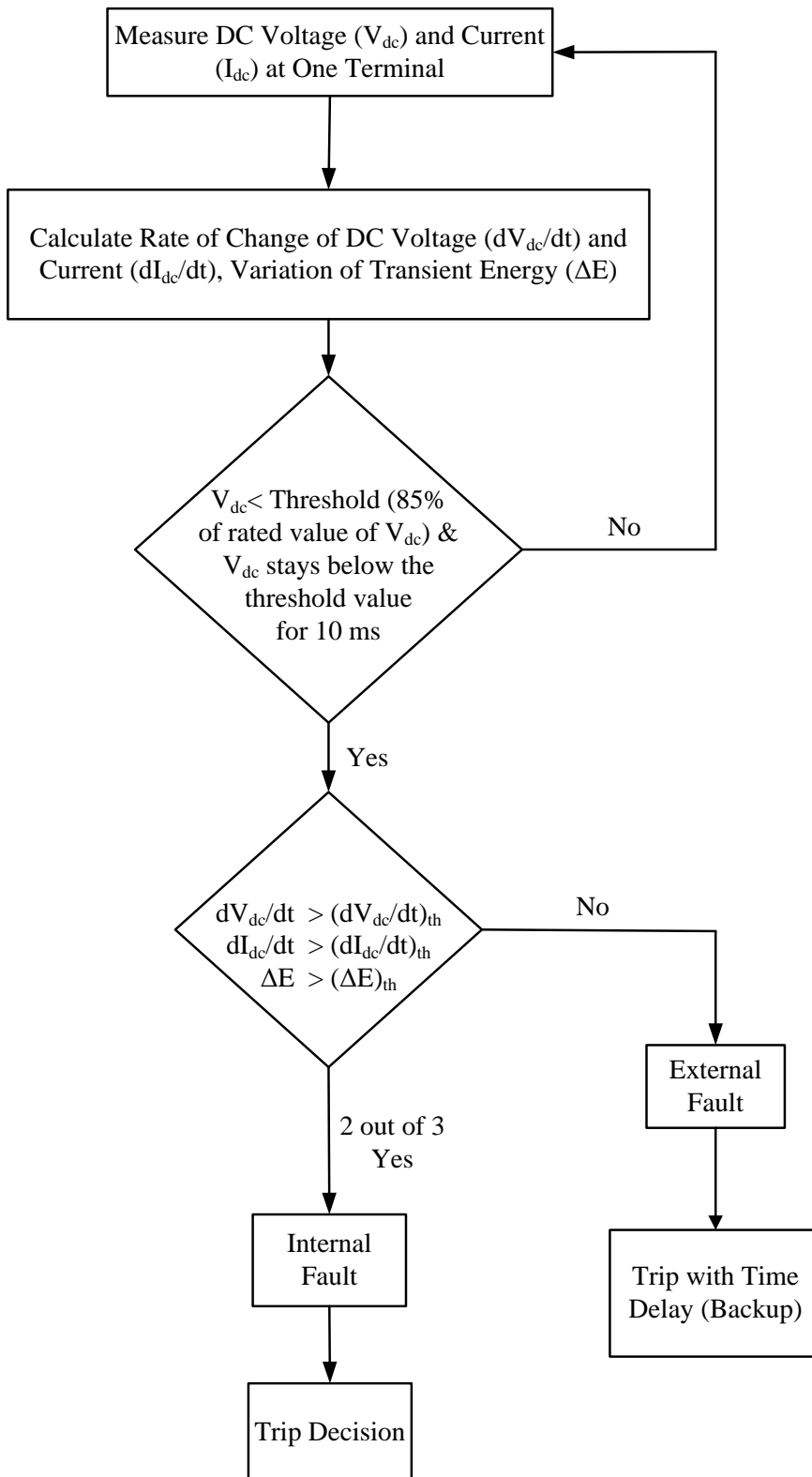


Figure 4.2 Single-ended protection logic flow diagram. (The subscript ‘th’ refers to the threshold value).

4.1.2 Fault Discrimination

After fault detection, the faulted line(s) are identified in a multi-terminal VSC-HVDC transmission system. The internal faults are discriminated from the external faults using the following relations.

The voltage derivative criterion is given as,

$$\frac{dV_{dc}}{dt} = \frac{V_{dc}(t_2) - V_{dc}(t_1)}{t_2 - t_1} \quad (4.1)$$

and check for,
$$\frac{dV_{dc}}{dt} > \left(\frac{dV_{dc}}{dt}\right)_{th} \quad (4.2)$$

Similarly, the current derivative criterion is given as,

$$\frac{dI_{dc}}{dt} = \frac{I_{dc}(t_2) - I_{dc}(t_1)}{t_2 - t_1} \quad (4.3)$$

and check for,
$$\frac{dI_{dc}}{dt} > \left(\frac{dI_{dc}}{dt}\right)_{th} \quad (4.4)$$

Finally, the variation of transient energy is calculated as,

$$\Delta V_{dc} = V_{dc}(t_2) - V_{dc}(t_1) \quad (4.5)$$

$$\Delta I_{dc} = I_{dc}(t_2) - I_{dc}(t_1) \quad (4.6)$$

$$\Delta t = t_2 - t_1 \quad (4.7)$$

$$\Delta E = \Delta V_{dc} \times \Delta I_{dc} \times \Delta t \quad (4.8)$$

and check for,
$$\Delta E > (\Delta E)_{th} \quad (4.9)$$

Here, V_{dc} and I_{dc} are the DC voltage and current respectively. ΔE is the increment of transient energy, and Δt is the sampling interval.

The voltage derivative as discussed in the literature is not secure due to the interference of measurement error and noise. Therefore, three conditions are used to discriminate the internal faults from the external faults. If all or any two of the conditions in equations (4.2), (4.4) and (4.9) are satisfied, the protection unit declares that fault has occurred within the protected zone, i.e., internal fault and commands trip decision without time delay. Otherwise, it is referred to an external fault, and the protection unit acts as backup protection.

4.2 Simulation Studies

In this Section, simulation studies are carried out to test the single-ended protection scheme for various DC fault cases in a three-terminal VSC-HVDC transmission system for both without and with current limiting reactor cases.

4.2.1 Three-terminal VSC-HVDC System without Current Limiting Reactors

The three-terminal VSC-HVDC transmission system without current limiting reactors is shown in Figure 4.3. The system considered for the study is same as the test case 2 which is presented in the section 3.2. Consider that a single-ended protection scheme is developed for the relay R_{13} in a three-terminal VSC-HVDC transmission system as shown in Figure 4.3. In steady-state, the pole-to-ground DC voltage is ± 150 kV. The relay logic program has been developed using MATLAB environment and tested by injecting the fault data sets. These fault data sets are obtained from the PSCAD/EMTDC simulation for various DC fault conditions.

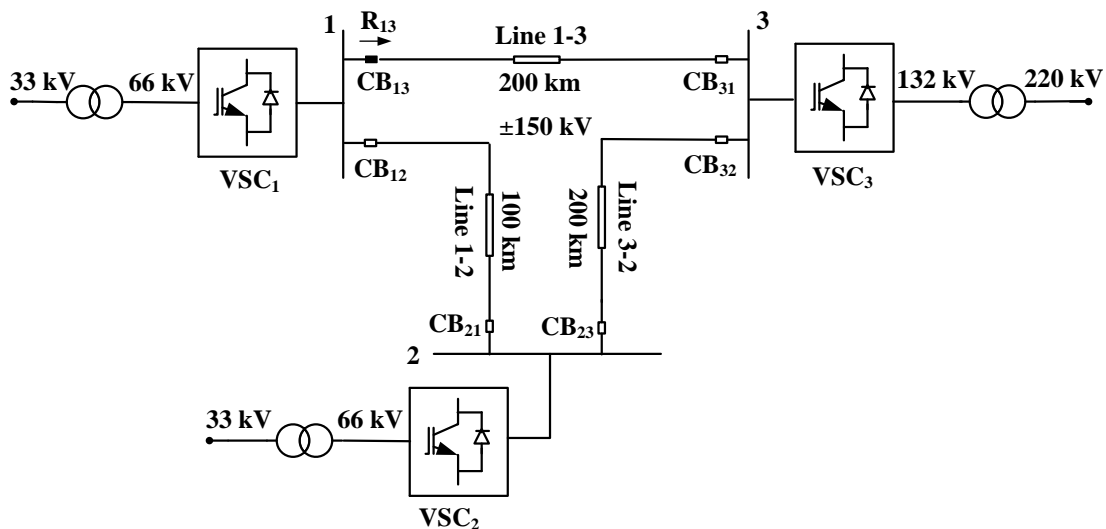
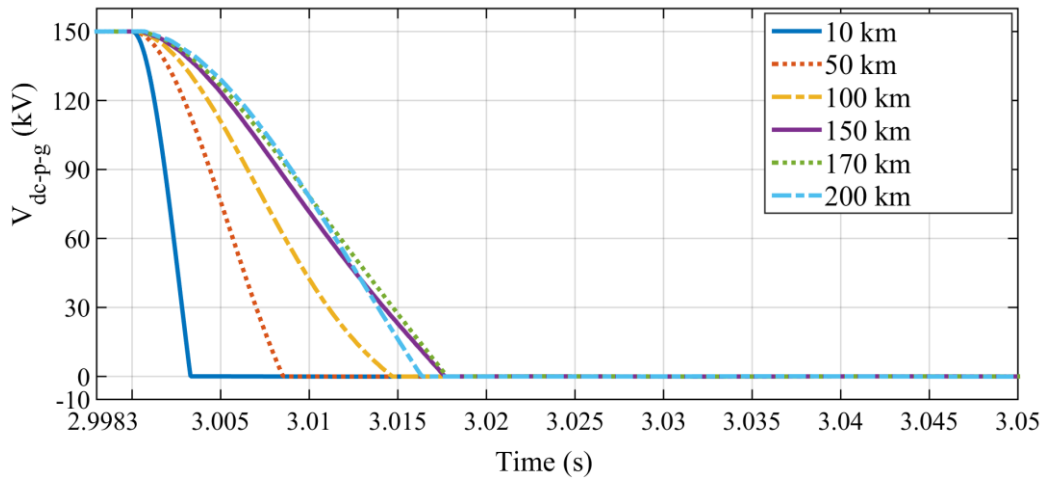


Figure 4.3 Three-terminal VSC-HVDC system without current limiting reactors.

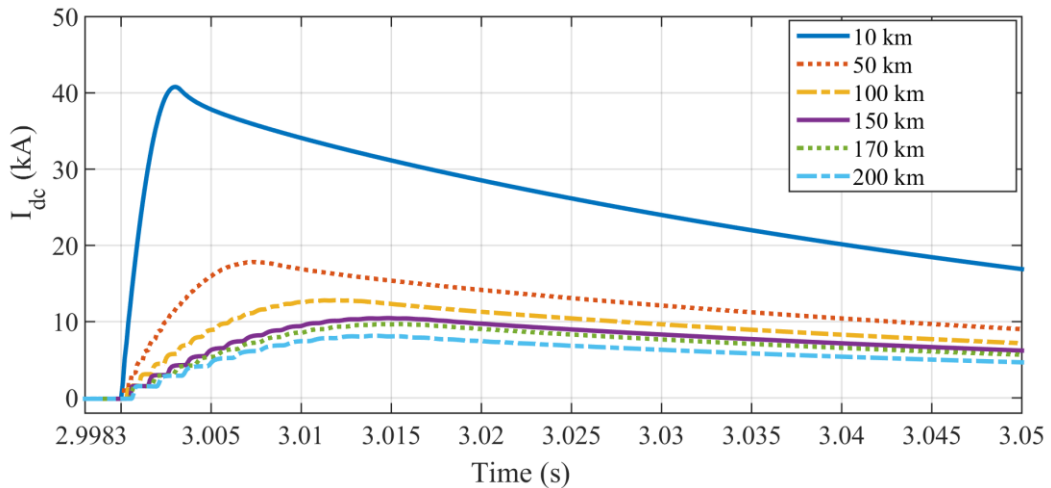
4.2.1.1 Pole-to-Pole Fault Condition

In this case, the performance of the relay R_{13} is tested with the pole-to-pole fault occurs at various locations (i.e., 10 km, 50 km, 100 km, 150 km, 170 km, 200 km) in a line between terminal-1 and terminal-3 in a three-terminal VSC-HVDC transmission system without current limiting reactors. The fault is applied at time $t = 3.0$ s, and the

duration of the fault is considered as 50 ms. The short circuit fault resistance is taken as 0.01Ω . The positive pole-to-ground DC voltage and DC current at the relay R_{13} location under pole-to-pole fault conditions is shown in Figure 4.4. At $t = 3.0$ s, the positive pole-to-ground DC voltage at the relay R_{13} location slowly decreased from 150 kV to zero when the fault distance gets increased. The DC fault current is rapidly growing within a few ms for short distance faults, and it gives less variation for the long-distance faults.



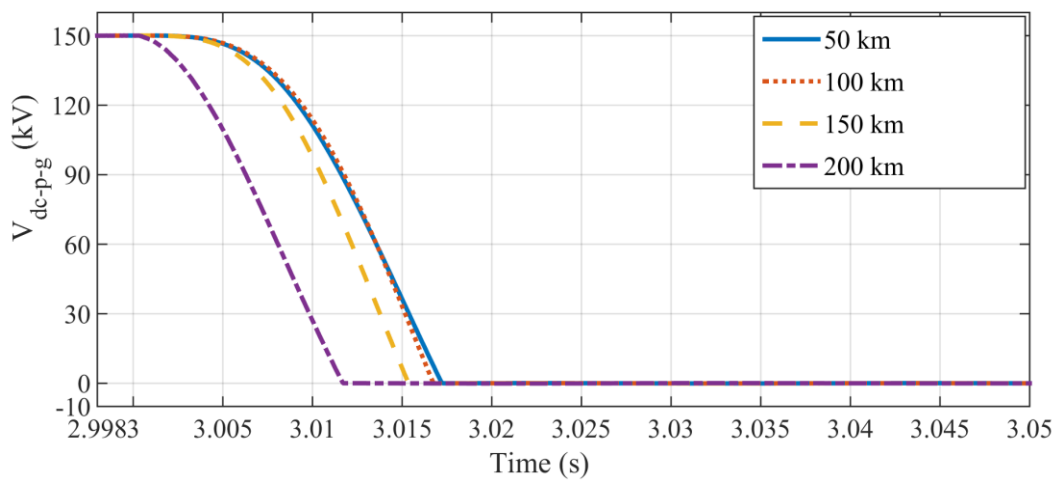
(a) Positive pole-to-ground DC voltage (V_{dc-p-g}).



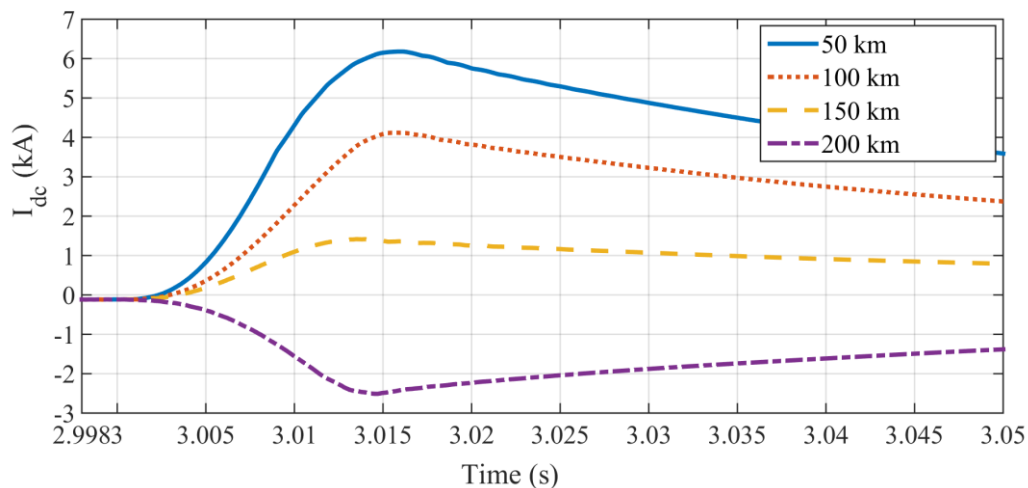
(b) DC Current (I_{dc}).

Figure 4.4 The DC voltage and current measured at the relay R_{13} location under pole-to-pole fault at various locations in a line 1-3.

Besides, the performance of the relay R_{13} is tested under the condition of fault on other lines. Figure 4.5 shows that the response of the proposed HVDC system measured at the relay R_{13} location under the occurrence of the pole-to-pole fault at various locations (i.e., 50 km, 100 km, 150 km, 200 km) in a line between terminal-3 and terminal-2. The fault distance is considered from the terminal-3. Also, the fault at 200 km distance from terminal-3 (i.e., the fault at terminal-2) is a short distance for the relay R_{13} through line 1-2.



(a) Positive pole-to-ground DC voltage (V_{dc-p-g}).



(b) DC Current (I_{dc}).

Figure 4.5 The DC voltage and current measured at the relay R_{13} location under pole-to-pole fault at various locations in a line 3-2.

The fault is identified when the DC voltage decreases below 127 kV (i.e., 85% of rated value of the pole-to-ground DC voltage), and it stays for 10 ms (i.e., 100 samples of the DC fault data). The sample number of 100 is selected from the analysis of the transients due to the faults and other switching events in the three-terminal VSC-HVDC transmission system. The DC voltage and current derivatives, and the increment of transient energy are used to distinguish the internal faults from the external faults once the fault is identified. The threshold setting of the rate of change of DC voltage and current, and the increment of transient energy for the pole-to-pole fault condition can be calculated with the help of Table 4.1. For setting the threshold value of fault discrimination criterion (i.e., DC voltage and current derivatives, and the increment of transient energy) of relay R₁₃, it is considered that the 85% length of primary line 1-3 is an internal fault. The internal fault is declared if all or any two of the calculated $\frac{dV_{dc}}{dt}$, $\frac{dI_{dc}}{dt}$, and ΔE value exceeds the preset threshold value.

Table 4.1 The threshold determination of voltage and current derivatives, and increment of transient energy for the pole-to-pole fault condition in a three-terminal VSC-HVDC system without current limiting reactors.

| Fault line | Fault distance (km) | $\frac{dV_{dc}}{dt}$ (kV/s) | $\frac{dI_{dc}}{dt}$ (kA/s) | ΔE (MW×s) |
|------------|---------------------|-----------------------------|-----------------------------|-------------------|
| Line 1-3 | 10 | 57255.0 | 8408.5 | 3.85142 |
| | 50 | 20350.0 | 2575.0 | 0.41921 |
| | 100 | 12720.0 | 1407.0 | 0.14317 |
| | 150 | 9770.0 | 931.0 | 0.07276 |
| | 170 | 8995.0 | 866.5 | 0.06235 |
| | 200 | 9260.0 | 540.5 | 0.04004 |
| Line 3-2 | 50 | 11155.0 | 687.0 | 0.06130 |
| | 100 | 11185.0 | 459.0 | 0.04107 |
| | 150 | 12770.0 | 188.5 | 0.01925 |
| | 200 | 13655.0 | 129.0 | 0.01409 |

The fault detection time of a relay R_{13} for the pole-to-pole fault condition is presented in Table 4.2. The relay R_{13} has identified that the fault occurred below 85% length of the line 1-3 is an internal fault, remaining 15 % of the primary line 1-3 and fault on line 3-2 is declared as an external fault. This indicates the very fact that the proposed protection scheme can detect and discriminate both the internal and external faults accurately.

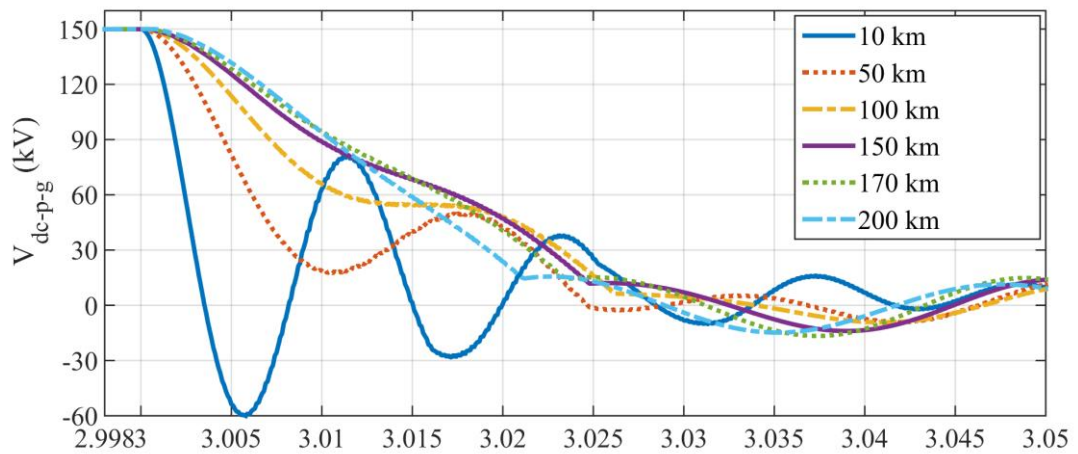
Table 4.2 The fault detection time of relay R_{13} under pole-to-pole fault condition in the three-terminal VSC-HVDC system without current limiting reactors.

| Fault line | Fault distance (km) | Type of fault | | Fault detection time of relay R_{13} (ms) |
|------------|---------------------|---------------|----------|---|
| | | Internal | External | |
| Line 1-3 | 10 | ✓ | | 11.1 |
| | 50 | ✓ | | 12.6 |
| | 100 | ✓ | | 13.7 |
| | 150 | ✓ | | 14.7 |
| | 170 | ✓ | | 15.0 |
| | 200 | | ✓ | 15.3 |
| Line 3-2 | 50 | | ✓ | 18.6 |
| | 100 | | ✓ | 18.8 |
| | 150 | | ✓ | 17.8 |
| | 200 | | ✓ | 13.7 |

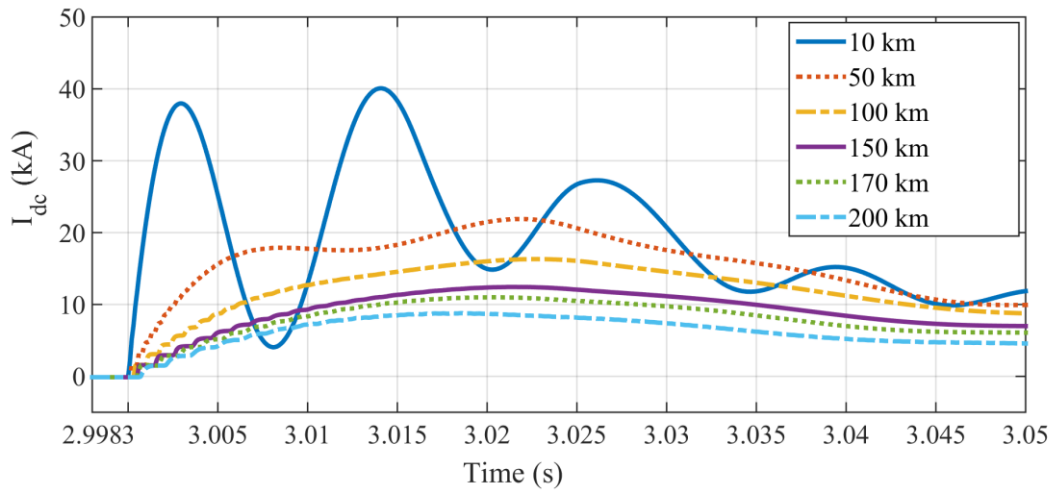
4.2.1.2 Pole-to-Ground Fault Condition

In this case, the performance of the relay R_{13} is tested with the positive and negative pole-to-ground faults at various locations (i.e., 10 km, 50 km, 100 km, 150 km, 170 km, 200 km) in a line between terminal-1 and terminal-3 in a three-terminal VSC-HVDC transmission system without current limiting reactors. The pole-to-ground fault is applied at $t = 3.0$ s, the duration of the fault is considered as 50 ms, and the fault resistance is taken as 1Ω . Figure 4.6 shows the HVDC system response measured at the relay R_{13} location under the positive pole-to-ground fault occurs at

various locations in the line 1-3. The rate of change of positive pole-to-ground DC voltage and DC current is decreased when the fault distance increases. In Figure 4.6 (a), the DC voltage is decreased below zero because it is measured for the pole-to-ground DC voltage. The DC fault current is increased to the abnormal value within a few ms which is exceeding the limits of the rating of the circuit breaker and HVDC converters as can be seen in Figure 4.6 (b).



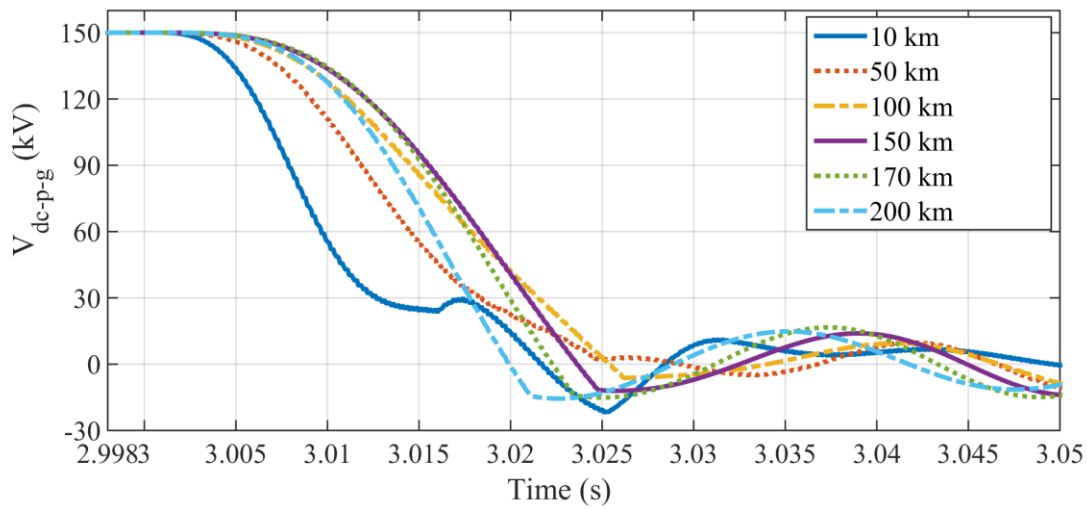
(a) Positive pole-to-ground DC voltage (V_{dc-p-g}).



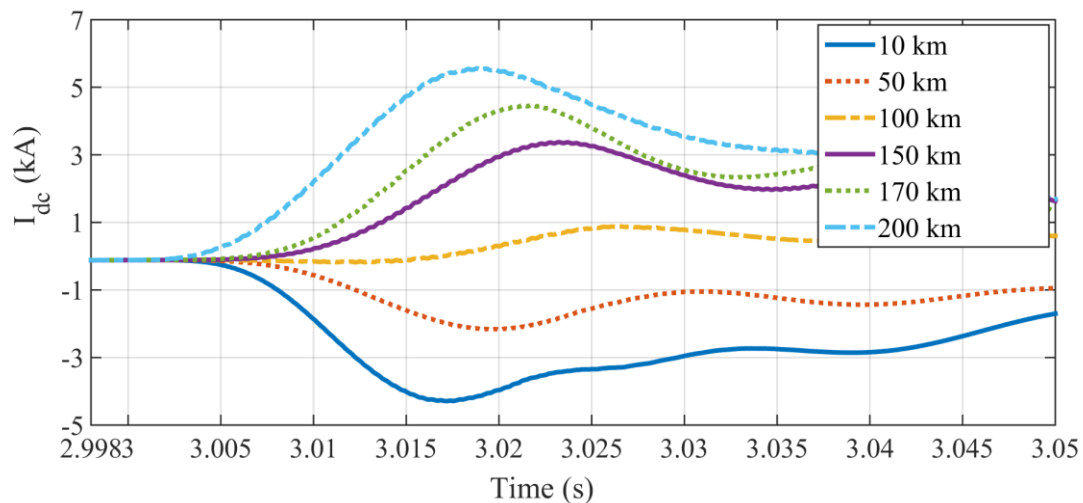
(b) DC Current (I_{dc}).

Figure 4.6 The DC voltage and current measured at the relay R_{13} location under positive pole-to-ground fault at various locations in a line 1-3.

The positive pole-to-ground DC voltage and DC current measured at the relay R₁₃ location under the negative pole-to-ground fault occurs at various locations in the line 1-3 is shown in Figure 4.7. The relay R₁₃ is located in the positive pole, but the fault has occurred on the negative pole. Therefore, the DC voltage and current change rate are very less which can be seen in Figure 4.7. The direction of the DC fault current has changed at the relay R₁₃ location due to fault on the negative pole.



(a) Positive pole-to-ground DC voltage (V_{dc-p-g}).



(b) DC Current (I_{dc}).

Figure 4.7 The DC voltage and current measured at the relay R₁₃ location under negative pole-to-ground fault at various locations in a line 1-3.

The threshold setting of the voltage and current derivatives and the increment of transient energy for the pole-to-ground fault condition are calculated based on Table 4.3. The fault detection time of a relay R₁₃ is presented in Table 4.4. This indicates that the relay R₁₃ has detected and discriminated the internal and external faults exactly for the positive and negative pole-to-ground fault conditions. Also, it is observed that the fault detection time of the relay R₁₃ gets increased when the fault distance is increased.

Table 4.3 The threshold determination of voltage and current derivatives, and increment of transient energy for the pole-to-ground fault condition in the three-terminal VSC-HVDC system without current limiting reactors.

| Fault line 1-3 | Fault distance (km) | $\frac{dV_{dc}}{dt}$ (kV/s) | $\frac{dI_{dc}}{dt}$ (kA/s) | ΔE (MW×s) |
|-------------------------------|------------------------|--------------------------------|--------------------------------|----------------------|
| Positive pole-to-ground fault | 10 | 53340.0 | 6485.5 | 2.76749 |
| | 50 | 18510.0 | 2476.5 | 0.36672 |
| | 100 | 11220.0 | 1350.0 | 0.12117 |
| | 150 | 7955.0 | 723.5 | 0.04604 |
| | 170 | 7160.0 | 863.5 | 0.04946 |
| | 200 | 7500.0 | 500.5 | 0.03003 |
| Negative pole-to-ground fault | 10 | 15435.0 | 247.0 | 0.03049 |
| | 50 | 9895.0 | 140.5 | 0.01112 |
| | 100 | 7780.0 | 7.5 | 0.00466 |
| | 150 | 7410.0 | 225.0 | 0.01333 |
| | 170 | 7925.0 | 383.0 | 0.02428 |
| | 200 | 9380.0 | 529.5 | 0.03973 |

Table 4.4 The fault detection time of relay R₁₃ under pole-to-ground fault condition in the three-terminal VSC-HVDC system without current limiting reactors.

| Fault line 1-3 | Fault distance (km) | Type of fault | | Fault detection time of relay R ₁₃ (ms) |
|-------------------------------|---------------------|---------------|----------|--|
| | | Internal | External | |
| Positive pole-to-ground fault | 10 | ✓ | | 11.2 |
| | 50 | ✓ | | 12.6 |
| | 100 | ✓ | | 13.8 |
| | 150 | ✓ | | 14.9 |
| | 170 | ✓ | | 15.2 |
| | 200 | | ✓ | 15.7 |
| Negative pole-to-ground fault | 10 | | ✓ | 15.6 |
| | 50 | | ✓ | 18.4 |
| | 100 | | ✓ | 20.2 |
| | 150 | | ✓ | 21.2 |
| | 170 | | ✓ | 21.2 |
| | 200 | | ✓ | 20.1 |

The fault resistance cannot be ignored in case of the pole-to-ground fault condition. The threshold setting of the fault discrimination criterion such as the voltage and current derivatives, and increment of transient energy might not work well when the fault resistance variation is very significant. In such cases, an adaptive threshold setting is a promising solution.

4.2.2 Three-terminal VSC-HVDC System with Current Limiting Reactors

In the previous case studies, the DC fault current has gone to the very high value which is exceeding the capacity of the DC circuit breaker (CB) before the protection unit comes to a decision due to its slow operating time. Therefore, current limiting reactors (CLR) are designed and connected in series with the circuit breaker to maintain the fault current within the breaker capacity. The meshed connection of the three-terminal VSC-HVDC transmission system with current limiting reactors is shown in Figure 4.8.

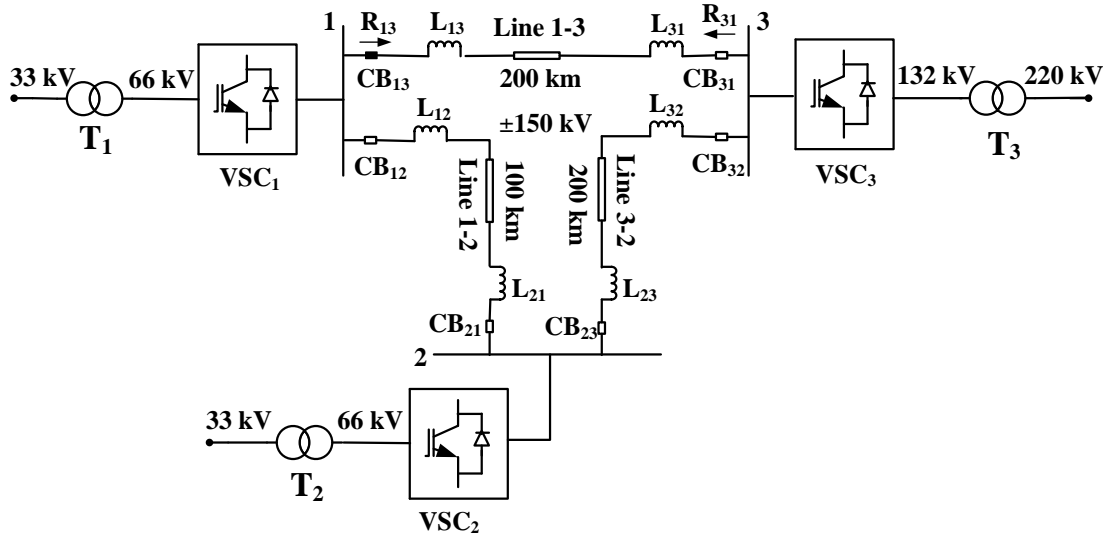


Figure 4.8 Three-terminal VSC-HVDC system with current limiting reactors.

4.2.2.1 Design of Current Limiting Reactors

Hybrid DC CB is the recent interest for the isolation of DC faults in the multi-terminal VSC-HVDC transmission systems. ABB has tested the hybrid DC CB with a maximum breaking current of 9 kA and an operating time of 2 ms. Fast disconnector and main DC CB is designed for the transient voltage capability of higher than 1.5 per unit during current breaking. ABB and Alstom have proposed the hybrid DC CB device with a maximum breaking current of 16 kA and an operating time of 2 ms.

From the DC fault studies, it is observed that the fault current goes to the very high value within a few ms. The peak fault current is increased more than the DC CB capacity, leads to the circuit breaker and other power electronic device damages. For example, in case of the pole-to-pole fault at 10 km and 50 km distance from the terminal-1 as shown in Figure 4.4 (b), the peak fault current exceeds 16 kA before to the protection processing time. In such cases, the current limiting reactors are essential to limit the peak fault current. The maximum breaking current of DC CB is very important while designing the current limiting reactors. The test HVDC system should limit the fault current within the maximum breaking capacity of DC CB until the protection unit isolates the faulty line.

The total protection processing time (t_{op}) is given as,

$$t_{op} = t_b + t_d + t_l \quad (4.10)$$

where, t_b is the operating time of hybrid DC CB and it is taken as 2 ms as per [J. Hafner and B. Jacobson 2011], [J. Seneath and A. D. Rajapakse 2016]. t_d is the time taken by the fault detection method. The fault detection time of single-ended protection scheme for the long-distance fault (i.e., the fault at 200 km distance from the relay point) in the three-terminal VSC-HVDC system without current limiting reactors is calculated as 16 ms using the DC fault data which is generated from the PSCAD/EMTDC simulation. t_l is the line transport delay from the fault point and it is given by,

$$t_l = \frac{d}{v} = \frac{d}{c/n} = d\sqrt{l \times c} \quad (4.11)$$

where, d is the length of the line, v is the traveling wave propagation speed, c is the speed of light in a vacuum, n is the refractive index, and l and c are the line inductance and capacitance per unit length [E. Kontos et al. 2015], [M. H. Nadeem et al. 2018]. The line transport delay for the long-distance of test HVDC system which includes the length of the line 1-3 and line 3-2 is calculated as 2 ms. Using equation (4.10), the total protection processing time (t_{op}) is calculated as 20 ms. The maximum breaking capacity of hybrid DC CB is 16 kA. Hence, the current rise rate should be 0.8 kA/ms.

The DC reactor (L_{dc}) value for the ± 150 kV three-terminal HVDC system can be calculated by,

$$L_{dc} \geq \frac{\Delta V}{dI_{dc}/dt} \geq \frac{150 \text{ kV}}{0.8 \frac{\text{kA}}{\text{ms}}} \quad (4.12)$$

$$L_{dc} \geq 187.5 \text{ mH} \quad (4.13)$$

where, ΔV is the DC reactor voltage, and dI_{dc}/dt is the rate of rise of DC current [K. Tahata et al. 2015], [D. Tzelepis et al. 2017], [J. Liu et al. 2017].

From equation (4.13), it is observed that the DC reactor value will be higher than 187.5 mH. Figure 4.9 shows the DC current at the relay R₁₃ location for different current limiting reactor values under pole-to-pole fault occurs at 10 km distance from the terminal-1. The peak value of the DC fault current is limited by increasing the

current limiting reactor values from 0 to 300 mH with 50 mH increments which can be seen from Figure 4.9. Also, it is noticed that the rate of change of DC fault current gets decreased when the current limiting reactor value is increased. Similarly, the DC voltage change rate also gets reduced when the CLR value rises. Therefore, the peak value of the DC fault current in the three-terminal VSC-HVDC system has maintained within the breaker capacity as 16 kA using the 300 mH current limiting reactors which are connected in series with the hybrid DC CB at each end of an HVDC grid.

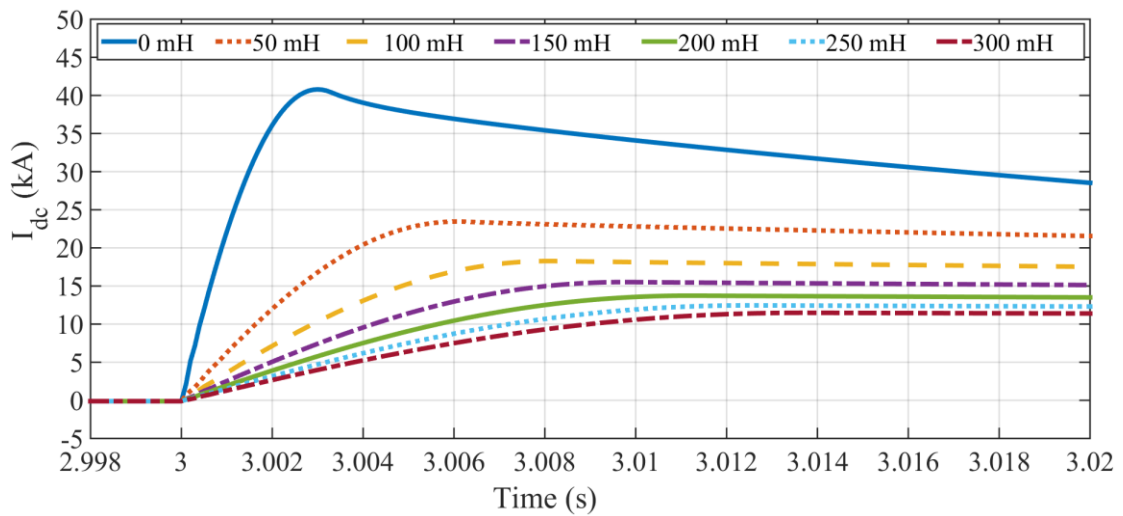
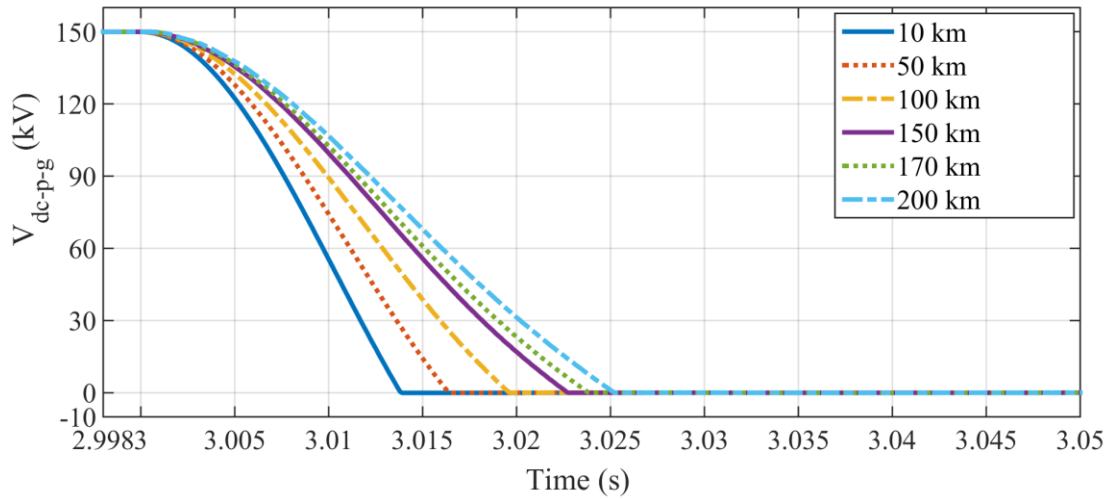


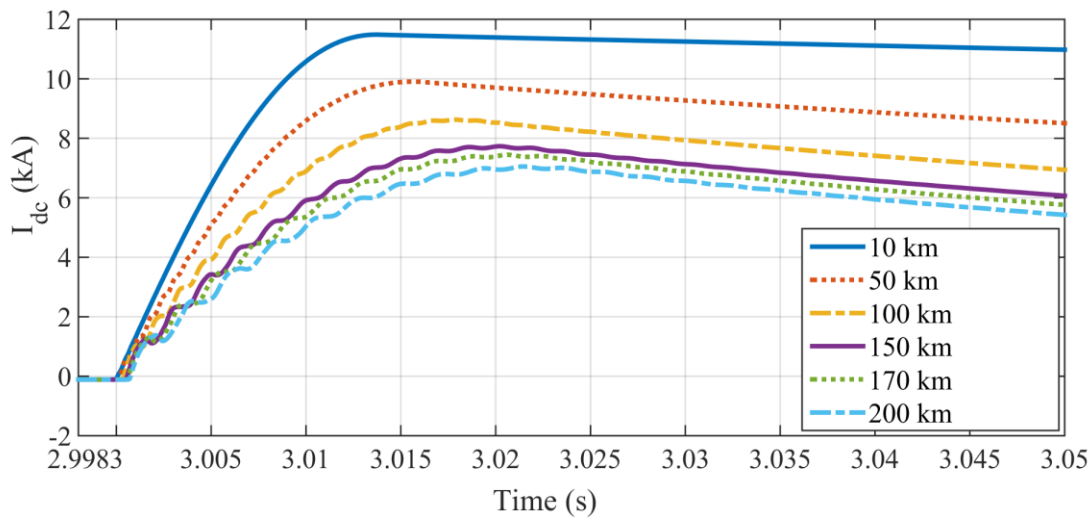
Figure 4.9 The DC current (I_{dc}) at the relay R_{13} location for the different value of current limiting reactors under pole-to-pole fault at 10 km distance from terminal-1.

4.2.2.2 Pole-to-Pole Fault Condition

The proposed protection scheme is tested for the pole-to-pole fault on the primary line (i.e., line 1-3) and secondary line (i.e., line 3-2) of the relay R_{13} in the three-terminal VSC-HVDC system with current limiting reactors as shown in Figure 4.8. In the first case, the pole-to-pole fault is applied at various locations (i.e., 10 km, 50 km, 100 km, 150 km, 170 km, 200 km distance from terminal-1) in the line 1-3. The fault has occurred at $t = 3.0$ s, the duration of fault is considered as 50 ms, and the fault resistance is taken as 0.01Ω . The positive pole-to-ground DC voltage and DC current measured at the relay R_{13} location under the pole-to-pole fault at various locations in the line 1-3 is shown in Figure 4.10.



(a) Positive pole-to-ground DC voltage (V_{dc-p-g}).

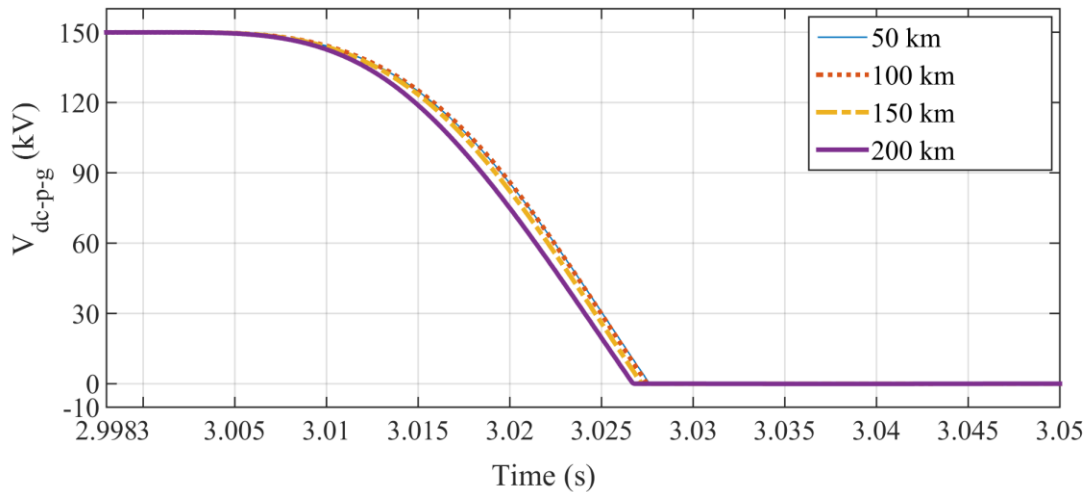


(b) DC Current (I_{dc}).

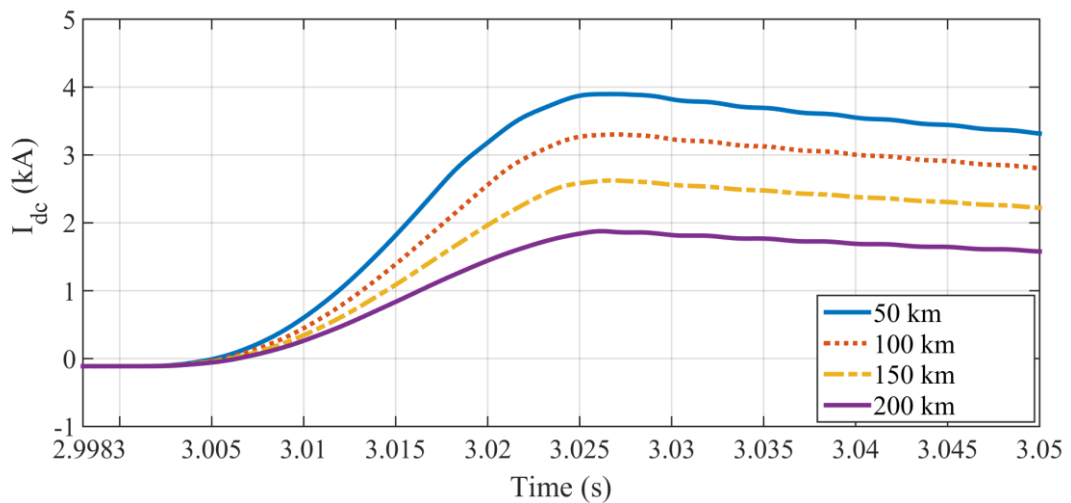
Figure 4.10 The DC voltage and current measured at the relay R_{13} location under pole-to-pole fault at various locations in a line 1-3.

After the occurrence of a fault, the DC link capacitor starts to discharge. The positive pole-to-ground DC voltage is decreased to zero within 14-25 ms for the fault at various locations in the line 1-3. The rate of change of the positive pole-to-ground DC voltage has decreased when the fault distance is increased from the relay location. After the DC link voltage reaches to zero, the line inductor drives the current through the antiparallel diode path of VSC. The DC fault current is rapidly rising within a few

ms for short distance faults. The peak value of the DC fault current has gone up to 11.5 kA within 14 ms for the fault at 10 km distance from the relay point. Also, the peak value of DC fault current has maintained within the rating of DC CB as 16 kA using the 300 mH current limiting reactors.



(a) Positive pole-to-ground DC voltage (V_{dc-p-g}).



(b) DC Current (I_{dc}).

Figure 4.11 The DC voltage and current measured at the relay R₁₃ location under pole-to-pole fault at various locations in a line 3-2.

The positive pole-to-ground DC voltage and DC current at the relay R₁₃ location under pole-to-pole fault at various locations (i.e., 50 km, 100 km, 150 km, and 200 km) in the line 3-2 is shown in Figure 4.11. The relay R₁₃ is located at the terminal-1. The fault distance (i.e., 50 km, 100 km, 150 km, and 200 km) is considered from the terminal-3. After the occurrence of the fault, the positive pole-to-ground DC voltage measured at the bus-1 terminal has slowly decreased to zero when compared to the previous case (i.e., the fault on line 1-3) due to the increment of distance between the relay location and the fault point. The peak value of the DC fault current has increased up to 4 kA within 27 ms for the fault at 250 km distance from the terminal-1 (i.e., the fault at 50 km distance from the terminal-3).

Table 4.5 The threshold determination of voltage and current derivatives, and increment of transient energy for the pole-to-pole fault condition in the three-terminal VSC-HVDC system with current limiting reactors.

| Fault line | Fault distance (km) | $\frac{dV_{dc}}{dt}$ (kV/s) | $\frac{dI_{dc}}{dt}$ (kA/s) | ΔE (MW×s) |
|------------|---------------------|-----------------------------|-----------------------------|-------------------|
| Line 1-3 | 10 | 11335 | 1064.5 | 0.09652 |
| | 50 | 9700 | 808.0 | 0.06270 |
| | 100 | 8230 | 564.0 | 0.03713 |
| | 150 | 7325 | 456.5 | 0.02675 |
| | 170 | 6990 | 496.5 | 0.02776 |
| | 200 | 6550 | 471.5 | 0.02470 |
| Line 3-2 | 50 | 6365 | 295.5 | 0.01504 |
| | 100 | 6300 | 229.0 | 0.01154 |
| | 150 | 6460 | 174.5 | 0.00901 |
| | 200 | 6775 | 125.0 | 0.00677 |

The protection unit declares that the HVDC system will be in normal condition if the DC voltage is maintained above the threshold value. The fault is identified when the DC voltage decreases below 85% of the rated value (i.e., 127 kV is taken for the

test HVDC system), and it stays for 10 ms. The voltage and current derivatives, and increment of transient energy are used to distinguish the internal faults from the external faults once the fault is identified. The threshold setting for the rate of change of DC voltage and current and the increment of transient energy for pole-to-pole fault condition are determined based on Table 4.5. The internal fault is declared if all or any two of the calculated $\frac{dV_{dc}}{dt}$, $\frac{dI_{dc}}{dt}$, and ΔE value exceeds the preset threshold value.

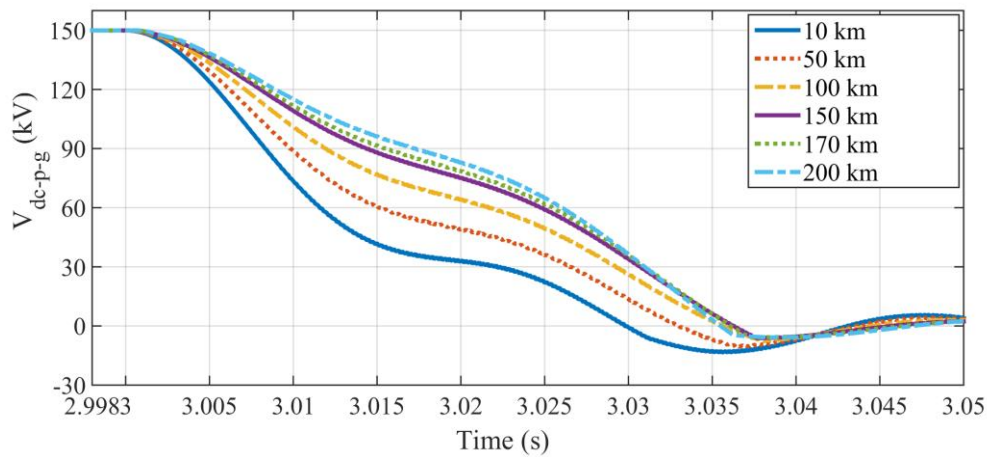
Table 4.6 The fault detection time of relay R₁₃ under pole-to-pole fault condition in the three-terminal VSC-HVDC system with current limiting reactors.

| Fault line | Fault distance (km) | Type of fault | | Fault detection time of relay R ₁₃ (ms) |
|------------|---------------------|---------------|----------|--|
| | | Internal | External | |
| Line 1-3 | 10 | ✓ | | 14.6 |
| | 50 | ✓ | | 15.2 |
| | 100 | ✓ | | 15.8 |
| | 150 | ✓ | | 16.5 |
| | 170 | ✓ | | 16.7 |
| | 200 | | ✓ | 17.0 |
| Line 3-2 | 50 | | ✓ | 24.7 |
| | 100 | | ✓ | 24.7 |
| | 150 | | ✓ | 24.4 |
| | 200 | | ✓ | 23.8 |

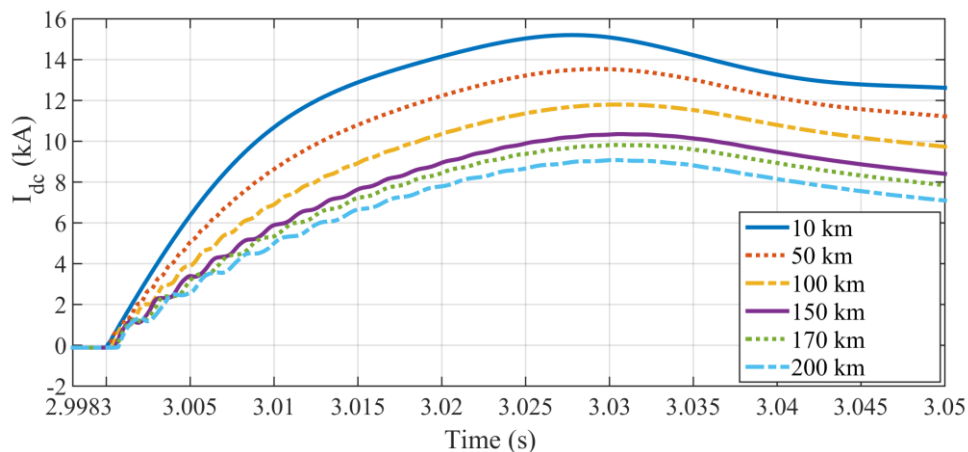
The fault detection time of a relay R₁₃ for the pole-to-pole fault condition is presented in Table 4.6. The relay R₁₃ has identified that the fault occurred below 85% length of the line 1-3 is an internal fault, remaining 15 % of the primary line 1-3 and fault on line 3-2 is declared as an external fault. This indicates the very fact that the proposed protection scheme can detect and discriminate both the internal and external faults accurately.

4.2.2.3 Pole-to-Ground Fault Condition

In this case, the performance of the relay R_{13} is tested with the positive and negative pole-to-ground faults at various locations (i.e., 10 km, 50 km, 100 km, 150 km, 170 km, 200 km) in a line between terminal-1 and terminal-3 in the three-terminal VSC-HVDC transmission system with current limiting reactors. The pole-to-ground fault is applied at $t = 3.0$ s, the duration of the fault is considered as 50 ms, and the fault resistance is taken as 1Ω . Figure 4.12 and 4.13 show the HVDC system response measured at the relay R_{13} location under the positive and negative pole-to-ground fault occurs at various locations in the line 1-3.

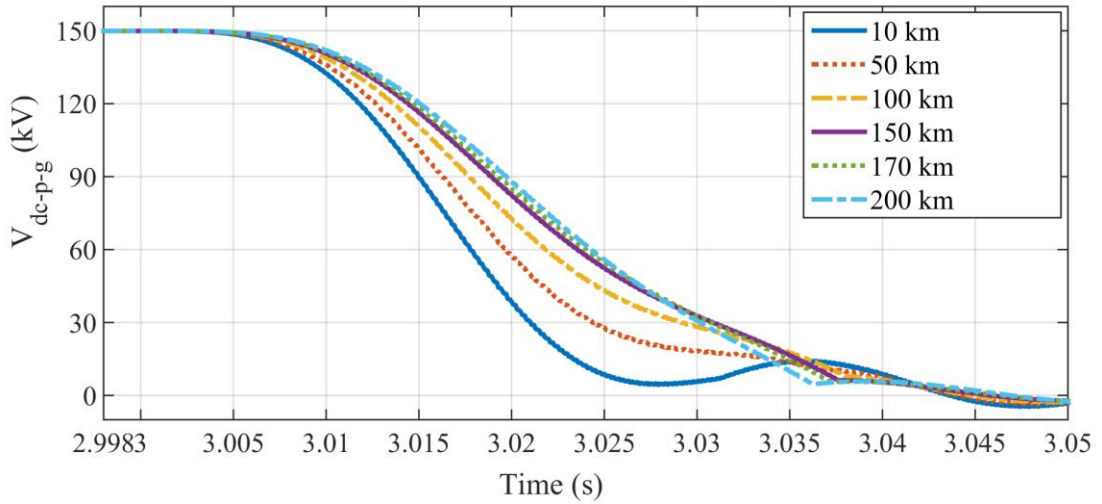


(a) Positive pole-to-ground DC voltage (V_{dc-p-g}).

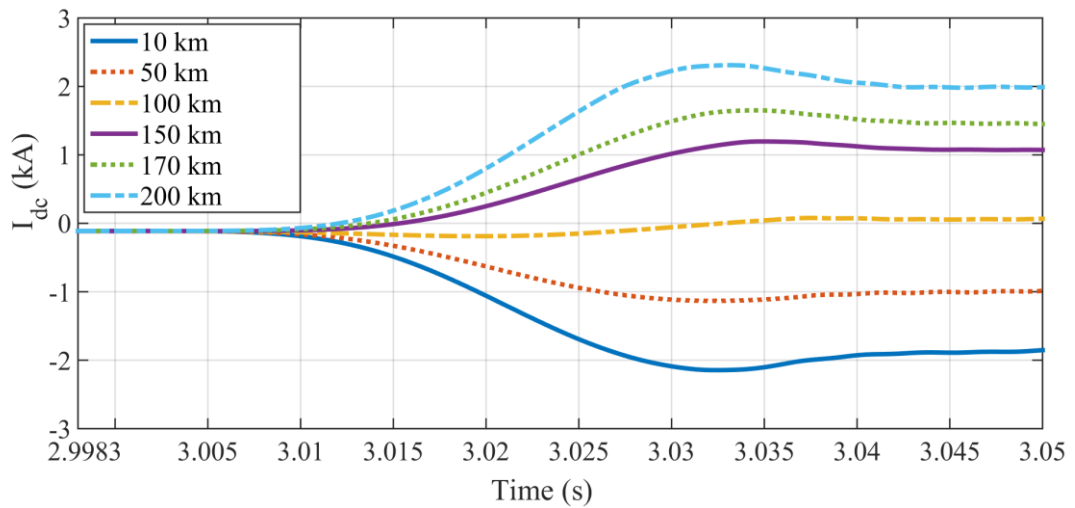


(b) DC Current (I_{dc}).

Figure 4.12 The DC voltage and current measured at the relay R_{13} location under positive pole-to-ground fault at various locations in a line 1-3.



(a) Positive pole-to-ground DC voltage (V_{dc-p-g}).



(b) DC Current (I_{dc}).

Figure 4.13 The DC voltage and current measured at the relay R_{13} location under negative pole-to-ground fault at various locations in a line 1-3.

In both positive and negative pole-to-ground fault cases, the peak value of the DC fault current is limited to the breaker rating using the current limiting reactors. The threshold setting of the voltage and current derivatives and the increment of transient energy for the pole-to-ground fault conditions are calculated based on Table 4.7. The fault detection time of a relay R_{13} is presented in Table 4.8. This indicates that the relay R_{13} has detected and discriminated the internal and external faults exactly for the

positive and negative pole-to-ground fault cases. Also, it is observed that the fault detection time increases when fault distance increases.

Table 4.7 The threshold determination of voltage and current derivatives, and increment of transient energy for the pole-to-ground fault condition in the three-terminal VSC-HVDC system with current limiting reactors.

| Fault Line 1-3 | Fault distance (km) | $\frac{dV_{dc}}{dt}$ (kV/s) | $\frac{dI_{dc}}{dt}$ (kA/s) | ΔE (MW×s) |
|-------------------------------|---------------------|-----------------------------|-----------------------------|-------------------|
| Positive pole-to-ground fault | 10 | 9785 | 1046.5 | 0.08192 |
| | 50 | 8100 | 806 | 0.05222 |
| | 100 | 6645 | 650.5 | 0.03458 |
| | 150 | 5640 | 439.5 | 0.01983 |
| | 170 | 5305 | 438.5 | 0.01860 |
| | 200 | 4800 | 392.5 | 0.01507 |
| Negative pole-to-ground fault | 10 | 7920 | 52 | 0.00329 |
| | 50 | 7105 | 34.5 | 0.00196 |
| | 100 | 6460 | 7.5 | 0.00387 |
| | 150 | 5785 | 28 | 0.00129 |
| | 170 | 5765 | 46.5 | 0.00214 |
| | 200 | 5680 | 82.5 | 0.00374 |

The fault resistance cannot be ignored in case of the pole-to-ground faults. The threshold setting of the fault discrimination criterion such as the voltage and current derivatives and increment of transient energy might not work well when the fault resistance variation is very significant. In such cases, an adaptive threshold setting is a promising solution. Therefore, further studies are needed to verify the proposed protection scheme for the DC pole-to-ground fault with higher resistance cases in the MT VSC-HVDC transmission systems.

Table 4.8 The fault detection time of relay R₁₃ under pole-to-ground fault condition in the three-terminal VSC-HVDC system with current limiting reactors.

| Fault Line 1-3 | Fault distance (km) | Type of fault | | Fault detection time of relay R ₁₃ (ms) |
|-------------------------------|---------------------|---------------|----------|--|
| | | Internal | External | |
| Positive pole-to-ground fault | 10 | ✓ | | 14.7 |
| | 50 | ✓ | | 15.4 |
| | 100 | ✓ | | 16.1 |
| | 150 | ✓ | | 16.8 |
| | 170 | ✓ | | 17.1 |
| | 200 | | ✓ | 17.5 |
| Negative pole-to-ground fault | 10 | | ✓ | 20.9 |
| | 50 | | ✓ | 21.7 |
| | 100 | | ✓ | 22.5 |
| | 150 | | ✓ | 23.2 |
| | 170 | | ✓ | 23.5 |
| | 200 | | ✓ | 23.8 |

4.3 Conclusions

In this chapter, the modeling of the single-ended protection scheme for the DC faults in a three-terminal VSC-HVDC transmission system is presented. Simulation studies are carried out to test the single-ended protection scheme with the DC fault datasets of the three-terminal VSC-HVDC transmission system for both without and with current limiting reactors. The obtained results indicate that the DC fault current reaches a higher value than the DC circuit breaker capacity before the protection unit comes into operation. Therefore, current limiting reactors are designed to limit the DC fault current within the breaker capacity.

From the obtained results, it is concluded that the relay has detected and discriminated the internal and external faults for both the DC pole-to-pole and pole-to-ground fault cases. The fault detection time of the relay has increased when the

distance between the relay location and the fault point increases due to the less DC voltage and current rise rate. Also, the fault detection time of the relay has increased for the three-terminal VSC-HVDC system with current limiting reactors when compared to the without current limiting reactors. In the case of DC pole-to-ground faults, the sensitivity of the fault discrimination criterion may get decreased when the variation of fault resistance is more significant. In such cases, the adaptive threshold setting for the fault discrimination criterion is an area for further investigation if fault resistance varies as huge value.

CHAPTER 5

THE IMPACT OF VSC-BASED HVDC SYSTEMS ON DISTANCE PROTECTION OF AC TRANSMISSION LINES

The protective relays are the most important equipment in the protection systems. Distance relay commonly referred to as impedance relay has been applied to protect the AC transmission lines. Under the present scenario in power system, developing a protection scheme for AC transmission line is very challenging since the power electronics devices such as flexible AC transmission systems (FACTS) and voltage source converters (VSC)-based high voltage direct current (HVDC) systems are penetrated to the AC system due to the requirement of high-power renewables integration with the existing AC grid. The VSC-based HVDC systems stand as a challenge for the distance relays to function normally as they can control both active and reactive power flow independently. Therefore, it is essential to investigate the distance relay performance in the presence of VSC-based HVDC systems. In the previous chapters, the modeling of the VSC-based HVDC link connected offshore wind farms are presented.

In this chapter, the modeling of the distance relay has been developed to analyze the VSC-based HVDC system influence. The analytical and simulation studies are carried out to evaluate the performance of the distance relays in the AC transmission line with the interconnection of the VSC-based HVDC transmission system under various fault conditions.

5.1 AC Grid Protection

Power system faults can occur in a system due to insulation failure which is caused by the short circuit, switching, and lightning. It can be divided into symmetric faults, i.e., three-phase short circuits and asymmetric faults that are classified as the phase-to-phase faults, phase-to-ground faults, and double phase-to-ground faults. In such cases, distance relays are used to protect the transmission lines. The distance relay uses the

voltage and current measured at the relay location to calculate the apparent impedance of the protected transmission line. Consider the fault on a power system network is indicated in Figure 5.1.

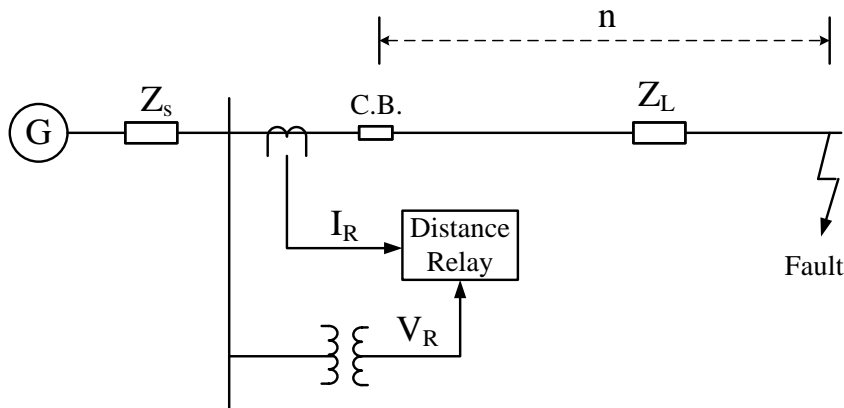


Figure 5.1 The principles of operation of distance relay.

The apparent impedance seen by the relay is given by,

$$Z_R = \frac{V_R}{I_R} = \frac{I_R \times n Z_L}{I_R} = n Z_L \quad (5.1)$$

where, V_R and I_R is the voltage and current measured at the relay location, Z_L is the line impedance. Then, the calculated impedance is compared with the relay characteristics to determine the faults.

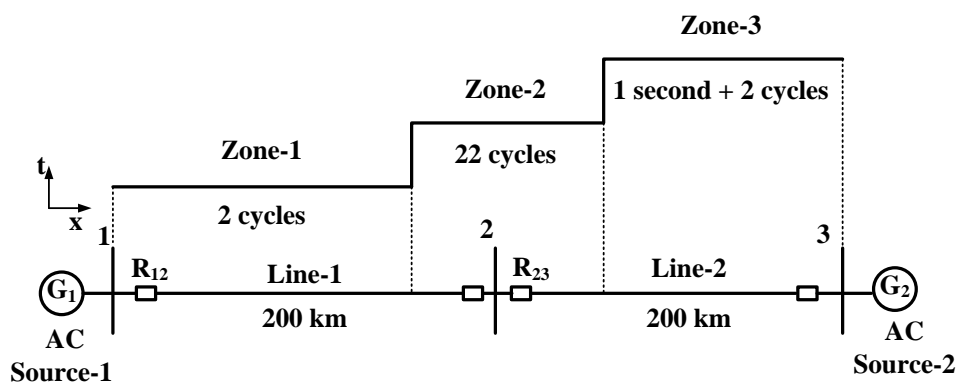


Figure 5.2 The three-bus system with distance relay model.

In a transmission system, the distance relays are commonly designed with primary and backup protection. The three-bus system with the distance relay model is shown in

Figure 5.2. The distance relay provides multiple zones while protecting the transmission lines. Zone-1 is set to cover 80 % length of the primary line, and it operates with zero-time delay. The operating time of Zone-1 relay is two cycles. Zone-2 is set to cover 120 % of the primary line impedance. It acts as backup protection and operates with 20 cycles (i.e., 0.4 seconds) time delay. Zone-3 provides remote backup protection with a time delay of 1 second.

5.2 Modeling of the Distance Relay

The flowchart illustrates the function of distance relaying as shown in Figure 5.3. First, the input AC voltage and current are measured at the relay location using the voltage and current transformers. For detecting the power system faults, every zone of the distance relay requires six monitoring units such as three units for detecting the faults amongst the phases and the other three units for detecting the phase-to-ground faults. The low pass anti-aliasing filter is used to remove the high-frequency contents of the input signal. However, it cannot remove decaying DC components and rejects lower-order frequency contents in the signal. Therefore, the fast Fourier transform (FFT) is employed to extract only the fundamental components of the signal.

Full cycle window Fourier (FCWF) algorithm can be applied to extract the amplitude and phase angle of the given input signal. Consider the sinusoidal input voltage signal of frequency ω is given by,

$$V(t) = V_{m1} \sin(\omega t + \phi_1) \quad (5.2)$$

where, V_{m1} and ϕ_1 are the peak amplitude and phase angle of the voltage signal.

The real and imaginary parts of the desired frequency signal are computed using FCWF algorithm is given by,

$$V_C = \frac{2}{N} \sum_{i=1}^N V_{(k-N+i)} \cos\left(\frac{2\pi i}{N}\right) \quad (5.3)$$

$$V_S = \frac{2}{N} \sum_{i=1}^N V_{(k-N+i)} \sin\left(\frac{2\pi i}{N}\right) \quad (5.4)$$

where, N is the number of samples per cycle and k is the sampling point. With the help of these real and imaginary components, the signal peak amplitude and phase is computed by the following expressions,

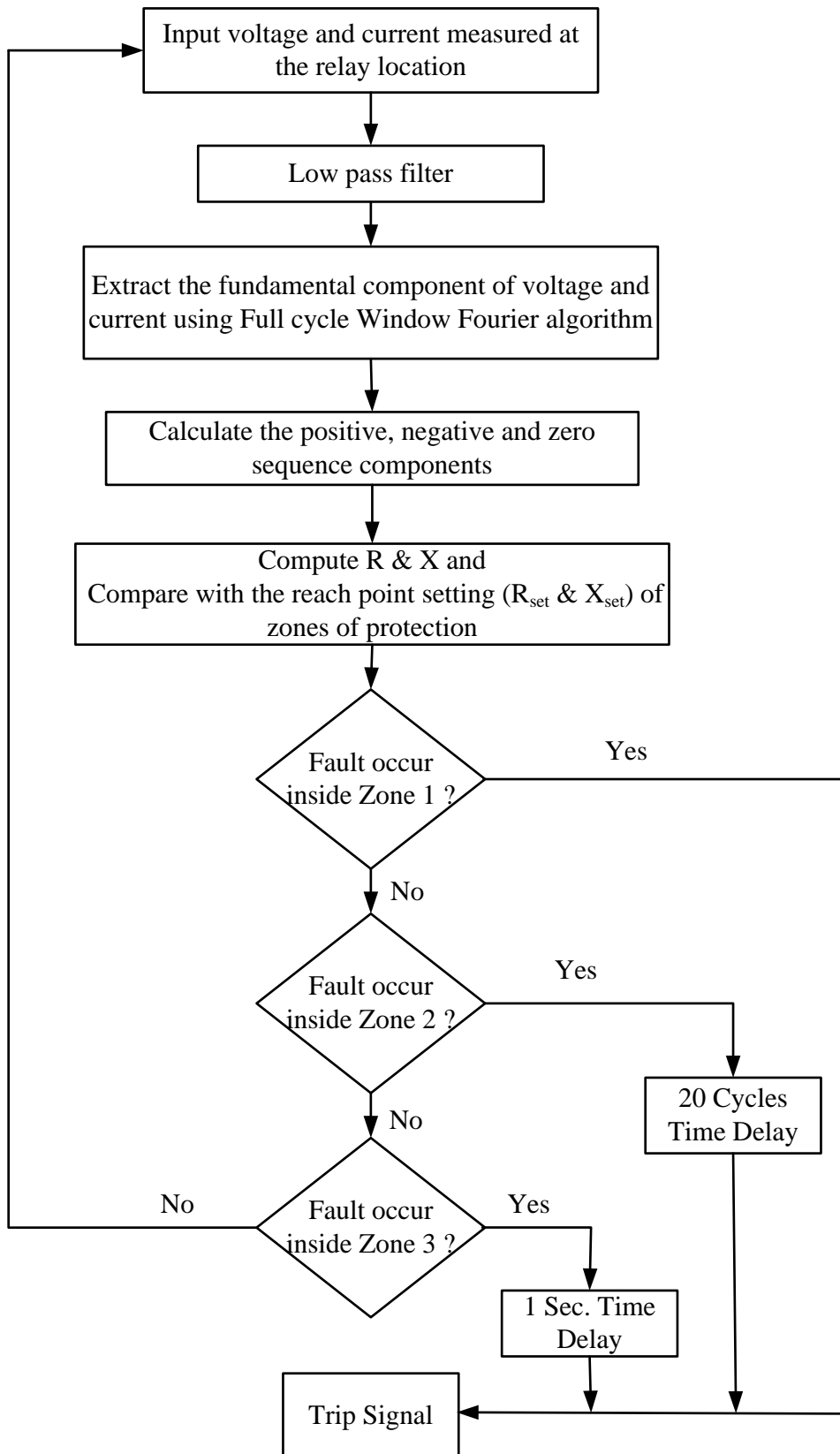
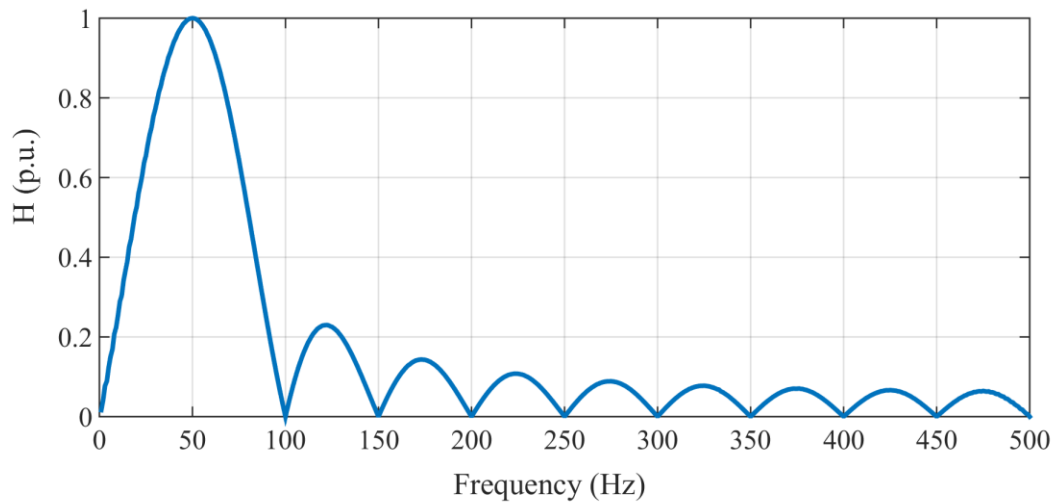


Figure 5.3 Flowchart Illustrates the Function of Distance Relaying.

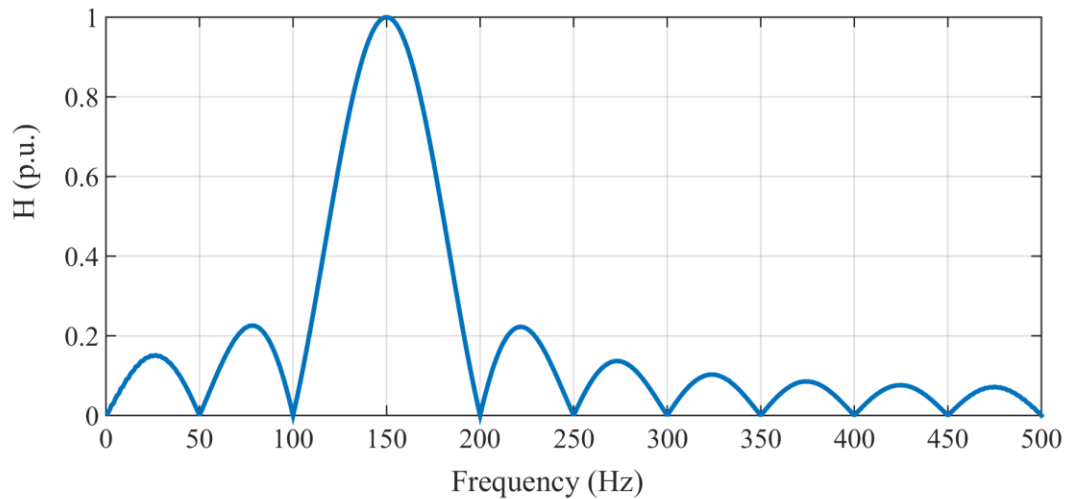
$$V_m = \sqrt{V_C^2 + V_S^2} \quad (5.5)$$

$$\phi = \tan^{-1} \left(\frac{V_S}{V_C} \right) \quad (5.6)$$

The frequency response for the fundamental and 3rd harmonic component extraction is shown in Figure 5.4. The frequency response characteristic consists of the fundamental and integral harmonic components with zero DC gain.



(a) Fundamental component extraction.



(b) 3rd Harmonic component extraction.

Figure 5.4 The frequency response of the full cycle window Fourier considering the number of samples per cycle (N) is 20.

Sequence components can be calculated using the extracted magnitude and phase of the fundamental frequency signal. The apparent impedance of the phase and ground faults are determined using the positive, negative, and zero sequence components. Table 5.1 presents the expression for finding the fault impedance value for both the phase and ground fault cases, where Z_0 and Z_1 are the zero sequence and positive sequence impedances respectively and I_0 is the zero-sequence current.

Table 5.1 Fault impedance calculation for the phase and ground faults.

| Fault Type | | Equations | |
|-----------------------|-------------------|-------------------------------------|-----------------------------|
| Phase-to-Ground Fault | Phase A | $Z_A = \frac{V_A}{I_A + 3kI_0}$ | $k = \frac{Z_0 - Z_1}{Z_1}$ |
| | Phase B | $Z_B = \frac{V_B}{I_B + 3kI_0}$ | |
| | Phase C | $Z_C = \frac{V_C}{I_C + 3kI_0}$ | |
| Phase-to-Phase Fault | Phase A – Phase B | $Z_{AB} = \frac{V_{AB}}{I_A - I_B}$ | - |
| | Phase B – Phase C | $Z_{BC} = \frac{V_{BC}}{I_B - I_C}$ | |
| | Phase C – Phase A | $Z_{CA} = \frac{V_{CA}}{I_C - I_A}$ | |

The calculated fault impedance ($Z = R + jX = Z\angle\theta$) is compared with the reach point setting (R_{set} & X_{set}) to determine the fault on a protected line. Mho relay is used for the reach point setting calculation using the positive and zero sequence impedances. Referring to Figure 5.2, the zone setting calculation for the phase and ground fault relays are given below:

The positive sequence impedance is given by,

$$\begin{aligned}
 Z_1 &= 0.42\angle 85.32^\circ \\
 &= (0.03 + j0.42) \Omega/km
 \end{aligned}
 \tag{5.7}$$

The zero sequence impedance is given by,

$$\begin{aligned} Z_0 &= 1.17 \angle 75.34^\circ \\ &= (0.29 + j1.13) \Omega/km \end{aligned} \quad (5.8)$$

The zero sequence compensation factor (k) is given by,

$$k = \frac{Z_0 - Z_1}{Z_1} = 1.79 \angle -15.50^\circ \quad (5.9)$$

The positive sequence impedance for 200 km line is given by,

$$\begin{aligned} &= 200 \times (0.42 \angle 85.32^\circ) \\ &= 84.79 \angle 85.32^\circ \\ &= (6.90 + j84.51) \Omega \end{aligned} \quad (5.10)$$

Zone-1 reach setting = $0.8 \times (84.79 \angle 85.32^\circ)$

$$\begin{aligned} &= 67.83 \angle 85.32^\circ \\ &= (5.52 + j67.60) \Omega \end{aligned} \quad (5.11)$$

Zone-1 mho circle radius = $33.91 \angle 85.32^\circ$

$$= (2.76 + j33.80) \Omega \quad (5.12)$$

Zone-2 reach setting = $1.2 \times (84.79 \angle 85.32^\circ)$

$$\begin{aligned} &= 101.75 \angle 85.32^\circ \\ &= (8.28 + j101.41) \Omega \end{aligned} \quad (5.13)$$

Zone-2 mho circle radius = $50.87 \angle 85.32^\circ$

$$= (4.14 + j50.70) \Omega \quad (5.14)$$

Zone-3 reach setting = $2.2 \times (84.79 \angle 85.32^\circ)$

$$\begin{aligned} &= 186.54 \angle 85.32^\circ \\ &= (15.19 + j185.92) \Omega \end{aligned} \quad (5.15)$$

Zone-3 mho circle radius = $93.27 \angle 85.32^\circ$

$$= (7.59 + j92.96) \Omega \quad (5.16)$$

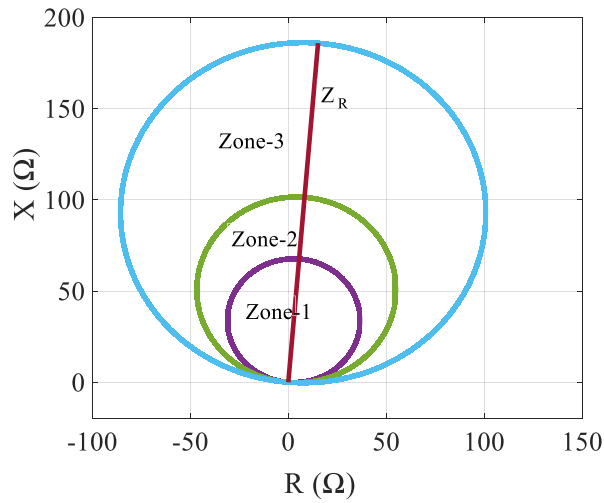


Figure 5.5 Mho relay with protection zones.

The Mho relay with protection zones is shown in Figure 5.5, where Z_R is the reach setting of the relay. The relay commands a trip signal when the measured impedance which contains resistance and reactance falls within the reach point setting of the protection zones.

5.3 Study of VSC-HVDC Impacts on Distance Protection of AC Transmission Lines

A VSC-HVDC transmission system is coupled to the typical three-bus system via bus-2 terminal as shown in Figure 5.6. In case of a short circuit fault F occurring on the line 2-3, the bus-2 voltage starts to collapse. In such a condition, the VSC-HVDC system will increase the bus-2 voltage by altering the reactive power due to the fast control action of the VSC. But, it does not affect the impedance seen by a relay R_{23} as fault F since the relay R_{23} is in the same section of the transmission line.

Considering the fault impedance to be zero, the impedance seen by a relay R_{12} ($Z_{R_{12}}$) is the line impedance between the relay location and the fault point. It is given by,

$$Z_{R_{12}} = \frac{V_1}{I_{12}} \quad (5.17)$$

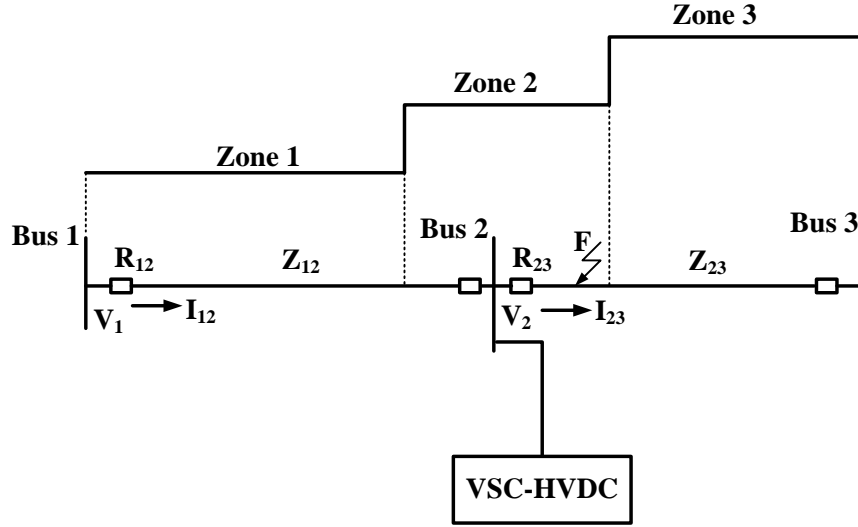


Figure 5.6 The three-bus system with VSC-HVDC.

where, V_1 and I_{12} are the voltage and current seen by the relay R_{12} . By using KVL, the bus-1 voltage (V_1) can be expressed as a function of bus-2 voltage (V_2). Therefore, the impedance seen by relay R_{12} is given by,

$$Z_{R_{12}} = \frac{V_2 + I_{12}Z_{12}}{I_{12}} = \frac{V_2}{I_{12}} + Z_{12} \quad (5.18)$$

where Z_{12} and Z_{23} are the impedance of the line 1-2 and line 2-3.

The fault F falls in the range of Zone-1 of relay R_{23} and Zone-2 of relay R_{12} . In case of failure of the primary protection provided by the relay R_{23} , the fault F is cleared by the relay R_{12} , which will act as backup protection for the same section and operate with a pre-set Zone-2 time delay. This time duration allows the VSC-HVDC system to readjust its reactive power flow. As a result, the bus-2 voltage (V_2) is boosted. Hence, the impedance seen by the relay R_{12} is increased, and the fault distance viewed by the relay R_{12} is over-estimated.

When a reactive power source is injected between the relay location and the fault point, the fault distance is over-estimated when seen by the relay. Due to the fast-acting control action of VSC, the voltage and current and thus impedance seen by Zone-2 relay might get affected. Therefore, a Zone-2 fault might be misunderstood as a Zone-3 event, which in turn will take more time to clear the existing fault. The error in the fault

distance estimation leads to the miscoordination between the distance relays. In case of the Zone-3 fault of a relay R_{12} , the apparent impedance seen by the relay R_{12} may go outside the protection zones.

5.4 Simulation Studies to Evaluate the VSC-HVDC Impacts on Distance Relay Performance

In this section, simulation studies are carried out to evaluate the impact of VSC-HVDC system on the performance of distance relays. The test system considered for the simulation study is shown in Figure 5.7. It consists of a 3-bus system with 420 kV, 50 Hz source connected at both ends and the load angle between the sources is 20° . The VSC-HVDC system is connected to the bus-2 terminal of the 3-bus system, and it is operating at 200 MW, ± 200 kV DC voltage which has presented in section 3.3. The length of the AC transmission lines 1 and 2 are 200 km, and the length of the DC line is 100 km. The mho characteristic-based distance relay R_{12} acts as the primary protection for line 1-2 and backup protection for line 2-3. The performance of the relay R_{12} is tested for the Zone-1, Zone-2, and Zone-3 operations under various fault conditions since it provides both the primary and backup protection. Also, the effect of fault resistance on the performance of the relay R_{12} is presented.

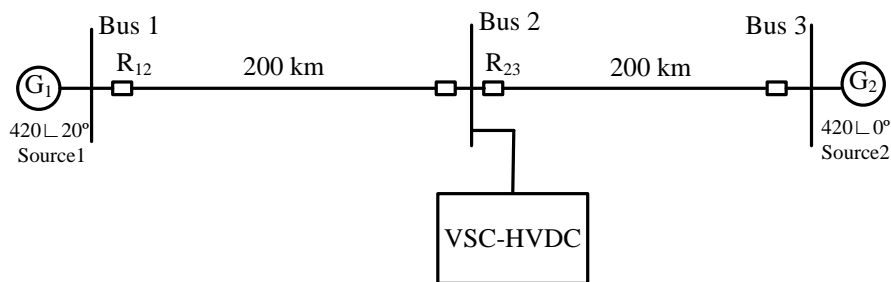


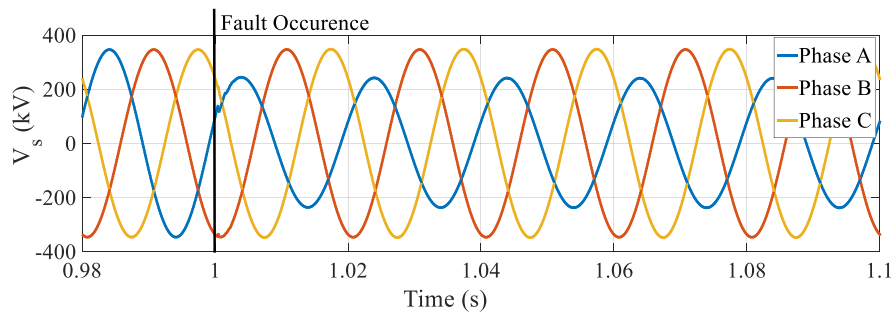
Figure 5.7 The simulation model of the three-bus system connected to a VSC-HVDC.

5.4.1 Fault on Zone-1 Area of Relay

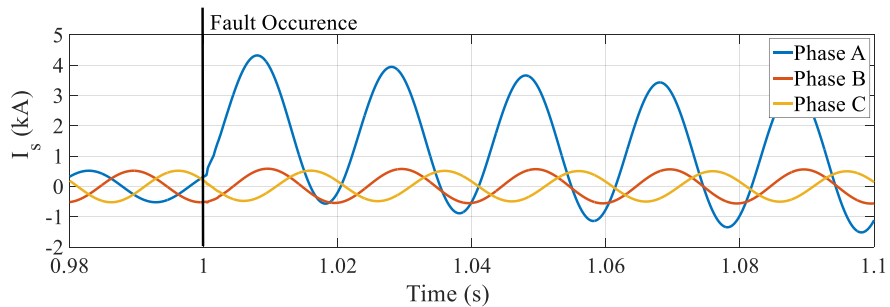
In this section, the performance of the distance relay is tested under the condition of fault on Zone-1 area of a relay R_{12} in the 3-bus system for both without and with VSC-HVDC system.

5.4.1.1 Phase-to-Ground Fault Condition

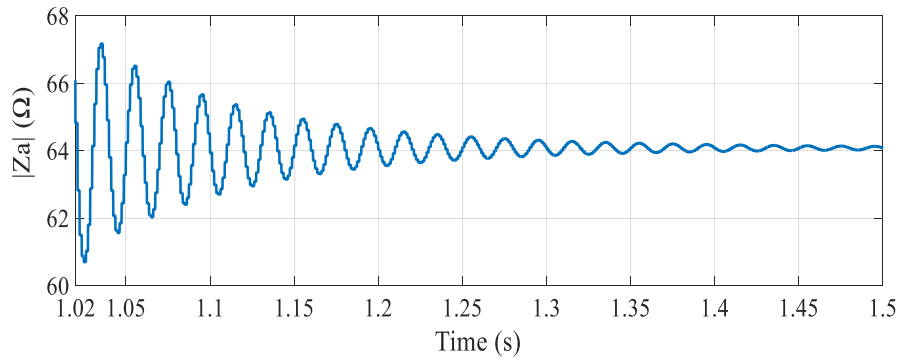
In the first case, the performance of the relay R_{12} is tested in an AC system without VSC-HVDC system under the condition of the phase-to-ground fault on Zone-1 area of the relay. The phase A to ground (A-G) fault is applied at 150 km distance from the bus-1 terminal, i.e., Zone-1 area of the relay R_{12} . The fault has applied at time $t = 1.0$ s, and the duration of the fault is considered as 1.0 s. The performance of the Relay R_{12} due to Phase A to ground fault occurs at 150 km distance from the relay R_{12} location in an AC system without VSC-HVDC is shown in Figure 5.8. The three-phase AC voltage and current measured at the bus-1 terminal has demonstrated in Figure 5.8 (a) and (b). The faulted phase voltage gets decreased, and reduction of the RMS voltage is 10 % and the peak value of the faulted phase current has gone up to 4.32 kA. The impedance of the faulted phase has reduced to $64.08\angle 85.42^\circ \Omega$, and that impedance trajectory is depicted in Figure 5.8 (c) and (d). The fault has occurred inside the Zone-1 area of the relay R_{12} . Therefore, the relay detects the fault and issues the trip decision without time delay which is demonstrated in Figure 5.8 (e).



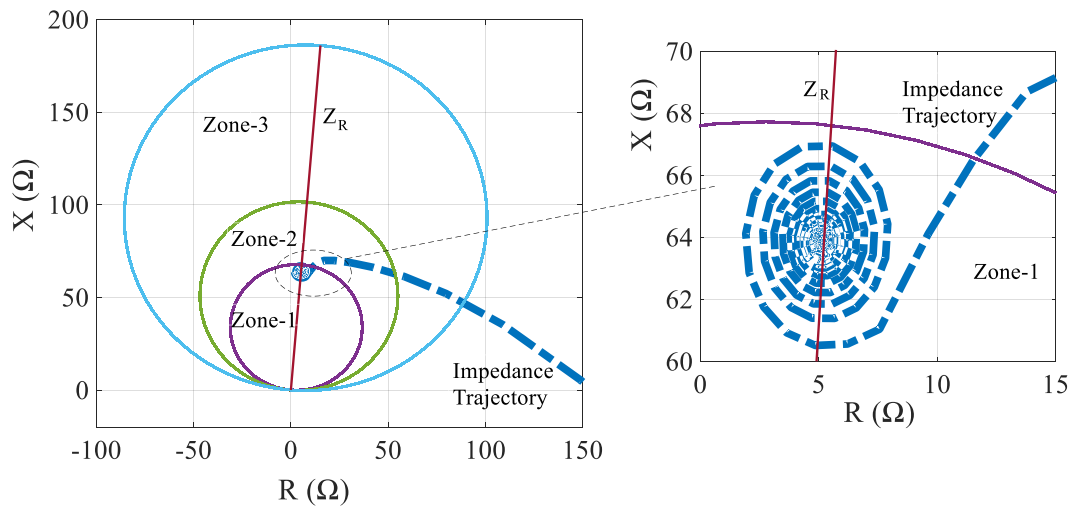
(a) Three-phase AC voltage (V_s) at bus-1 terminal.



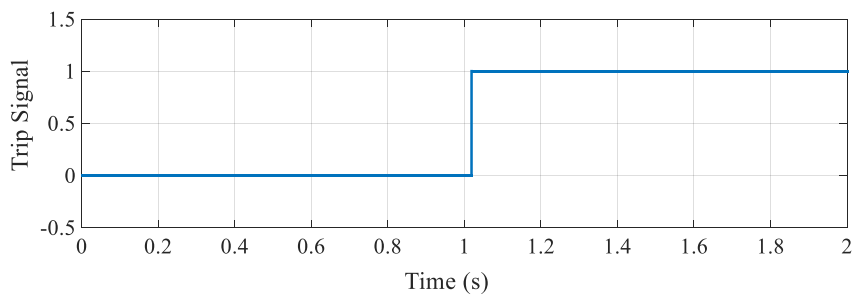
(b) Three-phase AC current (I_s) at bus-1 terminal.



(c) Magnitude of phase A fault impedance ($|Z_a|$) during A-G fault.

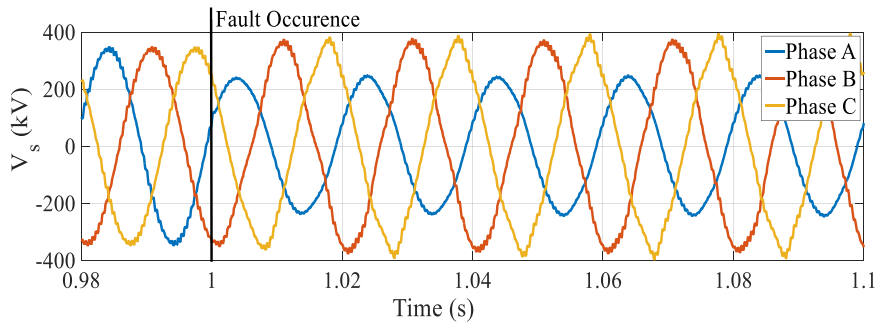


(d) Impedance trajectory during A-G fault.

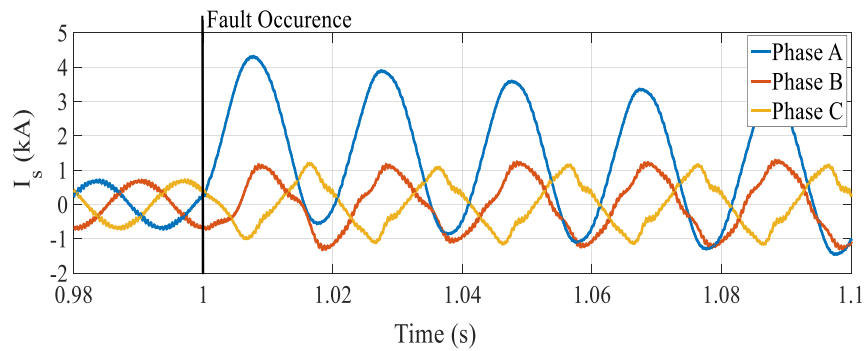


(e) Trip signal of relay R_{12} .

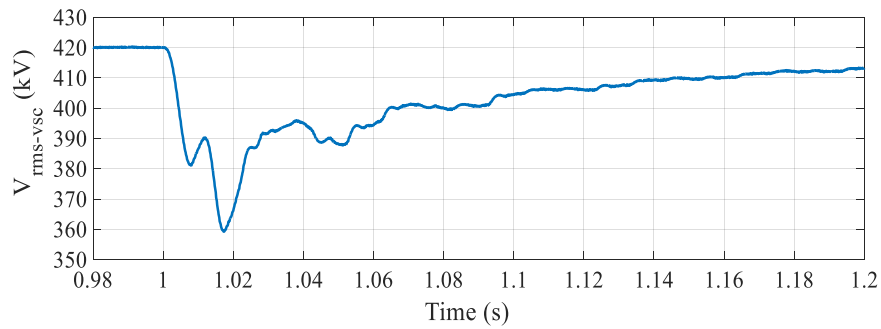
Figure 5.8 The performance of the relay R_{12} under the phase-to-ground (A-G) fault at 150 km distance from the bus-1 terminal in an AC system without VSC-HVDC.



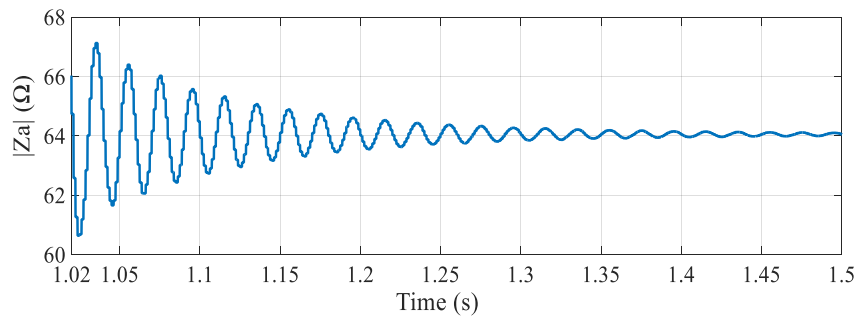
(a) Three-phase AC voltage (V_s) at bus-1 terminal.



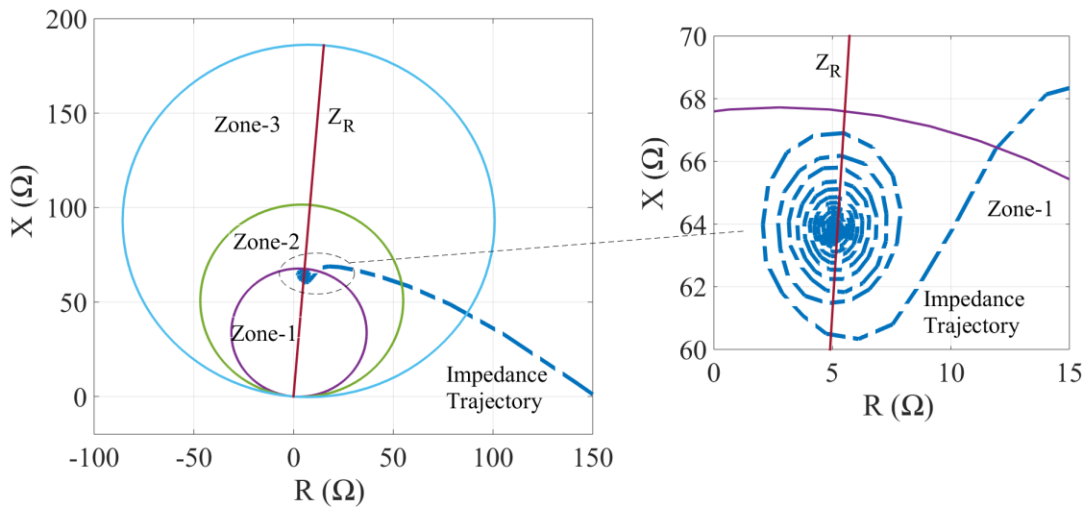
(b) Three-phase AC current (I_s) at bus-1 terminal.



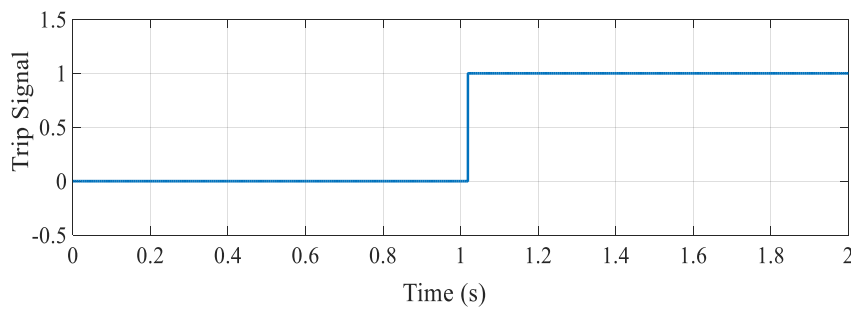
(c) RMS value of AC line voltage at grid side VSC (bus-2 connection point).



(d) Magnitude of Phase A fault impedance ($|Z_a|$) during A-G fault.



(e) Impedance trajectory during A-G fault.



(f) Trip signal of relay R_{12} .

Figure 5.9 The performance of the relay R_{12} under the phase-to-ground (A-G) fault at 150 km distance from the bus-1 terminal in an AC system with VSC-HVDC.

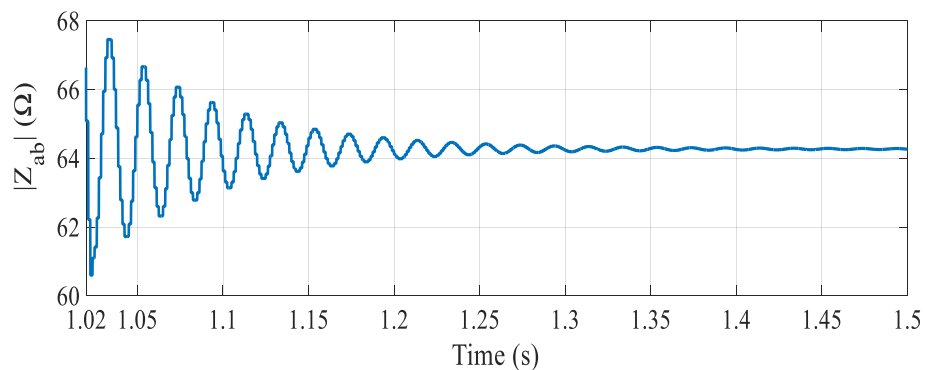
In the second case, the performance of the relay R_{12} is tested in an AC system with VSC-HVDC system under the condition of A-G fault on Zone-1 area of the relay. The fault data is similar to the previous case. Figure 5.9 shows the performance of the relay R_{12} during the phase A to ground fault at 150 km distance from the relay R_{12} location in an AC system with VSC-HVDC link connected at the bus-2 terminal. After the fault, the three-phase AC voltage and current of the healthy phases also get affected due to VSC-HVDC connection which can be seen in Figure 5.9 (a) and (b). Transients are produced in the AC line voltage measured at the bus-2 terminal (i.e., grid side VSC connection point) which is depicted in Figure 5.9 (c). However, this variation does not

affect the Zone-1 operation of the relay R_{12} . The apparent impedance seen by Zone-1 relay is $64.05\angle 85.44^\circ \Omega$ and that is depicted in Figure 5.9 (d) and (e). The relay R_{12} issues the trip decision since the fault stays inside Zone-1 area of the relay, and that is shown in Figure 5.9 (f). From the simulation results, it is observed that the VSC-HVDC system does not affect the Zone-1 operation of the relay R_{12} when the VSC-HVDC is connected at the bus-2 terminal, i.e., outside the boundary of Zone-1 area.

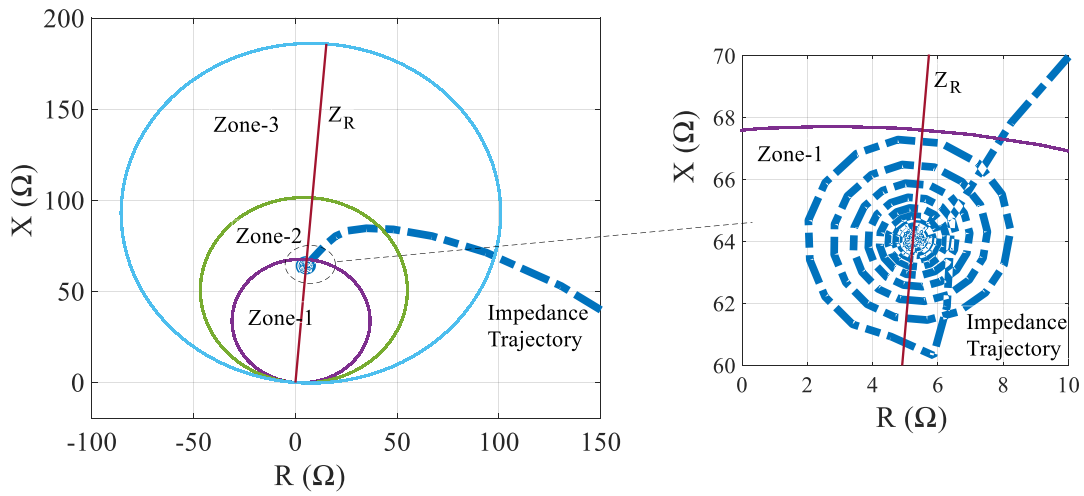
5.4.1.2 Phase-to-Phase Fault Condition

In this case, the performance of the relay is tested under the condition of phase-to-phase (A-B) fault occurs at 150 km distance from the bus-1 terminal in an AC system for both without and with VSC-HVDC system as shown in Figure 5.10 and 5.11. The fault is applied at $t = 1.0$ s, and the duration of the fault is 1.0 s.

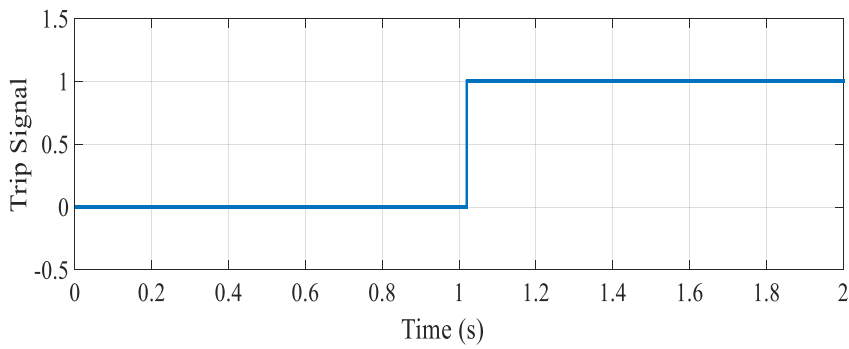
In case of A-B fault, the apparent impedance seen by the Zone-1 relay R_{12} is $64.27\angle 85.27^\circ \Omega$ for both without and with VSC-HVDC system, and that impedance trajectory is depicted in Figure 5.10 (a) and (b), 5.11 (a) and (b). In both cases, the VSC-HVDC influence on the response of Zone-1 relay is not significant. Hence, the relay will detect the fault and commands a trip decision without time delay for both the cases since the measured impedance falls within the Zone-1 area of relay R_{12} which can be seen in Figure 5.10 (c) and 5.11 (c). From the obtained results it is observed that the fault distance viewed by the Zone-1 relay R_{12} is not overestimated when the VSC-HVDC system is connected to the bus-2 terminal.



(a) Magnitude of fault impedance ($|Z_{ab}|$) during A-B fault.

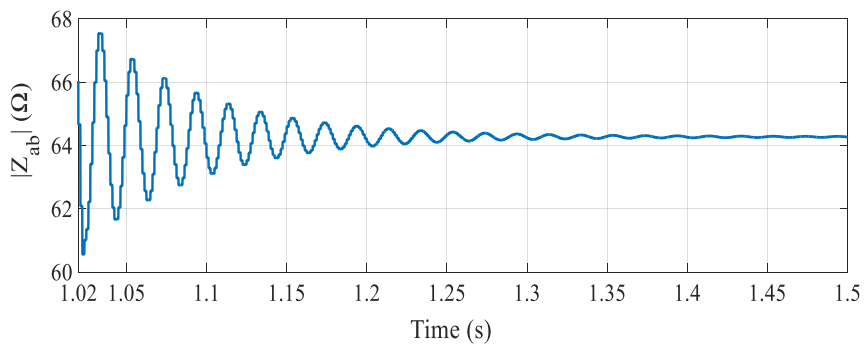


(b) Impedance trajectory during A-B fault.

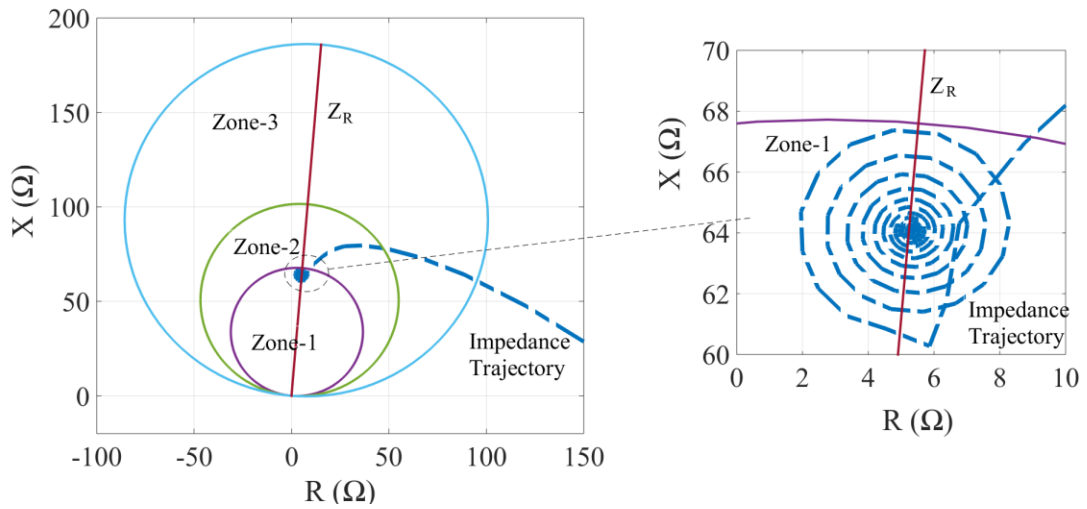


(c) Trip signal of relay R_{12} .

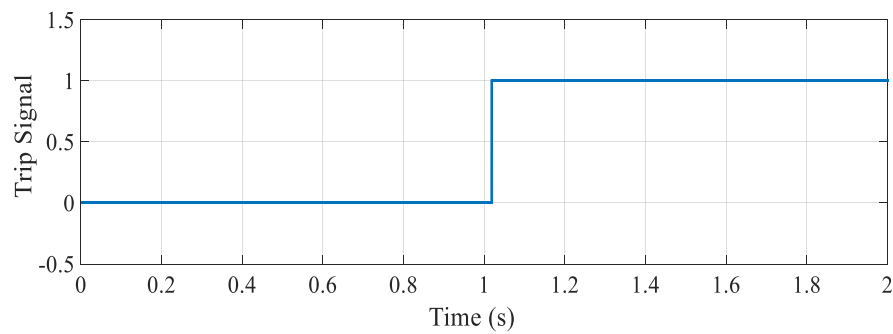
Figure 5.10 The performance of the relay R_{12} under the phase-to-phase (A-B) fault at 150 km distance from the bus-1 terminal in an AC system without VSC-HVDC.



(a) Magnitude of fault impedance ($|Z_{ab}|$) during A-B fault.



(b) Impedance trajectory during A-B fault.

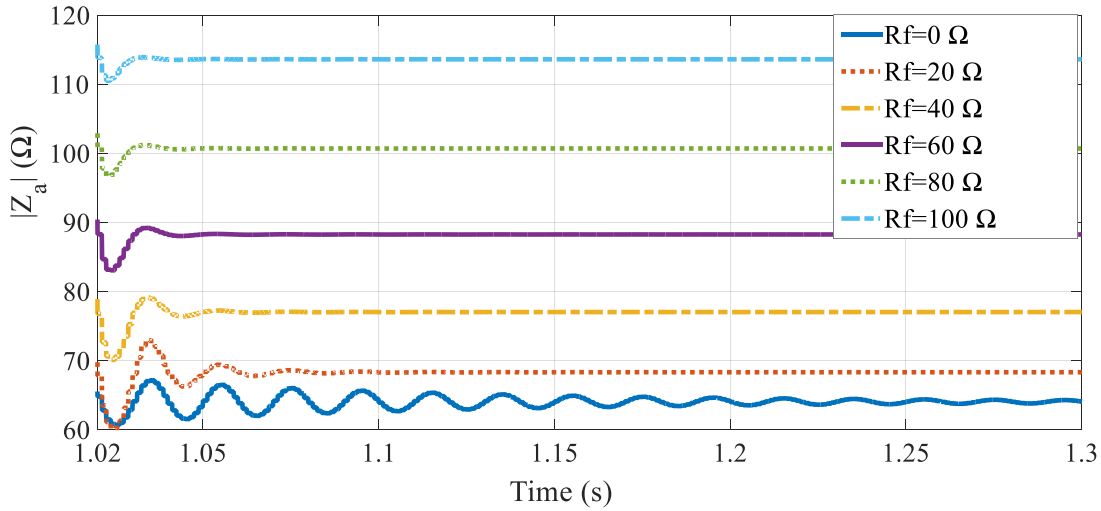


(c) Trip signal of relay R_{12} .

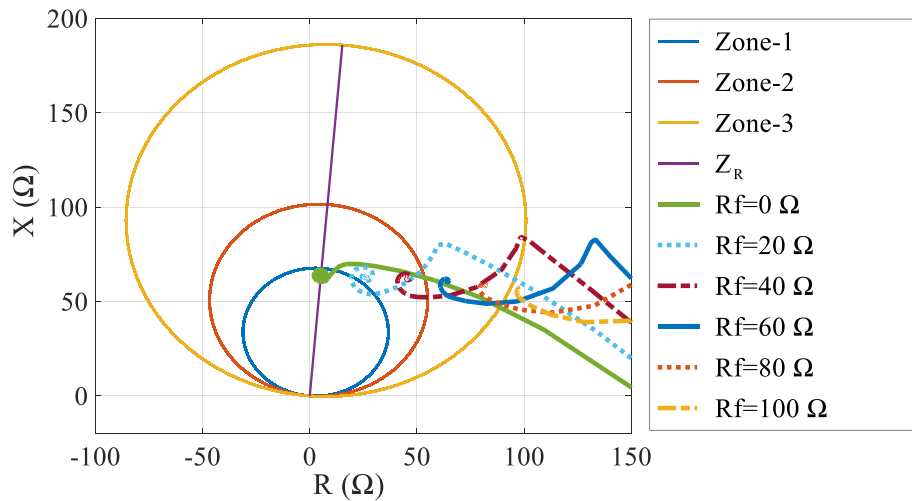
Figure 5.11 The performance of the relay R_{12} under the phase-to-phase (A-B) fault at 150 km distance from the bus-1 terminal in an AC system with VSC-HVDC.

5.4.1.3 Effect of Fault Resistance on Relay Performance under Phase-to-Ground Fault Condition

Distance relays can be called as either phase or ground relays. Fault resistance plays a significant role in the performance of ground relays. It introduces an error in the distance estimation obtained with the mho characteristic-based distance relay since the distance between the relay location and the fault point is not necessarily proportional to the impedance seen by the relay. Ground faults have higher fault resistance that causes the accuracy of the ground relays are affected significantly.



(a) Magnitude of fault impedance ($|Z_a|$) during A-G fault.

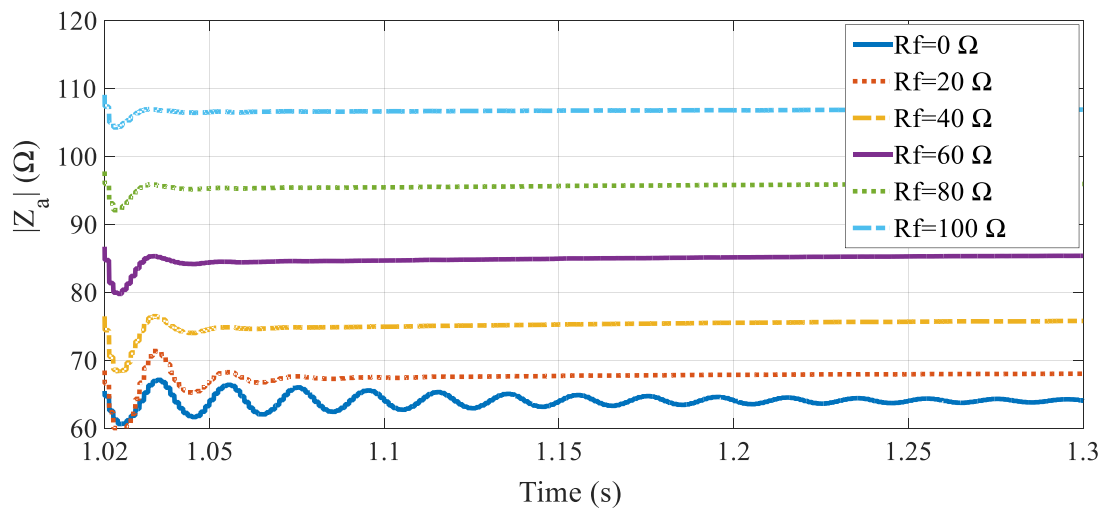


(b) Impedance trajectory during to A-G fault.

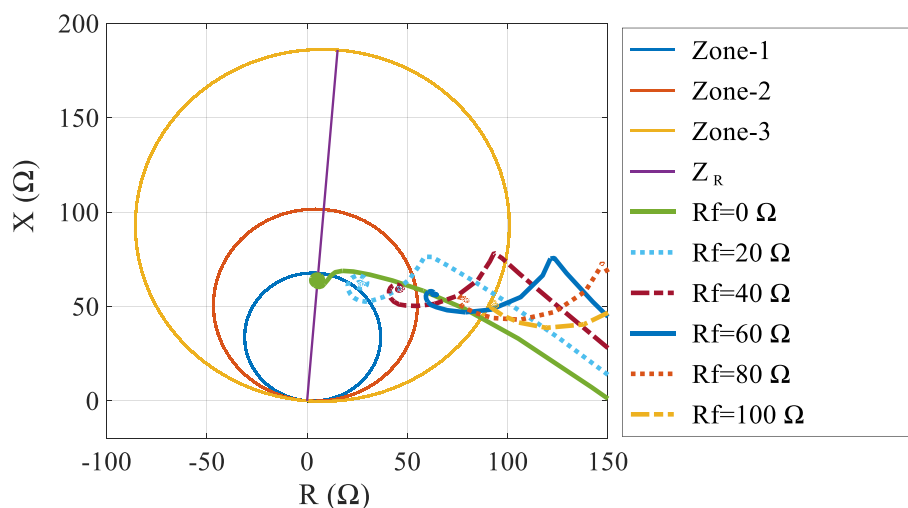
Figure 5.12 Effect of fault resistance (R_f) on relay R_{12} performance under A-G fault at 150 km distance from the bus-1 terminal in an AC system without VSC-HVDC.

In this case, the effect of fault resistance on ground relay performance is analyzed under phase-to-ground (A-G) fault occurs at 150 km distance from the bus-1 terminal in an AC system both without and with VSC-HVDC. The phase-to-ground fault (A-G) is applied at 150 km distance from the bus-1 terminal, i.e., relay R_{12} location. The fault resistance (R_f) considered for the simulation study is 20 Ω , 40 Ω , 60 Ω , 80 Ω and 100 Ω . The effect of fault resistance on the performance of Zone-1 relay in an AC system

both without and with VSC-HVDC is shown in Figure 5.12 and 5.13. The fault has occurred on inside the Zone-1 area of relay R_{12} , but the impedance trajectory which is shown in the R-X plot has increased towards the positive resistance axis due to the increment of fault resistance. Therefore, Zone-1 relay will not detect the fault when the fault resistance variation goes higher.



(a) Magnitude of fault impedance ($|Z_a|$) during A-G fault.



(b) Impedance trajectory during to A-G fault.

Figure 5.13 Effect of fault resistance (R_f) on relay R_{12} performance under A-G fault at 150 km distance from the bus-1 terminal in an AC system with VSC-HVDC.

The apparent impedance seen by the Zone-1 relay R_{12} for different fault resistances is given in Table 5.2. It can be seen from Table 5.2 that the measured impedance value is less in case of an AC system with VSC-HVDC when compared to without VSC-HVDC case. Also, the reactance value gets decreased when the fault resistance increases due to the phase angle between the voltage and current decreases.

Table 5.2 The apparent impedance (Z_a) seen by the Zone-1 relay for the A-G fault with various fault resistance (R_f) at 150 km distance from the bus-1 terminal in an AC system both without and with VSC-HVDC.

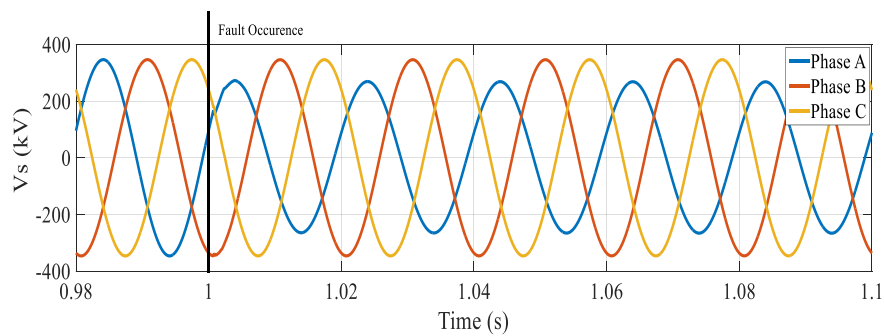
| Fault Resistance R_f (Ω) | Z_a (Ω) without VSC-HVDC | Z_a (Ω) with VSC-HVDC |
|--|---|---|
| 0 | $64.08 \angle 85.42^\circ =$ $5.116850669 + j63.87538054$ | $64.05 \angle 85.44^\circ =$ $5.092168553 + j63.84725773$ |
| 20 | $68.34 \angle 67.73^\circ =$ $25.89892385 + j63.24240147$ | $68.16 \angle 65.76^\circ =$ $27.9837501 + j62.15058592$ |
| 40 | $77.05 \angle 53.74^\circ =$ $45.57125259 + j62.12860402$ | $75.94 \angle 51.42^\circ =$ $47.3566971 + j59.3651989$ |
| 60 | $88.28 \angle 43.36^\circ =$ $64.18434226 + j60.6112911$ | $85.51 \angle 41.12^\circ =$ $64.41758001 + j56.23464667$ |
| 80 | $100.72 \angle 35.68^\circ =$ $81.81356394 + j58.74571607$ | $96.04 \angle 33.62^\circ =$ $79.97519903 + j53.17564424$ |
| 100 | $113.63 \angle 29.88^\circ =$ $98.52524377 + j56.60877352$ | $106.96 \angle 28.11^\circ =$ $94.34349528 + j50.39589763$ |

5.4.2 Fault on Zone-2 Area of Relay

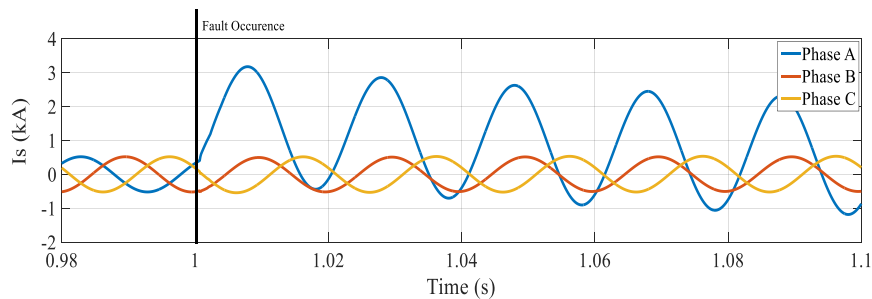
In this section, the performance of the distance relay is tested under the condition of fault on Zone-2 area of a relay R_{12} in an AC system both without and with VSC-HVDC. It is found that the distance relay mal-operates under such fault conditions. Therefore, the simulation study is carried out to mitigate the mal-operation of the relay using VSC-HVDC control action. Also, the effect of fault resistance on Zone-2 relay performance is analyzed.

5.4.2.1 Phase-to-Ground Fault Condition

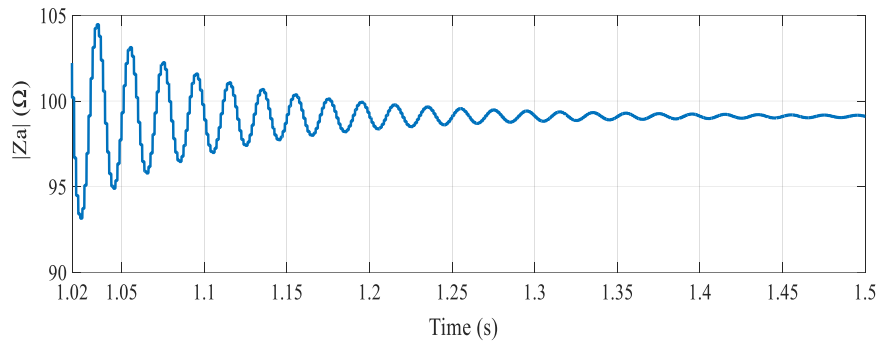
In the first case, the performance of the relay R_{12} is tested under the condition of phase A to ground fault at 30 km distance from the bus-2 terminal (i.e., 230 km distance from the relay location) in an AC system without VSC-HVDC as shown in Figure 5.14. The A-G fault is applied at $t = 1.0$ s, and the duration of the fault is 1.0 s. After the occurrence of the fault, the faulted phase voltage is reduced, and the reduction of RMS voltage is 7.5 %, and also the peak value of the faulted phase current has increased to 3.17 kA which is shown in Figure 5.14 (a) and (b). The impedance seen by relay gives an oscillation and settles at $99.10\angle 85.53^\circ \Omega$ when the AC system operated without VSC-HVDC, and that impedance trajectory is shown in Figure 5.14 (c) and (d). The fault impedance falls within the region of Zone-2 area of the relay R_{12} . Therefore, the Zone-2 relay commands the trip decision with the time delay of 0.4 s which can be seen in Figure 5.14 (e).



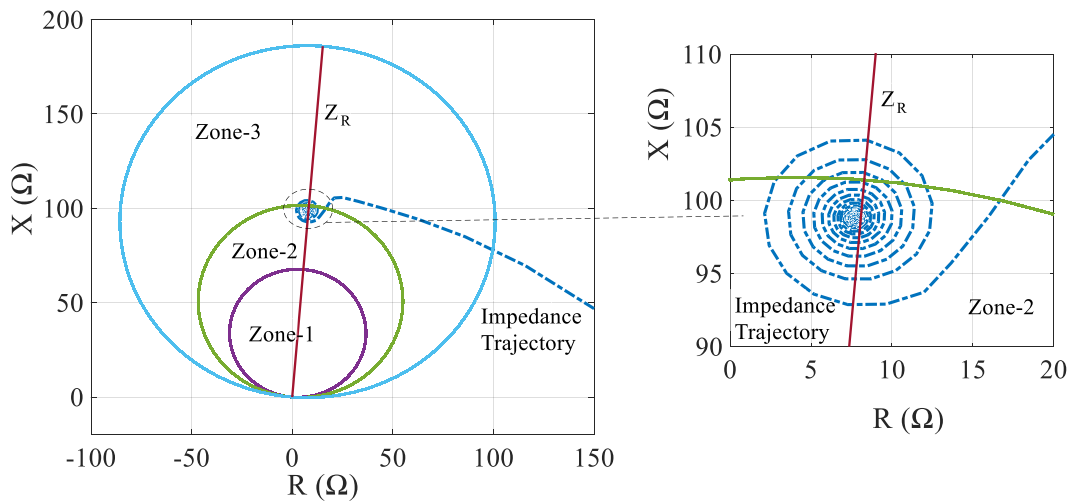
(a) Three-phase AC voltage (V_S) at bus-1 terminal.



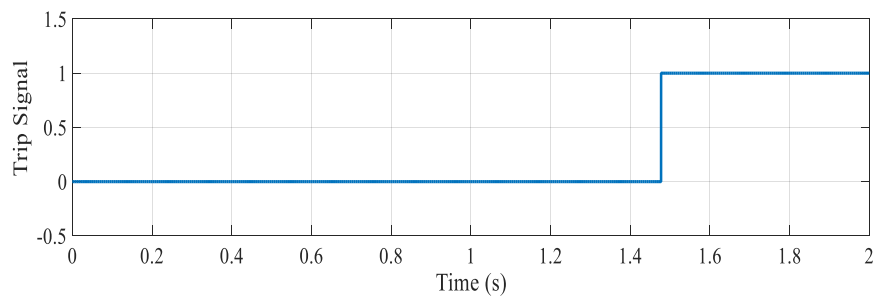
(b) Three-phase AC current (I_S) at bus-1 terminal.



(c) Magnitude of phase A fault impedance ($|Z_a|$) during A-G fault.



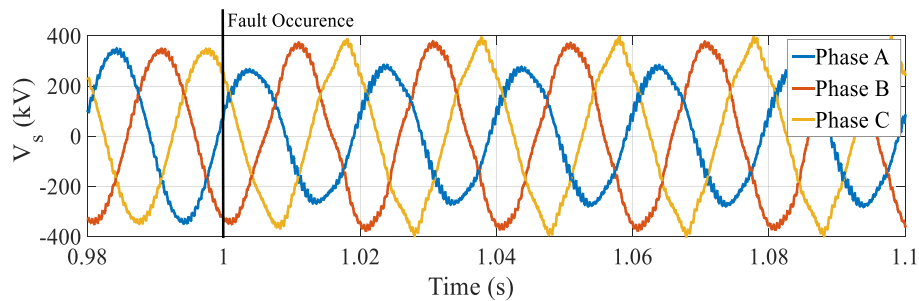
(d) Impedance trajectory during A-G fault.



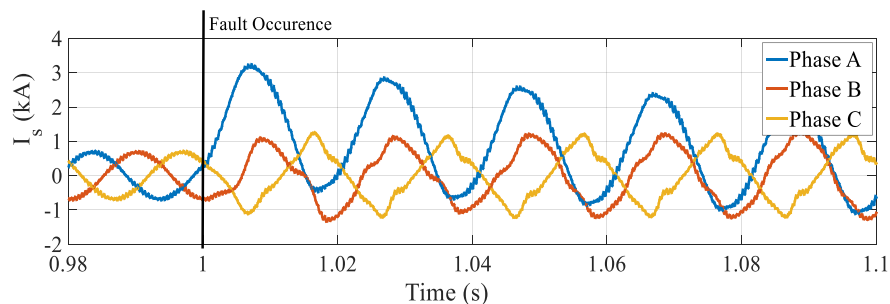
(e) Trip signal of relay R_{12} .

Figure 5.14 The performance of the relay R_{12} under the phase-to-ground (A-G) fault at 30 km distance from the bus-2 terminal in an AC system without VSC-HVDC.

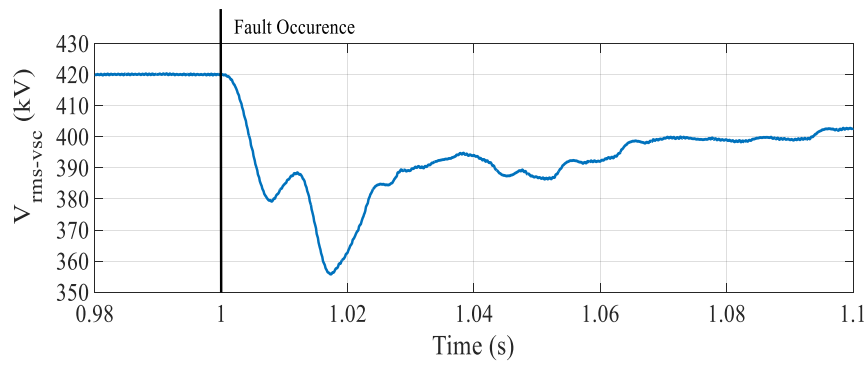
In the second case, the performance of the relay R_{12} is tested under the condition of phase A to ground fault at 30 km distance from the bus-2 terminal in an AC system with VSC-HVDC system as shown in Figure 5.15. The fault data is the same as the previous case. After fault occurring, the variation of the faulted phase voltage and current are very less when compared to the previous case (for example, the RMS voltage has decreased up to 2 % only) as can be seen in Figure 5.15 (a) and (b). This can happen due to the VSC-HVDC connection since it tries to inject the active and reactive power into the AC system which is depicted in Figure 5.15 (c) and (d). Therefore, the apparent impedance seen by the relay has raised to $106.32 \angle 84.72^\circ \Omega$ after an oscillation during the fault, and that impedance trajectory is shown in Figure 5.15 (e) and (f). This fault impedance has gone outside the boundary of the zone 2 relay R_{12} . Figure 5.15 (g) implies that no trip signal has given when the fault occurs on Zone-2 area of relay R_{12} in an AC system with VSC-HVDC since the impedance viewed by relay does not fall inside the zone of protection. Therefore, Zone-2 fault is cleared by Zone-3 time delay (i.e., 1 second), that causes the protection miscoordination can occur in the system.



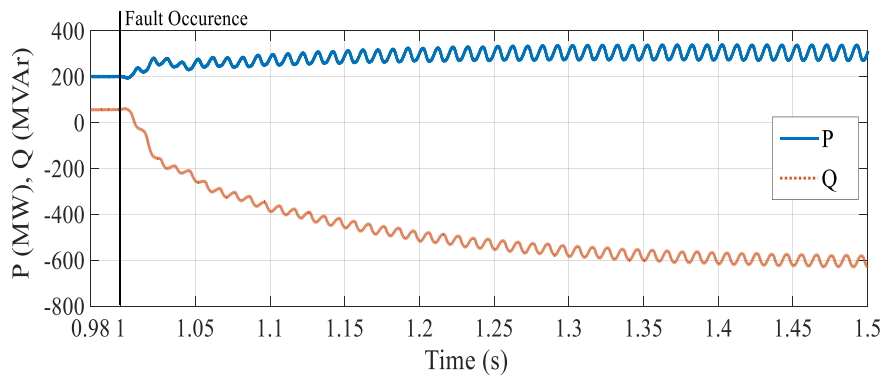
(a) Three-phase AC voltage (V_s) at bus-1 terminal.



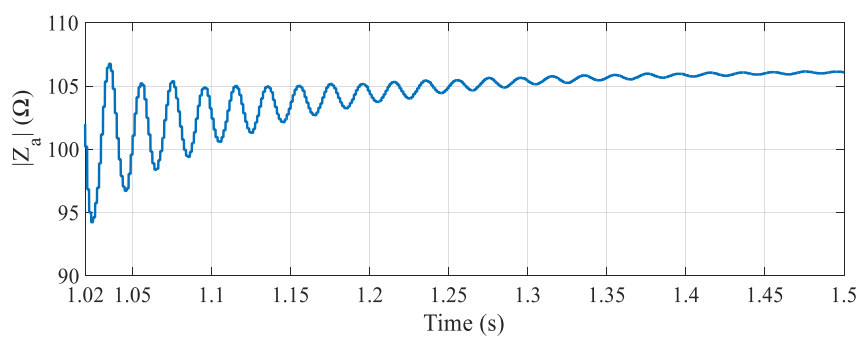
(b) Three-phase AC current (I_s) at bus-1 terminal.



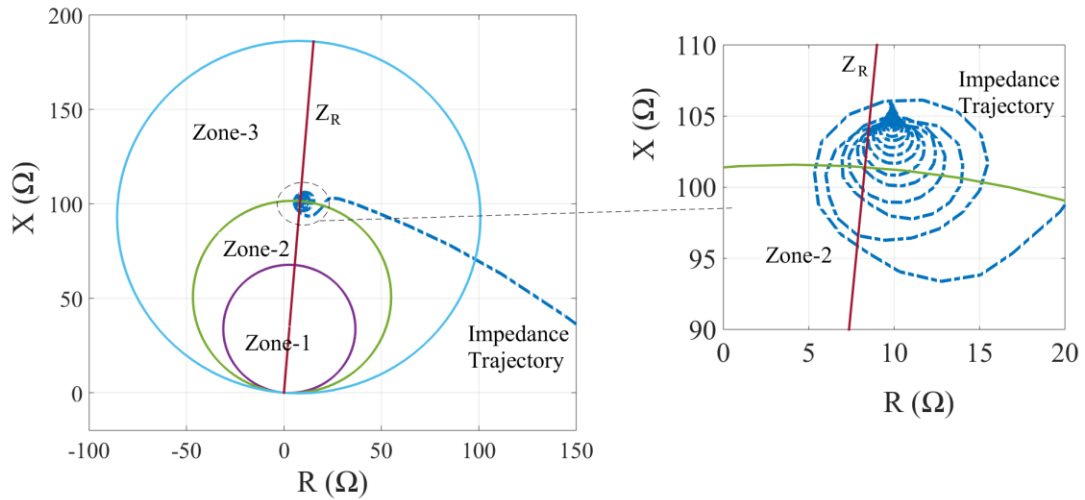
(c) RMS value of AC line voltage at grid side VSC (bus-2 connection point).



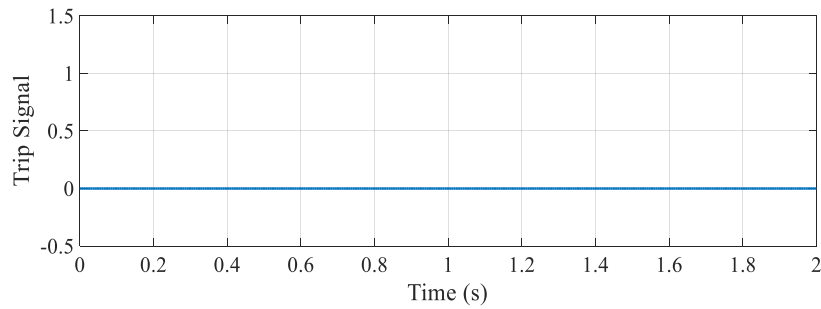
(d) Active Power (P) and reactive power (Q) at grid side VSC (bus-2 connection point).



(e) Magnitude of phase A fault impedance ($|Z_a|$) during A-G fault.



(f) Impedance trajectory during A-G fault.



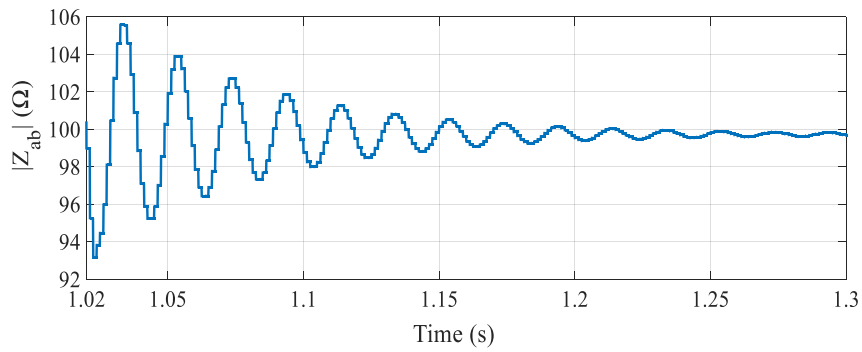
(g) Trip signal of relay R_{12} .

Figure 5.15 The performance of the relay R_{12} under the phase-to-ground (A-G) fault at 30 km distance from the bus-2 terminal in an AC system with VSC-HVDC.

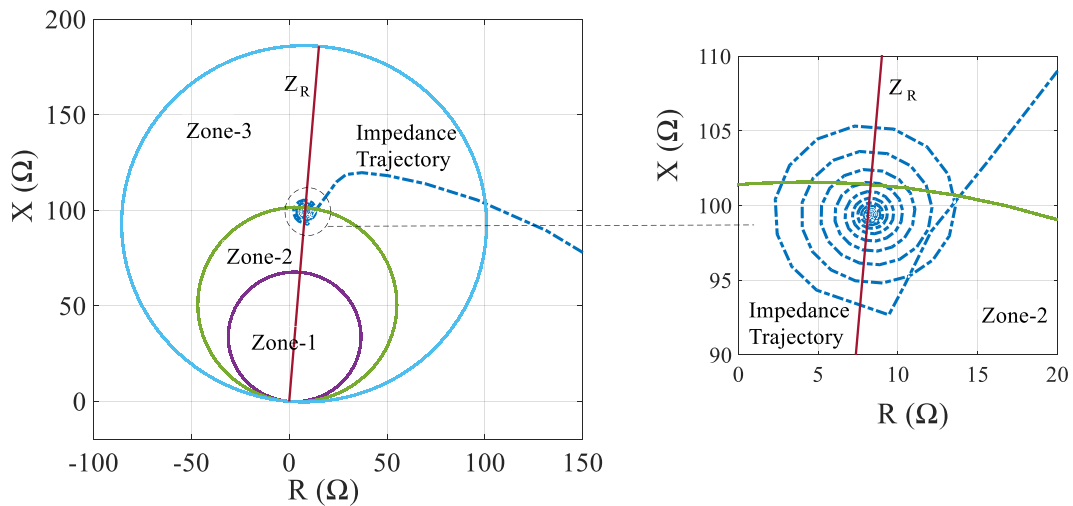
5.4.2.2 Phase-to-Phase Fault Condition

In this case, the performance of the relay R_{12} is tested under the condition of phase-to-phase (A-B) fault occurs at 30 km distance from the bus-2 terminal in an AC system both without and with VSC-HVDC system as shown in Figure 5.16 and 5.17. The fault is applied at $t = 1.0$ s, and the duration of the fault is 1.0 s. The apparent impedance seen by relay R_{12} has increased from $99.73 \angle 85.20^\circ \Omega$ (without VSC-HVDC) to $108.49 \angle 81.79^\circ \Omega$ (with VSC-HVDC) during fault period due to the injection of active and reactive power by VSC-HVDC connection. When the AC system operated with the VSC-HVDC, the A-B fault which would otherwise be sensed by the distance relay gets

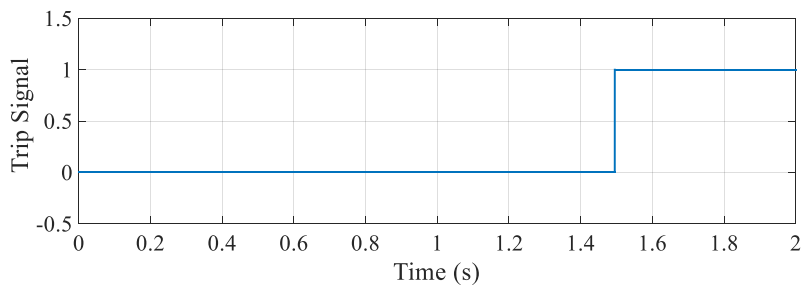
failed to get detected since the sensed impedance does not fall inside the predetermined zone of protection, leading to the maloperation of the distance relays.



(a) Magnitude of fault impedance ($|Z_{ab}|$) during A-B fault.

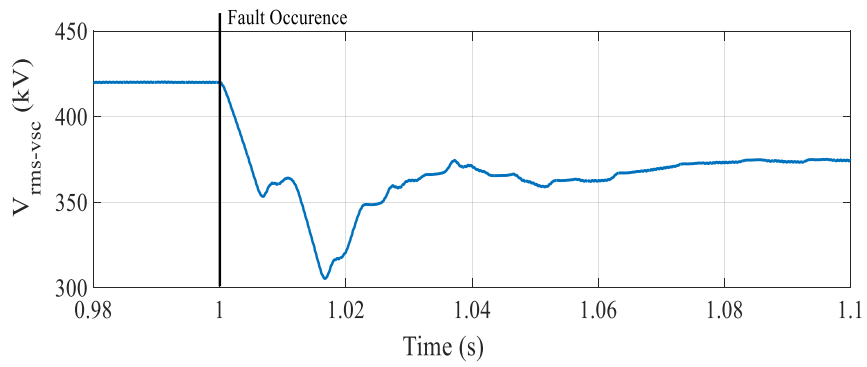


(b) Impedance trajectory during A-B fault.

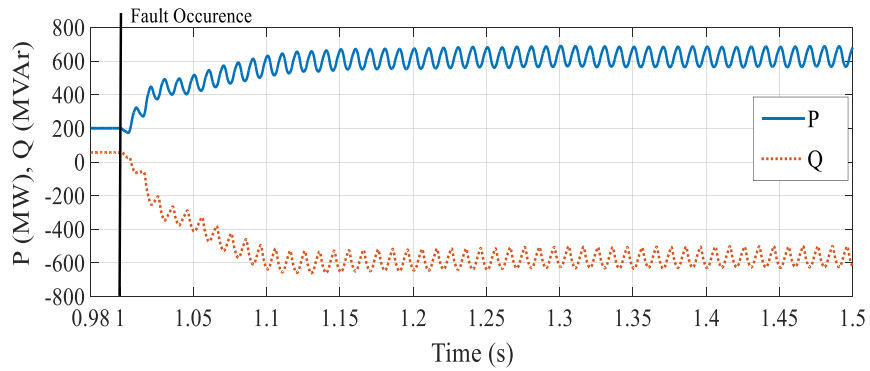


(c) Trip signal of relay R_{12} .

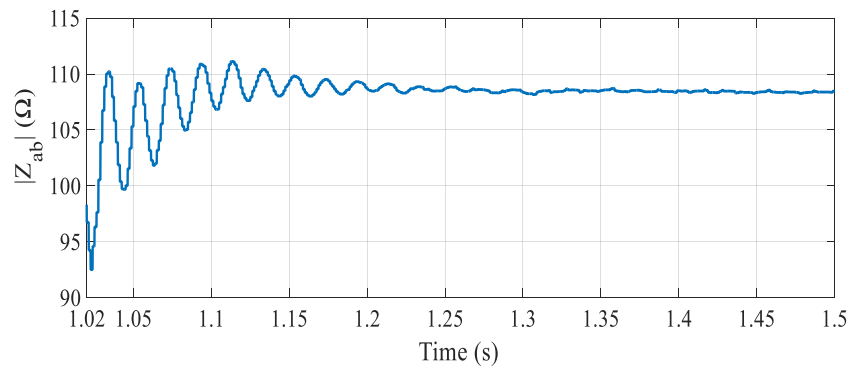
Figure 5.16 The performance of the relay R_{12} under A-B fault at 30 km distance from the bus-2 terminal in an AC system without VSC-HVDC.



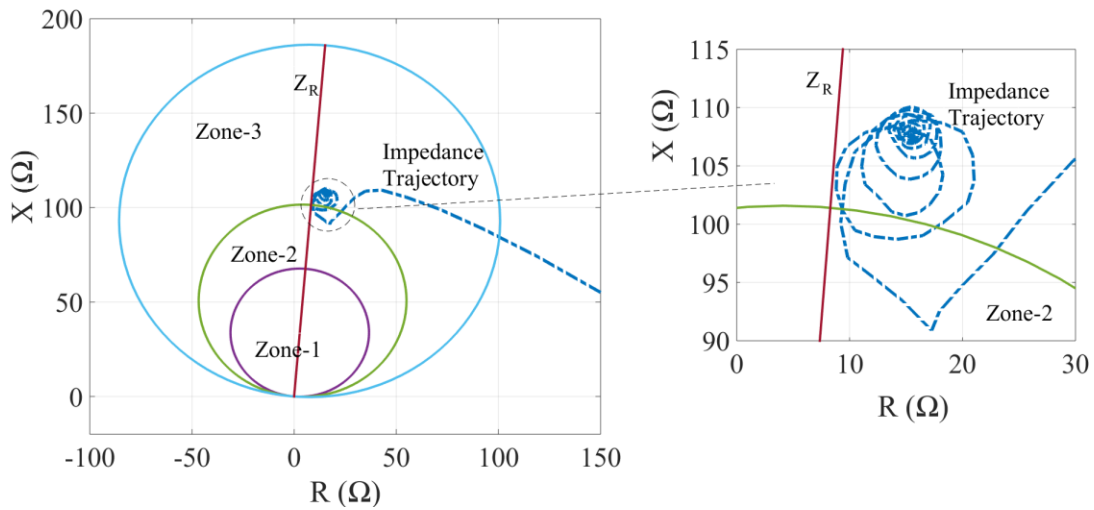
(a) RMS value of AC line voltage at grid side VSC (bus-2 connection point).



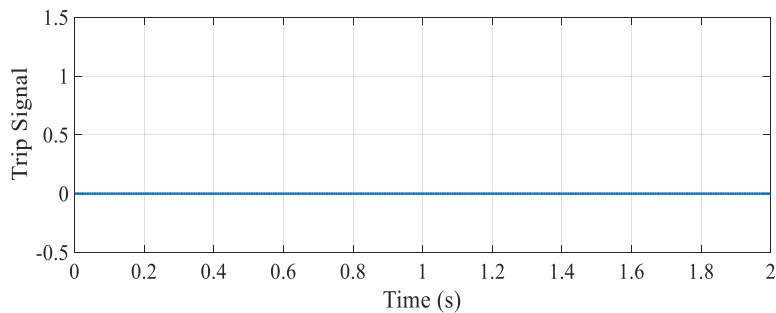
(b) Active power (P) and reactive power (Q) at grid side VSC (bus-2 connection point).



(c) Magnitude of fault impedance ($|Z_{ab}|$) during A-B fault.



(d) Impedance trajectory during A-B fault.



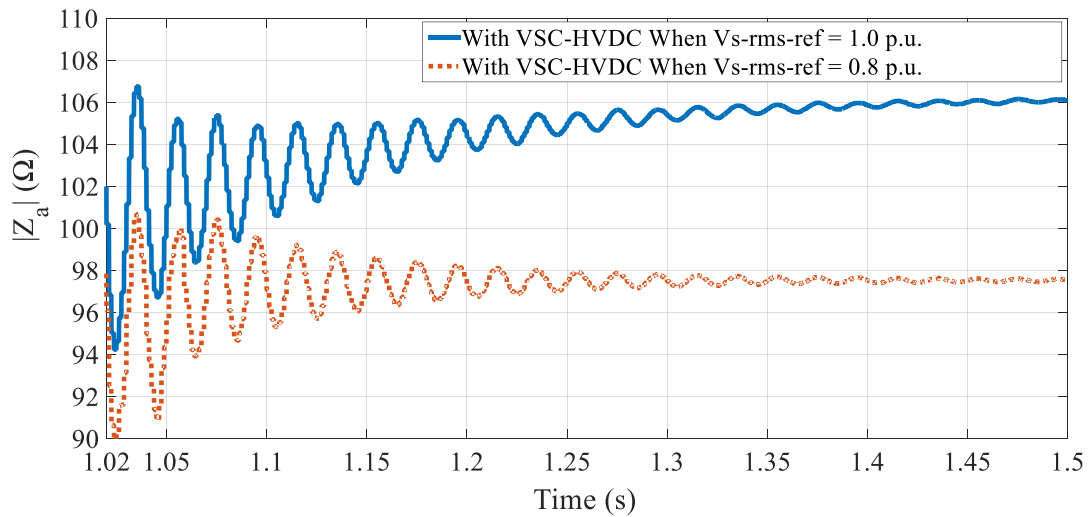
(e) Trip signal of relay R_{12} .

Figure 5.17 The performance of the relay R_{12} under A-B fault at 30 km distance from the bus-2 terminal in an AC system with VSC-HVDC.

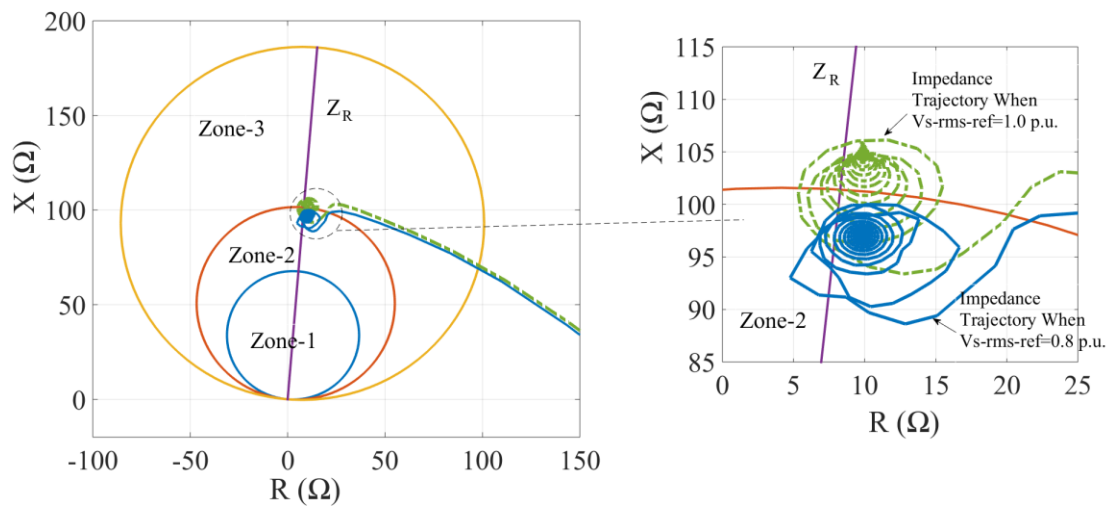
From the obtained results of the phase and ground faults, it is observed that the fault distance viewed by the relay is over-estimated when the VSC-HVDC system connected in-between the relay location and the fault point. Therefore, Zone-2 fault is pushed to the Zone-3 fault, and it is cleared with higher time delay, i.e., the time delay is increased from 0.4 s to 1 s. Hence, the system cannot maintain stability if the fault clearing time exceeds the critical clearing time.

5.4.2.3 Relay Performance under Change in VSC AC Voltage Reference Input

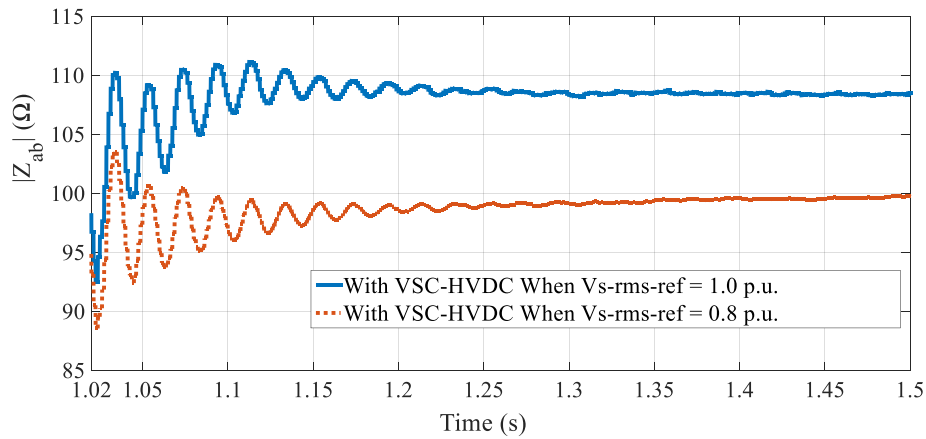
In this case, the performance of the relay R_{12} is tested under the condition of phase-to-ground (A-G) and phase-to-phase (A-B) fault occurs at 30 km distance from bus-2 terminal (i.e., 230 km distance from the relay location) in an AC system with VSC-HVDC considering VSC AC voltage reference ($V_{s-rms-ref}$) input variations as shown in Figure 5.18. The decoupled d-q controller of the VSC-HVDC is shown in Figure 3.11, and its modeling has explained in section 3.3.



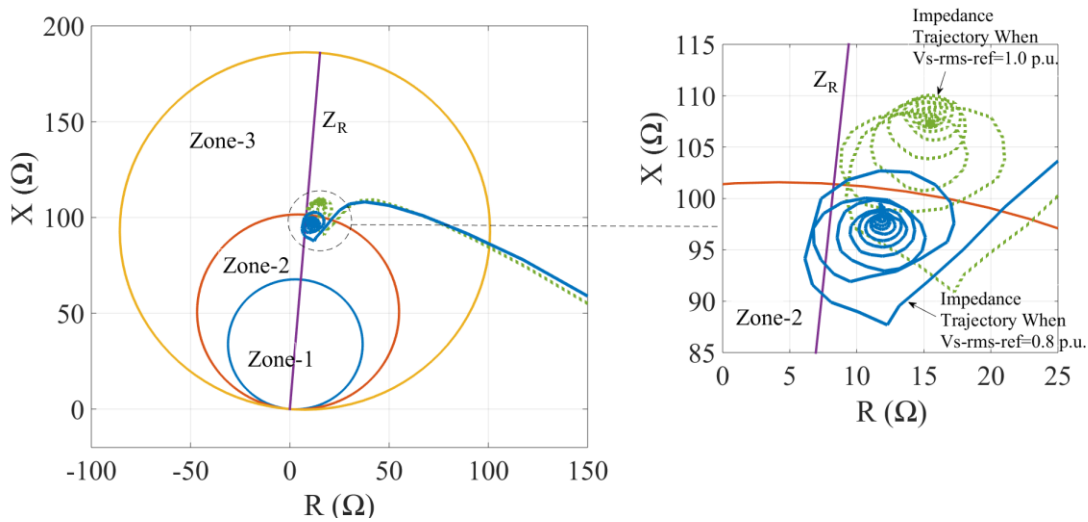
(a) Magnitude of fault impedance ($|Z_a|$) during A-G fault.



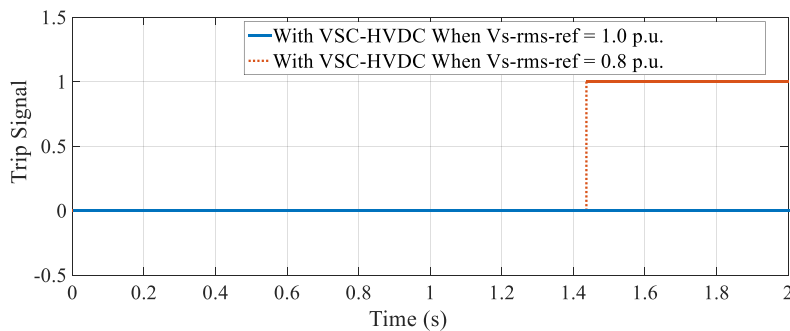
(b) Impedance trajectory during A-G fault.



(c) Magnitude of fault impedance ($|Z_{ab}|$) during A-B fault.



(d) Impedance trajectory during A-B fault.



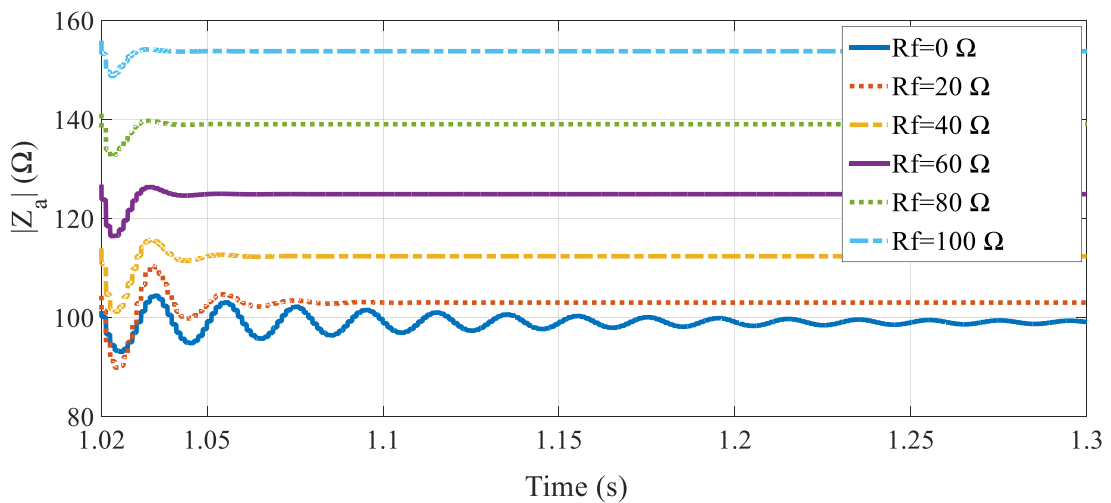
(e) Trip signal of relay R_{12} .

Figure 5.18 The performance of the relay R_{12} under A-G and A-B fault at 30 km distance from the bus-2 terminal in an AC system with VSC-HVDC for the different value of $V_{s-rms-ref}$ input during fault period.

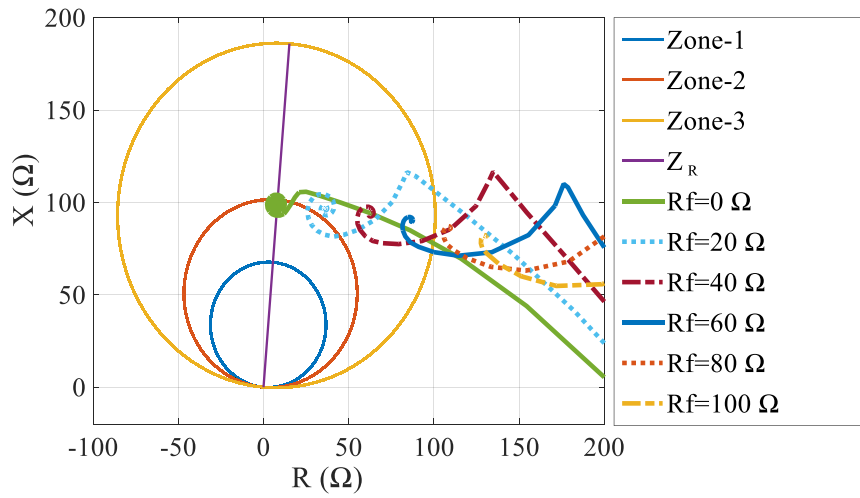
The apparent impedance seen by the relay R_{12} is $106.32\angle 84.72^\circ \Omega$ for A-G fault and $108.49\angle 81.79^\circ \Omega$ for A-B fault when the VSC AC voltage reference ($V_{s-rms-ref}$) input is 1.0 per unit. The apparent impedance seen by the relay is $97.54\angle 84.19^\circ \Omega$ for A-G fault and $99.8\angle 83.20^\circ \Omega$ for A-B fault when the $V_{s-rms-ref}$ input is step changed from 1.0 to 0.8 per unit during fault period. The reactive power at the bus-2 terminal is adjusted by step changing the $V_{s-rms-ref}$ input from 1.0 to 0.8 per unit during fault period, that causes the trajectory of the apparent impedance falls inside the Zone-2 area of relay R_{12} . Therefore, the relay will detect the fault and command the trip decision under such fault conditions. This method can be applied to mitigate the maloperation of the relay when the VSC-HVDC system connected in-between the fault point and the relay location.

5.4.2.4 Effect of Fault Resistance on Relay Performance under Phase-to-Ground Fault Condition

The fault resistance has a significant influence on the performance of the ground fault relays. In this case, the effect of fault resistance on ground relay performance is analyzed under phase-to-ground (A-G) fault occurs at 30 km distance from the bus-2 terminal in an AC system both without and with VSC-HVDC as shown in Figure 5.19 and 5.20. The A-G fault is applied at $t = 1.0$ s, and the duration of the fault is 1.0 s. The fault resistance (R_f) considered for the simulation study is 20Ω , 40Ω , 60Ω , 80Ω , and 100Ω .



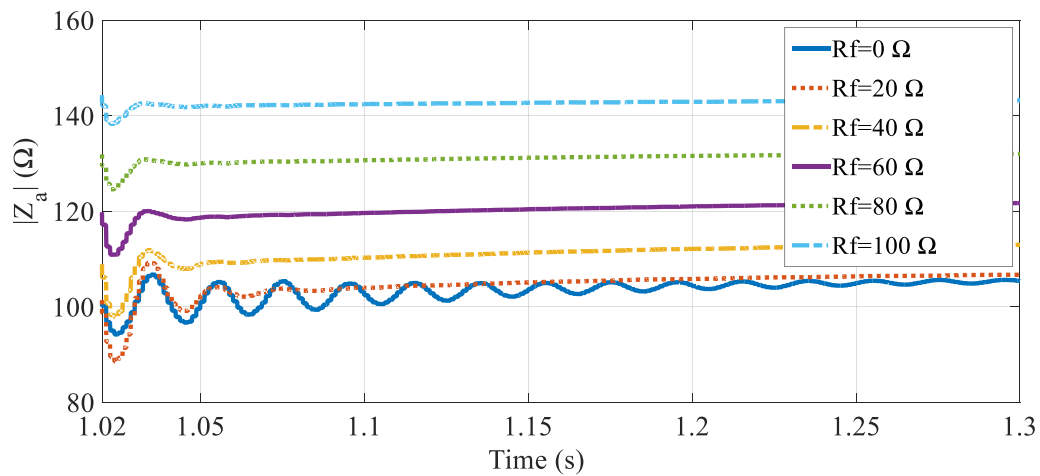
(a) Magnitude of fault impedance ($|Z_a|$) during A-G fault.



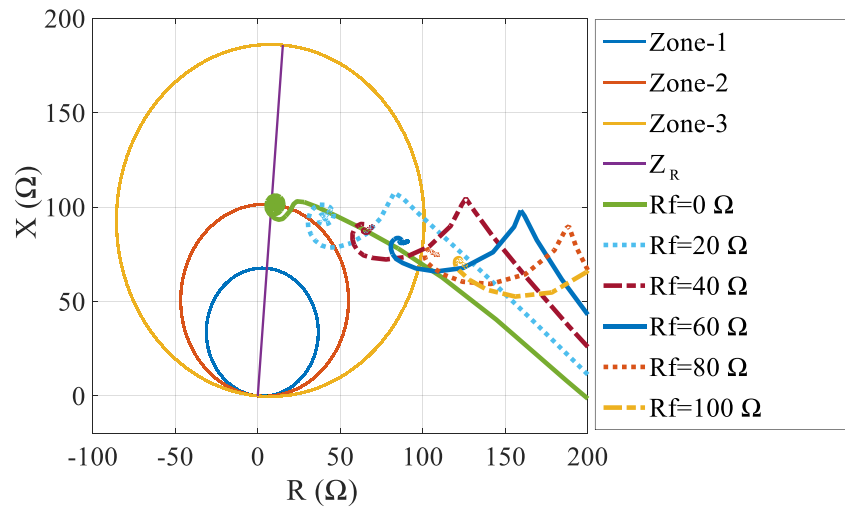
(b) Impedance trajectory during A-G fault.

Figure 5.19 Effect of fault resistance (R_f) on relay R_{12} performance under A-G fault at 30 km distance from the bus-2 terminal in an AC system without VSC-HVDC.

The phase-to-ground (A-G) fault is applied on inside the Zone-2 area of the relay R_{12} . But, the apparent impedance seen by the relay has gone outside the Zone-2 area of the relay R_{12} due to the increment of the fault resistance which can be seen in Figure 5.19 and 5.20. The apparent impedance (Z_a) seen by the Zone-2 relay for the A-G fault with various fault resistance (R_f) at 30 km distance from the bus-2 terminal in an AC system both without and with VSC-HVDC is presented in Table 5.3.



(a) Magnitude of fault impedance ($|Z_a|$) during A-G fault.



(b) Impedance trajectory during A-G fault.

Figure 5.20 Effect of fault resistance (R_f) on relay R_{12} performance under A-G fault at 30 km distance from the bus-2 terminal in an AC system with VSC-HVDC.

Table 5.3 The apparent impedance (Z_a) seen by the Zone-2 relay for the A-G fault with various fault resistance (R_f) at 30 km distance from the bus-2 terminal in an AC system both without and with VSC-HVDC.

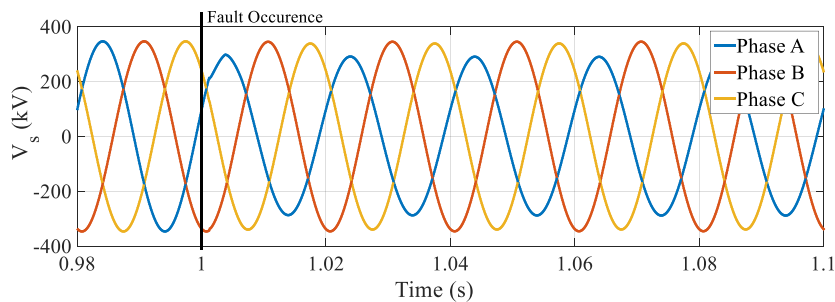
| Fault Resistance R_f (Ω) | Z_a (Ω) without VSC-HVDC | Z_a (Ω) with VSC-HVDC |
|--|--|--|
| 0 | $99.10\angle 85.53^\circ =$ $7.72356664+j98.79856537$ | $106.32\angle 84.72^\circ =$ $9.783886246+j105.8688716$ |
| 20 | $103.08\angle 69.50^\circ =$ $36.09937686+j96.55216927$ | $107.50\angle 65.89^\circ =$ $43.91265068+j98.12201134$ |
| 40 | $112.43\angle 56.30^\circ =$ $62.38115898+j93.53660195$ | $113.50\angle 52.19^\circ =$ $69.5806021+j89.67045116$ |
| 60 | $124.97\angle 46.03^\circ =$ $86.76437528+j89.9413369$ | $122.11\angle 42.10^\circ =$ $90.60266994+j81.86579444$ |
| 80 | $139.10\angle 38.13^\circ =$ $109.4177062+j85.88699298$ | $132.27\angle 34.46^\circ =$ $109.0594474+j74.84243335$ |
| 100 | $153.84\angle 31.99^\circ =$ $130.4779455+j81.50000815$ | $143.38\angle 28.69^\circ =$ $125.7772324+j68.83249384$ |

5.4.3 Fault on Zone-3 Area of Relay

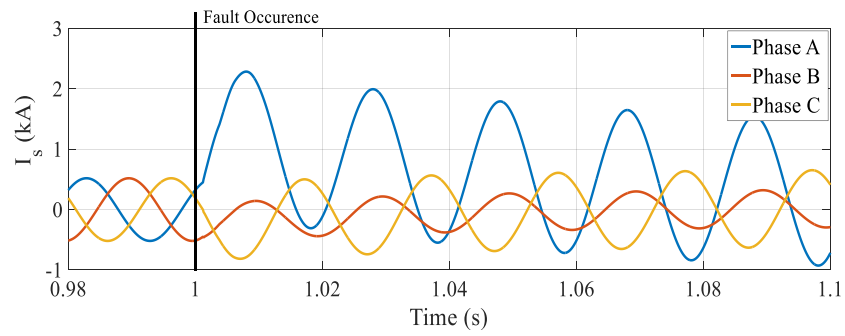
In this section, the performance of the relay R_{12} is tested under the condition of fault on Zone-3 area of a relay R_{12} in an AC system both without and with VSC-HVDC system. The simulation study is carried out on the relay R_{12} performance under the variation of the VSC AC voltage reference input during fault conditions. Also, the effect of fault resistance on Zone-3 ground relay performance is analyzed.

5.4.3.1 Phase-to-Ground Fault Condition

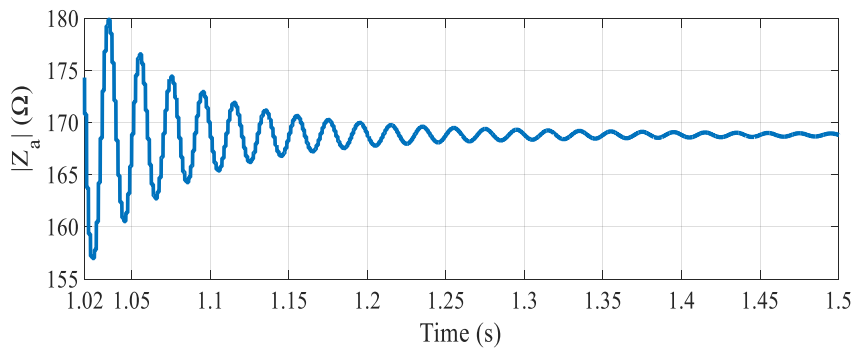
In this case, the performance of the relay is tested under the condition of phase A to ground (A-G) fault at 180 km distance from the bus-2 terminal (i.e., 380 km distance from the relay location) in an AC system both without and with VSC-HVDC system as shown in Figure 5.21 and 5.22. The A-G fault is applied at $t = 1.0$ s, and the duration of the fault is considered as 1.2 s. After fault occurring, the variation of the faulted phase voltage and current is very less in case of AC system with VSC-HVDC when compared to the without VSC-HVDC configuration. The RMS value of AC line voltage measured at the bus-1 terminal is decreased 1% in the case of AC system with VSC-HVDC whereas 6 % in case of AC system without VSC-HVDC configuration. It is caused by increment of the bus-2 voltage due to the action of reactive power injection into the AC system. Therefore, the apparent impedance seen by the relay has gone to $223\angle 79.68^\circ \Omega$ in the AC system with VSC-HVDC whereas $168.82\angle 85.72^\circ \Omega$ in case of AC system without VSC-HVDC configuration. The Zone-3 fault is pushed out of the protection zones of the relay R_{12} when the AC system is operated with VSC-HVDC. Therefore, the relay R_{12} will not issue a trip command since the measured impedance has not fallen inside the protection zones of the relay R_{12} .



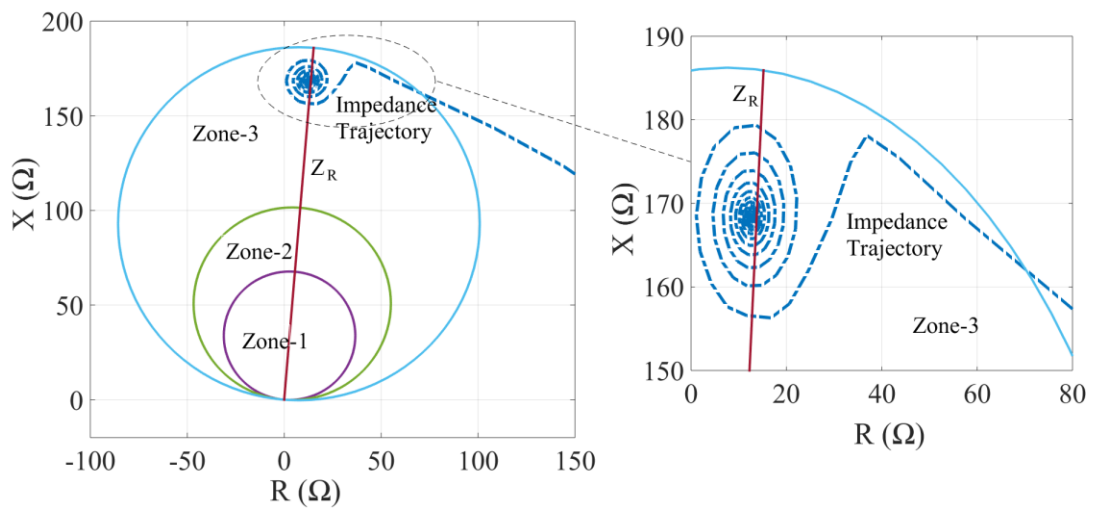
(a) Three-phase AC voltage (V_s) at bus-1 terminal.



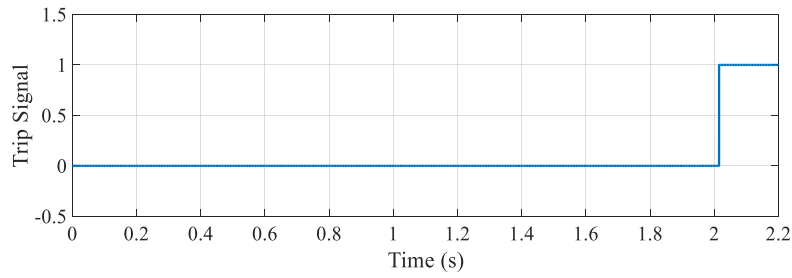
(b) Three-phase AC current (I_s) at bus-1 terminal.



(c) Magnitude of phase A fault impedance ($|Z_a|$) during A-G fault.

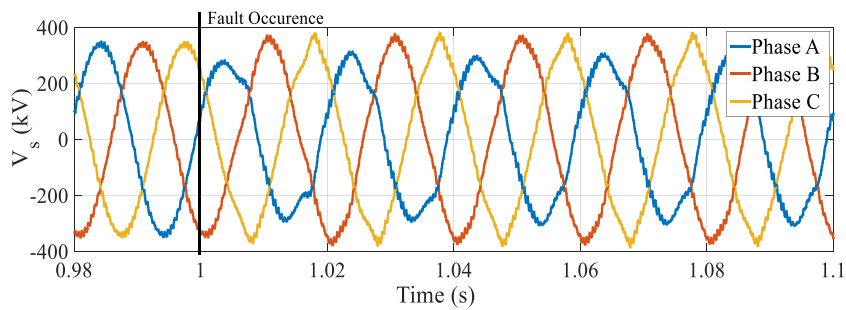


(d) Impedance trajectory during A-G fault.

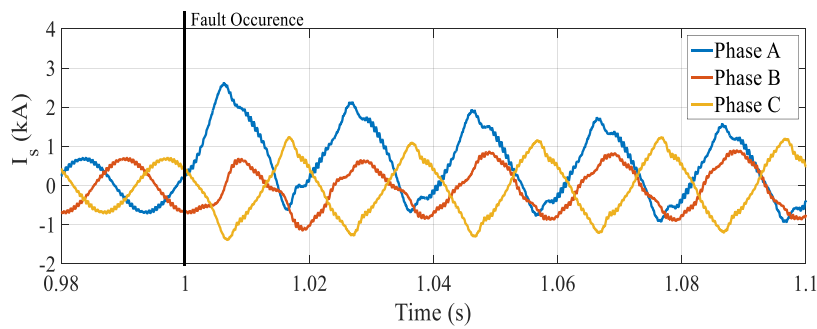


(e) Trip signal of relay R₁₂.

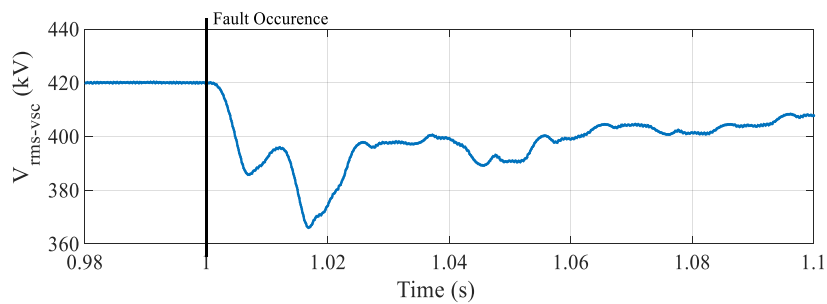
Figure 5.21 The performance of the relay R₁₂ under A-G fault at 180 km distance from the bus-2 terminal in an AC system without VSC-HVDC.



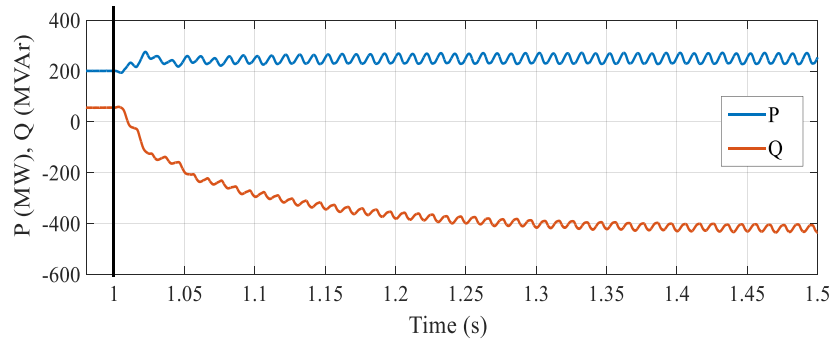
(a) Three-phase AC voltage (V_s) at bus-1 terminal.



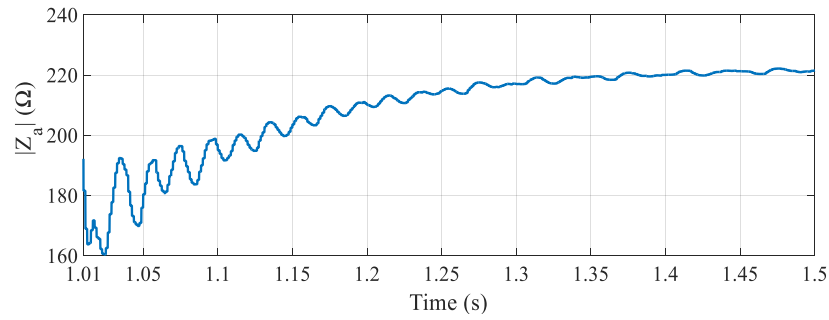
(b) Three-phase AC current (I_s) at bus-1 terminal.



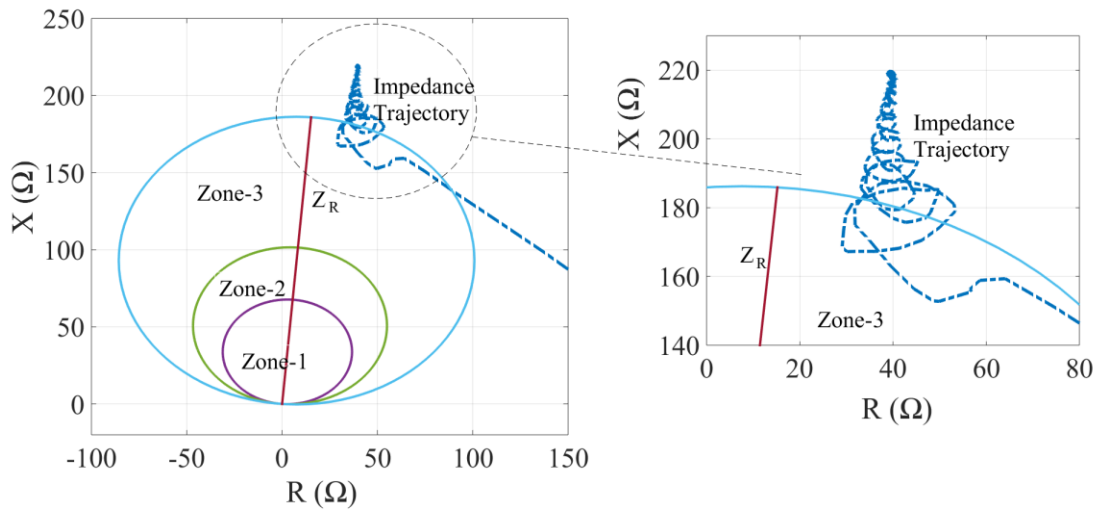
(c) RMS value of AC line voltage at grid side VSC (bus-2 connection point).



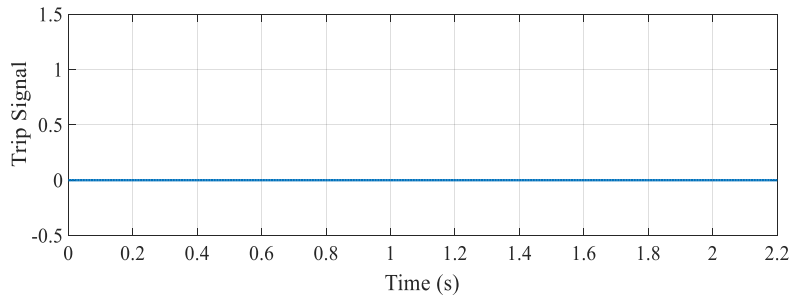
(d) Active power (P) and reactive power (Q) at grid side VSC (bus-2 connection point).



(e) Magnitude of phase A fault impedance ($|Z_a|$) during A-G fault.



(f) Impedance trajectory during A-G fault.

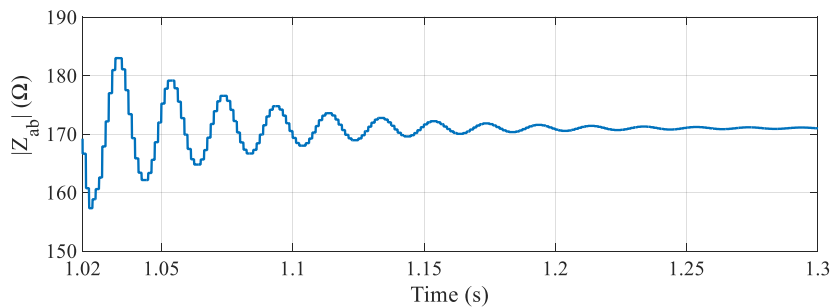


(g) Trip signal of relay R₁₂.

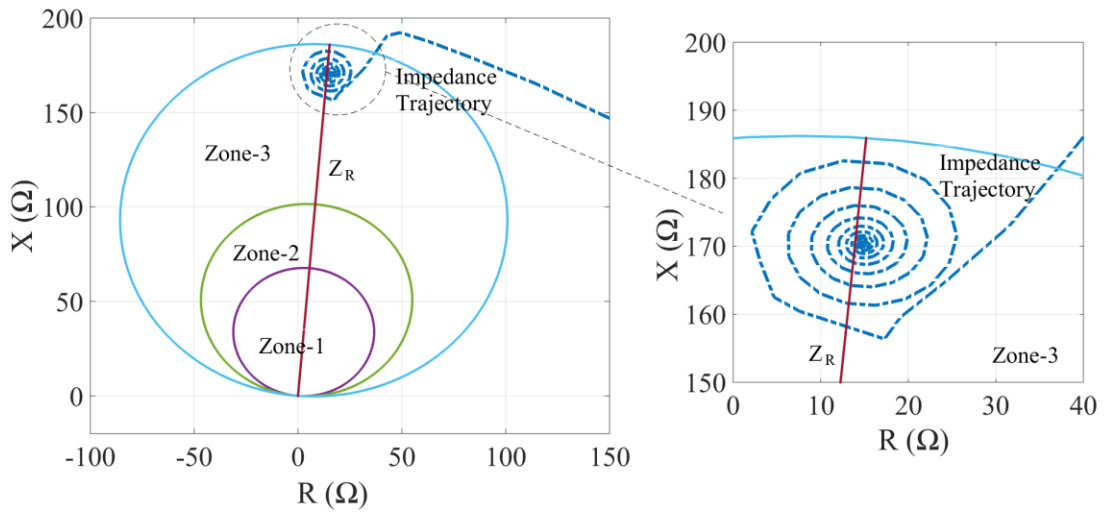
Figure 5.22 The performance of the relay R₁₂ under A-G fault at 180 km distance from the bus-2 terminal in an AC system with VSC-HVDC.

5.4.3.2 Phase-to-Phase Fault Condition

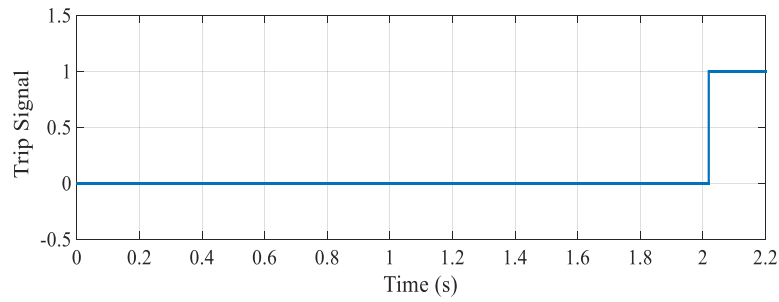
In this case, the performance of the relay is tested under the condition of phase-to-phase (A-B) fault at 180 km distance from the bus-2 terminal in an AC system both without and with VSC-HVDC system as shown in Figure 5.23 and 5.24. The fault is applied at $t = 1.0$ s, and the duration of the fault is 1.2 s. The apparent impedance seen by the relay R₁₂ is $439\angle 63.09^\circ \Omega$ in the case of AC system with VSC-HVDC whereas $171\angle 85.02^\circ \Omega$ in the case of AC system without VSC-HVDC configuration. This variation happens due to the injection of active and reactive power. The fault impedance has moved outside the protection zones of the relay R₁₂ due to which the relay R₁₂ remains non-operative for the fault on Zone-3 area of the relay in the AC system with VSC-HVDC link operation.



(a) Magnitude of fault impedance ($|Z_{ab}|$) during A-B fault.

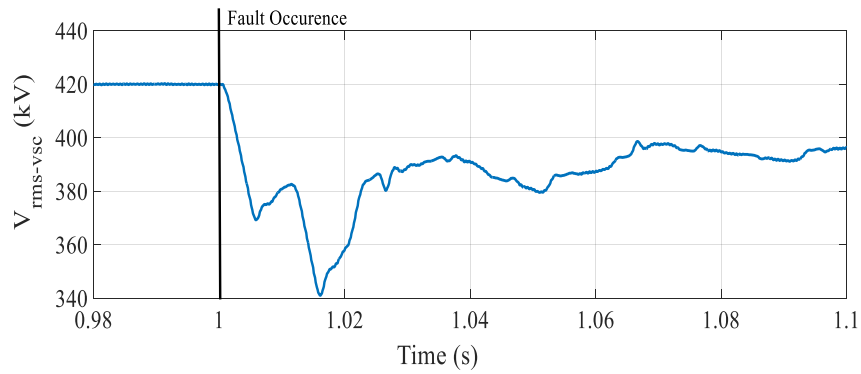


(b) Impedance trajectory during A-B fault.

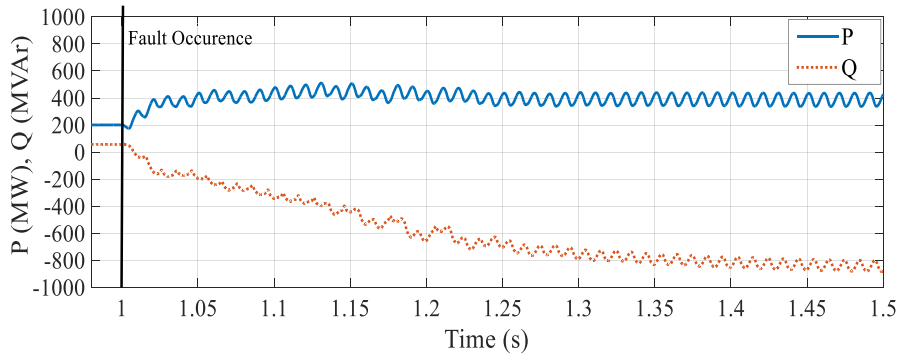


(c) Trip signal of relay R_{12} .

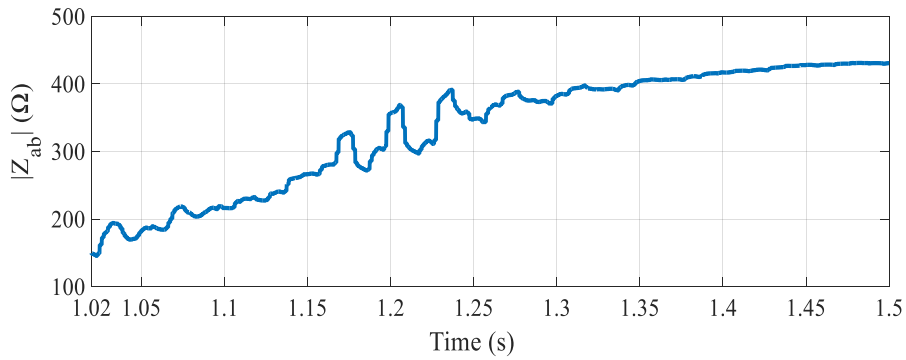
Figure 5.23 The performance of the relay R_{12} under A-B fault at 180 km distance from the bus-2 terminal in an AC system without VSC-HVDC.



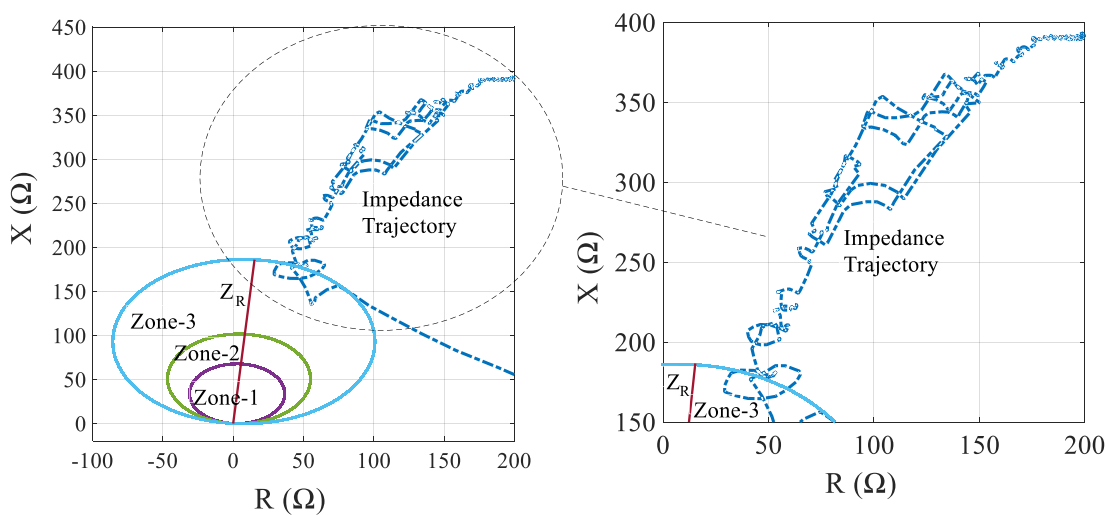
(a) RMS value of AC line voltage at grid side VSC (bus-2 connection point).



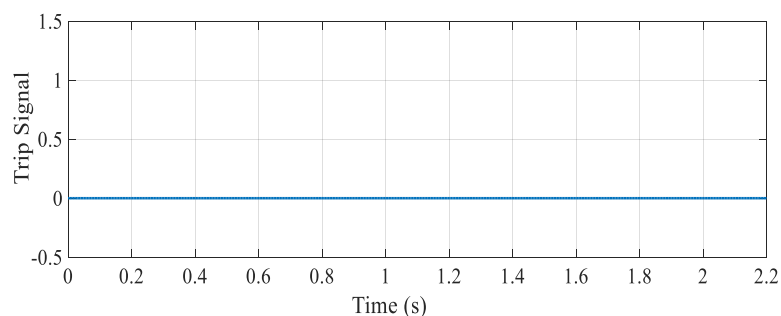
(b) Active power (P) and reactive power (Q) at grid side VSC (bus-2 connection point).



(c) Magnitude of fault impedance ($|Z_{ab}|$) during A-B fault.



(d) Impedance trajectory during A-B fault.



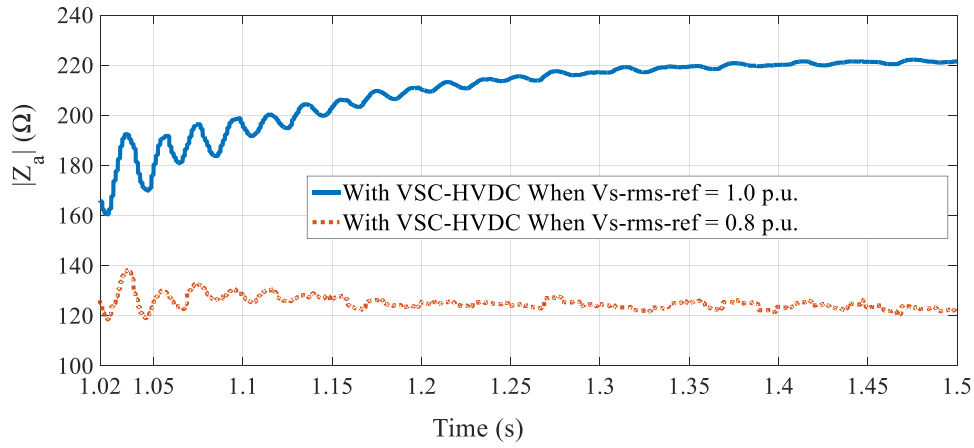
(e) Trip signal of relay R₁₂.

Figure 5.24 The performance of the relay R₁₂ due to A-B fault at 180 km distance from the bus-2 terminal in an AC system with VSC-HVDC.

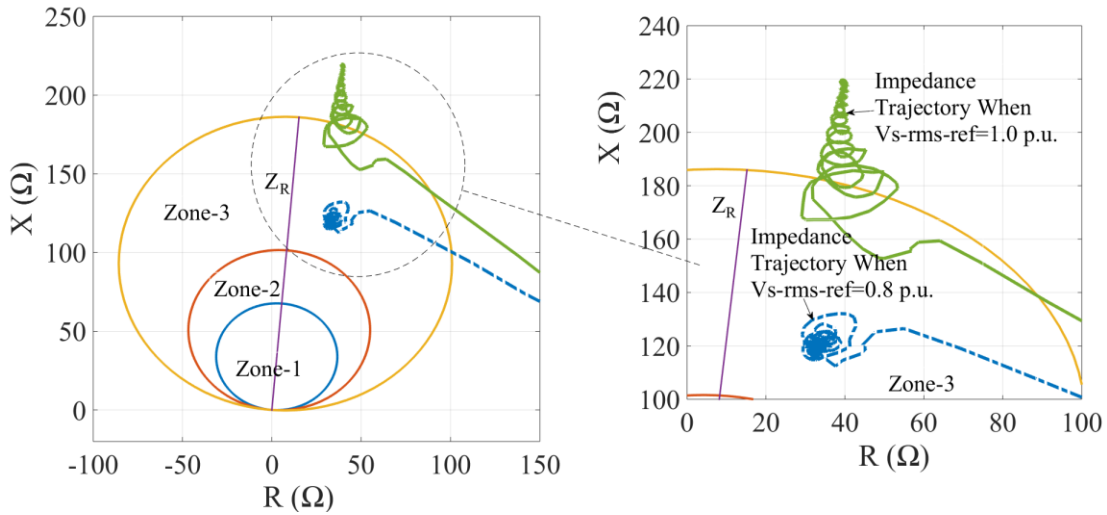
5.4.3.3 Relay Performance under Change in VSC AC Voltage Reference Input

In this case, the performance of the relay R₁₂ is tested under the condition of phase-to-ground (A-G) and phase-to-phase (A-B) fault at 180 km distance from the bus-2 terminal (i.e., 380 km distance from the relay location) in an AC system with VSC-HVDC considering the VSC AC voltage reference ($V_{s-rms-ref}$) input variations. The fault data is the same as the previous case. The performance of the relay under such conditions is shown in Figure 5.25.

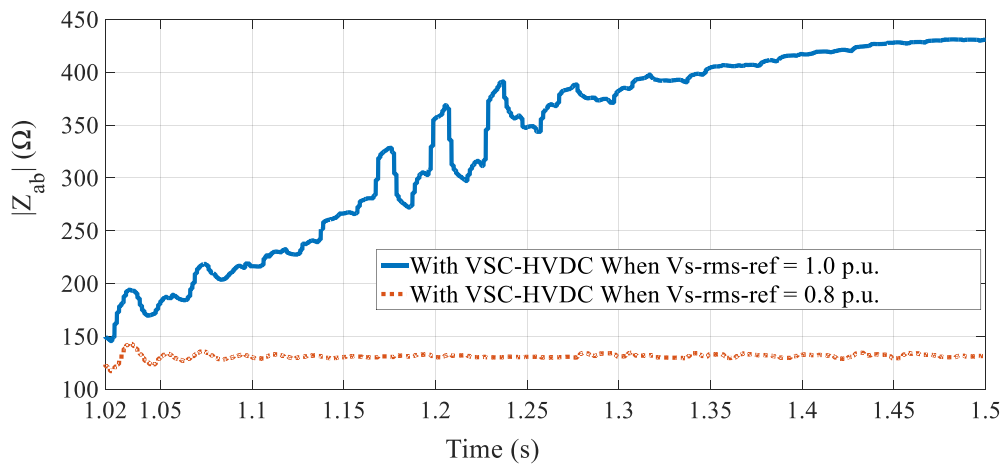
The apparent impedance seen by the relay R₁₂ is $223\angle 79.68^\circ \Omega$ for A-G fault and $439\angle 63.09^\circ \Omega$ for A-B fault when the $V_{s-rms-ref}$ is 1.0 per unit. In both the A-G and A-B fault cases, the measured fault impedance stays outside the Zone-3 area of the relay R₁₂. When the VSC AC voltage reference ($V_{s-rms-ref}$) input is step changed from 1.0 to 0.8 per unit during the fault period, the reactive power is altered into the AC system. Therefore, the impedance seen by the relay is $123\angle 74.81^\circ \Omega$ for A-G fault and $130.62\angle 80.46^\circ \Omega$ for A-B fault. In such condition, the fault impedance seen by the relay falls inside the protection zone, i.e., the Zone-3 area of the relay R₁₂. Hence, the relay provides the trip command with 1 second time delay. Therefore, the mal-operation of the backup relay, i.e., Zone-3 operation of the relay can be mitigated by altering the AC voltage reference input of the decoupled d-q control of the VSC.



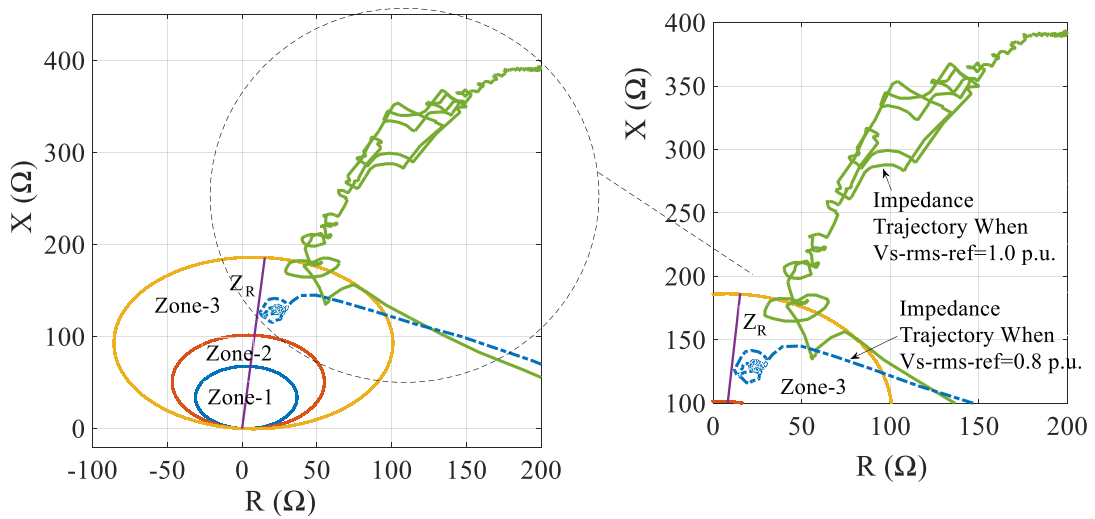
(a) Magnitude of fault impedance ($|Z_a|$) during A-G fault.



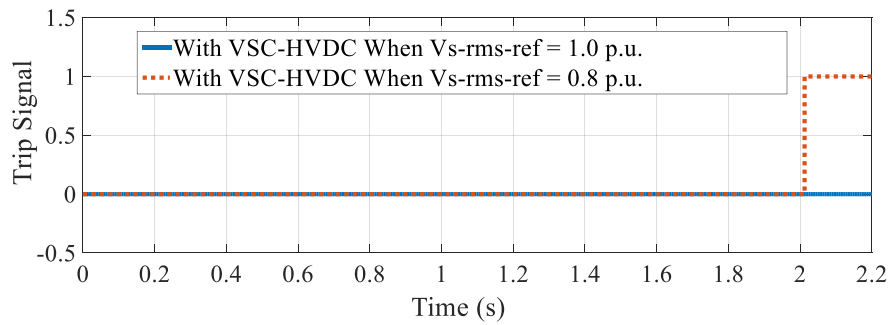
(b) Impedance trajectory during A-G fault.



(c) Magnitude of fault impedance ($|Z_{ab}|$) during A-B fault.



(d) Impedance trajectory during A-B fault.



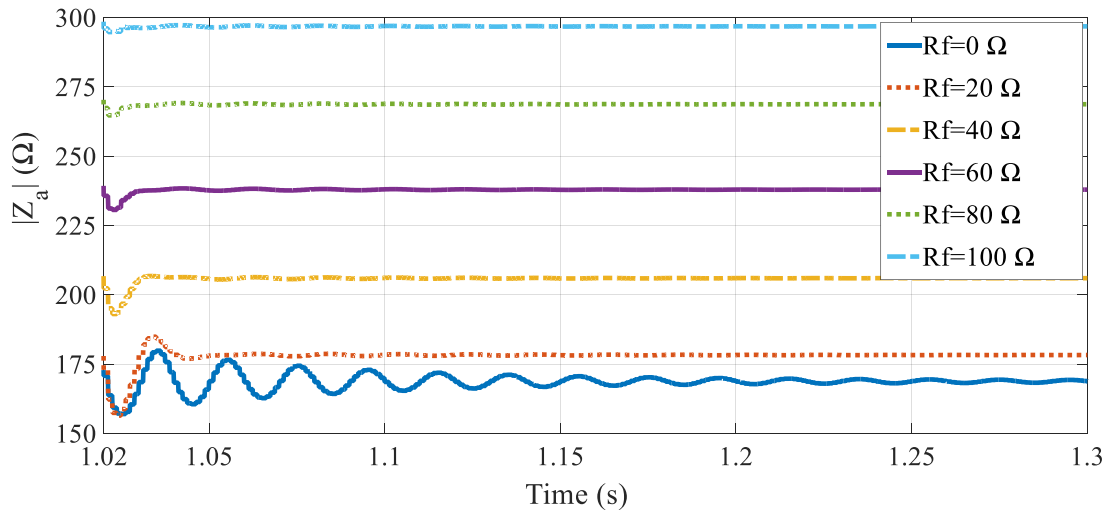
(e) Trip signal of relay R_{12} .

Figure 5.25 The performance of the relay R_{12} under A-G and A-B fault at 180 km distance from the bus-2 terminal in an AC system with VSC-HVDC for the different value of $V_{s-rms-ref}$ during fault period.

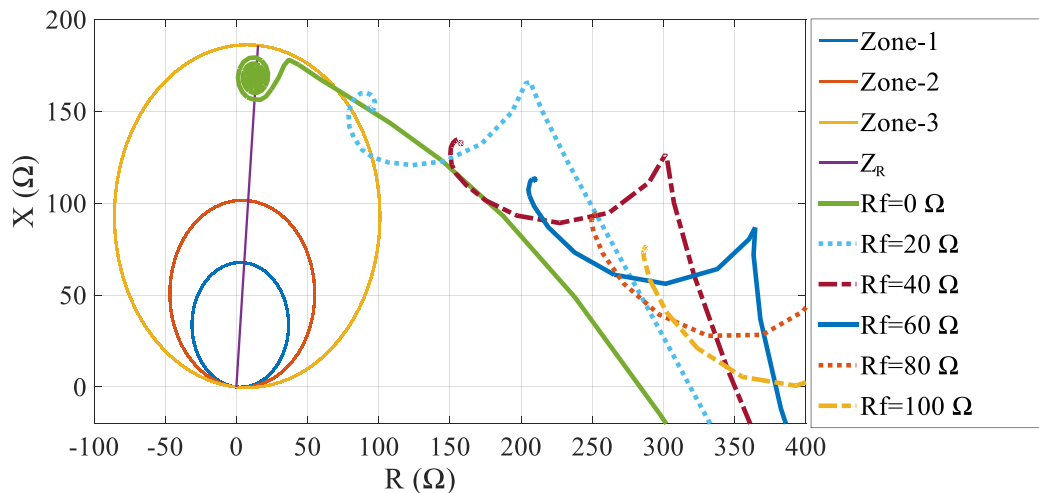
5.4.3.4 Effect of Fault Resistance on Relay Performance under Phase-to-Ground Fault Condition

In this case, the effect of fault resistance on Zone-3 relay performance is analyzed under phase-to-ground (A-G) fault which occurs at 180 km distance from the bus-2 terminal (i.e., 380 km distance from the relay location) in an AC system both without and with VSC-HVDC as shown in Figure 5.26 and 5.27. The fault is applied at $t = 1.0$ s, and the duration of the fault is 1.2 s. The fault resistance (R_f) considered for the simulation study is 20 Ω , 40 Ω , 60 Ω , 80 Ω , and 100 Ω . The A-G fault is applied in

Zone-3 area of the relay R₁₂. But, the apparent impedance seen by the relay has gone outside the zone 3 area of relay R₁₂ due to the higher fault resistance. Hence, the relay will not issue the trip command since the measured impedance does not fall inside the protection zones.

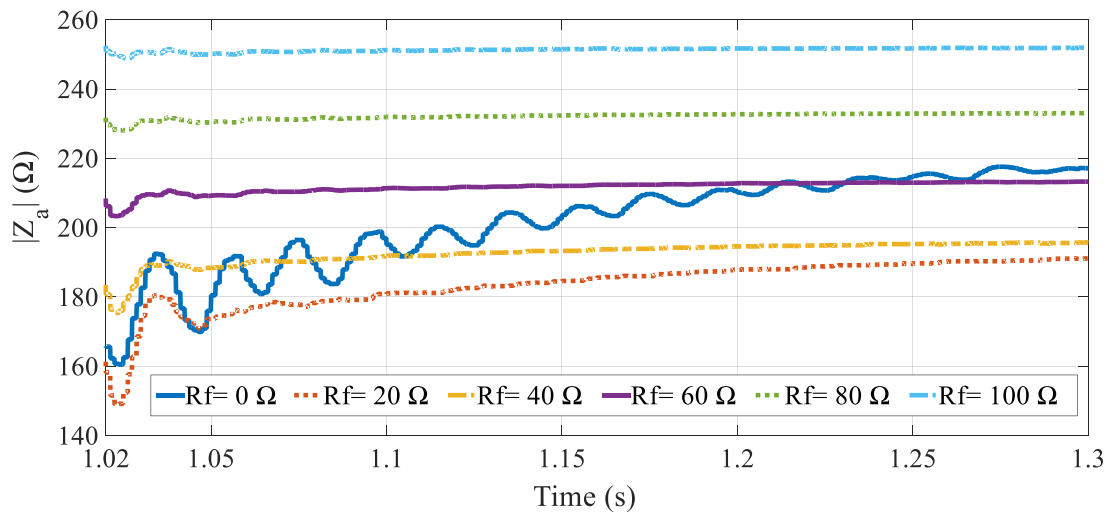


(a) Magnitude of fault impedance ($|Z_a|$) during A-G fault.

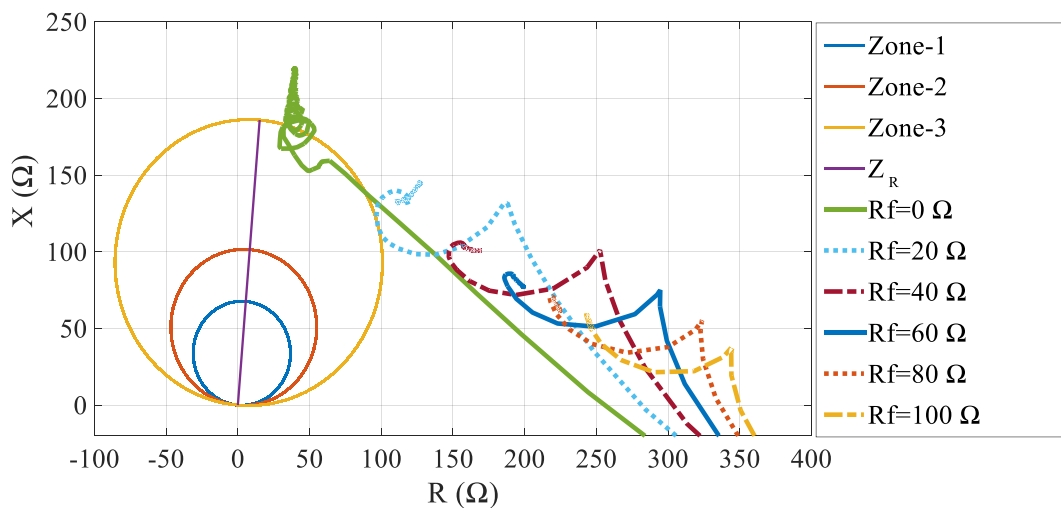


(b) Impedance trajectory during A-G fault.

Figure 5.26 Effect of fault resistance (R_f) on relay R₁₂ performance under A-G fault at 180 km distance from the bus-2 terminal in an AC system without VSC-HVDC.



(a) Magnitude of fault impedance ($|Z_a|$) during A-G fault.



(b) Impedance trajectory during A-G fault.

Figure 5.27 Effect of fault resistance (R_f) on relay R_{12} performance under A-G fault at 180 km distance from the bus-2 terminal in an AC system with VSC-HVDC.

The apparent impedance seen by the relay R_{12} under A-G fault with various fault resistance cases in an AC system both without and with VSC-HVDC is presented in Table 5.4. From Table 5.4, it is observed that the measured impedance value is less in case of an AC system with VSC-HVDC when compared to without VSC-HVDC case. Also, the decrement rate of the reactance value of the apparent impedance is higher in the case of Zone-3 fault when compared to Zone-1 fault.

Table 5.4 The apparent impedance (Z_a) seen by the Zone-3 relay R_{12} for A-G fault with various fault resistance (R_f) at 180 km distance from the bus-2 terminal in an AC system both without and with VSC-HVDC.

| Fault Resistance R_f (Ω) | Z_a (Ω) without VSC-HVDC | Z_a (Ω) with VSC-HVDC |
|--|--|--|
| 0 | $168.82\angle 85.72^\circ$ $12.59914447+j168.3492024$ | $223\angle 79.68^\circ$ $39.94947881+j219.3924318$ |
| 20 | $178.29\angle 58.44^\circ$ $93.31541005+j151.9195786$ | $193.02\angle 48.83^\circ$ $127.0641793+j145.2976763$ |
| 40 | $206.01\angle 40.10^\circ$ $157.5814578+j132.695909$ | $196.46\angle 30.93^\circ$ $168.5225822+j100.9785664$ |
| 60 | $237.96\angle 28.33^\circ$ $209.459293+j112.9237183$ | $213.52\angle 21.21^\circ$ $199.0562986+j77.24882126$ |
| 80 | $268.77\angle 20.39^\circ$ $251.9296277+j93.64174057$ | $233.21\angle 15.37^\circ$ $224.8690851+j61.81260946$ |
| 100 | $296.87\angle 14.72^\circ$ $287.1264641+j75.43335165$ | $251.99\angle 11.40^\circ$ $247.0185333+j49.8076732$ |

5.5 Conclusions

In this chapter, the analytical and simulation studies are carried out to evaluate the performance of distance relay on the transmission line in the presence of VSC-based HVDC system. From the obtained results, it is observed that the apparent impedance seen by the Zone-1 relay is not affected when the VSC-HVDC connected at the bus-2 terminal of the AC system. But, the VSC-HVDC system has a significant influence on the Zone-2 and Zone-3 relay performance due to the active and reactive power source connected in-between the relay location and the fault point. Therefore, Zone-2 faults are cleared with Zone-3 time delay, which causes the fault clearing time increases. If the fault clearing time exceeds the critical clearing time, then the system may lose stability. In the case of Zone 3 fault, the apparent impedance seen by the relay has not fallen inside the protection zones, which results the relay will not operate.

The obtained results indicate that the mal-operation of the Zone-2 and Zone-3 relay can be mitigated by altering the reactive power injected into the system using the VSC AC voltage reference input variations. However, the step variation of the VSC AC voltage reference input is controlled manually. Therefore, further studies are needed to develop an adaptive relaying scheme to mitigate the problem of maloperation of the relay in the presence of VSC-HVDC system.

The apparent impedance seen by the relay has moved out of the protection zones when the fault resistance variation is more significant. The table results show that the reactance value of the apparent impedance gets decreased when the fault resistance increases due to the phase angle between the voltage and current decreases. Also, the decrement rate of the reactance value of the apparent impedance is higher in the case of Zone-3 fault when compared to Zone-1 fault.

CHAPTER 6

DESIGN AND SIMULATION OF EARTH FAULT QUADRILATERAL RELAYS FOR AC TRANSMISSION LINES WITH VSC-BASED HVDC SYSTEMS

6.1 Introduction

In the earlier chapter, the performance analysis of the mho characteristic-based distance relay with the effect of VSC-based HVDC system is presented. In the case of a phase-to-ground fault, the fault resistance cannot be neglected since it has a very high value. The fault resistance affects the performance of the distance relay since the distance between the relay location and fault point is not necessarily proportional to the impedance seen by the relay. In such condition, the conventional distance relay cannot give accurate fault detection in an AC transmission line.

The numerical relay can be applied for the protection of high voltage (HV) transmission line since the conventional distance relay takes the decision based on the local measurements only such as AC voltage and current measured at the relay location. Therefore, the numerical relay with quadrilateral characteristics might be an excellent option to protect the AC transmission line where the resistance and reactance can be altered according to the system.

M. M. Eissa [2006] have proposed a new compensation method to avoid the underreach problem for ground relays based on the calculation of fault resistance. Also, the performance of the quadrilateral characteristic-based relay is analyzed in a 500-kV power system under symmetrical and unsymmetrical fault cases with the effect of fault resistance up to 300 Ω using electromagnetic transients program (EMTP). A new Bergeron distance relay scheme is presented for the 1000-kV ultra-high voltage (UHV) line using the distributed parameter line model [Z. Y. Xu et al. 2008].

The performance of the mho and quadrilateral characteristic-based relays are analyzed under faults with different fault resistance in an IEEE 39 bus 10 generator test system using PSCAD/EMTDC simulation [M. Harikrishna 2010]. The new method for

resistive reach setting of quadrilateral characteristics is presented [E. Sorrentino et al. 2009]. J. Ma et al. [2016] have proposed a new adaptive distance protection scheme based on the complex impedance plane which is immune to the fault resistance, applicable to the various type of faults and adaptable to different operating conditions in a 500-kV transmission system.

M. Zellagui and A. Chaghi [2013] have analyzed the performance of the mho characteristic-based distance relay in a 400-kV transmission line with static var compensators (SVC) such as thyristor controlled reactor (TCR) and thyristor switched capacitor (TSC). N. Chauhan et al. [2014] have presented the effect of unified power flow controller (UPFC) on the performance of the mho and quadrilateral characteristic-based relays in a 230-kV transmission line. It was showed that the mho relay gives the underreaching and overreaching problems under high resistance fault on UPFC compensated lines where the quadrilateral relay provides better performance.

L. He and C. C. Liu [2013], H. Wang [2014], L. He et al. [2014] have presented the impact of HVDC system on distance protection of transmission line. M. M. Alam et al. [2017] have analyzed the dynamic impact of the VSC-HVDC system on the quadrilateral characteristic-based distance relay in an AC transmission line. However, the reach setting of the quadrilateral characteristics might be different for the phase and ground fault relays since the variation of the fault resistance is more significant for the phase-to-ground fault when compared to the phase-to-phase fault.

In this chapter, the quadrilateral characteristic-based distance relay is designed, and its simulation studies are carried out to test the performance under phase-to-ground fault with the consideration of fault resistance up to 100 Ω in an AC transmission line with the effect of VSC-based HVDC system. The impact of the dynamic operating conditions of the VSC-HVDC system on the performance of the quadrilateral relays under phase-to-ground fault with fault resistance cases is presented. Also, the comparison of the quadrilateral relays with the mho relays under such conditions are presented.

6.2 Study System

The three-bus system with VSC-based HVDC system is presented in Figure 6.1. In this system, 420 kV, 50 Hz, two area power system connected each other via the three-

bus system. The load angle between the two sources is 20° . The length of the AC transmission line-1 and line-2 is 200 km. The distance relay R_{12} is located at the bus-1 terminal. The VSC-based HVDC system is connected to the bus-2 terminal of the AC system. The decoupled d-q controlled two-level VSC is used at both sides of the HVDC station. The VSC-based HVDC system and its decoupled d-q control model is the same as the test system presented in section 3.3.

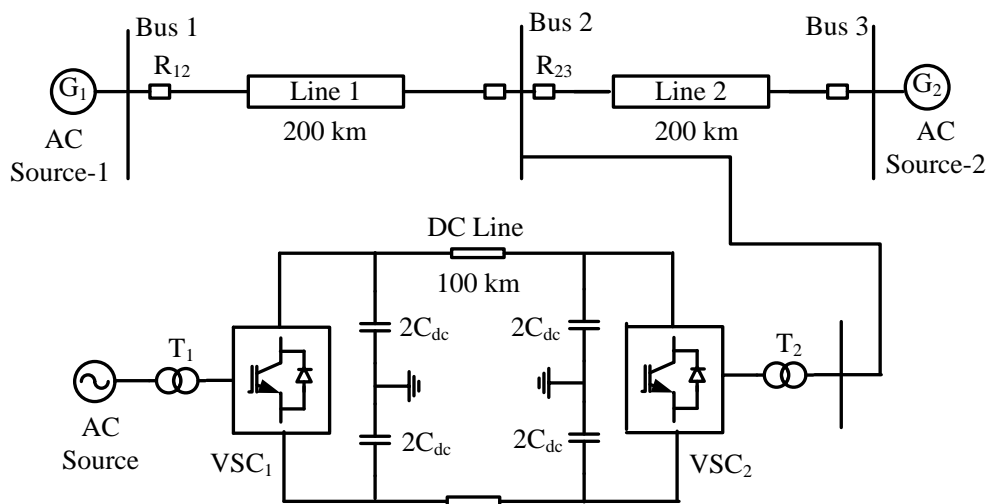


Figure 6.1 The three-bus system with VSC-HVDC.

6.3 Design of Quadrilateral Relays

When the phase-to-ground fault occurs in a system, the fault resistance will be the considerable factors since it introduces an underreach problem in the distance relay. Numerical distance relay with the quadrilateral characteristics can be applied to protect the high voltage AC transmission line under such condition since the setting of the resistance and reactance of the characteristics can be altered accordingly. The three-zone quadrilateral characteristic-based distance relay is shown in Figure 6.2. The design of the quadrilateral characteristics for Zone-1, Zone-2 and Zone-3 relay has been implemented with the help of references Z. Y. Xu et al. [2008], Sub-committee on relay/protection under task force for power system analysis under contingencies [2014], User Manual of CSC-101 Line Protection IED [2012], M. M. Alam [2018] and the details of design procedure followed in presently is briefed following subsections.

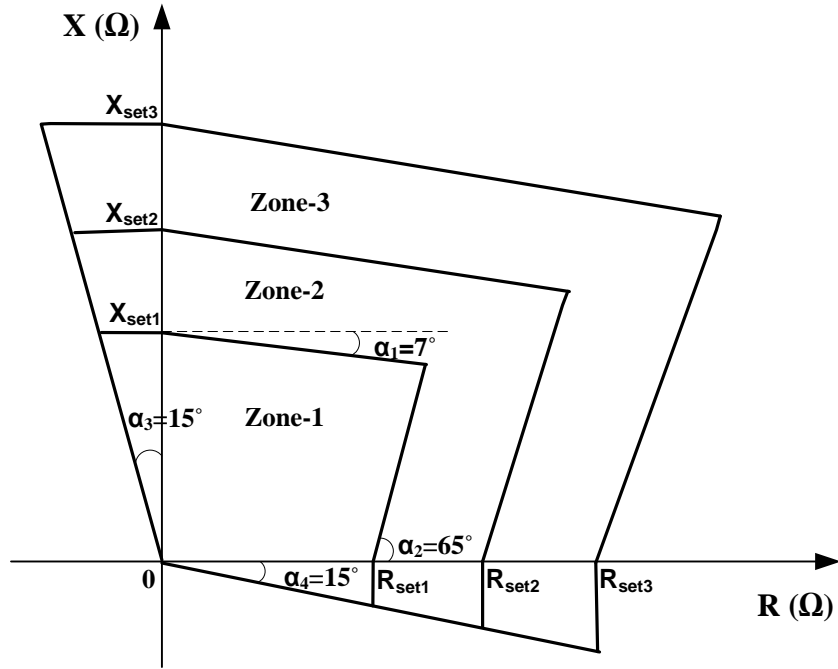


Figure 6.2 Three-zone quadrilateral characteristic-based distance relay.

6.3.1 Zone-1 Setting

Consider the protection zones are designed for relay R_{12} which is indicated in Figure 6.1. Zone-1 relay is designed to protect the 80 % of the primary line (i.e., Line-1 as indicated in Figure 6.1) without intentional time delay. The reactive reach of Zone-1 relay is considered as 80 % reactance ($0.8 \times X$) of the primary line impedance ($Z_{Line1} = R + jX$). The resistive reach of Zone-1 relay consists of the 80 % resistance ($0.8 \times R$) of the primary line impedance and the additional resistive coverage of 70Ω to overcome the problem of Zone-1 high resistance faults.

The reactance line in the first quadrant of the R-X plane is set to decline 7° (i.e., $\alpha_1 = 7^\circ$) with respect to the resistance line in order to overcome the steady-state overreach problem due to resistive faults. The relay characteristic is extended in the second and fourth quadrant of the R-X plane with the slope of 15° (i.e., α_3 and α_4 is 15°) to perform the correct operation during close-in high resistance faults. The resistance line in the first quadrant of the R-X plane is designed with the slope of 65° (i.e., $\alpha_2 = 65^\circ$) to avoid incorrect tripping during high load conditions. The calculation used for the Zone-1 setting has given below:

The positive sequence impedance (as given in equation 5.7) is given by,

$$\begin{aligned} Z_1 &= 0.42 \angle 85.32^\circ \\ &= (0.03 + j0.42) \Omega/\text{km} \end{aligned}$$

The zero-sequence impedance (as given in equation 5.8) is given by,

$$\begin{aligned} Z_0 &= 1.17 \angle 75.34^\circ \\ &= (0.29 + j1.13) \Omega/\text{km} \end{aligned}$$

The positive sequence impedance for the line-1 (i.e., 200 km line) is given by,

$$\begin{aligned} &= 200 \times (0.42 \angle 85.32^\circ) \\ &= 84.79 \angle 85.32^\circ \end{aligned} \tag{6.1}$$

$$Z_{Line1} = R + jX = (6.90 + j84.51) \Omega \tag{6.2}$$

Using equation (6.1), Zone-1 reach setting is calculated by,

$$\begin{aligned} &= 0.8 \times (84.79 \angle 85.32^\circ) \\ &= 67.83 \angle 85.32^\circ \\ &= (5.52 + j67.60) \Omega \end{aligned} \tag{6.3}$$

Reactive reach of Zone-1 relay (X_{set1}) is calculated by,

$$= (0.8 \times X) = 67.60 \Omega \tag{6.4}$$

Resistive reach of Zone-1 relay (R_{set1}) is calculated by,

$$= (0.8 \times R) + 70 \Omega = 75.52 \Omega \tag{6.5}$$

6.3.2 Zone-2 Setting

Zone-2 relay is designed to protect the 120 % of the primary line (i.e., Line-1 which is indicated in Figure 6.1) with the time delay of 20 cycles (i.e., 0.4 seconds). The reactive reach of Zone-2 relay is considered as 120 % reactance ($1.2 \times X$) of the primary line impedance ($Z_{Line1} = R + jX$). The resistive reach of Zone-2 relay consists of the 120 % resistance ($1.2 \times R$) of the primary line impedance and the additional resistive coverage of 100 Ω to cover the Zone-2 high resistance faults. The calculation used for the Zone-2 setting has given below:

Using equation (6.1), Zone-2 reach setting is calculated by,

$$\begin{aligned}
 &= 1.2 \times (84.79 \angle 85.32^\circ) \\
 &= 101.75 \angle 85.32^\circ \\
 &= (8.28 + j101.41) \Omega
 \end{aligned} \tag{6.6}$$

Reactive reach of Zone-2 relay (X_{set2}) is calculated by,

$$= (1.2 \times X) = 101.41 \Omega \tag{6.7}$$

Resistive reach of Zone-2 relay (R_{set2}) is calculated by,

$$= (1.2 \times R) + 100 \Omega = 108.28 \Omega \tag{6.8}$$

6.3.3 Zone-3 Setting

Zone-3 relay is designed to protect the 220 % of the primary line (i.e., Line-1 as indicated in Figure 6.1) with the time delay of 1 second. The reactive reach of Zone-3 relay is considered as 220 % reactance ($2.2 \times X$) of the primary line impedance ($Z_{Line1} = R + jX$). The resistive reach of Zone-3 relay consists of the 220 % resistance ($2.2 \times R$) of the primary line impedance and the additional resistive coverage of 200 Ω to cover the Zone-3 high resistance faults. The calculation used for the Zone-3 setting has given below:

Using equation (6.1), Zone-3 reach setting is calculated by,

$$\begin{aligned}
 &= 2.2 \times (84.79 \angle 85.32^\circ) \\
 &= 186.54 \angle 85.32^\circ \\
 &= (15.19 + j185.92) \Omega
 \end{aligned} \tag{6.9}$$

Reactive reach of Zone-3 relay (X_{set3}) is calculated by,

$$= (2.2 \times X) = 185.92 \Omega \tag{6.10}$$

Resistive reach of Zone-3 relay (R_{set3}) is calculated by,

$$= (2.2 \times R) + 200 \Omega = 215.19 \Omega \tag{6.11}$$

6.3.4 PSCAD Simulation Model

The PSCAD simulation model of the Zone-1 characteristics is shown in Figure 6.3 and its simulated output waveform is shown in Figure 6.4 [K. Pipaliya and V.

Makwana et al. 2015]. The Zone-2 and Zone-3 characteristics can be modeled in a similar way and the modeled three-zone quadrilateral characteristic-based distance relay is presented in Figure 6.5.

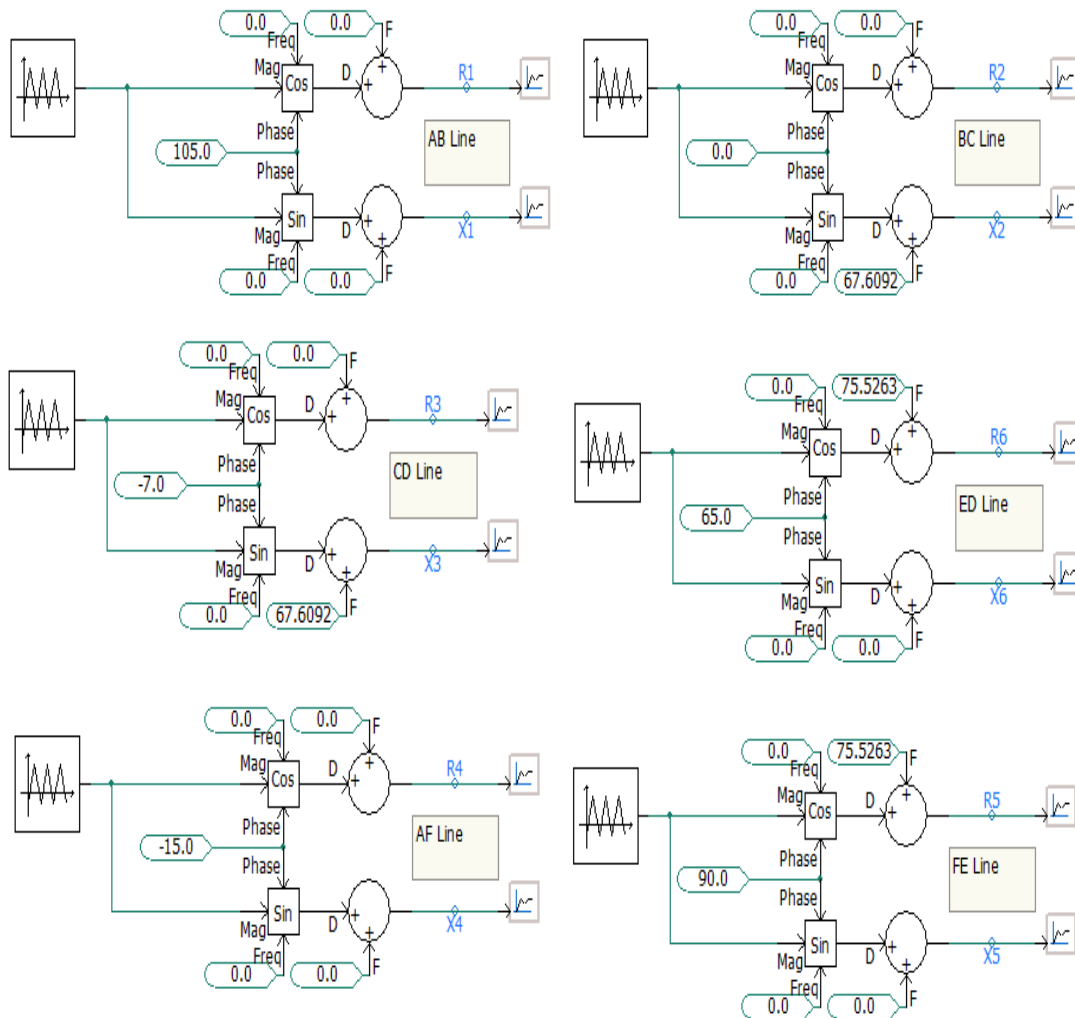


Figure 6.3 The PSCAD simulation model of Zone-1 quadrilateral relay.

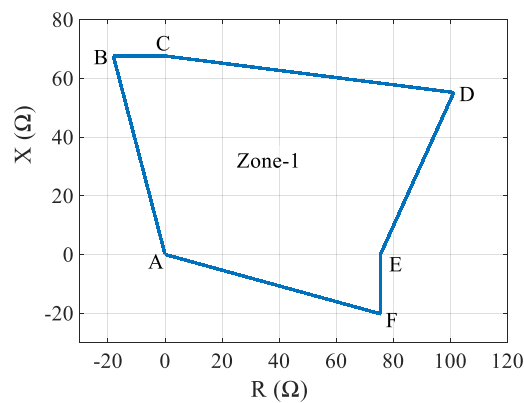


Figure 6.4 Zone-1 quadrilateral relay in PSCAD.

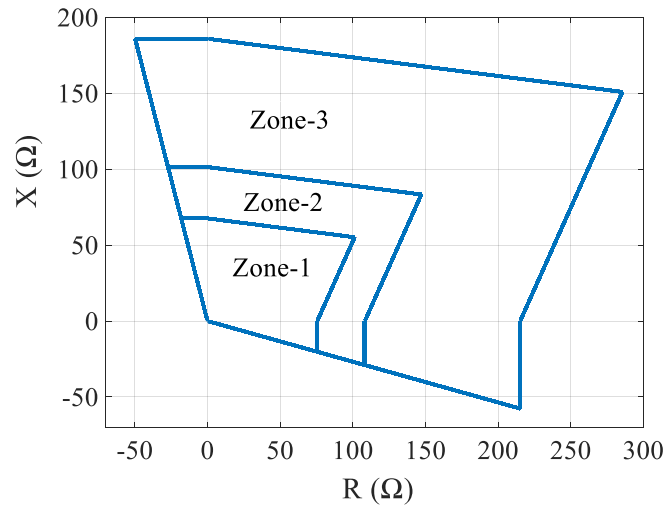
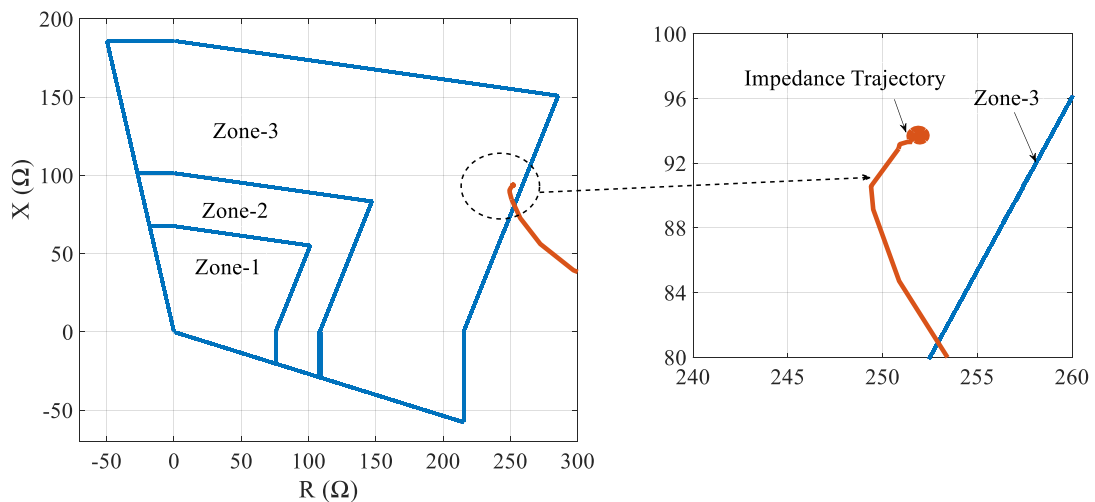
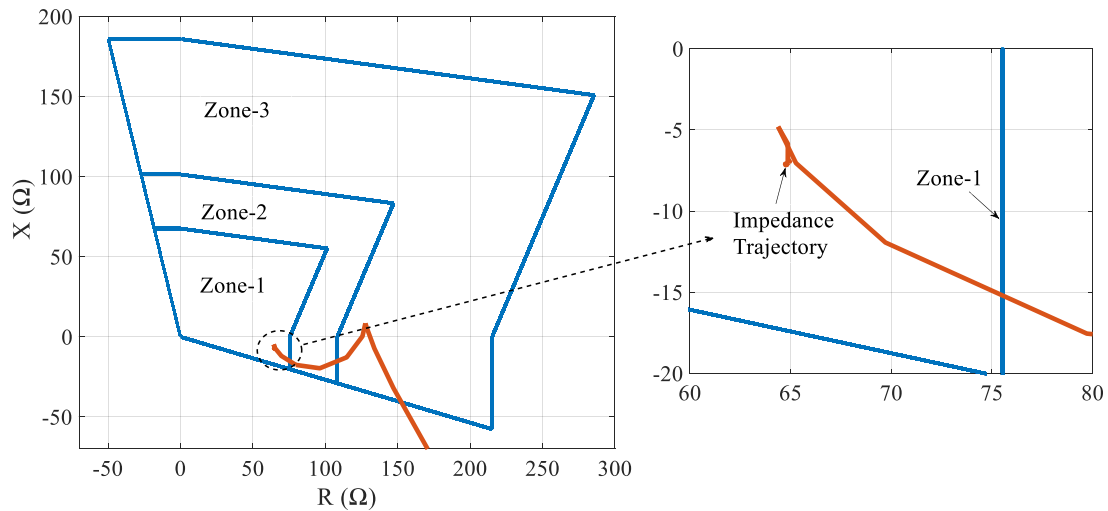


Figure 6.5 Three-zone quadrilateral relay in PSCAD.

The simulation study of the fault cases is carried out in all the quadrant of the quadrilateral relay to verify its characteristics. In Figure 6.1, the three-bus system without VSC-HVDC is considered for this simulation study. In the first case, the phase-to-ground (A-G) fault is applied at 380-km distance from relay R_{12} location with the consideration of fault resistance 80Ω . In the second case, the three-phase to ground (ABC-G) fault is applied at the relay R_{12} location with the consideration of fault resistance 60Ω . The performance of the quadrilateral relay under such fault conditions is shown in Figure. 6.6.



(a) A-G fault at 380 km distance from the relay location.



(b) ABC-G fault at the relay location.

Figure. 6.6 Simulation cases for testing all the quadrant in the quadrilateral relay.

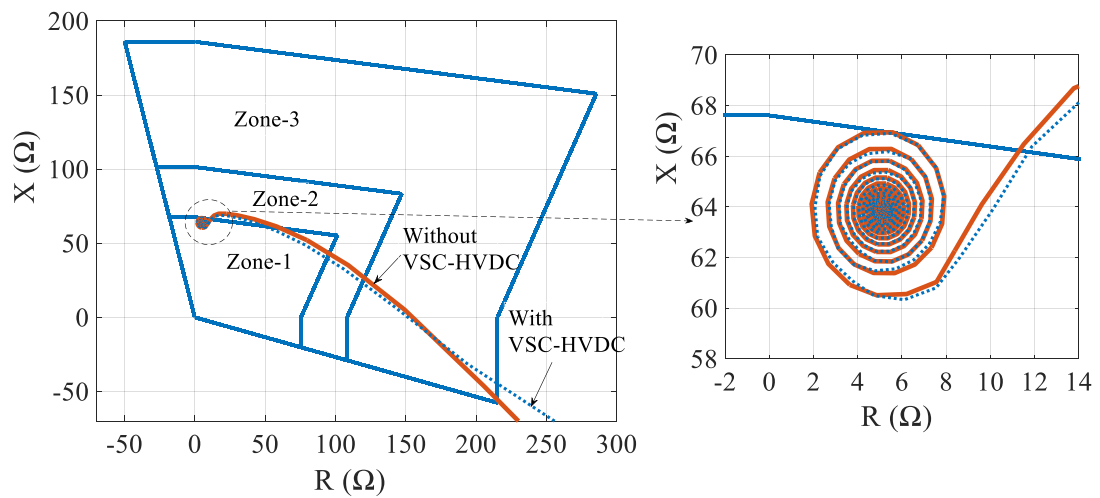
In the case of A-G fault, the apparent impedance seen by the relay R_{12} is $251.95+j93.67 \Omega$ and this impedance trajectory is located in the first quadrant of the relay characteristics. In the case of ABC-G fault, the apparent impedance seen by the relay R_{12} is $65.17-j7.21 \Omega$ and this impedance trajectory is located in the fourth quadrant of the relay characteristics. Generally, the angle of the line impedance is not higher than 90° . Though, the slope of 15° ($\alpha_3 = 15^\circ$) is given in the second quadrant to make sure the correct operation of the quadrilateral relay [User Manual of CSC-101 Line Protection IED 2012].

6.4 Simulation Studies

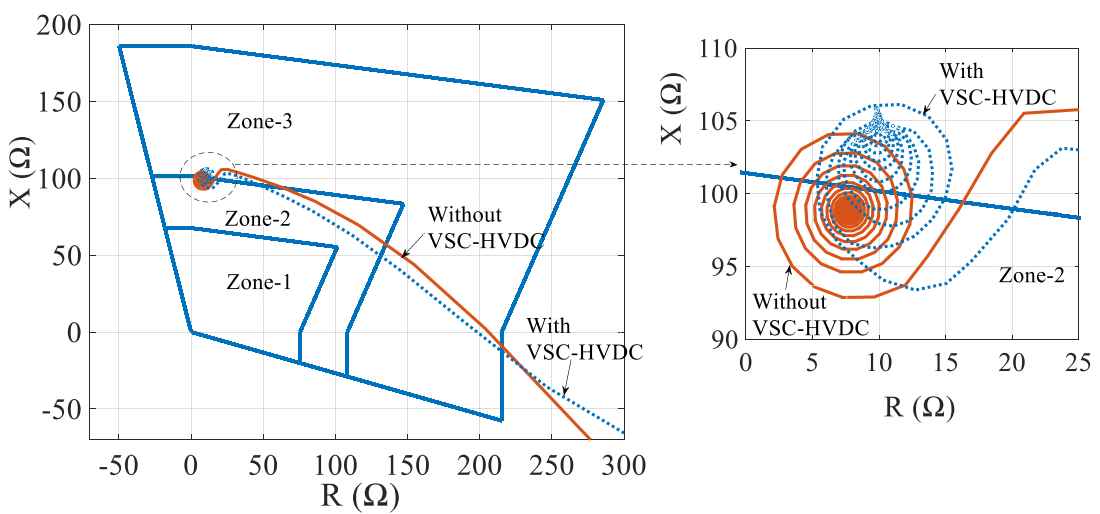
In this section, simulation studies are carried out to analyze the performance of the quadrilateral relays under the phase-to-ground fault condition in the 3-bus system with the effect of VSC-based HVDC system. The ground faults in all three zones (i.e., Zone-1, Zone-2, and Zone-3 area of the relay R_{12}) are considered for the simulation study. Also, the effect of fault resistance on the quadrilateral relays and its comparison with the mho relay is presented. The simulation studies are carried out using PSCAD/EMTDC software.

6.4.1 Phase-to-Ground Fault condition

In this case, the performance of the Zone-1, Zone-2 and Zone-3 operation of the quadrilateral relay is analyzed under phase A to ground (A-G) fault which occurs at 150 km, 230 km and 380 km distance from the relay R_{12} location (i.e., bus-1 terminal) in the 3-bus system both without and with VSC-HVDC cases. The performance of the quadrilateral relay R_{12} under A-G fault condition has shown in Figure 6.7. Table 6.1 shows the apparent impedance measured by the relay R_{12} under A-G fault condition.



(a) Zone-1 fault (fault at 150 km distance from the relay location).



(b) Zone-2 fault (fault at 230 km distance from the relay location).

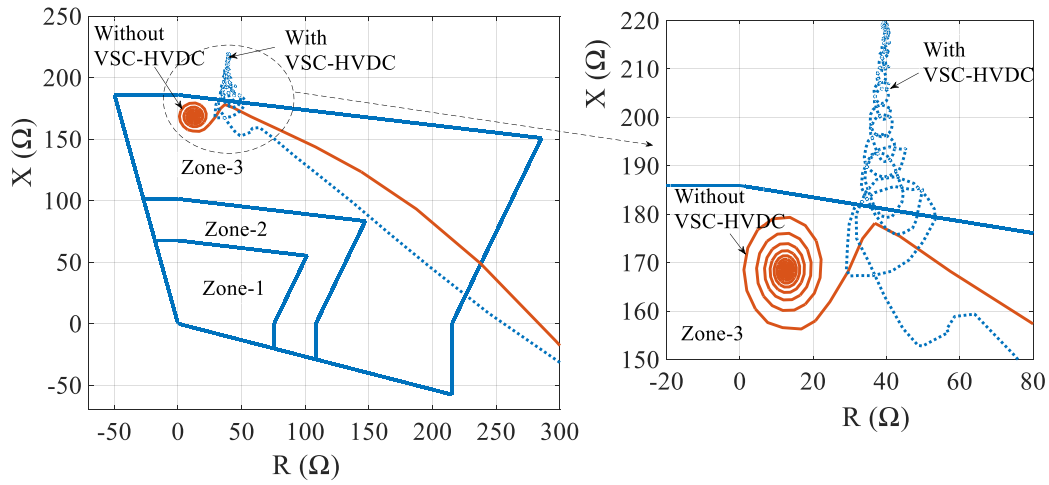


Figure 6.7 The performance of the quadrilateral relay R_{12} under A-G fault in an AC system both without and with VSC-HVDC.

Table 6.1 The apparent impedance (Z_a) seen by the relay R_{12} under A-G fault condition.

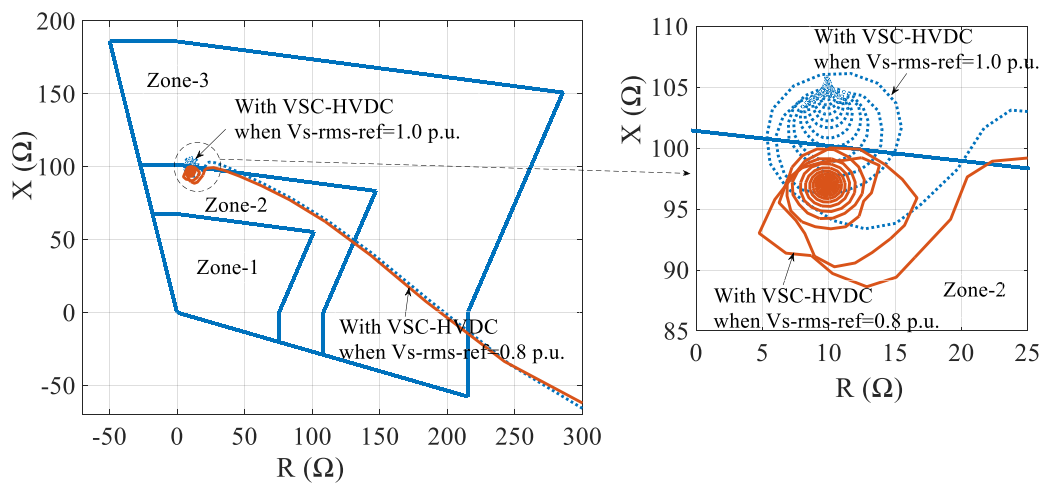
| Fault Location | $Z_a (\Omega)$ (without VSC-HVDC) | $Z_a (\Omega)$ (with VSC-HVDC) |
|----------------|--------------------------------------|-----------------------------------|
| Zone-1 | $64.08 \angle 85.42^\circ$ | $64.05 \angle 85.44^\circ$ |
| Zone-2 | $99.10 \angle 85.53^\circ$ | $106.32 \angle 84.72^\circ$ |
| Zone-3 | $168.82 \angle 85.42^\circ$ | $223 \angle 79.68^\circ$ |

In case of fault on the Zone-1 area of the relay R_{12} , the apparent impedance seen by the relay has not changed for both without and with VSC-HVDC cases. But in the case of fault on Zone-2 and Zone-3 area of the relay R_{12} , the apparent impedance seen by the relay has increased significantly when the VSC-HVDC is connected at the bus-2 terminal of the 3-bus system which can be seen from Figure 6.7 and Table 6.1.

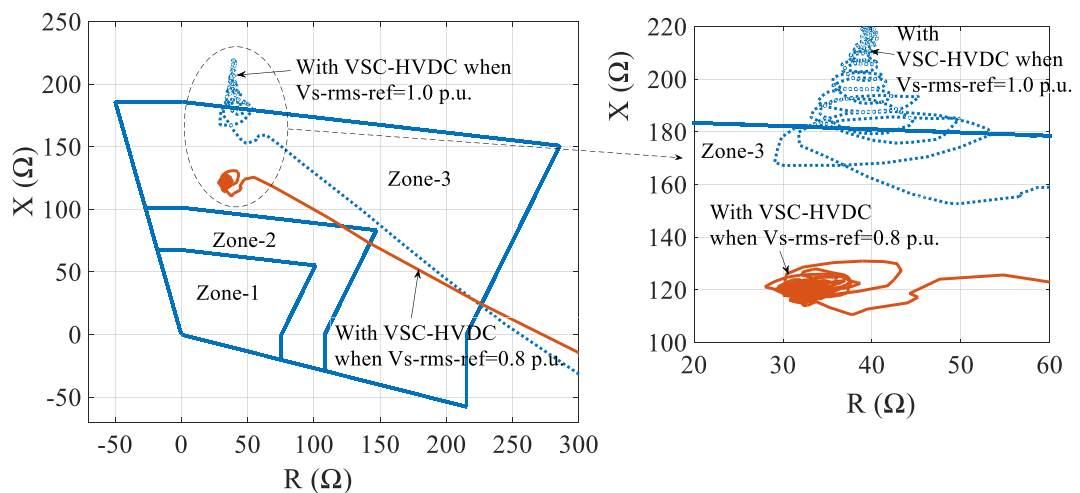
Due to the interconnection of VSC-HVDC into the AC system, the impedance viewed by the relay for Zone-2 and Zone-3 fault has gone outside the Zone-2 and Zone-3 area of the relay which can lead to the maloperation of the relay. In such cases, adaptive reactive reach setting of the quadrilateral relay or adjusting the reactive power of VSC during fault period might work well since the reactive power of the AC network is varied due to the interconnection of VSC-HVDC system.

6.4.2 Step Change in VSC AC voltage Reference Input during Phase-to-Ground Fault Condition

In this case, the performance of the Zone-2 and Zone-3 quadrilateral relay is analyzed under A-G fault at 230 km and 380 km distance from the relay location in the 3-bus system with VSC-HVDC and step variation of reference AC voltage ($V_{s-rms-ref}$) of decoupled d-q control of grid side VSC (i.e., VSC₂) during fault period. The performance of the Zone-2 and Zone-3 relay has shown in Figure 6.8.



(a) Zone-2 fault (fault at 230 km distance from the relay location).



(b) Zone-3 fault (fault at 380 km distance from the relay location).

Figure 6.8 The performance of quadrilateral relay R_{12} under A-G fault in an AC system with VSC-HVDC and step variation of $V_{s-rms-ref}$ of VSC₂ from 1.0 to 0.8 per unit during fault period.

Table 6.2 The apparent impedance (Z_a) seen by the relay R_{12} under A-G fault condition in an AC system with VSC-HVDC for different value of reference AC voltage ($V_{s-rms-ref}$).

| Fault Location | $Z_a (\Omega)$ ($V_{s-rms-ref} = 1.0$ per unit) | $Z_a (\Omega)$ ($V_{s-rms-ref} = 0.8$ per unit) |
|----------------|---|---|
| Zone-2 | $106.32 \angle 84.72^\circ$ | $97.54 \angle 84.19^\circ$ |
| Zone-3 | $223 \angle 79.68^\circ$ | $123 \angle 74.81^\circ$ |

When the reference AC voltage ($V_{s-rms-ref}$) is step changed from 1.0 to 0.8 per unit during the fault period, the apparent impedance seen by the relay has reduced which can be seen from Figure 6.8 and Table 6.2. Due to this reduction of apparent impedance measured by the relay, the impedance trajectory has located inside the protection zones. Therefore, Zone-2 and Zone-3 relay will issue the trip decision for the fault at 230 km and 380 km distance from the relay point. From the simulation results, it is observed that the maloperation of the backup relay can be resolved by altering the reactive power of the system using the variation of the reference AC voltage ($V_{s-rms-ref}$) of decoupled d-q control of grid side VSC.

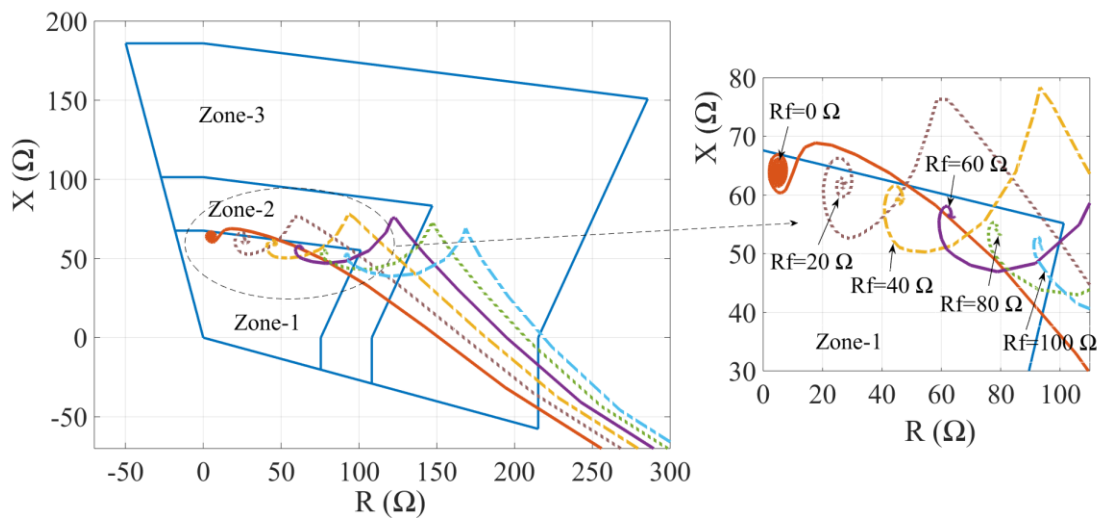
6.4.3 Comparison of Mho and Quadrilateral Relay

6.4.3.1 Zone-1 Fault

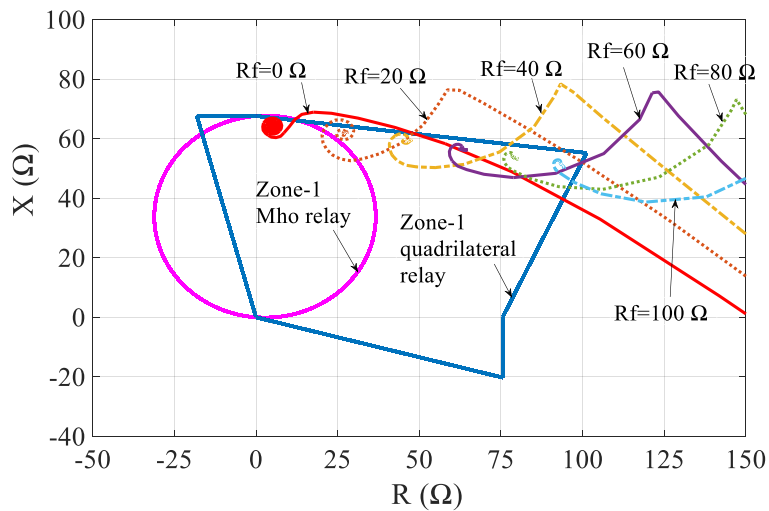
In this case, the performance of the Zone-1 mho and quadrilateral relay is analyzed under phase A to ground fault (A-G) with various fault resistance (R_f) which occurs at 150 km distance from the relay R_{12} location in an AC system with VSC-HVDC. The fault resistance is considered as 0 to 100 Ω with 20 Ω increments for the simulation study. The comparison of Zone-1 mho and quadrilateral relay has shown in Figure 6.9. For Zone-1 mho relay, 80 % of the primary line impedance has considered for the Zone-1 setting without intentional time delay which is presented in chapter 5.

The effect of fault resistance on the three-zone quadrilateral relay has shown in Figure 6.9 (a). The impedance trajectory of all the fault cases (i.e., A-G fault with fault resistance varies from 0 to 100 Ω) falls within the relay characteristics. But, in the case of Zone-1 mho relay, the impedance trajectory of A-G fault with $R_f = 0 \Omega$ case only

falls within the relay characteristics which is indicated in Figure 6.9 (b). When fault resistance increases, the impedance trajectory has moved in the positive resistance axis which leads to the maloperation of the mho relay. In such cases, the Zone-1 quadrilateral relay has given better performance since the resistive reach of the characteristics has changed according to the system.



(a) Effect of fault resistance on three-zone quadrilateral relay.



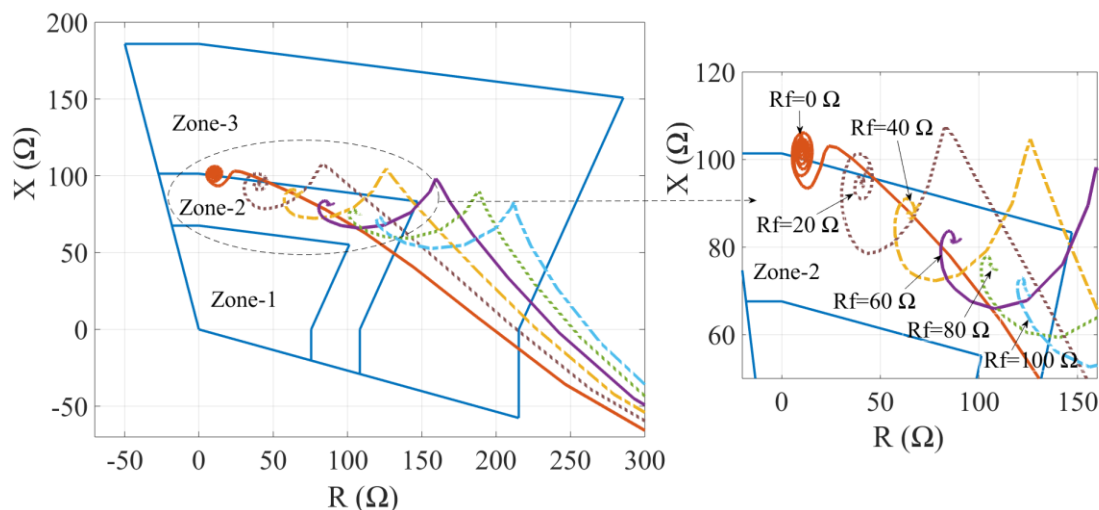
(b) Zone-1 mho and quadrilateral relay.

Figure 6.9 The comparison of Zone-1 mho and quadrilateral relay R_{12} under A-G fault with various fault resistance (R_f) at 150 km distance from the relay location in an AC system with VSC-HVDC.

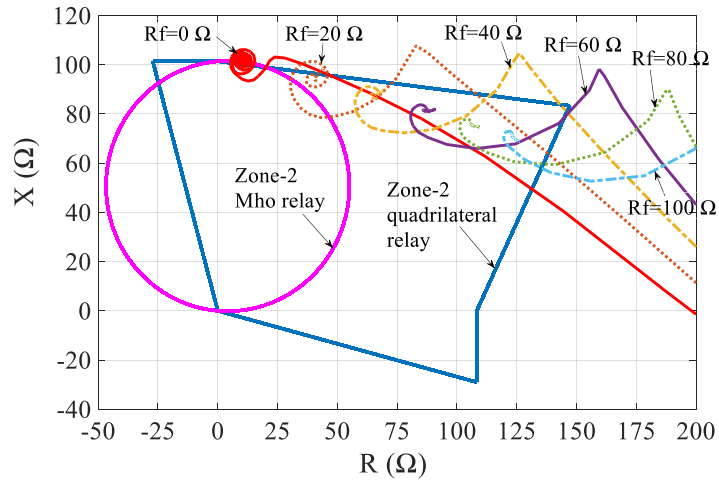
6.4.3.2 Zone-2 Fault

In this case, the performance of the Zone-2 quadrilateral and mho relay is analyzed under the condition of A-G fault with various fault resistance which occurs at 230 km distance from the relay location in an AC system with VSC-HVDC including the variation of $V_{s-rms-ref}$ of decoupled d-q control of VSC_2 . Figure 6.10 shows the performance of the Zone-2 relay under A-G fault with fault resistance varies from 0 to 100 Ω when the $V_{s-rms-ref}$ of VSC_2 is 1.0 per unit. For Zone-2 mho relay, 120 % of the primary line impedance is considered for the Zone-2 setting with 20 cycles delay which is explained in chapter 5.

When the fault resistance increases, the impedance trajectory has falling inside the Zone-2 quadrilateral relay even the $V_{s-rms-ref} = 1.0$ per unit which is indicated in Figure 6.10 (a). The comparison of Zone-2 quadrilateral relay with the mho relay has presented in Figure 6.10 (b). It demonstrates that the impedance trajectory has moved in the positive resistance axis of the R-X plane which is not locating inside the protection zone of the Zone-2 mho relay when the fault resistance increases. Also, the impedance trajectory for the fault with $R_f = 0 \Omega$ has not fallen inside the Zone-2 mho and quadrilateral relay.



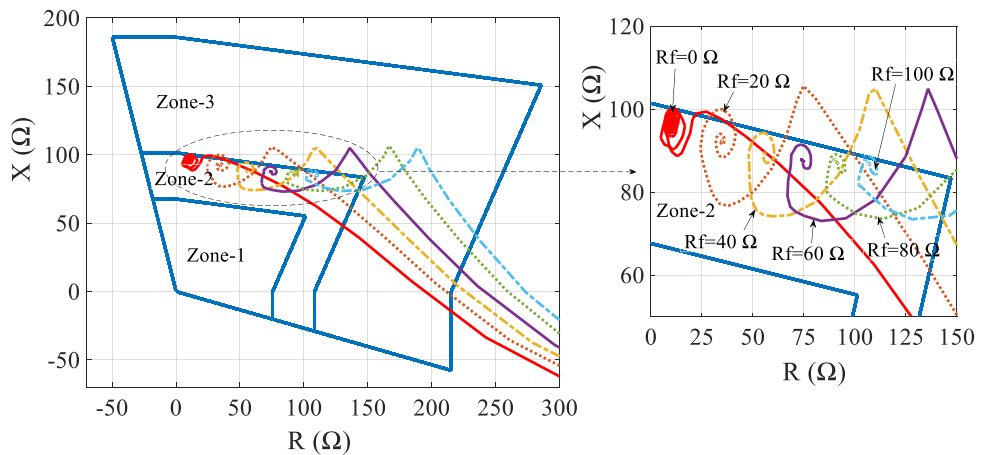
(a) Effect of fault resistance on three-zone quadrilateral relay.



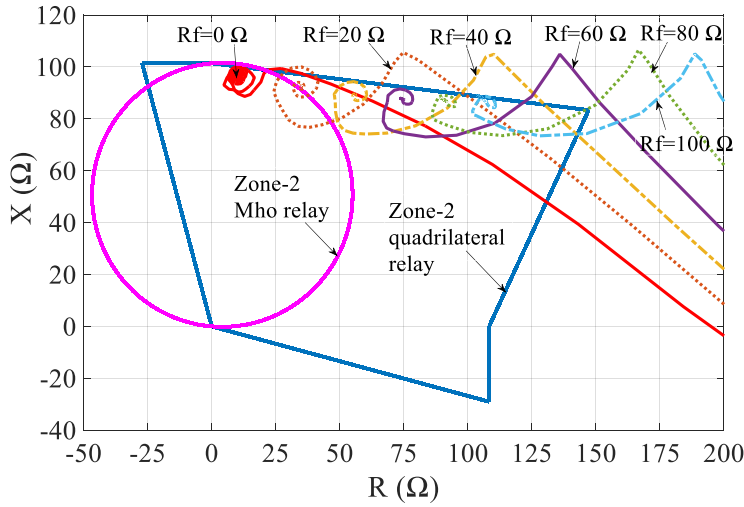
(b) Zone-2 mho and quadrilateral relay.

Figure 6.10 The comparison of Zone-2 mho and quadrilateral relay R_{12} under A-G fault with various fault resistance (R_f) at 230 km distance from the relay location in an AC system with VSC-HVDC. ($V_{s-rms-ref} = 1.0$ per unit).

The performance of the Zone-2 mho and quadrilateral relay is shown in Figure 6.11 when the $V_{s-rms-ref}$ of VSC₂ is step varied from 1.0 to 0.8 per unit during the fault period. The fault situation is similar to the previous case. In this case, the impedance trajectory for the fault with $R_f = 0 \Omega$ has fallen inside the protection zone which is indicated in Figure 6.11 (a). Also, the decrement rate of the reactance value for different fault resistance case is very less when compared to the previous case due to the alteration of reactive power using the step variation of $V_{s-rms-ref}$ of grid side VSC (i.e., VSC₂) which can be observed from Figure 6.10 (b) and 6.11 (b).



(a) Effect of fault resistance on three-zone quadrilateral relay.



(b) Zone-2 mho and quadrilateral relay.

Figure 6.11 The comparison of Zone-2 mho and quadrilateral relay R_{12} under A-G fault with various fault resistance (R_f) at 230 km distance from the relay location in an AC system with VSC-HVDC and step variation of $V_{s-rms-ref}$ of VSC_2 from 1.0 to 0.8 per unit during fault period.

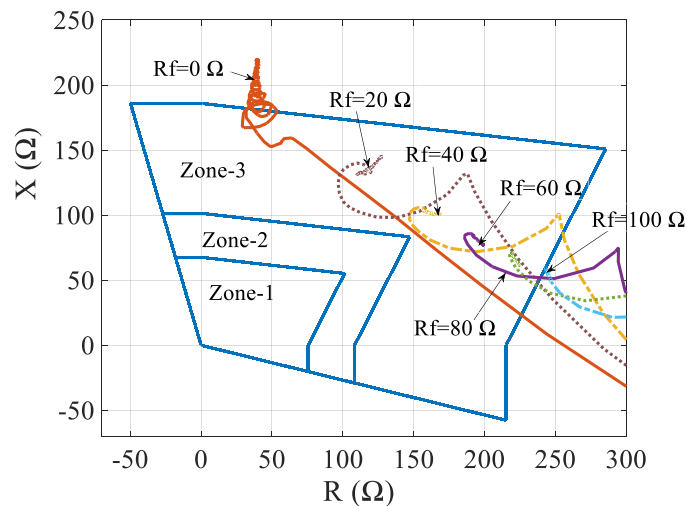
Table 6.3 The comparison of apparent impedance (Z_a) seen by the Zone-2 relay R_{12} for different value of $V_{s-rms-ref}$ of VSC_2 under A-G fault with different fault resistance (R_f) at 230 km distance from the relay location.

| R_f (Ω) | Z_a (Ω) | Z_a (Ω) |
|--------------------|--|--|
| | with VSC-HVDC ($V_{s-rms-ref} = 1.0$ per unit) | with VSC-HVDC ($V_{s-rms-ref} = 0.8$ per unit) |
| 0 | $106.32 \angle 84.72^\circ$ | $97.54 \angle 84.19^\circ$ |
| 20 | $107.50 \angle 65.89^\circ$ | $98.63 \angle 69.30^\circ$ |
| 40 | $113.50 \angle 52.19^\circ$ | $105.20 \angle 57.92^\circ$ |
| 60 | $122.11 \angle 42.10^\circ$ | $114.75 \angle 49.93^\circ$ |
| 80 | $132.27 \angle 34.46^\circ$ | $125.59 \angle 44.43^\circ$ |
| 100 | $143.38 \angle 28.69^\circ$ | $136.75 \angle 40.57^\circ$ |

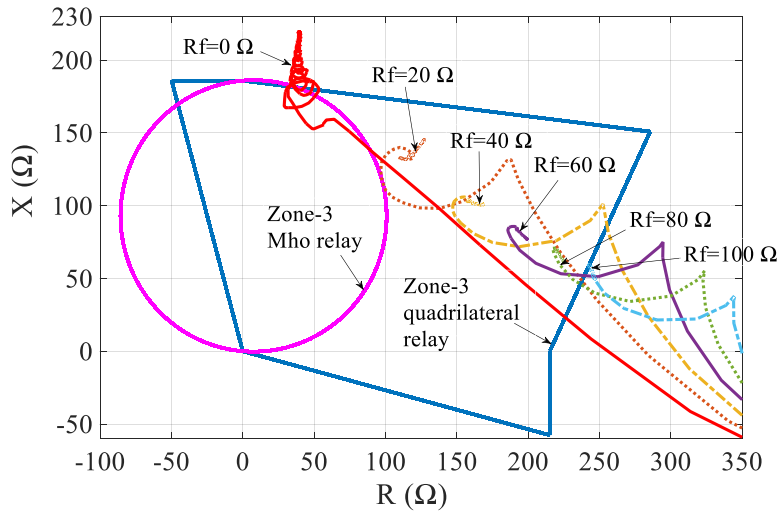
Table 6.3 shows the comparison of the apparent impedance seen by the Zone-2 relay for different value of $V_{s-rms-ref}$ of VSC₂ under the condition of A-G fault with various fault resistance which occurs at 230 km distance from the relay location in an AC system with VSC-HVDC. When the $V_{s-rms-ref}$ is step changed from 1.0 to 0.8 per unit during the fault period, the reactive power of the AC network has varied which can lead to the variation of the apparent impedance seen by the relay. Hence, the Zone-2 relay R₁₂ will trip the line for the fault which occurs on Zone-2 area even if the VSC-HVDC is connected in-between the relay location and fault point.

6.4.3.3 Zone-3 Fault

In this case, the performance of the Zone-3 mho and quadrilateral relay is analyzed under the condition of A-G fault with various fault resistance (R_f) at 380 km distance from the relay location in an AC system with VSC-HVDC including the variation of $V_{s-rms-ref}$ of decoupled d-q control of VSC₂. The performance of the Zone-3 relay under A-G fault with various fault resistance (i.e., R_f is considered as 0 Ω , 20 Ω , 40 Ω , 60 Ω , 80 Ω and 100 Ω) which occurs at 380 km distance from the relay point has shown in Figure 6.12. For Zone-3 mho relay, 220 % of the primary line impedance is considered for the Zone-3 setting with the 1-second delay which has explained in chapter 5.



(a) Effect of fault resistance on three-zone quadrilateral relay.

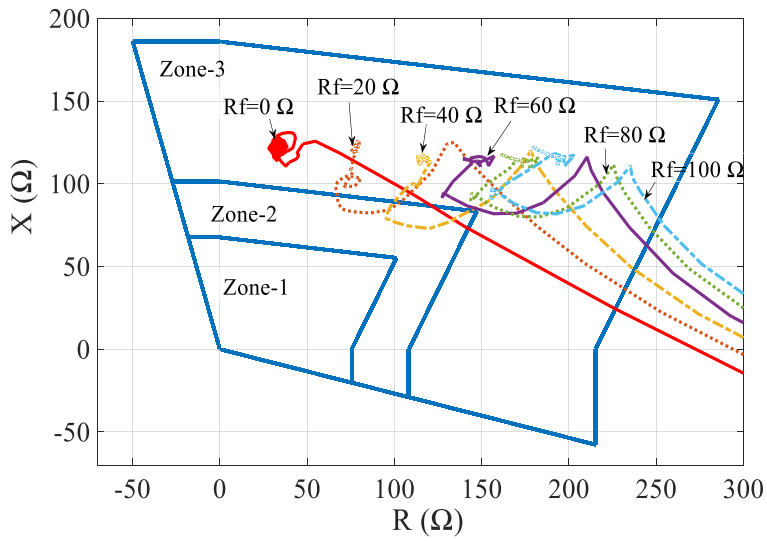


(b) Zone-3 mho and quadrilateral relay.

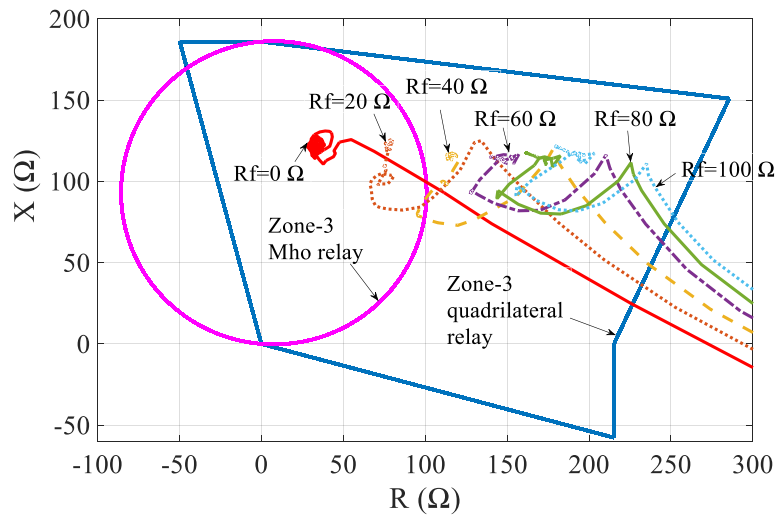
Figure 6.12 The comparison of Zone-3 mho and quadrilateral relay R_{12} under A-G fault with various fault resistance (R_f) at 380 km distance from the relay location in an AC system with VSC-HVDC. ($V_{s-rms-ref} = 1.0$ per unit).

The impedance trajectory for the fault with $R_f = 0 \Omega$ has moved outside the boundary of Zone-3 area. The reactance value in the R-X plane gets decreased when the fault resistance increases which can be seen in Figure 6.12 (a). The impedance trajectory of all the fault cases has not located inside the Zone-3 mho relay due to the increment of fault resistance which is indicated in Figure 6.12 (b). Therefore, the resistive reach setting of the Zone-3 quadrilateral relay has increased to cover the high resistance faults.

The performance of the Zone-3 mho and quadrilateral relay is shown in Figure 6.13 when the $V_{s-rms-ref}$ of decoupled d-q control of VSC₂ is step varied from 1.0 to 0.8 per unit during the fault period. The fault situation is similar to the previous case. In this case, the impedance trajectory for the fault with $R_f = 0 \Omega$ has fallen inside the Zone-3 area which can be seen in Figure 6.13 (a). Here also, the decrement rate of the reactance value for different fault resistance cases has reduced when compared to the previous case due to the variation of the reactive power of the AC network using the step variation of $V_{s-rms-ref}$ of VSC₂ which can be noticed from Figure 6.12 (b) and 6.13 (b).



(a) Effect of fault resistance on three-zone quadrilateral relay.



(b) Zone-3 mho and quadrilateral relay.

Figure 6.13 The comparison of Zone-3 mho and quadrilateral relay R_{12} under A-G fault with various fault resistance (R_f) at 380 km distance from the relay location in an AC system with step variation of $V_{s-rms-ref}$ of VSC₂ from 1.0 to 0.8 per unit during fault period.

Table 6.4 The comparison of apparent impedance (Z_a) seen by the Zone-3 relay R_{12} for different value of $V_{s-rms-ref}$ of VSC₂ under A-G fault with different fault resistance (R_f) at 380 km distance from the relay location.

| R_f (Ω) | Z_a (Ω) with VSC-HVDC ($V_{s-rms-ref} = 1.0$ per unit) | Z_a (Ω) with VSC-HVDC ($V_{s-rms-ref} = 0.8$ per unit) |
|--------------------|--|--|
| 0 | $223 \angle 79.68^\circ$ | $123 \angle 74.81^\circ$ |
| 20 | $193.02 \angle 48.83^\circ$ | $148.01 \angle 57.33^\circ$ |
| 40 | $196.46 \angle 30.93^\circ$ | $162.48 \angle 45.51^\circ$ |
| 60 | $213.52 \angle 21.21^\circ$ | $181.22 \angle 39.32^\circ$ |
| 80 | $233.21 \angle 15.37^\circ$ | $199.82 \angle 35.97^\circ$ |
| 100 | $251.99 \angle 11.40^\circ$ | $216.88 \angle 34.04^\circ$ |

Table 6.4 shows the comparison of the apparent impedance seen by the Zone-3 relay for different value of $V_{s-rms-ref}$ of VSC₂ under the condition of A-G fault with different fault resistance which occurs at 380 km distance from the relay location in an AC system with VSC-HVDC. When the $V_{s-rms-ref}$ is step changed from 1.0 to 0.8 per unit during the fault period, the apparent impedance seen by the relay has reduced which comes inside the Zone-3 area of the relay.

6.5 Conclusions

In this chapter, the performance of the numerical distance relay is analyzed in an AC system with the effect of the VSC-based HVDC system. The three-zone quadrilateral characteristic-based distance relay is designed and modeled in PSCAD/EMTDC. Simulation studies are carried out to test the performance of the quadrilateral relay in an AC system with the impact of VSC-based HVDC system. From the simulation results, it is observed that the Zone-2 fault is moved to the Zone-3 area and Zone-3 fault has gone outside the boundary of the protection zones when the VSC-HVDC is connected at the bus-2 terminal of the AC system. Therefore, the correct operation of

the backup relay is performed by adjusting the reactive power of the system using the variation of the reference AC voltage ($V_{s-rms-ref}$) of decoupled d-q control of VSC₂. In such cases, adaptive reactive reach setting of the quadrilateral relay also may give a better result.

The performance of the quadrilateral relay is analyzed and compared with the mho relay under the condition of the phase-to-ground fault with the effect of fault resistance which occurs on Zone-1, Zone-2 and Zone-3 area of the relay in the AC system with VSC-HVDC including the variation of $V_{s-rms-ref}$ of VSC₂. From the simulation results, it is noticed that the impedance trajectory has located inside the protection zones of the quadrilateral relay even the fault resistance variation is a large value since the characteristics has altered accordingly. The obtained results indicate that the reactance value of the measured apparent impedance gets decreased when fault resistance increases due to the variation of reactive power which is caused by the interconnection of VSC-HVDC. The variation range of the reactance value of apparent impedance is very less in case of Zone-1 fault when compared to the Zone-3 fault. The decrement rate of the reactance value of apparent impedance is reduced when the $V_{s-rms-ref}$ of VSC₂ is step changed from 1.0 to 0.8 per unit during the fault period.

CHAPTER 7

CONCLUSIONS

Following conclusions are drawn from the research work presented in this thesis,

- In recent years, offshore wind energy has increased significantly. The continuous increase in the offshore wind power generation level brings the requirement of the offshore wind farms (OWF) integration with an AC grid. The multi-terminal (MT) voltage source converters (VSC)-based high voltage direct current (HVDC) transmission system is an emerging technology and also the best option to interconnect the large-scale OWF with the AC grid.
- The performance of the grid and windmill connected VSC on no-load condition is greatly influenced by the various fault and wind speed conditions such as the gust, ramp, and noisy variation of the wind speed. Also, the harmonic content and total harmonic distortion (THD) of the AC voltage measured at the converter terminal is reduced significantly when the high pass filter and LC filter are connected with the grid and windmill connected VSC.
- The DC faults have very high peak fault current within a few ms (i.e., high peak and steady fault current with low-rise time) and it is the most critical stage in the multi-terminal VSC-HVDC link operation. In the MT VSC-based HVDC system, the wind variability has the significant influence on the response of the wind power generation output and converter terminals, no impact on the response of the DC voltage during steady-state and fault conditions.
- Developed a single-ended protection scheme for the DC pole-to-pole and pole-to-ground fault conditions in a three-terminal VSC-HVDC transmission system without current limiting reactors. Test results showed that the DC fault current reaches a higher value than the DC circuit breaker (CB) capacity before the

proposed protection scheme comes into operation. Therefore, current limiting reactors are designed and connected in series with the DC CB to limit the DC fault current within the breaker capacity. Test results showed that the relay has detected and discriminated the internal and external faults for both the DC pole-to-pole and pole-to-ground fault conditions in the three-terminal VSC-based HVDC transmission system with current limiting reactors. The fault detection time of the relay has increased when the distance between the relay location and the fault point increases due to the less DC voltage and current rise rate. Also, the fault detection time of the relay has increased for the three-terminal VSC-HVDC system with current limiting reactors when compared to the without current limiting reactors.

- The apparent impedance seen by the Zone-1 relay is not affected when the VSC-HVDC connected at the bus-2 terminal of the AC system. But, the VSC-HVDC system has a significant influence on the Zone-2 and Zone-3 relay performance due to the active and reactive power source connected in-between the relay location and the fault point. Therefore, Zone-2 faults are cleared with Zone-3 time delay, which causes the fault clearing time increases. If the fault clearing time exceeds the critical clearing time, then the system may lose stability. In the case of Zone 3 fault, the apparent impedance seen by the relay has not fallen inside the protection zones, which results the relay will not operate. Therefore, the mal-operation of the backup relay (i.e., Zone-2 and Zone-3 operation of the relay) is mitigated by altering the reactive power injected into the system using the variation of the reference AC voltage input of the decoupled d-q control of the VSC.
- The apparent impedance seen by the mho distance relay has moved outside the protection zones when the fault resistance variation is more significant. However, the impedance trajectory has located inside the protection zones of the quadrilateral relay even the fault resistance variation is a large value since the characteristics have altered accordingly. The reactance value of the measured apparent impedance gets decreased when fault resistance increases due to the

variation of reactive power which is caused by the interconnection of VSC-HVDC. The variation range of the reactance value of apparent impedance is very less in case of Zone-1 fault when compared to the Zone-3 fault. The decrement rate of the reactance value of apparent impedance is reduced when the AC voltage reference input of the decoupled d-q control of the VSC is step changed during the fault period.

Scope for Further Investigations:

Based on the research work carried out in this thesis, further investigations can be focused in the following areas,

- In the case of the DC fault in two-level VSC-based HVDC system, the IGBT switches of the VSC can block the fault current. The two-level VSC will act like an uncontrolled diode rectifier. The fault current in the DC grid can flow to the AC system through the antiparallel diode path. The DC fault current has a huge peak and steady value which will damage the converters and other components in the AC system. The modular multilevel converter (MMC) is more attractive for multi-terminal (MT) HVDC grid since it can able to block the DC fault current, and also it has various voltage levels, low switching losses and harmonics, etc. Hence, the transient behaviour of the MMC-based HVDC grid-connected offshore wind farms under various power system disturbances can be analyzed.
- In the case of DC pole-to-ground fault, the sensitivity of the fault discrimination criterion of the single-ended protection scheme may get decreased when the variation of fault resistance is more significant. In such cases, the adaptive threshold setting for the fault discrimination criterion is an area for further investigation.

- Experimental validation of the developed single-ended protection scheme is required to test the performance in real-time.
- The three-bus system with point-to-point VSC-based HVDC link is taken to evaluate the performance of the distance relay with the effect of VSC-based HVDC system. In the next step, the studies can be extended to the larger network with the interconnection of the MT VSC-based HVDC systems.
- Further studies are needed to develop the adaptive distance relaying scheme for the AC grid with VSC-based HVDC system since this work has considered the manual control of the AC voltage reference input of decoupled d-q control of the VSC to mitigate the mal-operation of the backup relay. In such cases, adaptive reactive reach setting of the quadrilateral relay also may give a better result.

REFERENCES

R. Perveen, N. Kishor, and S. R. Mohanty (2014). “Offshore wind farm development: Present status and challenges.” *Renew. Sustain. Energy Rev.*, 29, 780-792.

M. R. Islam, Y. Guo, and J. Zhu (2014). “A review of offshore wind turbine nacelle: Technical challenges, and research and development trends.” *Renew. Sustain. Energy Rev.*, 33, 161-176.

L. Xu, L. Yao, and C. Sasse (2007). “Grid integration of large DFIG-based wind farms using VSC transmission.” *IEEE Trans. power sys.* 22(3), 976-984.

C. M. Franck (2011). “HVDC Circuit breakers: A Review Identifying Future Research Needs.” *IEEE Trans. Power Del.*, 26(2), 998-1006.

M. K. Bucher, R. Wiget, G. Anderson, and C. M. Franck (2014). “Multiterminal HVDC Networks – What is the Preferred Topology?.” *IEEE Trans. Power Del.*, 29(1), 406-413.

W. Leterme, P. Tielens, S. De Boeck, and D. Van Hertem (2014). “Overview of Grounding and Configuration Options for Meshed HVDC Grids.” *IEEE Trans. Power Del.*, 29(6), 2467-2475.

E. Kontos, R. Teixeira Pinto, S. Rodrigues, and P. Bauer (2015). “Impact of HVDC Transmission System Topology on Multiterminal DC Network Faults.” *IEEE Trans. Power Del.*, 30(2), 844-852.

A. F. Abdou, A. Abu-Siada, and H. R. Pota (2015). “Impact of VSC faults on dynamic performance and low voltage ride through of DFIG.” *International Journal of Electrical Power and Energy Systems*, 65, 334-347.

J. Yang (2011). "Fault Analysis and Protection for Wind Power Generation Systems." Ph.D. Thesis, University of Glasgow, Scotland.

N. R. Chaudhuri, B. Chaudhuri, R. Majumder, and A. Yazdani (2014). "*Multi-terminal Direct-Current Grids: Modeling, Analysis, and Control.*" John Wiley & Sons.

D. Jovcic, D. V. Hertem, K. linden, J. P. Taisne, and W. Grieshaber (2011). "Feasibility of DC Transmission Networks." *Proc. 2nd IEEE PES International Conference and Exhibition on Innovative Smart Grid Technologies (ISGT Europe)*, Manchester, U.K., 1-8.

H. Ha, and S. Subramanian (2015). "Implementing the protection and control of future dc grids." *Alstom Grid Technology Centre, Innovation and Technology Department.*

L. Tang (2003). "Control and protection of multi-terminal dc transmission systems based on voltage-source converters." Ph.D. Thesis, McGill University, Montreal, Canada.

L. Tang, and B. T. Ooi (2007). "Locating and Isolating DC faults in Multi-Terminal DC systems." *IEEE Trans. Power Del.*, 22(3), 1877-1883.

J. Suonan, G. Song, and Q. Xu (2006). "Time-domain fault location for parallel transmission lines using unsynchronized currents." *Elect. Power Energy Sys.*, 28(4), 253-260.

X. Yang, M. Choi, S. Lee, C. Ten and S. Lim (2008). "Fault Location for Underground Power Cable Using Distributed Parameter Approach." *IEEE Trans. Power Sys.*, 23(4), 1809-1816.

J. Suonan, S. Gao, G. Song, Z. Jiao, and X. Kang (2010). "A novel fault location method for HVDC transmission lines." *IEEE Trans. Power Del.*, 25(2), 1203-1209.

L. Yuansheng, W. Gang, and L. Haifeng (2015). "Time Domain Fault Location method on HVDC Transmission Lines under Unsynchronized Two end measurement and Uncertain Line Parameters." *IEEE Trans. Power Del.*, 30(3), 1031-1038.

J. Yang, J. E. Fletcher, and J. O' Reilly (2010). "Multiterminal DC Wind Farm Collection Grid Internal Fault Analysis and Protection Design." *IEEE Trans. Power Del.*, 25(4), 2308-2318.

J. Yang, J. E. Fletcher, and John O' Reilly (2012). "Short circuit and Ground Fault analyses and Location in VSC based DC Network Cables." *IEEE Trans. Ind. Electron.*, 59(10), 3827-3837.

J. Suonan, J. Zhang, Z. Jiao, L. Yang, and G. Song (2013). "Distance Protection for HVDC Transmission Lines Considering Frequency Dependent Parameters." *IEEE Trans. Power Del.*, 28(2), 723-732.

H. Packard (1997). *Traveling Wave Fault Location in Power Transmission Systems*, Application Note 1285.

M. A. Baseer (2013). "Travelling waves for finding the fault location in transmission lines." *Journal Electrical and Electronic Engineering*, 1(1), 1-19.

X. Liu, A. H. Osman, and O. P. Malik (2009). "Hybrid Travelling wave/boundary protection for Monopolar HVDC line." *IEEE Trans. Power Del.*, 24(2), 569-578.

X. Liu, A. H. Osman, and O. P. Malik (2011). "Real time implementation of a Hybrid Protection Scheme for Bipolar HVDC Line using FPGA." *IEEE Trans. Power Del.*, 26(1), 101-108.

Y. Zhang, N. Tai, and B. Xu (2012). "Fault analysis and traveling-wave protection scheme for bipolar HVDC lines." *IEEE Trans. Power Del.*, 27(3), 1583-1591.

O. K. Nanayakkara, A. D. Rajapakse, and R. Wachal (2012). "Travelling Wave based Line Fault Location in Star connected Multiterminal HVDC systems." *IEEE Trans. Power Del.*, 27(4), 2286-2294.

G. W. Swift (1979). "The spectra of fault-induced transients." *IEEE Trans. Power Apparatus and systems*, 98(3), 940-947.

Z. Y. He, K. Liao, X. Peng Li, S. Lin, J. W. Yang, and R. K. Mai (2014). "Natural frequency-based line fault location in HVDC lines." *IEEE Trans. Power Del.*, 29(2), 851-859.

S. Guobing, C. Xinlei, G. Shuping, S. Jiale, and L. Guang (2011). "Natural frequency based protection and fault location for VSC-HVDC transmission lines." *Proc. 2011 International Conference on Advanced Power System Automation and Protection (APAP)*, Beijing, China, 177-182.

S. Guobing, C. Xu, C. Xinlei, G. Shuping, and R. Mengbing (2014). "A Fault Location Method for VSC HVDC Transmission Lines based on Natural Frequency of Current." *International Journal of Electrical Power and Energy Systems*, 63, 347-352.

R. Polikar (1996). The Wavelet Tutorial. <http://users.rowan.edu/~polikar/WAVELETS>

D. C. Robertson, O. I. Camps, J. S. Mayer, and W. B. Gish (1996). "Wavelets and electromagnetic power system transients." *IEEE Trans. Power Del.*, 11(2), 1050-1058.

F. B. Costa, B. A. Souza, and N. S. D. Brito (2010). "Real-time detection of fault-induced transients in transmission lines." *IET Electron. Lett.*, 753-755.

H. Zhengyou, G. Shibin, C. Xiaoqin, Z. Jun, B. Zhiqian, and Q. Qingquan (2011). "Study of a new method for power system transients classification based on wavelet entropy and neural network." *International Journal of Electrical Power & Energy Systems*, 33(3), 402-410.

S. A. Gafoor, and P. V. R. Rao (2011). "A transient current based busbar protection scheme using Wavelet Transforms." *International Journal of Electrical Power & Energy Systems*, 33(4), 1049-1053.

N. Perera, and A. D. Rajapakse (2012). "Development and hardware implementation of a fault transients recognition system." *IEEE Trans. Power Del.*, 27(1), 40–52.

F. E. Perez, R. Aguilar, E. Orduna, J. Jager, and G. Guidi (2012). "High-speed non-unit transmission line protection using single-phase measurements and an adaptive wavelet: zone detection and fault classification." *IET Gen. Trans. Distrib.*, 6(7), 593–604.

K. D. Kerf, K. Srivastava, M. Reza, D. Bekaert, S. Cole, D. V. Hertem, and R. Belmans (2011), "Wavelet based Protection strategy for DC faults in Multi-terminal VSC HVDC Systems." *IET Generation, Transmission & Distribution*, 5(4), 496-503.

Y. M. Yeap, and A. Ukil (2014). "Wavelet based fault analysis in HVDC system," *Proc. IECON 2014 - 40th Annual Conference of the IEEE Industrial Electronics Society*, Dallas, TX, USA, 2472-2478.

J. Cheng, M. Guan, L. Tang, and H. Huang (2014). "A Fault Location Criterion for MTDC Transmission Lines using Transient Current Characteristics." *International Journal of Electrical Power & Energy Systems*, 61, 647-655.

S. H. A. Niaki, H. K. Karegar, and M. G. Monfared (2015). "A Novel Fault Detection Method for VSC HVDC Transmission system of Offshore Wind Farm." *International Journal of Electrical Power & Energy Systems*, 73, 475-483.

X. Zheng, T. Nengling, Y. Guangliang, and D. Haoyin (2012). "A Transient Protection Scheme for HVDC Transmission Line." *IEEE Trans. Power Del.*, 27(2), 718-724.

M. You, B. Zhang, and R. Cao (2009). "Study of non-unit transient-based protection for HVDC transmission lines." in *Proc. Asia-Pacific Power Energy Eng. Conf.*, 1–5.

S. Zhang, B. Zhang, M. You, and Z. Bo (2010). "Realization of the transient-based boundary protection for HVDC transmission lines based on high frequency energy criteria." in *Proc. Power Syst. Technol. Int. Conf.*, 1–7.

F. Kong, Z. Hao, S. Zhang, and B. Zhang (2014). "Development of a novel protection device for bipolar HVDC transmission lines." *IEEE Trans. Power Del.*, 29(5), 2270-2278.

Z. X. Dong, T. Neng-Ling, James S. Thorp, and Y. Guang-Liang (2012). "A Transient Harmonic Current Protection Scheme for HVDC Transmission line." *IEEE Trans. Power Del.*, 27(4), 2278-2285.

J. Wang, B. Berggren, K. Linden, J. Pan, and R. Nuqui (2015). "Multi-terminal DC system line protection requirement and high speed protection solutions." *Proc. 2015 CIGRE Symposium*, Cape Town, South Africa, 26-30.

J. Seneath, and A. D. Rajapakse (2016). "Fault Detection and Interruption in an Earthed HVDC Grid using ROCOV and Hybrid DC Breakers." *IEEE Trans. Power Del.*, 31(3), 973-981.

R. Li, L. Xu, and L. Yao (2017). "DC fault detection and location in meshed multiterminal HVDC systems based on DC reactor voltage change rate." *IEEE Trans. Power Del.*, 32(3), 1516-1526.

W. Leterme, J. Beerten, and D. V. Hertem (2016). "Non-unit protection of HVDC grids with inductive dc cable termination." *IEEE Trans. Power Del.*, 31(2), 820-828.

P. K. Dash, A. K. Pradhan, G. Panda, and A. C. Liew (2000). "Digital protection of power transmission lines in the presence of series connected FACTS devices." *Proc. IEEE Power Eng. Soc. Winter Meeting*, 3, 1967–1972.

M. Khederzadeh (2002). "The impact of FACTS device on digital multifunctional protective relays." *Proc. IEEE Power Eng. Soc. Transmission and Distribution Conf. Exhibit., Asia Pacific*, 3, 2043–2048.

W. G. Wang, X. G. Yin, J. Yu, X. Z. Duan, and D. S. Chen (1998). "The impact of TCSC on distance protection relay." *Proc. Int. Conf. Power System Technology (POWERCON '98)*, 1, 18–21.

K. El-Arroudi, G. Joos, and D. T. McGillis (2002). "Operation of impedance protection relays with the STATCOM." *IEEE Trans. Power Del.*, 17(2), 381–387.

T. S. Sidhu, R. K. Varma, P. K. Gangadharan, F. A. Albasri, and G. R. Ortiz (2005). "Performance of distance relays on shunt—FACTS compensated transmission lines." *IEEE Trans. Power Del.*, 20(3), 1837–1845.

M. V. Sham, and K. P. Vittal (2011). "Simulation studies on the distance relay performance in the presence of STATCOM." *Journal of Electrical Engineering*, 11(3), 11-18.

X. Zhou, H. Wang, R. K. Aggarwal, and P. Beaumont (2006). "Performance evaluation of a distance relay as applied to a transmission system with UPFC." *IEEE Trans. Power Del.*, 21(3), 1137–1147.

M. Alizadeh, N. Khodabakhshi-Javani, G. B. Gharehpetian, and H. A. Abyaneh (2015). "Performance analysis of distance relay in presence of unified interphase power controller and voltage-source converters-based inter phase controller." *IET Generation, Transmission & Distribution*, 9(13), 1642–1651.

H. Wang (2014). "The protection of transmission networks containing ac and dc circuits." Ph.D. Thesis, University of Bath.

L. He, C. C. Liu, A. Pitto, and D. Cirio (2014). "Distance Protection of AC Grid with HVDC-Connected Offshore Wind Generators." *IEEE Trans. Power Del.*, 29(2), 493-501.

M. M. Alam, H. Leite, J. Liang, and A. da Silva Carvalho (2017). "Effects of VSC based HVDC system on distance protection of transmission lines." *International Journal of Electrical Power & Energy Systems*, 92, 245-260.

M. M. Alam, H. Leite, N. Silva, and A. da Silva Carvalho (2017). "Performance evaluation of distance protection of transmission lines connected with VSC-HVDC system using closed-loop test in RTDS." *Electric Power Systems Research*, 152, 168-183.

F. Deng, and Z. Chen (2011). "An offshore wind farm with DC grid connection and its performance under power system transients." *Proc. IEEE Power Energy Soc. Gen. Meeting*, Detroit Michigan, USA, 1-7.

J. G. Slootweg, S. W. H. De Haan, H. Polinder, and W. L. Kling (2003). "General model for representing variable speed wind turbines in power system dynamics simulations." *IEEE Trans. Power Sys.*, 18(1), 144-151.

O. Anaya-Lara, D. Campos-Gaona, E. Moreno-Goytia, and G. Adam (2014). *Offshore Wind Energy Generation: Control, Protection and Integration to Electrical Systems*. John Wiley & Sons.

O. Carranza, E. Figueres, G. Garcerá, and R. Gonzalez-Medina (2013). "Analysis of the control structure of wind energy generation systems based on a permanent magnet synchronous generator." *Appl. Energy*, 103, 522-538.

Ohm, D. Y. (2000). Dynamic model of PM synchronous motors. *Drivetech, Inc., Blacksburg, Virginia, www.drivetechinc.com, 16.*

Krause, P., Wasynczuk, O., Sudhoff, S. D., and Pekarek, S. (2013). *Analysis of electric machinery and drive systems, 75*, John Wiley & Sons.

M. Cheah-mane, J. Liang, and N. Jenkins (2014). “Permanent magnet synchronous generator for wind turbines: modelling, control and inertial frequency response,” *Proc. 49th Int. Univ. Power Eng. Conf.*, Romania, 1-6.

Gamesa G128-5.0MW Offshore - 5 MW - Wind turbine. <https://en.wind-turbine-models.com> › *Turbines* › *Gamesa* › *G128-5.0MW Offshore*

C. Du (2003). “The control of VSC-HVDC and its use for large industrial power systems”. Ph.D. Thesis, Chalmers University of Technology, Sweden.

D. P. Dorantes, J. L. M. Morales, and M. H. Ángeles (2013). “A filter design methodology of a VSC-HVDC system.” *In Proc. 2013 IEEE International Autumn Meeting on Power Electronics and Computing (ROPEC)*, Mexico, 1-6.

G. Shi, X. Cai, and Z. Chen (2012). “Design and control of multi-terminal VSC-HVDC for large offshore wind farms.” *Przegląd Elektrotechniczny*, 88(12a), 264- 268.

C. Bajracharya, M. Molinas, J. A. Suul, and T. M. Undeland (2008). “Understanding of tuning techniques of converter controllers for VSC-HVDC.” *Proc. Nordic Workshop on Power and Ind. Electron. (NORPIE/2008)*, Espoo, Finland, 1-6.

L. Xu and S. Li (2010). “Analysis of HVDC control using conventional decoupled vector control technology.” *Proc. IEEE Power Energy Soc. Gen. Meeting*, Minnesota, USA, 1-8.

E. Kontos, R. T. Pinto, and P. Bauer (2013). “Control and protection of VSC-based multi-terminal DC networks.” M.S. Thesis, Delft Univ. of Technology, Netherlands.

T. W. Shire (2009). “VSC-HVDC based Network Reinforcement.” M.Sc. Thesis, Delft Univ. of Technology, Netherlands.

D. Jovcic, and K. Ahmed (2015). *High voltage direct current transmission: converters, systems and DC grids*, Scotland, UK, John Wiley & Sons.

PSCAD/EMTDC online help, version 4.2.1, Manitoba, Canada.

B. Gustavsen et al. (1999). “Transmission line models for the simulation of interaction phenomena between parallel AC and DC overhead lines.” *IPST’99 - International Conference on Power System Transients*, 61-68.

J. R. Marti (1982). “Accurate modeling of frequency-dependent transmission lines in electromagnetic transient simulations.” *IEEE Trans. Power App. Syst.*, 101(1), 147, 1982.

J. R. Marti, L. Marti, and H. W. Dommel (1993). “Transmission line models for steady-state and transients analysis.” *Proc. IEEE/Nat. Tech. Univ. Athens Power Tech. Conf.: Planning, Operation, Control of Today’s Electric Power Systems*, 744–750.

T. K. Vrana, S. Denetière, J. Jardini, Y. Yang, D. Jovcic, and H. Saad (2013). “The CIGRE B4 DC grid test system version 2013.” in *Electra*, 270(1), 10-19.

Chien, C. H., and Bucknall, R. W. (2007). Analysis of harmonics in subsea power transmission cables used in VSC–HVDC transmission systems operating under steady-state conditions. *IEEE Trans. Power Del.*, 22(4), 2489-2497.

N. Bayati, A. Hajizadeh, and M. Soltani. (2018). Protection in DC microgrids: a comparative review. *IET Smart Grid*, 1(3), 66-75.

W. Christiansen, and D. T. Johnsen (2006). Analysis of requirements in selected Grid Codes. *Prepared for Orsted-DTU Section of Electric Power Engineering, Technical University of Denmark (DTU)*.

M. R. I. Network (2013). "Collation of European grid codes." in version 01.

J. Hafner, and B. Jacobson (2011). "Proactive hybrid HVDC breakers—A key innovation for reliable HVDC grids." in *Proc. CIGRE*, Bologna, Italy, pp. 1-8.

M. H. Nadeem, X. Zheng, N. Tai, M. Gul, and S. Tahir (2018). "Analysis of Propagation Delay for Multi-Terminal High Voltage Direct Current Networks Interconnecting the Large-Scale Off-Shore Renewable Energy." *Energies*, 11(8), 2115.

K. Tahata et al. (2015). "HVDC circuit breakers for HVDC grid applications." *Proc. CIGRE AORC Tech. Meeting*, Tokyo, Japan.

D. Tzelepis, A. Dyśko, G. Fusiek, J. Nelson, P. Niewczas, D. Vozikis, P. Orr, N. Gordon, and C. Booth (2017). "Single-ended differential protection in MTDC networks using optical sensors." *IEEE Trans. Power Del.*, 32(3), 1605-1615.

J. Liu, N. Tai, C. Fan, and S. Chen (2017). "A Hybrid Current-Limiting Circuit for DC Line Fault in Multiterminal VSC-HVDC System." *IEEE Trans. Ind. Electron.*, 64(7), 5595-5607.

M. M. Eissa (2006). "Ground distance relay compensation based on fault resistance calculation." *IEEE Trans. Power Del.*, 21(4), 1830-1835.

Z. Y. Xu, S. F. Huang, L. Ran, J. F. Liu, Q. X. Yang, and J. L. He (2008). "A distance relay for a 1000-kV UHV transmission line." *IEEE Trans. Power Del.*, 23(4), 1795–1804.

M. Harikrishna (2010). "Development of quadrilateral relay for EHV/UHV lines." Master Thesis, Indian Institute of Technology, Roorkee.

E. Sorrentino, E. Rojas, and J. Hernández (2009), "Method for setting the resistive reach of quadrilateral characteristics of distance relays." *Proc. 44th Int. Univ. Power Engineering Conf.*, Glasgow, U.K., 1–5.

J. Ma, X. Xiang, P. Li, Z. Deng, & J. S. Thorp (2016). "Adaptive distance protection scheme with quadrilateral characteristic for extremely high-voltage/ultra-high-voltage transmission line." *IET Generation, Transmission & Distribution*, 11(7), 1624-1633.

M. Zellagui, and A. Chaghi (2013). "Impact of SVC devices on distance protection setting zones in 400 kV transmission line." *UPB Scientific Bulletin, Series C: Electrical Engineering*, 75(2), 249-262.

N. Chauhan, M. Tripathy, and R. P. Maheshwari (2014). "Performance Evaluation of Mho and Quadrilateral Characteristic Relays on UPFC Incorporated Transmission Line." *International Journal of Electronic and Electrical Engineering*, 7(8), 827-835.

L. He, and C. C. Liu (2013). "Effects of HVDC connection for offshore wind turbines on AC grid protection." *Proc. 2013 IEEE Power and Energy Society General Meeting (PES)*, Vancouver, BC, Canada, 1-5.

M. M. Alam (2018). "Distance Protection of Networks Supplied from VSC-HVDC," Ph.D. Thesis, University of Porto, Portugal.

Sub-committee on relay/protection under task force for power system analysis under contingencies (2014). "Model setting calculations for typical IEDs line protection setting guide lines protection system audit checklist recommendation for protection management." New Delhi, India.

User Manual of CSC-101 Line Protection IED (2012), Sifang Automation, Beijing, China.

K. Pipaliya, and V. Makwana (2015). "Modeling and Simulation of Digital Distance Protection Scheme for Quadrilateral Characteristics using PSCAD." *International Journal of Advance Engineering and Research Development (IJAERD)*, 2(5), 1238-1246.

PUBLICATIONS BASED ON THESIS

Refereed Journals:

1. M. Mohan, and K. Panduranga Vittal, "DC Fault Protection in Multi-terminal VSC-Based HVDC Transmission Systems with Current Limiting Reactors," *Journal of Electrical Engineering & Technology, (JEET) - Springer*, vol. 14, no. 1, pp. 1-12, Jan. 2019. (SCIE and Scopus).
2. M. Mohan, and K. Panduranga Vittal, "Performance Evaluation of Distance Relay in the Presence of Voltage Source Converters-Based HVDC Systems," *Journal of Electrical Engineering & Technology (JEET) - Springer*, vol. 14, no. 1, pp. 69-83, Jan. 2019. (SCIE and Scopus).
3. M. Mohan, and K. Panduranga Vittal, "Design and Simulation of Quadrilateral Relays in AC Transmission Lines with VSC-Based HVDC Systems Under Phase-To-Ground Fault Condition," *University POLITEHNICA of Bucharest Scientific Bulletin, Series C: Electrical Engineering and Computer Science*. vol. 81, no. 3, pp. 153-168, Aug. 2019. (ESCI and Scopus).
4. M. Mohan, and K. Panduranga Vittal, "Design and Transient Studies on Multi-terminal VSC-HVDC Systems Interconnecting Offshore Wind Farms," *ECTI Transactions on Electrical Engineering, Electronics, and Communications*, vol. 17, no. 2, pp. 182-193, Aug. 2019. (Scopus).

Conference Proceedings:

1. M. Mohan, and K. Panduranga Vittal, "Modeling and Simulation of PMSG-Based Wind Power Generation System," in *Proc. 3rd IEEE International Conference on Recent Trends in Electronics, Information and Communication Technology (RTEICT-2018)*, Bangalore, Karnataka, India, May 2018, pp. 57-62. (Scopus).
2. M. Mohan, and K. Panduranga Vittal, "Modeling and simulation studies on performance evaluation of three-terminal VSC-HVDC link connected offshore wind farms," in *Proc. IEEE International Conference on Energy, Communication, Data Analytics and Soft Computing (ICECDS-2017)*, Chennai, Tamil Nadu, India, Aug. 2017, pp. 473-478. (Scopus).

3. Snigdha Tale, M. Mohan, and K. P. Vittal, "Performance analysis of distance relay in an AC grid with VSC-HVDC connection," in *Proc. IEEE International Conference on Intelligent Computing, Instrumentation and Control Technologies (ICICT-2017)*, Kannur, Kerala, India, July 2017, pp. 1363-1368. (Scopus).
4. Mohan M, and K. P. Vittal, "Simulation of HVDC Transmission System in PSCAD/EMTDC and Protection Scheme under Fault Conditions," in *Proc. National Conference on Power System Protection*, Central Power Research Institute (CPRI), Bangalore, Karnataka, India, Feb. 2015, pp. 105-112.

CURRICULUM VITAE

Name: M. Mohan

Date of birth: May 4, 1989

E-mail: mmohanphd@gmail.com

Mobile: +91-9916649710



ADDRESS

S/o: C. Muniappan

Nathapatti (Post), Vedasandur (Taluk)

Dindigul (District), Tamil Nadu – 624710, India.

EDUCATION

- Master of Engineering (M.E.) in Power Systems Engineering
(July 2010 – May 2012)
Institute: Thiagarajar College of Engineering (TCE), Madurai, (Government-aided Autonomous Institution Affiliated to Anna University, Chennai), Tamil Nadu.
CGPA: 8.78/10 (Class Obtained: First Class with Distinction)

- Bachelor of Engineering (B.E.) in Electrical and Electronics Engineering
(July 2006 – May 2010)
Institute: Christian College of Engineering and Technology (CCET), Dindigul,
(Affiliated to Anna University, Chennai), Tamil Nadu.
Percentage: 73 (Class Obtained: First Class)

TEACHING EXPERIENCE

- Assistant Professor, Department of Electrical and Electronics Engineering, Christian College of Engineering and Technology (CCET), Dindigul, Tamil Nadu.
Duration: June 2012 – May 2014 (02 years)